Computational modeling of calcium diffusion reveals nanoscale biophysics in neuronal spines

Kanishka Chathuranga Basnayake Basnayake Mudiyanselage

PSL
UNIVERSITÉ PARIS

THÈSE DE DOCTORAT
DE L'UNIVERSITÉ PSL

Préparée à l'ÉCOLE NORMALE SUPÉRIEURE

Computational modeling of calcium diffusion reveals nanoscale biophysics in neuronal spines

Soutenue par
BASNAYAKE MUDIYANSELAGE Kanishka Chathuranga Basnayake
Le 15 décembre 2020

Ecole doctorale n° 564
Physique en Île-de-France

Spécialité
Biophysique

ENS
ÉCOLE NORMALE SUPÉRIEURE

Composition du jury :

David, BENSIMON Directeur de recherche École Normale Supérieure University of California Los Angeles	*Président du jury*
Renaud, JOLIVET Professeur University of Geneva	*Rapporteur*
Krasimira, TSANEVA-ATANASOVA Professeur University of Exeter	*Rapporteur*
David, DIGREGORIO Directeur de recherche Institut Pasteur	*Examinateur*
Dmitri, RUSAKOV Professeur University College London	*Examinateur*
Peter, JEDLICKA Professeur University of Giessen Goethe University Frankfurt	*Examinateur*
Yulia, TIMOFEEVA Professeur University of Warwick	*Examinateur*
David, HOLCMAN Directeur de recherche École Normale Supérieure	*Directeur de thèse*

"Experiments are the only means of knowledge at our disposal. The rest is poetry, imagination."

Max Planck

Acknowledgements

First and foremost, I am extremely grateful to my thesis advisor Professor David Holcman for providing me the opportunity to join the group and for the continuous support and invaluable scientific feedback during the whole PhD.

I would also like to thank for the experimental collaborations with the groups headed by Professor Eduard Korkotian and Professor Nathalie Rouach that immensely improved the scientific quality of my work. I am very grateful also to the collaborators and co-authors: the late Professor Zeev Schuss, Dr. David Mazaud, Dr. Alexis Bemelmans, Lilia Kushnireva and Akim Hubl for the contributions towards the scientific achievements during the PhD.

My gratitude extends to the president of the jury Professor David Bensimon, the two rapporteurs Professor Krasimira Tsaneva-Atanasova and Professor Renaud Jolivet as well as to all examiners: Professor Dmitri Rusakov, Professor David DiGregorio, Professor Peter Jedlička and Professor Yulia Timofeeva for the insightful and encouraging remarks about the manuscript and the defense.

In addition, I would like to thank everyone of my group, particularly Dr. Jürgen Reingruber, the alumni Drs. Claire Guerrier, Jérôme Cartailler, and Ofir Shukron as well as the current members Dr. Andrea Papale, soon-to-be Drs. Lou Zonca, Matteo Dora, Annia Abtout, Suney Toste, Christophe Sun, and the masters interns during all these years for their remarkable support and good cheer.

I am also thankful to my previous advisors and mentors, particularly Professor Taishin Nomura, Professor Ichiro Fujita, Professor Izumi Ohzawa, Professor Hiromichi Sato, Professor Keiji Imoto, Professor Satoshi Shimegi, Professor Naito Tomoyuki, Dr. Willem Wybo, Dr. Pierre Yger, Professor Kirthi Walgama, Professor Danushka Bollegala, Professor Thevamaran Ramathasan, Professor Robert O'Mochain and Dr. Tyler LeBrun. Their teaching, feedback and encouragement during my undergraduate and postgraduate studies have helped enormously to reach this milestone of my academic career.

Furthermore, I would also like to thank my family: particularly my parents Sriya and Warnasiri, my life partner Charitha, my sister Shanika, and Isuru malli for their tremendous encouragement and support during all these years.

Last but not least, I would like to express my gratitude to all funding agencies: the Sri Lankan Ministry of Education, Japanese Government Monbukagakusho Scholarship Programme, International Excellence Fellowship of EPFL Switzerland and the French Fondation Recherche Médicale that have allowed me continuously to access free education and research opportunities in this long academic journey totalling 27 years.

Lay abstract

Dendritic spines that form the receiving terminals of neuronal signals are regulated biochemically by calcium. Fast calcium transmissions in spines remain poorly understood as they occur in a few milliseconds and cannot be explained by classical diffusion theory. I developed mathematical models and stochastic simulations based on extreme statistics to compute the time taken by the fastest ions to arrive at a target via an optimal path. This novel framework not only explained fast calcium transients in spines, but also predicted accurately the spatial distributions of three calcium channels in spines controlling intake, storage and release. I also modeled their interplay during calcium regulation that could lead to synaptic changes underlying learning and memory. These new paradigms of nanoscale molecular organization and extreme statistics could also characterize the timescales of many other biophysical processes driven by random arrivals of the fastest particles to a small target.

Résumé de thèse pour le grand publique

La plupart des terminaux post-synaptiques neuronaux sont formés par des épines dendritiques dont l'activité biochimique est régulée par le calcium. Les transmissions rapides de calcium dans les épines se produisent en quelques millisecondes et ne peuvent pas être expliquées par la théorie de la diffusion et restent donc mal comprises. J'ai développé des modèles mathématiques et des simulations basées sur les statistiques extrêmes pour calculer le temps mis par les ions les plus rapides pour arriver à une cible. Ce nouveau cadre explique les activités transitoires rapides du calcium dans les épines et il prédit également avec précision l'emplacement des canaux contrôlant l'apport, le stockage et la libération du calcium. Ces idées, issues de l'organisation moléculaire à l'ordre nanométrique et des statistiques extrêmes pourraient également être appliquées pour déterminer les différentes échelles temporelles de nombreux processus biophysiques, activés par les particules les plus rapides.

Abstract

Post-synaptic transmission of neuronal synapses can occur on a dendritic spine, a microdomain revealed more than a century ago. Calcium in spines is known to regulate synaptic plasticity, a process that underlies learning and memory. With strong calcium influxes similar to synaptic inputs, a very fast signal transmission occurs from the spine's head to its base in a timescale of a few milliseconds that could not be explained with classical diffusion theory. During my thesis, I developed a framework of computational physics and stochastic modeling that could explain these fast responses based on extreme statistics of the times taken by diffusing particles to arrive at a distant, autocatalytic reaction site.

Through this novel framework, I showed that when many calcium ions flow into a spine head, the fastest among them arrive at the base and trigger an amplification process in the same timescale revealed by fluorescence imaging. The amplification arises from calcium-induced calcium release (CICR) upon the activation of ryanodine receptors (RyRs) that release calcium from the organelle called spine apparatus (SA)—the spine's internal calcium store.

I also showed how a calcium-deprived SA after a CICR event could get replenished from inputs to the spine heads without triggering another RyR-induced outflow. I found two main conditions that guarantee refilling: (1) a weak calcium influx from ORAI channels into the spine, and (2) a close proximity of a few tens of nanometers between SERCA pumps that refill SA stores and ORAI inputs. Thereby I predicted computationally the nanoscale geometric organization of calcium regulators in spines: RyRs are located at the SA base; SERCA pumps are on the SA head, while ORAI channels colocalize with SERCA pumps. These predictions were verified using STED super-resolution imaging of immunostained in vivo slices of mouse hippocampal neurons.

I extended the theoretical framework, showing that when N independent and identically distributed Brownian particles search for a small target in a bounded domain, the timescale set by the first few arrivers is much faster in general than the mean first passage time of N particles. I also confirmed that in 1, 2, and 3 dimensions, fastest arrival times decrease logarithmically with the number of searchers N. Moreover, I analyzed the trajectories of the fastest arrivers in 2D confined domains and showed that even when there are obstacles in the shortest path between the source of the random searchers and

their small target, the trajectories taken by the fastest arrivers tend to concentrate around the shortest possible geodesic between the source and the target. While the trajectories chosen by the first arrivers converge to the optimal path with increasing N, both the first and second moments of the first arrival times decrease.

Consequently, these results propose the new redundancy principle in biology, where starting from stochastic regimes satisfying the diffusion assumptions, search processes could utilize a highest possible number of copies of a random explorator to converge deterministically towards optimality in signal transmission speed. I also verified that the arrival time distributions of such phenomena remain largely independent from the domain geometry other than the shortest possible distance from the source to the target. However, when the target is hidden inside a cusp-like geometry, I showed that the first arrival times depend also on properties such as the curvature of the opening.

These insights from my thesis propose that for determining timescales of activation processes with many copies of the same molecule, extremely fast arrival rates should be considered instead of the classical Smoluchowski's reaction rate used in Gillespie-like algorithms. Such computations would not only delineate the biochemical dynamics in neurons, but would also quantify timescales of other biophysical processes driven by the fastest arrivals of random particles.

Résumé

La transmission neuronale post-synaptique peut se produire sur les épines dendritiques. La dynamique du calcium dans les épines régule la plasticité synaptique, un processus qui sous-tend l'apprentissage et la mémoire. Lors de forts afflux de calcium comme lors de l'activation d'une synapse, une transmission de signal très rapide de l'ordre de quelques millisecondes se produit de la tête à la base de l'épine. Ce phénomène ne peut pas être expliqué par la théorie de la diffusion classique. Dans ma thèse, j'ai développé un cadre de biophysique computationnelle qui peut expliquer ces réponses à partir des statistiques extrêmes des temps mis par les particules les plus rapides à arriver par diffusion à une cible éloignée.

Dans ce cadre, j'ai montré que lorsque de nombreux ions de calcium entrent dans la tête de l'épine, les plus rapides arrivent à la base en quelques millisecondes. Cela conduit à un processus d'amplification de la libération de calcium induite par le calcium (CICR) par l'ouverture des récepteurs de Ryanodine (RyR) qui libèrent le calcium du stockage interne de l'épine appelé "spine apparatus" (SA).

J'ai aussi montré comment un SA vidé de son calcium après un événement CICR pouvait se remplir à partir d'influx calciques sans que les RyR n'induisent un épuisement du stockage en parallèle. Deux conditions garantissent le remplissage: (1) un faible afflux de calcium des canaux ORAI dans l'épine, et (2) une proximité de quelques dizaines de nanomètres entre les afflux ORAI et les pompes SERCA qui remplissent le stockage du SA.

J'ai ainsi prédit l'organisation géométrique à l'échelle nanométrique des régulateurs du calcium dans les épines dendritiques: les RyR sont situés à la base du SA, les pompes SERCA se trouvent sur la tête du SA et les canaux ORAI se colocalisent avec les pompes SERCA. Ces prédictions ont été vérifiées en utilisant l'immuno-marquage et l'imagerie super-résolution dans des neurones de l'hippocampe de la souris.

J'ai élargi le cadre théorique, montrant que lorsque N particules browniennes indépendantes et identiquement distribuées cherchent une petite cible, le temps mis par les premiers arrivants est beaucoup plus court que le temps moyen de premier passage. J'ai également confirmé que les temps d'arrivée les plus rapides diminuent logarithmiquement avec N.

En outre, j'ai montré que même lorsqu'il y a des obstacles sur le chemin le plus court entre la source des N chercheurs aléatoires initiaux et leur petite cible, les trajectoires

empruntées par les particules les plus rapides ont tendance à se concentrer autour de la géodésique entre la source et la cible. Lorsque les trajectoires convergent vers le chemin optimal avec l'augmentation de N, la moyenne et la variance des premiers temps d'arrivée diminuent.

Ces résultats introduisent donc un nouveau principe de redondance : les processus de recherche biologique rapide, basés sur des régimes stochastiques de diffusion, pourraient converger de manière déterministe vers l'optimalité temporelle en utilisant le plus grand nombre possible de copies d'un explorateur aléatoire. J'ai également vérifié que les premiers temps d'arrivée de tels phénomènes dépendent principalement de la géodésique et qu'ils restent largement indépendants du reste de la géométrie du domaine. Cependant, lorsque la cible est cachée à l'intérieur d'une géométrie de type cuspide, ils dépendent également de propriétés telles que la courbure de l'ouverture.

En conclusion, les idées développées dans ma thèse montrent que pour déterminer les échelles de temps des processus d'activation qui dépendent de nombreuses copies de la même molécule, les temps de première arrivée devraient être utilisés à la place du taux moyen de réaction chimique de Smoluchowski. Ces calculs s'appliquent à la dynamique calcique dans les neurones mais ils pourraient également quantifier les échelles temporelles d'autres processus biophysiques basés sur l'arrivée des particules aléatoires les plus rapides.

Résumé des résultats

À partir d'analyses asymptotiques et de simulations de particules browniennes diffusant en 1, 2 et 3 dimensions, j'ai montré que

- Le temps $t^{(1)}$ pris par la première parmi N particules browniennes (démarrant simultanément) pour trouver une petite cible diminue de façon logarithmique lorsque N augmente.
- Le temps $t^{(1)}$ est largement indépendant des paramètres caractérisant la géométrie du domaine autres que la distance de la source à la cible.
- La dépendance logarithmique des temps d'arrivée par rapport à N se généralise également au temps $t^{(2)}$, mis par les deux premières particules (parmi $N >> 2$) pour arriver à une petite cible.
- Pour un domaine 3D confiné, de la forme d'une épine dendritique (avec une tête sphérique reliée à un col fin), le temps de diffusion des premiers ions calcium depuis la tête prend en moyenne 1 à 2 millisecondes pour atteindre un récepteur situé à la base, lorsque $N = 500$ à 1000 ions étaient initialement présents dans la tête de l'épine.

Grâce à des simulations stochastiques de diffusion dans des domaines 2D confinés et des méthodes d'analyse de trajectoires, j'ai trouvé que:

- Lorsqu'il y a des obstacles réfléchissants sur le chemin le plus court entre la source des N chercheurs aléatoires initiaux et leur petite cible, la trajectoire empruntée par les particules les plus rapides à arriver se concentre autour du chemin le plus court possible entre la source et la cible.
- La moyenne et la variance des premiers temps d'arrivée $t^{(1)}$, ainsi que la distance (en norme L1) entre la trajectoire optimale et les trajectoires choisies par les premières particules arrivées diminuent avec N.
- A l'instar des domaines sans obstacles, les distributions des temps d'arrivée sont largement indépendantes de la géométrie du domaine en dehors de la géodésique la plus courte de la source à la cible. Cependant, lorsque la cible reste cachée à

l'intérieur d'une ouverture de cuspide étroite, les temps d'arrivée du premier parmi N sont légèrement modifiés par des propriétés telles que la courbure de l'ouverture, mais obéissent toujours à la décroissance logarithmique avec l'augmentation de N.

- L'évasion la plus rapide des domaines de type cuspide et l'optimisation de chemin avec des obstacles, que j'ai approchés ici avec des simulations discrètes, relèvent des régimes stochastiques qui satisfont les hypothèses de mouvement brownien. Par conséquent, les arrivées les plus rapides sont bien dues à l'optimisation de la trajectoire, et pas à des trajectoires effectuant de très grands pas à chaque étape et échantillonnées à partir des queues de la distribution normale.

Grâce à des simulations stochastiques de diffusion du calcium à l'intérieur d'un modèle géométrique d'une épine dendritique, j'ai trouvé que:

- Les récepteurs Ryanodine (RyR) sont situés à la base du *Spine Apparatus* (SA), en groupe d'environ 36 récepteurs, tandis que les pompes SERCA sont réparties dans la tête du SA.

- Suite à la relâche instantanée de calcium dans la tête de l'épine, les deux premiers ions calcium arrivant au même RyR prennent environ 2 à 4 millisecondes. Cela conduit à une amplification immédiate du signal calcique par une libération de calcium induite par le calcium (CICR) par l'activation des autres RyR, ce qui pourrait expliquer les échelles de temps observées expérimentalement.

- La distribution des temps d'initiation du CICR dépend du nombre d'ions calcium initialement libérés dans la tête de l'épine. Ces temps ne dépendent que peu de la géométrie de l'épine ou la présence de SA.

- A l'arrivée de deux ions calcium, chaque ouverture d'un RyR se produit après un délai d'environ 0,25 ms. Le nombre total d'ions libérés par un seul RyR est d'environ 20 ions par cycle de libération. L'estimation supérieure du nombre de pompes calciques dans la tête de l'épine est de 50.

- La disposition nanométrique de l'épine permet non seulement des temps d'activation rapides de l'amplification du signal de calcium dans la base, mais assure également que le signal de calcium se propage principalement de manière unidirectionnelle de la tête à la base, et seulement de façon minimale dans la direction opposée.

A travers l'analyse d'un modèle de champ moyen, ainsi que des simulations stochastiques similaires de diffusion mais avec différentes conditions d'entrée du calcium dans l'épine dendritique, j'ai trouvé que:

- Des courants calciques faibles sur des échelles de temps lentes ($\approx$ 300-500 ions en quelques secondes) de type *Store Operated Calcium Entry* (SOCE) remplissent les réserves de calcium du SA.

- Par rapport à de fortes injections de calcium avec des échelles de temps rapides, similaires à l'entrée de calcium dans le cas d'une activation synaptique ($\approx$ 500-1000 ions en quelques millisecondes), les entrées de type SOCE ont beaucoup moins de chances de déclencher les RyRs pour épuiser les réserves de calcium du SA. Cependant, le temps conditionnel moyen pour que le SOCE ouvre un RyR est extrêmement long par rapport à celui des entrées fortes. Par conséquent, pendant les entrées de SOCE, il est très probable que le stock de calcium du SA soit préservé.

- Les pompes de surface situées sur les têtes des épines modulent les processus de remplissage et d'épuisement du calcium du SA: leur présence réduit la probabilité d'activation d'un RyR et retarde également leur temps d'ouverture conditionnel.

- Afin d'augmenter l'efficacité du remplissage, les pompes SERCA sur la membrane du SA sont situées à une courte distance, de quelques dizaines de nanomètres, des canaux ORAI où le SOCE se produit à travers la membrane plasmique.

- Lors des protocoles expérimentaux induisant la potentialisation synaptique à long terme (LTP) et la dépression synaptique à long terme (LTD), l'organisation nanométrique des épines sous-tend les différences de concentrations locales de calcium, notamment au niveau de sa base.

List of Publications

Research articles:

- **Basnayake, K.**, Mazaud, D., Kushnivera, L., Rouach, N., Korkotian, E. & Holcman, D. (2021). Nanoscale molecular architecture controls calcium diffusion and ER replenishment in dendritic spines. *Science Advances*, 7(38): eabh1376. https://doi.org/10.1126/sciadv.abh1376

- **Basnayake, K.**, & Holcman D. (2020). Extreme escape from a cusp: When does geometry matter for the fastest Brownian particles moving in crowded cellular environments? *The Journal of Chemical Physics* 152.13: 134104. https://doi.org/10.1063/5.0002030

- **Basnayake, K.**, Mazaud, D., Bemelmans, A., Rouach, N., Korkotian, E. & Holcman, D. (2019). Fast calcium transients in neuronal spines driven by extreme statistics. *PLOS Biology* 17.6: e2006202. https://doi.org/10.1371/journal.pbio.2006202

- **Basnayake, K.**, Schuss, Z., & Holcman, D. (2019). Asymptotic formulas for extreme statistics of escape times in 1, 2 and 3-dimensions. *Journal of Nonlinear Science*, 29(2), 461-499. https://doi.org/10.1007/s00332-018-9493-7

- **Basnayake, K.**, Hubl, A., Schuss, Z. & Holcman, D. (2018). Extreme Narrow Escape: Shortest paths for the first particles among n to reach a target window. *Physics Letters A*, 382(48), pp.3449-3454. https://doi.org/10.1016/j.physleta.2018.09.040

Reviews and comments:

- **Basnayake, K.**, & Holcman, D. (2019). Fastest among equals: a novel paradigm in biology. Reply to comments: Redundancy principle and the role of extreme statistics in molecular and cellular biology. *Physics of life reviews*, 28, 96-99. https://doi.org/10.1016/j.plrev.2019.03.017

- Schuss, Z., **Basnayake, K.** & Holcman, D. (2019). Redundancy principle and the role of extreme statistics in molecular and cellular biology. *Physics of Life Reviews*, 28, 52-79. https://doi.org/10.1016/j.plrev.2019.01.001

Acronyms

ER	Endoplasmic Reticulum
SA	Spine Apparatus
SP	Synaptopodin
(s)ER	(smooth) Endoplasmic Reticulum
RyR(s)	Ryanodine Receptor(s)
IP3Rs	Inositol trisphosphate receptors
SERCA	Sarco/Endoplasmic Reticulum Calcium^{2+}-ATPase,
CICR	Calcium-induced calcium release
SOCE	Store-Operated Calcium Entry
AMPAR	Alpha-amino-3-hydroxy-5-methyl-4-isoxazolepropionic acid receptor
NMDAR	N-methyl-D-aspartate receptor
STIM	Stromal Interaction Molecule
LTP	Long Term Potentiation
LTD	Long Term Depression
PDE	Partial Differential Equation
SDE	Stochastic Differential Equation
NEP	Narrow Escape Problem
NET	Narrow Escape Theory/Time
MFPT	Mean First Passage Time

Contents

Introduction

In this chapter, I introduce first the biological questions related to neuronal calcium dynamics that are addressed in the thesis. Next I outline the computational and mathematical concepts utilised for solving these problems. I then summarize my main results obtained during the thesis, combining both mathematical and biophysical findings from the subsequent chapters 1-7 based on my published work.

0.1 Synaptic transmission in dendritic spines

Unraveling the computational complexity of the brain

The human brain is undoubtedly the most complex mass of protoplasm on earth. Its complexity is first due to its structure, which is made of nearly 100 billion each of neurons and glia cells [1], with the former being interconnected through more than 100 trillion connections called synapses [2]. Functionally, it is with this 1.5kg protoplasm (working with the same wattage as a table lamp) that we have conceived the nearly 100 billion light years of the known universe [3].

Learning more about the brain at any level would not only serve as a fundamental scientific discovery, but would also make it possible to understand its pathologies and potential damage by disease. This would lead certainly to medical cures and protections of the brain, and towards improvements of its performance in best-case scenarios. Moreover, understanding the efficient and sophisticated signal processing mechanisms in the brain could potentially enrich the computational technologies such as biologically inspired computing.

Taking the visual system as an example, in 1982, David Marr formalised the study of the brain's information processing with the framework known as Marr's Tri-Level Hypothesis [4]. The first of the three levels introduced in this framework was the *representational* level that involves understanding "what" computational problems does the brain solve. Second, the *algorithmic* level involves understanding the "how" of the executed problem-solving process. Finally, the *hardware* level is related to the physical implementation of cellular and molecular structures.

The biophysical regulation of calcium dynamics studied in my thesis particularly falls into this last level, which could in turn decide the algorithmic capabilities that eventually determine cognitive functions. In this thesis, since the primary focus is on the neurons

from the brain area of hippocampus, the underlying cognitive functions involve memory, learning and spatial navigation [5].

Neurotransmission in chemical synapses

When the brain is studied as a massive information processing machine, the signals are carried by numerous types of ions and molecules belonging to classes such as neurotransmitters, secondary messengers, hormones, etc. The synaptic connection between two neurons typically consists of a pre-synaptic (sending) terminal located on the axon of one neuron and the post-synaptic (receiving) terminal on the dendrite of another neuron. The major type of excitatory post-synaptic terminals are the dendritic spines, which are protrusions from the dendrite formed by a thin neck and a bulky head [6]. There is a spatial separation of a few nanometers between pre- and post-synaptic terminals, which is termed the synaptic cleft.

An excitatory signalling event between two terminals involves a release of neurotransmitter chemicals (eg: glutamate) from the pre-synaptic terminal into the synaptic cleft. The head of a dendritic spine has an area (termed post-synaptic density) densely covered with receptor proteins (eg: AMPA, NMDA) that are activated by the binding of neurotransmitters. Such activation events of receptors lead to trans-membrane influxes of cations (eg: Na^+, K^+ and Ca^{2+}) from the extracellular space into the dendritic spine [7].

Consequences of synaptic calcium signalling

Among all cation currents, calcium plays a role ubiquitously important across different signalling cascades that particularly result in different long-term consequences on the synapse [8–10]. Specially, the amplitude and timescale of the calcium signal can change the way how the synapse responds to future inputs, which is denoted by the strengths of the influx currents drawn into the spine under the same input conditions. The phenomenon in which the currents get stronger for prolonged timescales (longer than a few hours) is termed long-term potentiation (LTP), whereas an analogous weakening of the synapse is a long-term depression (LTD). In hippocampal neurons, LTP and LTD are considered the fundamental physiological mechanism underlying memory and learning [11].

Calcium regulation in dendritic spines

In terms of calcium regulation, the dendritic spine functions as a complex signalling unit governed by its molecular organisation. In addition to the calcium influx channels located on its membrane such as glutamate receptors and voltage-sensitive calcium channels, spines also contain calcium buffers and pumps that sequester and regulate its calcium concentration [12, 13]. During synaptic inputs and experimental stimulation protocols, calcium transients inside spines are determined by the interplay in the dynamics of these different molecular players.

In addition to calcium influx and outflux channels, an important role in regulating calcium dynamics in dendritic spines is played by its internal calcium stores. The organelle called

spine apparatus (SA), which is often found inside spines as a derivative of the smooth endoplasmic reticulum (ER) could serve as a calcium store in spines (Fig.1) [14].

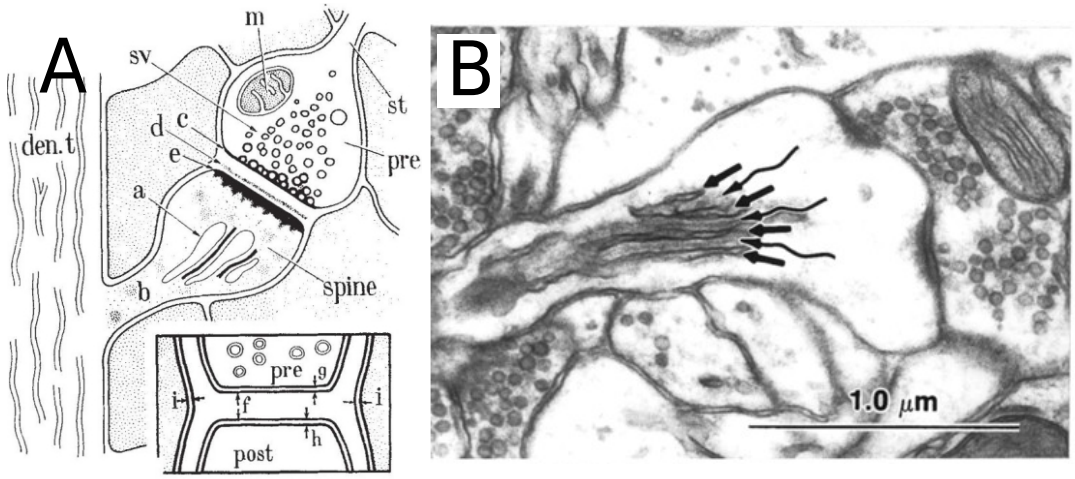

Figure 1: **(A).** First known illustration of SA (shown by (a) here) by E. Gray in 1959 [15][a]. No function was ascribed to it at that time. **(B).** Electron micrograph of a dendritic spine containing spine apparatus in a hippocampal CA1 neuron. Image is taken from Spacek et al.(1997) [16][b].

An experimental verification about the presence of spine apparatus is provided by the protein called synaptopodin (SP): SA is predominantly present in spines tested positive for SP, while SP negative ones lack spine apparatus [17]. In addition, cognitive importance of SA towards learning and memory in the mammalian brain has been confirmed also through behavioral experiments under the conditions of synapdopodin deficiency [18, 19].

Dynamics of spine apparatus calcium stores

In terms of molecular machinery associated to ER calcium stores, IP3 and ryanodine receptors (RyRs) have been identified as two channels that release calcium from the stores into the spine [20] (RyR2 is predominant in the brain among all three isoforms RyR1-3 expressed [21]). In contrast to the slow calcium dynamics induced by IP3 receptors that are mostly present in dendritic shafts [22, 23], RyRs present in the dendritic spines of hippocampal neurons play an instrumental role in regulating the spines' fast response to glutamate inputs [24].
In previous studies of cardiac myocytes, RyRs have been found to form nano-clusters [25] and they generate an auto-catalytic calcium release triggered and amplified by calcium itself. This phenomenon is known as calcium-induced calcium release (CICR) [26]. However in dendritic spines, the precise nanoscale organisation of RyRs to generate CICR is not known (Fig.2).

[a]Reproduced with permission from *Nature*. Order no: 4992690279119
[b]Reproduced with permission from *The Journal of Neuroscience*. Order license ID = 1092354-2

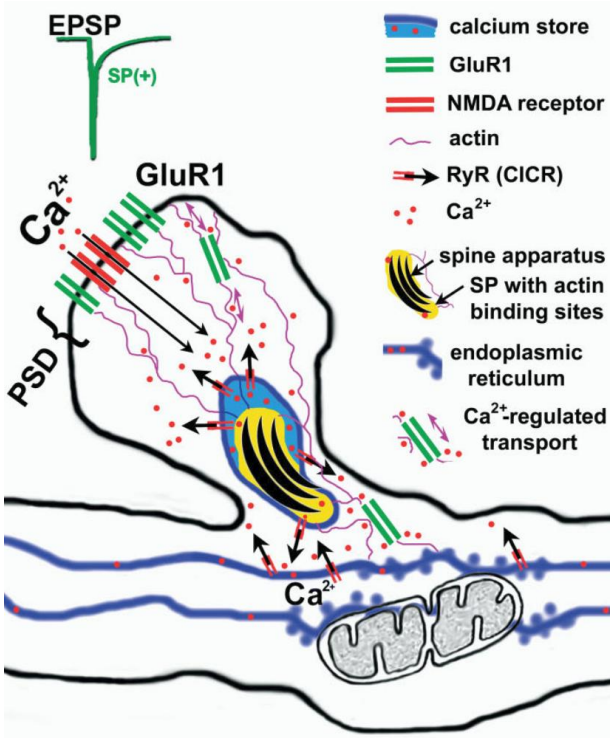

Figure 2: Schematic of a synaptopodin-positive spine published in Vlachos et al.(2009) [19][a]). The spine contains spine apparatus and RyRs. A major goal of the thesis is to investigate the precise location and the dynamic interplay of different molecular components outlined in this schematic.

When the calcium level of internal storage becomes low, STIM transmembrane proteins (encoded by the homologue STIM1 [27]) located within the ER stores are capable of sensing this concentration drop. Through a complex molecular interaction, this sensing is transformed eventually to an inward trans-membrane flow of calcium into the spines through ORAI channels [28] (encoded primarily by the homologue ORAI1 [29]). This process is termed Store-operated calcium entry (SOCE), and has critical physiological implications [30, 31]. Calcium entering through this STIM-ORAI pathway could then refill the stores through SERCA pumps (encoded as SERCA3 isoform by the homologue SERCA3 in non-muscular cells), an important molecular device associated with SA [32]. A parallel goal of this thesis is to understand these calcium release (CICR) and refilling (SOCE) pathways, as well as the effects of their interplay towards long-term calcium regulation and synaptic changes. Particularly, I examine the timescales of the molecular components in these pathways and model the role of their nanoscale geometric organisation within the spine.

[a]Reproduced with permission from *The Journal of Neuroscience*. Order license ID = 1092354-1

0.2 Stochastic analysis and simulations

Mathematical modeling and stochastic simulations are the major tools used in this thesis to understand the calcium dynamics of dendritic spines. I summarize here the principal notions in mathematical and computational physics utilised in the subsequent sections.

Einstein's theory of diffusion of and Langevin Equation

To model the movement of calcium ions in spines, I use the stochastic description of Brownian motion. The early work of Boltzmann first identified Brownian motion as a stochastic process, and its theoretical framework was then developed with the pioneering contributions from Einstein, Langevin and Smoluchowski. Particularly, in 1905, Einstein [33] derived the well-known partial differential equation (PDE) for particles moving irregularly due to thermal fluctuations under a diffusion coefficient D:

$$\frac{\partial p(x,t)}{\partial t} = D\frac{\partial^2 p(x,t)}{\partial x^2} \tag{1}$$

The solution of this equation results in the formula for the density function $p(x,t)$ that denote the probability of finding a one-dimensional Brownian particle at location x at the elapse of time t:

$$p(x,t) = \frac{1}{\sqrt{4\pi Dt}}\exp(-\frac{x^2}{4Dt}). \tag{2}$$

In contrast to this purely phenomenological nature of the Einstein's PDE, an alternative approach to study Brownian motion was introduced by Langevin [34], with a microscopic model departing from Newton's second law. Langevin equation for a single tagged particle with mass m is the stochastic differential equation:

$$m\ddot{x}(t) = F_{ext}(t) + \eta(t) - m\gamma\dot{x}(t). \tag{3}$$

Here, $\dot{x}$ and $\ddot{x}$ are the instantaneous velocity and acceleration of the particle, while $F_{ext}(t)$ is the resultant of any external forces acting on the particle. The force η is the fluctuational force, which results from the random collisions of the particle with molecules of the surrounding medium. (This is a purely random force and therefore has equal probabilities of taking positive and negative values.) Finally, the frictional force is considered separately in the third term, in which γ (a positive constant) is the friction coefficient per unit mass. This constant is related to Einstein's diffusion coefficient through what is known as the fluctuation-dissipation relation as:

$$D = \frac{k_B T}{m\gamma}, \tag{4}$$

where k_B is the Boltzmann coefficient and T is the absolute temperature.

Smoluchowski's limit and simulating Brownian motion

Smoluchowski [35] showed that in the large frictional limit ($\gamma\dot{x}(t) >> m\ddot{x}(t)$) the trajectories of the particles governed by Langevin equation could be approximated as:

$$\dot{x}(t) = -\frac{1}{m\gamma}U'_{ext}(x) + \frac{1}{m\gamma}\eta(t) \tag{5}$$

This equation considering such over-damped limit is the Smoluchowski equation, in which U_{ext} is the potential that derives the force F_{ext} acting on the particle. In the absence of any external forces, this approximation could be simplified to the scaled stochastic equation:

$$\dot{x}(t) = \sqrt{2D}\dot{w}, \tag{6}$$

where $\dot{w}$ is δ-correlated Gaussian white noise, which is the time derivative of Wiener process.
From Langevin equation, it could also be shown that γ^{-1} characterizes the timescale of the velocity's autocorrelation, which decays exponentially. Moreover, Einstein's equation (Eq.1) is an approximation that is valid for the *diffusion regime*, which is a timescale that is much larger than γ^{-1}. For the diffusion regime, the above stochastic equation (Eq.6) could also be derived starting from the PDE 1 by using the Fokker-Planck formalism [36]. Therefore, in the absence of external forces, Eq.6 could be used under any formalism to model stochastic motion in the diffusion regime. For studying the diffusion of calcium ions, I utilised Euler's algorithm to simulate the discrete numerical form of this stochastic equation.

First-passage time and the Narrow escape problem

The first passage time of a diffusing particle departing from an arbitrary point X_0 is the first instance of time when it arrives at the point $X(\neq X_0)$. Mean of the first passage time (MFPT) is therefore, the average time a particle takes to arrive at a certain window starting from a particular departure point.
In cellular and molecular biology, the diffusion of particles occur in confined domains, whereas the target (reaction) sites are usually small molecular clusters located on the surface of this domain. The narrow escape problem (NEP) is a framework to compute the mean first passage time of a Brownian particle in confined domains until it reaches a small absorbing window $\partial\Omega_a$ in an otherwise reflecting surface boundary $\partial\Omega$ ($\backslash\partial\Omega_a$) of a confined domain Ω [37]. MFPTs calculated in these conditions using the theoretical framework of narrow escape theory are called Narrow Escape Times (NET).

Extreme statistics of Narrow Escape Times

MFPTs and hence NETs are useful to quantify the average occurrence time of diffusion-limited chemical reactions and to compute the average concentration of a molecule at the

elapse of a certain duration. However, the accuracy of NET-based temporal predictions depend primarily on the assumptions that all diffusing particles arrive at the target with similar timescales.

When there are N Brownian particles in a bounded domain Ω, the shortest arrival time is defined by $\tau^{(1)}$=min$(t_1, t_2....., t_N)$, where t_i is the arrival time of the i th particle in the ensemble. The heterogeneity of these arrival times could be particularly large when there are many copies of the same particle that simultaneously undertake a random search for the same target. In neural signalling, this scenario occurs regularly due to the many copies of the signalling molecules (eg: calcium ions) that enter and leave cells.

As the main conceptual framework of this thesis, I show that the fastest among many random biological particles typically have arrival times $\tau^{(1)}$ to the target that are extremely faster than the MFPT, hence the reaction onsets could be realized within much shorter times. Thereby, I develop a novel computational framework that extends the narrow escape theory by accounting for the extremes of the arrival time distributions during diffusion in confined domains.

0.3 Summary of results: Part I

Extreme statistics of escape times in 1, 2 and 3-dimensions

Background and goal

When N particles diffuse randomly from a single source point towards a small target, what is the time taken by the first particle to arrive at the target? The properties of this fastest arrival time $\tau^{(1)}$ determine the activation times of cellular and molecular processes that are triggered by a few fastest among many cells or molecules released at a distance. For example, during the mammalian reproduction process in the uterus, diffusing sperm cells have to find an ovule located inside a fallopian tube. In this key step of fertilization, it is critical that sperms' search process is successful within the short time it is fertile. The initial number N in this example is indeed the number of spermatozoa initially ejaculated (ranging a few millions), and a reduction of this number by a factor four could cause infertility [38]. Previous computational work has also shown that the mean arrival time of spermatozoa to the target ovule increases when the sperm count N decreases [39].
The main question I consider in this thesis is "how does the time taken by the first arriver depend on the number N of Brownian searchers that were initially present?" In the context of calcium diffusion in dendritic spines, this dependency of $\tau^{(1)}$ on the initial number of calcium ions N has a profound importance in explaining the activation times of rapid transients.

Results

Through stochastic modeling and simulations of Brownian particles diffusing in 1, 2 and 3 dimensions, I showed that

- *the time $t^{(1)}$ taken by the first among N (simultaneously-starting) Brownian particles to find a small target decreases logarithmically when N increases.*
- *the time $t^{(1)}$ is largely independent of the parameters characterising the geometry of the domain other than the distance from the source to the target.*
- *the logarithmic dependency of the arrival times on N also generalizes to the time $t^{(2)}$, the time of the first two (among $N >> 2$) particles to arrive at a small target.*
- *when a 3D confined domain has the shape of a dendritic spine (with a spherical head connected to a thin neck), the time for the first diffusing calcium ions from the head takes about 1-2 milliseconds in average to reach a single target receptor at the base when there are N=500 to 1000 ions initially released in the spine head.*

Time for the first among many Brownian particles to find a small target

I computed the averages of first arrival times $t^{(1)}$ through 1, 2 and 3 dimensional stochastic simulations. The 2D and 3D results are shown in Figures 3 & 4, respectively. Here diffusion was simulated under fully-reflecting boundary conditions of the domain while the target sizes were small (<1 %) compared to the domain radius.

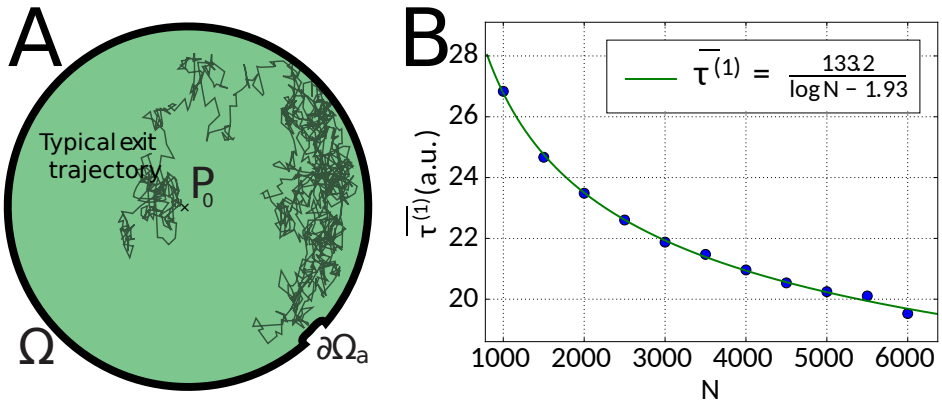

Figure 3: Escape through a narrow opening in a planar disk. **(A).** The geometry of the two-dimensional narrow escape problem and a typical trajectory of a particle diffusing from P_0 and arriving at the target. **(B).** Plot of the mean first passage time of the fastest particles $\overline{\tau^{(1)}}$ versus the number of particles N that were initially present at P_0. The fitted green curve takes the form $\frac{\alpha}{\log(N)+\beta}$.

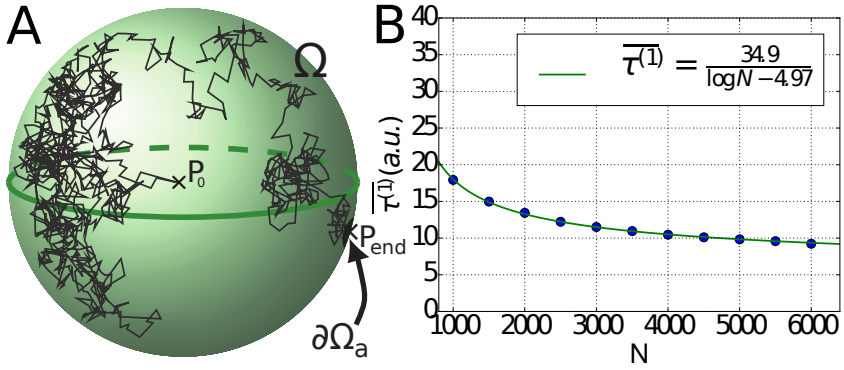

Figure 4: Extreme statistics of narrow escape times through a small window in 3D. **(A).** The geometry of the narrow escape problem and a typical trajectory. The trajectory starts at point P_0 (cross), and ends at point P_{end} inside the target space. **(B).** Plot of the MFPT of the fastest particles $\overline{\tau^{(1)}}$ versus the number of particle N. For each value of N, 2000 trials were simulated. The fit (green curve) takes the form $\frac{\alpha}{\log(N)+\beta}$.

These computational findings on the logarithmic dependency of $\overline{\tau^{(1)}}$ on N are proven by the analytical derivations of the asymptotic formulas (in Sections 1.3-1.5):

$$\text{Dimension } 1 : \overline{\tau^{(1)}} \approx \frac{\delta_{min}^2}{4D\log(\frac{N}{\sqrt{\pi}})} \text{ valid for } N \gg 1 \tag{7}$$

$$\text{Dimension } 2 : \overline{\tau^{(1)}} \approx \frac{\delta_{min}^2}{4D\log(\frac{\pi\sqrt{2}N}{8\log(\frac{1}{\epsilon})})} \text{ valid for } \frac{N}{\log(\frac{1}{\epsilon})} \gg 1 \tag{8}$$

$$\text{Dimension } 3 : \overline{\tau^{(1)}} \approx \frac{\delta_{min}^2}{4D\log(2N\frac{\epsilon^2}{\pi^{1/2}\delta_{min}^2})} \text{ valid for } \frac{N\epsilon^2}{\delta_{min}^2} \gg 1 \tag{9}$$

Here D is the diffusion coefficient and δ_{min} is the length of the shortest ray from the initial point of N number of particles to their small exiting window of size ϵ.

Arrival times of the first two Brownian searchers to a target at the base of a dendritic spine

During calcium transmission in a dendritic spine, calcium ions diffusing from the spine head find a small receptor target (RyR with about a 10 nm radius) at the base of the spine. Upon the arrival and binding of two such consecutive ions to a single receptor, the receptor is able to open and release calcium.
When N such particles start to diffuse from the spine head, I derived the arrival time distributions of the first one and the first two among such particles to a small target located at the base. I first confirmed that the logarithmic dependency on N of the arrival time $t^{(1)}$ to a target taken by the first one particle generalizes also to the arrival times $t^{(2)}$ of the first two particles (section 1.6), and verified these results with stochastic simulations (section 1.7). Indeed these arrival processes occur within a few milliseconds (Fig.5). Moreover, when the initial number of particles in the head was increased (from N=500 to N=1000), both the first and the second arrival times decrease.

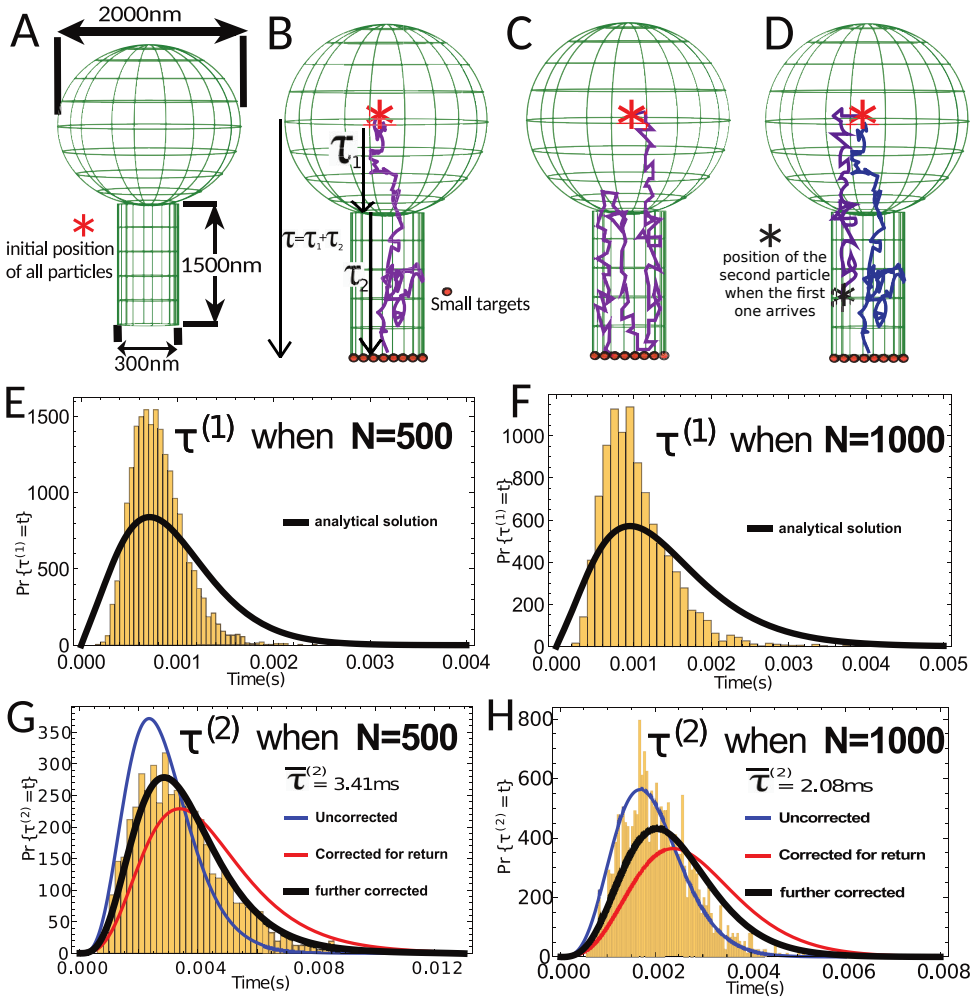

Figure 5: **First- and second-arrival time computations of a particle from the head to the base in a geometrical model of a dendritic spine. (A)-(D):** The geometry of the spine has a spherical head and cylindrical neck. The targets at the base are distributed as detailed in section 4.3.2. Brownian particles are released at the center of the spine head, they first have to reach the opening at the top of its neck before diffusing through the neck to reach the targets at the base. Time taken for each process is represented in (B) with the notation τ_1 and τ_2, making the total time to be $\tau = \tau_1 + \tau_2$. **(E) & (F).** Plots of the two distributions of $\Pr\{\tau^{(1)} = t\}$ for the two initial numbers N=500 and 1000 with their analytical approximations. **(G) & (H).** Probability density function $\Pr\{\tau^{(2)} = t\}$ of times taken by the second ion to arrive at the target. The first analytical approximation (blue curve) assumes two straightforward, independent arrivals (as panel B). This solution was corrected (red curve) for the possibility that the first ions arriving to the neck could return to the head (as panel C). Finally, it was corrected further (black curve) for the fact that during the arrival time of the first ion, the second one is already closer to the target (shown in panel D). The diffusion coefficient for calcium in spines is taken as $D = 600\mu m^2 s^{-1}$.

Trajectory analysis of extreme narrow escape with obstacles and cusps

Background and goals

In the analytical calculations of the first arrival times in the previous section, unlike for the stochastic simulations, I did not consider the presence of SA within the spine. However, the simulation results of both the first and the second arrival times were in excellent agreement with the analytical results. In the formula for the mean first passage time that I describe in section 0.4, most of the terms increase when a, the radius of opening in the spine head towards the neck (neck radius), is increased. The presence of a SA corresponds to the scenario of decreasing a (the effective size of the passage space from head to base), and thereby should increase diffusion times. Moreover, previous work has shown that such physical barriers to diffusion slows down the mean-first passage timescales of Brownian motion [40], and calculating such increases of MFPTs is possible with the introduction of an "effective" diffusion coefficient that accounts for the crowding in the media. In contrast to MFPTs, the hypothesis I tested here with extreme narrow escape times is whether their timescales depend only very weakly on the geometry of the domain as the fastest particles should only "see" the shortest path between the source and the target.

Results

Through stochastic simulations of diffusion in 2D confined domains and trajectory analysis methods, I found that:

- *When there are impermeable obstacles in the shortest path between the source of N initial random searchers and their small target, the trajectory taken by the fastest arrivers concentrate around the shortest possible path between the source and the target.*

- *Both the mean and the variance of the first arrival times $\tau^{(1)}$, as well as the deviation (L1-norm) between the optimal path and the trajectories chosen by the first arrivers decrease with N.*

- *The arrival time distributions are largely independent of the domain geometry apart from the shortest distance from the source to the target. When the target remains hidden inside a narrow cusp-like opening, the arrival times of the first among N are slightly modified by the domain's geometrical properties such as the curvature of the opening, but it still obeys the logarithmic decay with increasing N.*

- *Extreme narrow escape from cusps and path optimisation with obstacles I approximated here with the discretized simulation setups fall within the stochastic regimes that satisfy Brownian motion assumptions. Therefore, the fastest arrivals do not occur due to successive large trajectory steps coming from the tails of the normal distribution, but certainly from the path optimisation.*

Convergence to a deterministic regime through path optimisation of the first arrivers

I implemented stochastic simulations of 2D diffusion to study the paths associated with the fastest arrivals among n particles, when the domain contains an obstacle between their initial position and the target. When the geometry of the search is symmetric, there are two symmetric shortest paths. Fig.6A shows the paths obtained from simulations for three different values of n that concentrate around the shortest geodesic. In Fig.6B & C, I show how the mean first arrival time for the fastest arrivers and their associated trajectory lengths decay with n. Since the variances also decrease, I conclude here that the search process reaches a temporal and spatial optimality with increasing n.

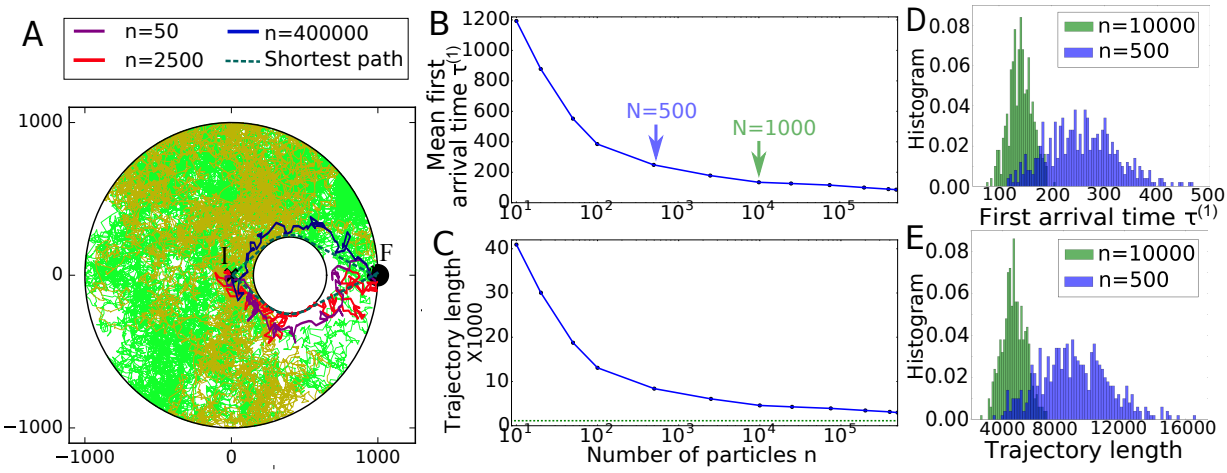

Figure 6: **Optimal paths associated to the fastest arrival time $\tau^{(1)}$ of n i.i.d. Brownian trajectories. (A).** The initial position of Brownian particles is I, and they diffuse within a domain avoiding a circular impermeable obstacle. They can escape into a small window (F) of size $\varepsilon = 0.01 * R$ (R = domain radius). Classical escaping trajectories (green and brown) that explore the whole space are very different from the ones associated to $\tau^{(1)}$ (dark lines) that concentrate along geodesics. **(B)-(C)** MFPTs and trajectory lengths associated to $\tau^{(1)}$ vs the number of particles n. **(D)-(E).** Distributions of $\tau^{(1)}$ and their trajectory lengths for $n = 500$ and 10^4.

In order to confirm that the fastest trajectory (eg: $\gamma(t)$ in Fig.7A) is located near the optimal path (dotted line in Fig.7A), I estimated their L1-norm summation $(l(1)+l(2)+...)$ along the discretized approximations and plotted the averaged distances ($\frac{1}{T}\int_0^T l(t)dt$ in Fig.7A). With the result shown by Fig.7B, I conclude that the trajectory is indeed converging to the geodesic because the average deviation between the geodesic and the first arrivers' trajectories is strictly decreasing with n.

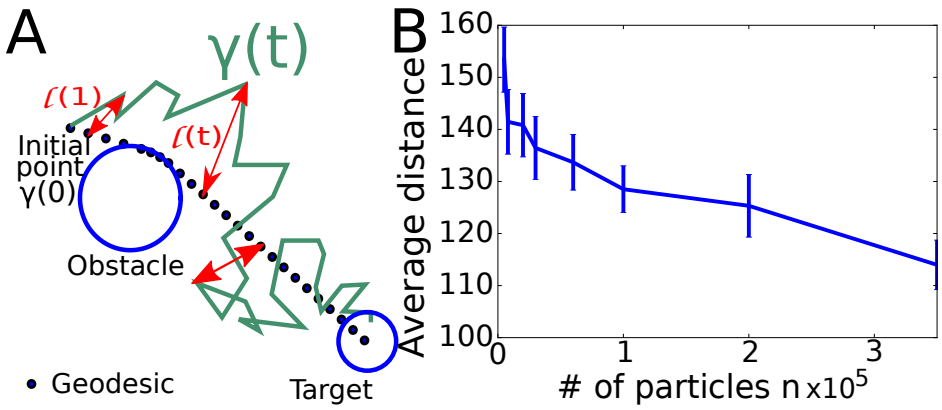

Figure 7: **Geometrical properties of the paths associated to the fastest arrival time among n diffusers. (A).** The trajectory of the fastest arriver (green) is denoted by $\gamma(t)$ and the distance $l(t)$ is computed from each discretised point to its corresponding point in the geodesic (doted line). The corresponding points were obtained by discretizing the geodesic to an equal number of time steps as the trajectory in question. **(B).** Empirically-approximated value of the average distance $\frac{1}{T}\int_0^T l(t)dt$ plotted with the number n of initial particles.

Extreme escape from a cusp: the fastest Brownian searchers in crowded environments

Navigating crowded environments is a ubiquitous modality of cellular signaling because stochastic molecules should find their targets across domains paved with many impermeable obstacles. With the heretofore results about the fastest arrival times and their trajectory optimisation in 2D confined domains, I extended the simulation framework to study crowded geometries. Particularly, I focus here on the generic geometrical shape of a two dimensional region between circular obstacles: a cusp funnel (Fig.8).

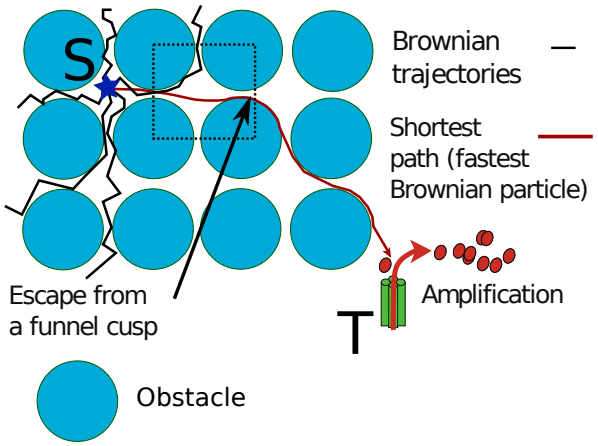

Figure 8: **Schematic representation of signaling activation using the fastest Brownian messenger.** When the initial position of the source (blue star S) of the particles is distant from the cusp funnel of the obstacles, all diffusers (black) have to avoid many impermeable physical obstacles (blue circles). The trajectory (red) of the fastest particles is an optimal path from the source to the target passing through several cusps. At the target site (T), the fastest arriving particle(s) could activate a secondary messenger pathway, leading to an amplification of the signal.

I implemented stochastic simulations of 2D-Brownian motion of particles inside a cusp funnel geometry, where all n particles were initially at the center S (Fig.9) and search for a small absorbing target.

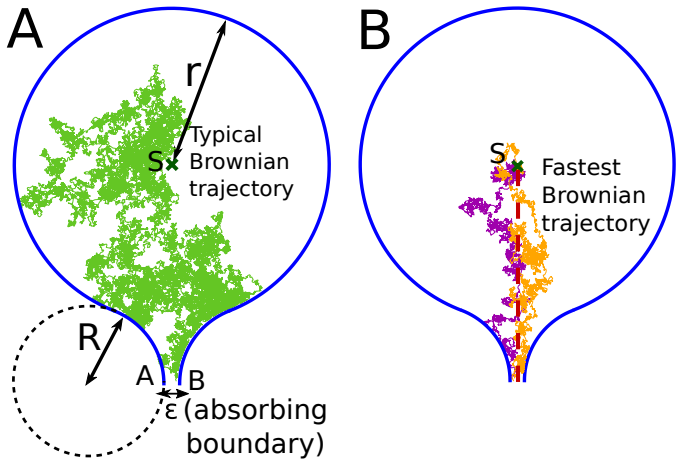

Figure 9: **Escape path for a typical and the fastest among n i.i.d. Brownian trajectories. (A).** Typical brownian diffusers (eg: green trajectory) start initially at position S and escape into a narrow cusp opening ($2\epsilon = |AB|$). R is the radius of curvature. **(B).** Two example trajectories for the fastest among $n = 100$ that start simultaneously from S.

Using the simulation setup shown in Fig.9, I confirmed that the time ($\tau^{(1)}$) taken by the first among n to reach the hidden target also decreases logarithmically with n (Fig.10) similar to what I confirmed in the previous section (Eq.8). By testing the predictions from the theoretical formula derived in section 3.2, I also examine the dependency of extreme arrival times on the geometrical properties of the domain (section 3.3).

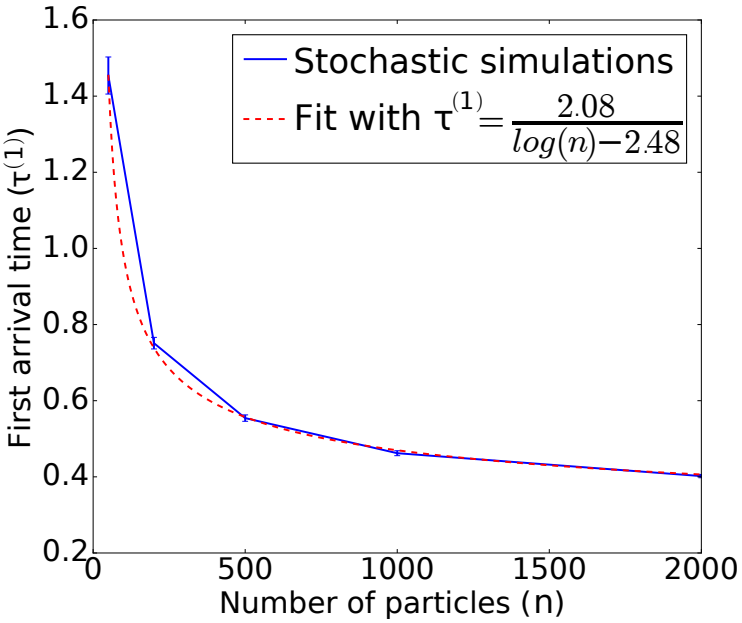

Figure 10: **First arrival time statistics to a target inside a cusp vs the number of initial particles n.** First arrival times from stochastic simulations (blue) fitted with the logarithmic decay (dotted red line). Plotted averages and SEM values are computed over 350 trials.

Optimizing in the Brownian regime: path selection rather than jumping

When considering a discretized narrow escape simulation of N Brownian diffusers, a particle could arrive at a target faster than its rivals utilizing two strategies: (1) always choose displacement direction towards the target, and (2) explore the domain by diffusing with longer jump steps that arise from the tail of the Brownian distribution. Indeed particles that could combine the two strategies definitely arrive first, which would be the case if infinitely many particles are simulated.

However, I confirm here that in the simulation regimes of the narrow escape problem with Brownian diffusers that I study, the fastest arrivers do not occur due to their selection of excursion steps any larger than other "normal" rivals. Therefore, it could be concluded that only the path optimization (strategy 1 above) is observed in the scale of search problems that I have studied.

In Fig.11, I plot the displacement steps of three fastest arrivers of the search process shown in Fig.6 with different values chosen as the initial number N. From the simulation setup, it could be computed that the speed (mean displacement per timestep, here $\Delta t = 1$) of a typical particle is $\mu = \langle |X(t+\Delta t) - X(t)| \rangle = 20\sqrt{\pi} \approx 35.44$, while its standard deviation is $\sigma = \sqrt{|X(t+\Delta t) - X(t)|^2} = 20\sqrt{4-\pi} \approx 18.53$. These values are indeed in agreement with the empirical values I found in Fig.11 for the fastest arrivers. This result confirms that the extreme trajectories do not take unusually longer jumps exploring the domain. Therefore, to arrive first, the trajectories of the fastest should concentrate along the optimal path.

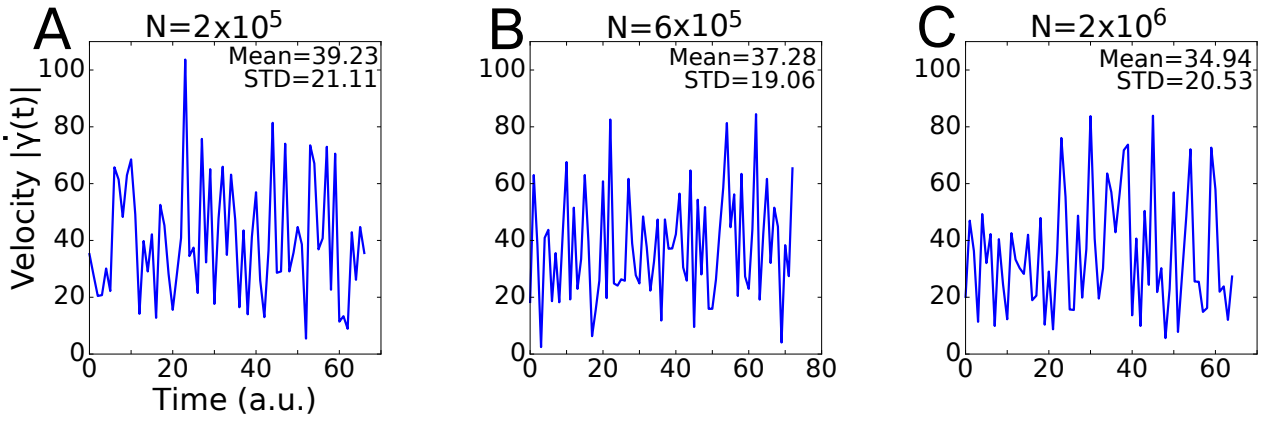

Figure 11: Amplitude of the velocity $|\dot{\gamma}(t)|$ of three fastest arriving Brownian trajectories in the NEP of Fig.6 & Fig.7. The mean speed of a simulated particle = 35.44. Standard deviation = 18.53.

I also analysed the results of the search problem with the cusp (Fig.10) to confirm the same "no-jumping" condition. Here for different numbers N of initial diffusers, by summing up all discrete steps during the displacement from the source to the target, I computed the length of the trajectory they followed (Fig.12B). Then for each N, I plotted the ratio between these trajectory lengths and the mean times taken by the fastest ones.

The ratios were constant up to the limit of N=2000 that I simulated. Thereby I conclude that also when the target is hidden inside the cusp, the reduction of arrival times with N did not occur because winners from larger N values made specially large displacements per time step, but because they diffused closer and closer to the optimal path towards the target, still taking normal diffusion steps.

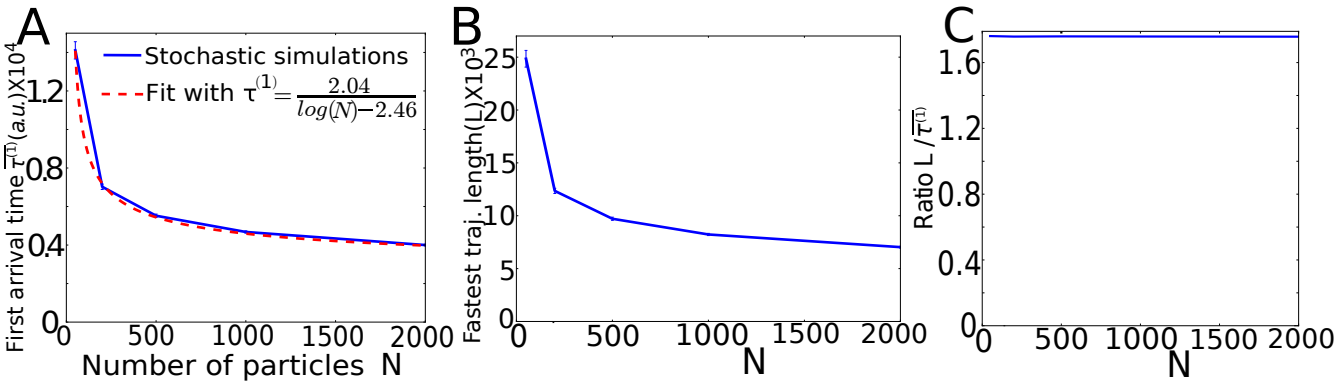

Figure 12: **Arrival time statistics vs number of particles N with the same simulation setup as in Fig.9. (A).** First arrival times ($\bar{\tau}$) and its fit, same as Fig.10. **(B)** Approximated lengths (L) of the trajectories.**(C)** Ratio $\frac{L}{\bar{\tau}^{(1)}}$ vs N.

0.4 Summary of results: Part II

Fast calcium transients in dendritic spines driven by extreme statistics

Background and goals

The main physiological observation that motivates the computational modeling, simulations and mathematical analysis of the thesis is the fast timescales of calcium dynamics in dendritic spines. Calcium fluorescence data showed that when calcium ions are uncaged with photolysis inside spine heads, the signal propagates and triggers a huge increase in the spine base within a few milliseconds. As shown in Fig.13, this result was unique to spines that were SP positive (spines with SA)

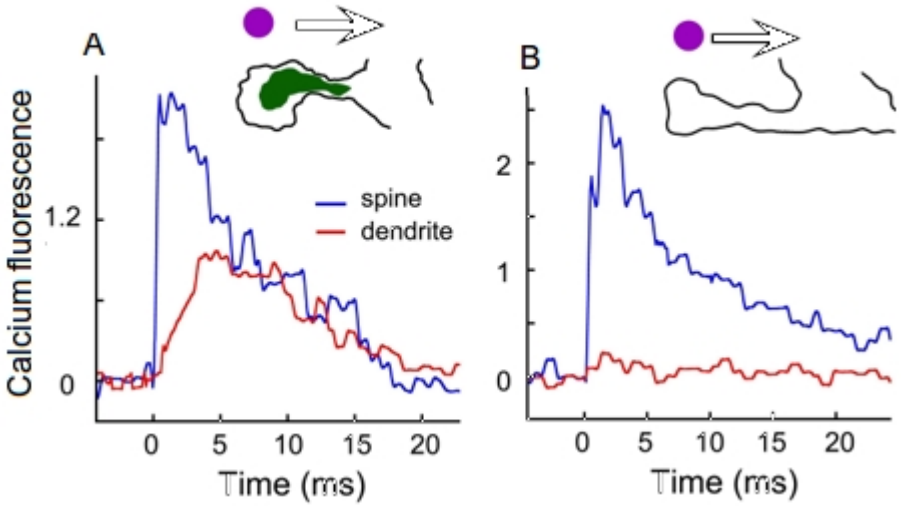

Figure 13: **Calcium transients measured through fluorescence imaging of dendritic spines with (A) and without (B) spine apparatus.** Traces of calcium transients for the spine heads (blue) and their parent dendrites (red) are shown following flash photolysis events of caged calcium in spine heads at t=0. Presence and absence of SA corresponds to synaptopodin positive and negative conditions, respectively.

When calcium ions were modeled as Brownian diffusers starting from the spine head, the mean arrival time to the base of the spine has been computed asymptotically in [41] as:

$$\bar{\tau} = \frac{V}{4Da}[1 + \frac{a}{\pi R}\log(\frac{R}{a})] + \frac{L^2}{2D} + \frac{VL}{\pi Da^2}. \tag{10}$$

Using typical spine data of hypocampal neurons, $D = 600\mu m^2 s^{-1}$ (diffusion coefficient), $V = 3.14\mu m^3$ (spine head volume), $a = 0.15\mu m$ (spine neck radius), R=$1\mu m$ (head radius) and $L = 1.5\mu m$ (neck length), we obtain $\bar{\tau} \approx 167ms$ for this mean first passage time. This timescale is indeed considerably slower than the transmission times of a few milliseconds

shown in Fig.13. Using the extreme statistics framework to explain this discrepancy in timescales led to the main nanophysiological findings of the thesis.

Results

Through stochastic simulations of calcium diffusion inside a computational model of a spine, I found that:

- *Ryanodine receptors (RyRs) are located as a cluster of about 36 receptors at the base of the SA, while SERCA pumps are in the SA head.*
- *Following an uncaging in the head, the first two calcium ions arriving at a single RyR takes about 2-4 milliseconds and leads to an opening of the receptor that releases calcium. By the activation of remaining RyRs, such a release event results in an immediate amplification of the calcium signal through calcium-induced calcium release (CICR), which could explain the experimentally-observed timescales.*
- *The distribution of CICR initiation times depends on the number of calcium ions initially uncaged in the spine head. These times are modulated only slightly by the presence of the SA.*
- *Upon the arrival of two calcium ions, each opening of a RyR occurs after an approximate delay of 0.25ms. The total number of ions released by a single RyR is about 20 ions per one release cycle. The upper estimation for the number of calcium pumps in the spine head is 50.*
- *The nanoscale arrangement of receptors in the spine not only allows fast activation times of calcium signal amplification in the base, but also assures that the calcium signal propagates primarily from head to base, and only minimally to the opposite direction.*

The location of SERCA and RyRs in spines

RyRs are channels that release calcium from internal calcium stores (SA) and increase calcium concentration in the spine, while SERCA pumps uptake calcium from spines and increase the SA reservoir. However, the location of both channels in spines were unknown. I predicted that SERCA are located in the head of the SA while RyRs are clustered at the base of the spine (Fig.14A). This arrangement not only avoids an inefficient competition for calcium ions between the two opposing pathways, but stochastic simulations showed that it also guarantees the fast calcium signal rise at the base of the spine similar to what is observed in uncaging experiments.
My predictions were confirmed later by collaborators through immunostaining experiments, both in cultured hippocampal neurons (Fig.14B & C) and also from mouse in vivo slices examined under STED superresolution microscopy. (See section 4.3.2 Fig.4.3)

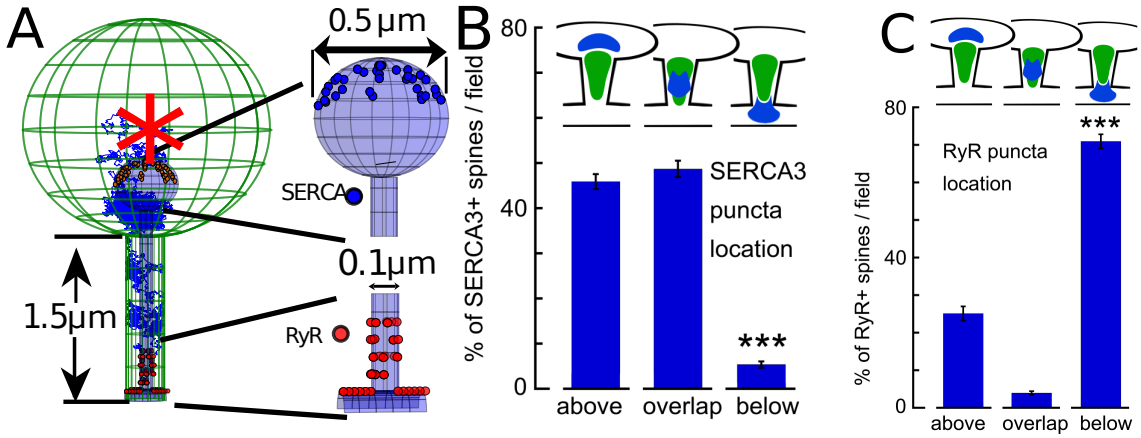

Figure 14: **Distributions of SERCA and RyRs in dendritic spines with SA: computational prediction and experimental verification from cultured hippocampal neurons.** **(A)** Computational model of the spine containing SA with SERCA pumps and RyRs. Magnification on the right shows the distribution of SERCA pumps in the upper hemisphere of the SA head and RyRs located at the SA base on its shaft and neck. Uncaging experiments were simulated as the motion of Brownian particles starting at the center of the head (red star). A typical stochastic trajectory of an ion arriving at a RyR located at the base is shown in blue. **(B)** Prevalence of SERCA3 puncta in cultured rat hippocampal neuronal spines above the SP puncta or overlapping with it (left and middle bars). Here the number of spines is given as percentages when the total SP+ and SERCA+ spines per standard field is taken as 100%. **(C)** Prevalence of RyRs located below the SP puncta (right bar) in SP+ dendritic spines. The percentages are calculated similar to B.

RyR-mediated CICR triggered by fastest calcium ions

To gain quantitative insights about how the SA could affect the calcium transient, I implemented stochastic simulations with the model construction of Fig.14A. Initially, 1000 ions diffuse from the spine head (red star) at t=0. Significant calcium increase occurs at the base of the spine in less than $2ms$ (Fig.15A). This effect is already present when 3 calcium ions per one RyR release event are released (red curve), and further amplified with 5 ions (blue curve), compared to spines with no SA (green curve).
To clarify the origin of the observed fast calcium transients of Fig. 15A, I recall the computations of arrivals times for the two fastest calcium ions to a single RyR located at the spine base. As I showed in section 0.3, when there were 1000 ions initially present in the spine head, the average time for this arrival process could be in the range 2-4 milliseconds. This underlies the initiation timescale of calcium amplification at the base of the spine. When two ions arrive and get bound to a RyR for the first time, this first receptor releases n calcium ions from SA to the cytoplasm (Fig. 15B). The number of ions (n) released by each RyR is a parameter of the model, and I explored with minimal numbers ranging from 3 to 8. Two among these n ions could in turn become the first two to activate some of the neighboring receptors that are positioned as a nanocluster

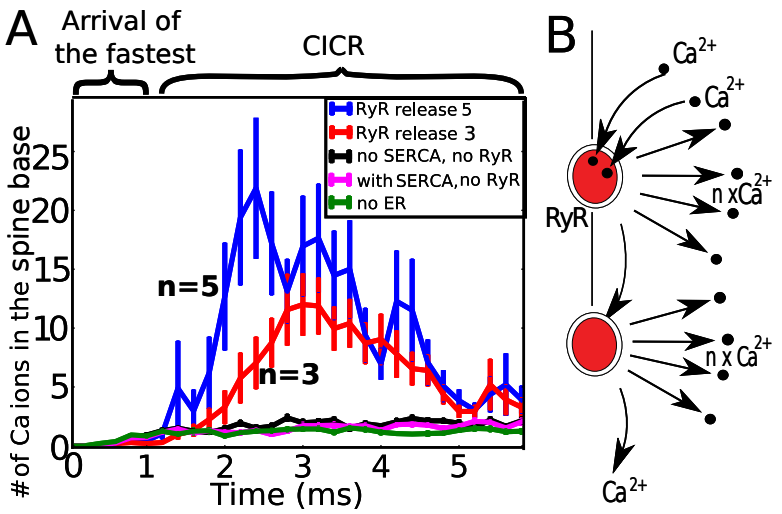

Figure 15: **(A)** Calcium ions in the spine base following an uncaging event in the head. Compared to the simulations with no RyRs at the base (green, magenta and black curves), RyRs were present and $n = 3$, 5 ions per one RyR opening is released in the other two cases (red and blue curves, respectively). **(B)** A schematic showing the triggering of two calcium ions for starting a calcium release from one RyR, which leads to a chain reaction by activating neighbours: calcium-induced calcium release.

(of 36 receptor units in the computational model). Thereby, all RyRs in the cluster participate in the amplification process of the calcium signal and this phenomenon is the calcium-induced calcium release by RyRs. I also found that the amplification dynamics was modulated only slightly by the distribution of SERCA pumps (Fig 4.4). Moreover, the timescale does not depend on the distances between RyRs within the range below 150nm (Chapter 5; Fig.S5).
Therefore, I conclude that the observed calcium dynamics is due to the presence of RyR clusters at the base of a spine, and the activation timescale is determined primarily by the first two of the randomly-arriving calcium ions at one of the RyRs that activate a calcium release and trigger neighbours.

Parameter estimations from the analysis of calcium dynamics

When calcium ions gradually leaves the SA through RyR-mediated CICR, the local concentration at the spine base increases, while the SA internal storage depletes. Both trends are expected to contribute to a reduction of flux from SA to outside through RyRs. I used the experimental calcium transient signal (Fig.13A red curve) to recover this decrease of flux during the first $20ms$ following calcium release. Thereby in the computational model, I found that a consecutive release of 8, 7 and 6 ions per RyR could assure similar dynamics.

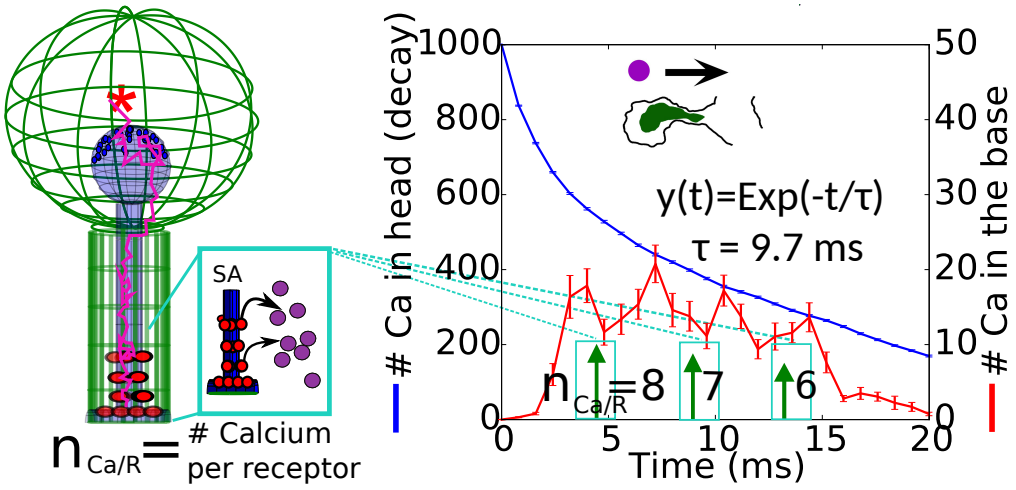

Figure 16: Stochastic simulations of the calcium transient following an uncaging of 1000 calcium ions in the spine head. The release cycle of RyRs is 8, 7, and 6 ions, occurs with an initial delay of $0.25ms$, at times on average, and at the time points indicated by the green arrows. The RyR refractory period between each release is 3ms.

In addition, the calcium ions were released with a delay of 0.25ms after the arrival of a second ion to the RyR binding site. This delay assures a prevention of a blow-up scenario due to CICR, and was calibrated with the experimental timescale. Finally, a refractory period of 3ms after each release (where RyRs were inactive) was estimated based on the total duration of the experimental CICR transient (Fig.13A red curve). In summary, each of the parameter values characterising RyR release and CICR were obtained from their biophysical significance, and they collectively reproduced the experimentally-observed timescale as shown in Fig.16 with minimal number (n) of calcium ions released per receptor. Therefore, I conclude that with higher n values the large transient amplifications should be possible as observed experimentally, and should be modeled also accounting for the interplay of calcium clearance mechanisms in the dendrite that were not considered in the present model.

Nanoscale organisation contributing to the diode effect in spines

The simulations and experiments prove that the asymmetric distributions of RyRs that are restricted to the spine base underlie the asymmetry of calcium transmission in spines. I showed that, in a hypothetical scenario where RyRs are also located in the head of SA, they can get activated immediately by the arriving calcium ions. Thereby the stores get depleted immediately, and does not allow the transmission to the base to occur (Chapter 5: Fig S6). Putting all my findings about the quantitative values and geometrical arrangement together, I have described here a novel diffusion-amplification calcium transmission mechanism in spines containing a SA that reflects the role of a chemical diode that amplifies ion transmission from the spine head to the dendrite, but not in the opposite direction. (Fig.17)

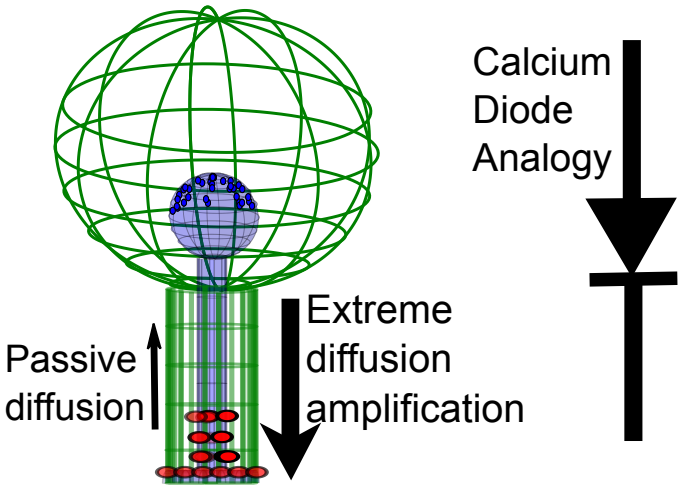

Figure 17: Dendritic spine with the presence of SA plays the role of a calcium diode, amplifying ion transmission from the head to the dendrite, but not in the opposite direction.

Mechanisms underlying SA refilling vs depletion and long-term calcium dynamics

Background and goals

A major question arose from the previous study was how SA could get refilled after a CICR event. According to the mechanism I found with extreme statistics, a large calcium influx such as a synaptic current into the spine could trigger a CICR, with a very few calcium ions arriving at the base. I showed that CICR leads to a local increase of calcium concentration at the spine base, while in its head, most of the remaining calcium ions are absorbed by surface pumps.

Calcium fluorescence data showed that when synaptic inputs were blocked in cultured hippocampal neurons placed in a calcium bath, large spontaneous calcium fluctuations are observed specifically in spines containing SA (Fig.18 A, B Top). These fluctuations are local to spine heads and are not present in dendrites. Therefore, we associate these spontaneous fluctuations to the Store-Operated-Calcium-Entry (SOCE) pathway involving the STIM1-ORAI1 complex that was not blocked.

The same experiment also confirmed that the SOCE pathway led to calcium accumulation in the SA: when a spine with a fully-depleted SA was maintained in these conditions, in response to an eventual caffeine-induced store emptying, an asymmetric calcium increase occurred at the base (Fig.18B Bottom). This result is in agreement with the timescale and the location of RyRs that I found before [42].

We quantified the timescales of the spontaneous events by segmenting the calcium time series recorded in the spine head over several minutes. The transient response was extracted from background fluctuations by defining a threshold of one standard deviation for considering events (Fig.18C Top). Averaging such collected events (Fig.18C Bottom) resulted in a 2s stereotypical response which I used for simulating the SOCE inputs into spine heads. We conclude that the spontaneous calcium transients measured in spine heads during possible refilling events are much slower (of the order of seconds) and have smaller amplitudes compared to the ones triggered by synaptic (AMPA/NMDA) inputs that occur in the timescales with the order of a few tens of milliseconds (Chapter 7 Fig.S1).

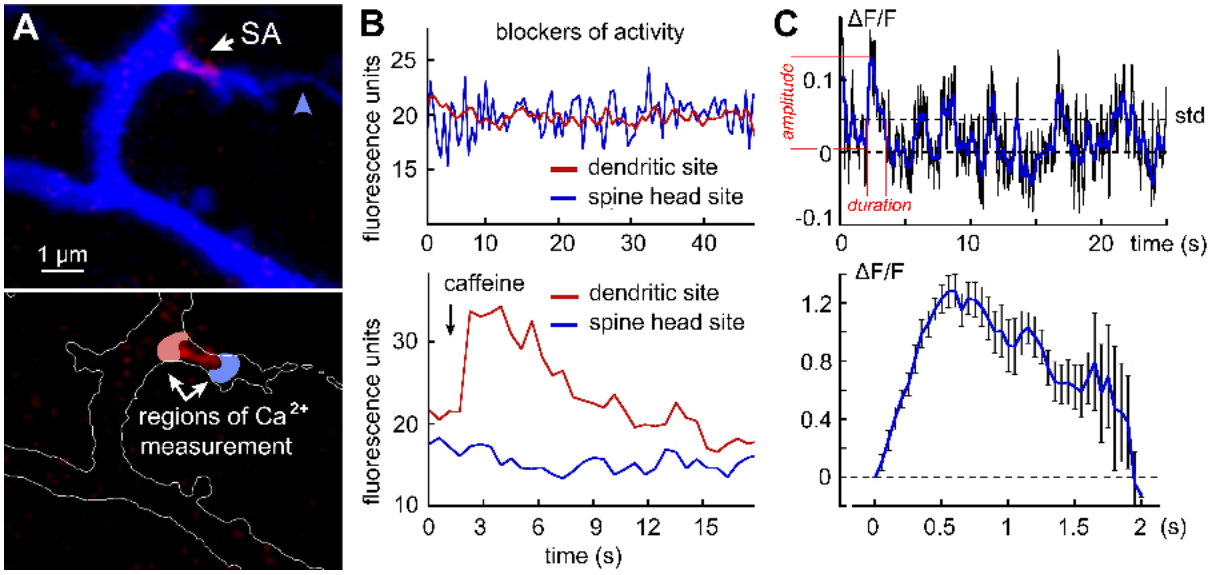

Figure 18: **Experimental evidence for slow calcium fluctuations in spine heads. (A).** Top: Cultured hippocampal neuron co-transfected Blue fluorescent protein (blue) and SP (red), loaded with Fluo2 high affinity calcium sensor. A large SP positive spine attached to an axon (blue arrowhead) and several SP-negative spines can be seen. Bottom: same region, with a contour of segment marked in white and two regions of interest: above SP (blue) and below SP (red). **(B).** Top: spontaneous calcium activity due to SOCE, only located in the spine head (blue). Bottom: time course of calcium activity in the head vs base following caffeine addition of 5 mM. Calcium level increase is observed towards the base of the spine, but not in the spine head. **(C).** Top: segmented recording of spontaneous calcium activity in the spine head. Bottom: overlapped average of the fluctuation segments (18 traces) larger than a threshold in the example trial shown in the Top figure.

The precise question I addressed is how the spine could compute the separation between a depletion event (synaptic input) and a refilling period of the SA (from the SOCE pathway). The former should be signalled to the base via CICR leading to a calcium store depletion, while the latter should avoid store depletion. I investigated the possible SA refilling mechanism first through a mean-field model of calcium dynamics in spines and then by extending the stochastic simulations of my previous nanoscale physiological modeling framework also accounting for the refilling pathway.

Results

Using a mean-field computational model and stochastic simulations of calcium diffusion following different conditions of calcium entry into a dendritic spine, I found that:

- *Weak calcium currents of slow timescales (≈300-500 ions over a few seconds) similar to store-operated calcium entry (SOCE) refills SA calcium stores.*
- *Compared with strong calcium injections with fast timescales similar to synaptic calcium entry (≈600-1000 ions in a few milliseconds), SOCE-like inputs have a much less probability to deplete SA calcium stores by triggering RyRs. Even when SOCE does open a RyR, the average conditional time for such events is extremely longer compared to opening events with strong inputs. Therefore, during SOCE inputs, it is highly likely that the SA calcium storage is preserved.*
- *Surface pumps located in spine heads modulate the refilling and depletion processes of SA calcium: their presence reduces the probability of RyRs opening and also increases their conditional opening times.*
- *In order to increase the refilling efficiency, SERCA pumps on the SA membrane are located closely within a distance of a few tens of nanometers from the ORAI channels where SOCE occurs in the plasma membrane.*
- *During the experimental protocols inducing synaptic long-term potentiation (LTP) and depression (LTD), the nanoscale organisation of the spine underlies the differences of local calcium concentrations, particularly at its base region.*

Separation of SA depletion and replenishment through calcium influx strengths

To study the consequences of fast synaptic inputs and SOCE, I constructed a mean-field computational model of calcium dynamics in a spine compartment (Ch. 7: Section 4), and analyzed it under the two different initial conditions: (1) instant injection of calcium ions into the spine head, simulating a fast entry from synaptic inputs through AMPA or NMDA receptors. (2) a slow calcium injection, similar to what was extracted from florescence data during SOCE activity (fitted from the 2s response from Fig.18C Bottom).
Numerical solutions of the model confirmed that the probabilities of opening a RyR have very different saturation characteristics under the two conditions (Fig.19). Particularly, due to the slow gain in the probability, with a small number of injected ions, SOCE-like slow inputs are associated with a low probability of a RyR opening (N<600: light blue area associated to the brown curve in Fig.19). This contrasts drastically with the instantaneous inputs that almost surely trigger a CICR under the input conditions with a much smaller number of ions. Therefore, in contrast to SOCE inputs, fast synaptic currents (with N>600 ions during synaptic activation) are very likely to result in SA depletion by RyR-triggered CICR (Fig.19 pink area under the blue curve). In conclusion, the RyR opening probability for the SOCE versus fast input regimes has a clear separation

in terms of the total number of injected ions, and during SOCE-like input conditions, it is more likely that the SA calcium stores are preserved without the occurrence of depletion events.

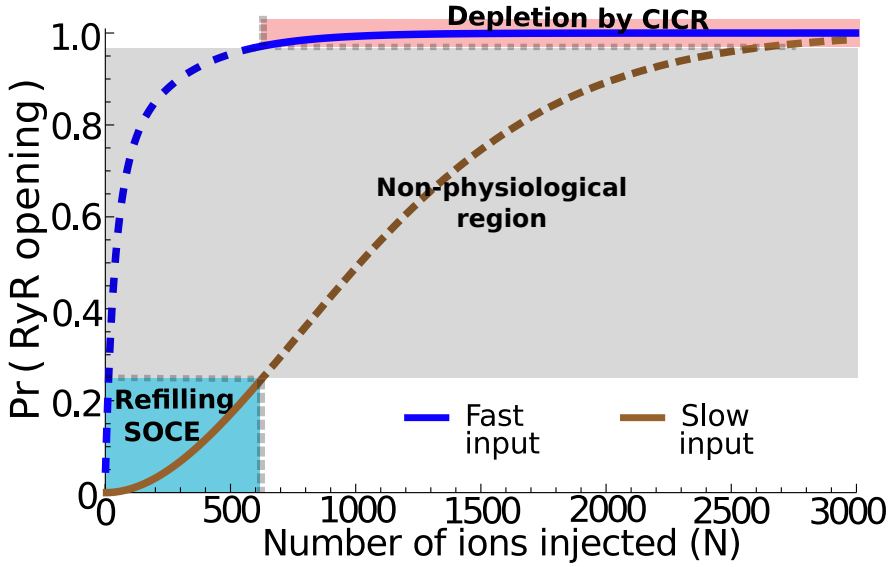

Figure 19: **Distinct separation of the two pathways through the modulation of RyR opening probability**. In the physiological conditions of slow inputs (0-600 ions in 2s), RyR opening probability remains below 0.25, thus the refilling of SA is dominant (light blue area, solid brown curve). During fast, synaptic inputs with more than 600 ions, RyR probability guarantees CICR and is associated to SA depletion that increases calcium level at the spine base (pink area, solid blue curve).

Spine calcium dynamics following slow versus fast calcium entry

To confirm the separative conditions predicted by the mean-field model and to determine other conditions that favor calcium accumulation in the SA, I used the geometric computational model of the spine and implemented stochastic simulations of calcium diffusion (Fig.20A). I used two influx conditions to spine head, mimicking synaptic and SOCE fluxes. In the first simulation, I injected 300 ions into the spine head instantaneously at t=0 to reproduce fast synaptic inputs and considered calcium dynamics in the spine head and base (Fig.20B-D). I confirmed that when starting from 500 ions as the initial reservoir, after three stimulations, the SA gets depleted due to the CICR events occurring due to the first activation of one RyR at the base, as predicted by my previous results under these conditions. The small increases in between the depletion events in SA calcium level occur due to the uptake of ions into SA through SERCA pumps.

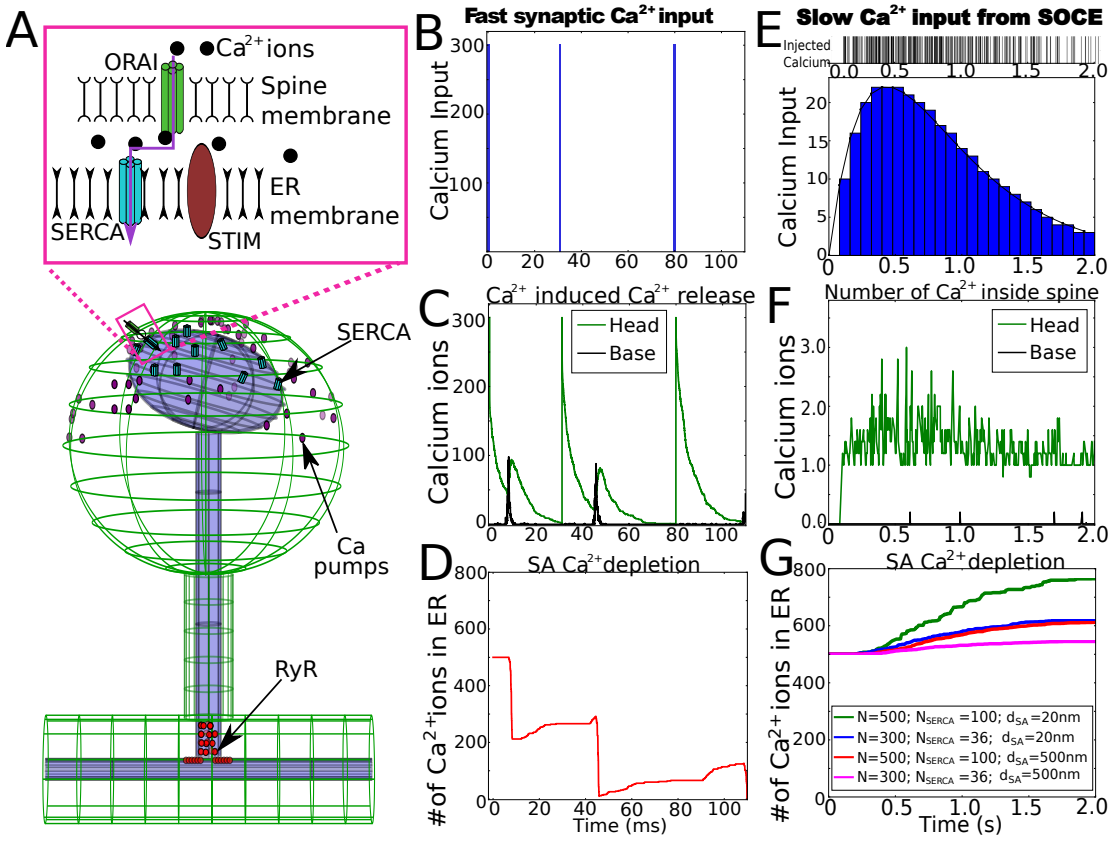

Figure 20: **(A).** Schematic representation of the SOCE regulators in the spine. Calcium inputs in the simulations occur at the top of the spine head. Ions diffuse inside the domain (green) and eventually reach the bottom to disappear into the dendrite. Calcium pumps on the spine head, SERCA pumps on the SA head and RyRs at the base could capture the diffusing ions. **(B).** Synaptic calcium input into the spine from the top of the spine head are simulated as instantaneous spikes of N=300 ions. The first spike is at t=0, and spikes are repeated each time when the calcium in the spine decays to zero. (eg: at t=30.9s and t=80.1s) **(C).** Typical simulation result shows a sharp increase of calcium due to CICR occurring at the base, after a few milliseconds following each calcium injection into the head. Calcium decay in the head is due to the uptake through SERCA pumps, the diffusion towards the base and the absorption by surface pumps. Smaller second peaks (about 10ms following each input spike) manifest due to calcium ions 'generated' by CICR at the base and diffuse into spine head. **(D).** SA reservoir of 500 ions depleted during fast inputs upon three CICR events. **(E).** Approximated slow calcium activity in spines as a difference of exponentials $I(t) = Q.(\mathrm{e}^{-2.3.t} - \mathrm{e}^{-2.31.t})$ (black curve). This function was discretized within the total 2s duration by dividing it into 25 equal bins (histogram) and normalized such that the total number of calcium in 2s is N (either N=300 or 500 were chosen). Single calcium ion injections times then follow a uniform random distribution according to the number of ions corresponding to each time bin. (Barcode representation: top panel). **(F).** Number of calcium ions in the spine head and the arrivals at the base of the spine (average over 5 trials with N=300). Maximum calcium arrival at the base was about 1 ion, and no calcium release events occur from RyRs. **(G).** Total number of calcium ions in the SA for different distances (d_{SA}) between spine head and SA, and different number of SERCA pumps N_{SERCA}. In all cases, the SA calcium level is increasing gradually via SOCE refilling throughout the 2s duration of the calcium input because SA is not depleted by CICR events.

In contrast, during slow injection conditions, I found that although the number of calcium ions in the head was much reduced compared to synaptic inputs, the SA gets refilled with calcium without triggering a CICR at the base (Fig.20E-G). For this mechanism to occur, I also found the distance d_{SA} between SERCA and ORAI also as an important parameter to be examined further. Moreover, I confirmed that the calcium intake into the SA could be increased by increasing the number of SERCA pumps or by increasing the calcium input (from N=300 to 500).
To characterize the distribution of calcium fluxes in the SA, the extrusions by the calcium pumps and the arrivals at the base of the spine, I followed the fate of each ion during the simulations and found that most of the injected ions were absorbed by calcium pumps. When 300 injected ions were simulated over a 2s duration when the distance between the membranes was 20nm (blue curve in Fig.20E), 236 ions were captured on average by surface pumps, while SERCA pumps captured and refilled the stores by about 46 ions. The average number of ions that reached the base was 4, and the rest remained in the spine domain or stayed as single-occupants in SERCA or RyRs. Therefore, since such calcium concentration at the base of the spine was too low to trigger CICR events, I concluded that slow influx conditions favour SA calcium refilling, without triggering a depletion.

SOCE-mediated refilling is modulated by SERCA-ORAI distance and by the presence of calcium pumps

I evaluated numerically the role of SERCA-ORAI distances d_{SA}, on influencing the number of ions entering the SA during slow calcium inputs representing SOCE. I implemented again the calcium injection protocol following the double-exponential lasting 2s with different number of injected ions N (same as Fig.20E). For all cases N=100, 300 and 500, the fraction of calcium ions entering SA decreases gradually when d_{SA} increases (Fig.21A). To evaluate the effect of calcium pumps on the SA uptake, I executed the same simulations after removing all pumps. In that case, the fraction of SA calcium uptake increases to $\approx$ 75% (green curve) as expected, as more ions remain in the cytoplasm.
Therefore, to assure an efficient SA refilling, it is possible to hypothesize that ORAI1, which is the source of slow calcium entry from the plasma membrane, should be located close to (within a few tens of nanometers) SERCA pumps that refill the SA. In addition, the simulations of spines containing SA imply that this close-localization should predominately occur in the spine heads. These predictions about the association of SERCA and ORAI1 localisations, were confirmed by experimental collaborators through immunostaining and super-resolution STED microscopy (Fig.21B-C).

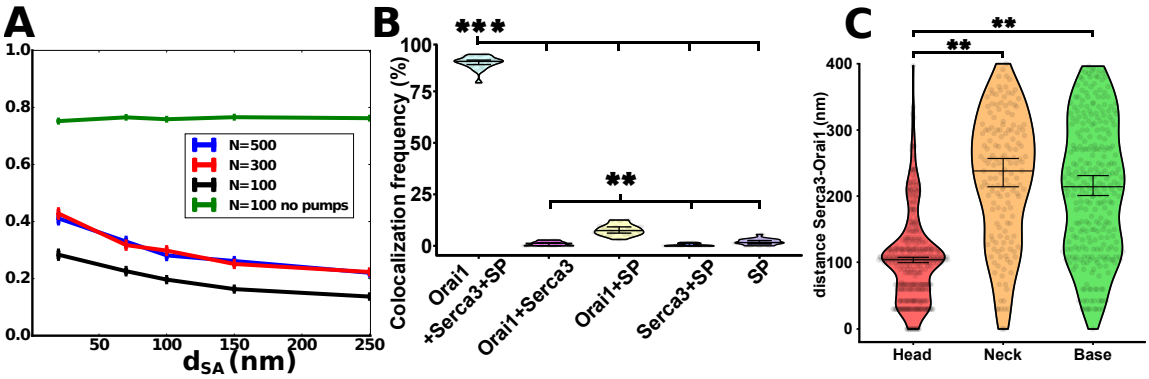

Figure 21: **Predictions from the computational model on the SERCA-ORAI distance and verifications from superresolution imaging (A)**. Normalized fraction of calcium ions entering SA in the computational model, following a slow calcium entry. Here I use a single repetition of the injection protocol lasting 2s showed in Fig.20E, with N=100, 300 and 500 and calcium pumps removed for N=100. **(B)** Super-resolution imaging based quantification of the colocalization of the spines from mouse hippocampal neurons immunostained against the three proteins SP, ORAI1 and SERCA3. The colocalization frequency of ORAI1 and SERCA3 in spine heads is significantly higher when SP is present (88.9±0.73%, n=19, p<0.001). **(C)** Quantification of the distances between SERCA3 and ORAI1 in spine head, neck or base. SERCA3 and ORAI1 are significantly closer to each other in the head (106±4 nm, n=4) than in the other parts of the spine (neck: 221±14 nm, n=4, p=0.0067; base: 210±8 nm, n=4, p=0.0034).

CICR occurrence times during slow and fast inputs

The previous results confirmed that in the range of 300-500 ions' slow influx lasting 2s, SA is able to get refilled, especially when there are short distances between SERCA and these inputs. The mean field model and stochastic simulations confirmed that the probability for RyR opening under such conditions is also lower compared to the probability with fast, instantaneous input conditions. I also confirmed with simulations that the conditional opening time for RyR opening is also delayed during slow inputs compared to fast inputs (Fig.22).

The conditional opening times from fast inputs to trigger a RyR ranges up to a few tens of milliseconds (Fig.22 A), while the slow inputs trigger RyRs only after few hundreds of milliseconds (Fig.22 B). I confirmed that this prediction also agrees with the timescales predicted by the mean-field model (Chapter 7 Fig.S6). Therefore, I conclude that SOCE-like slow inputs not only reduce the probability of RyR opening, but also delays this process, thereby in both ways facilitate the replenishment conditions of SA.

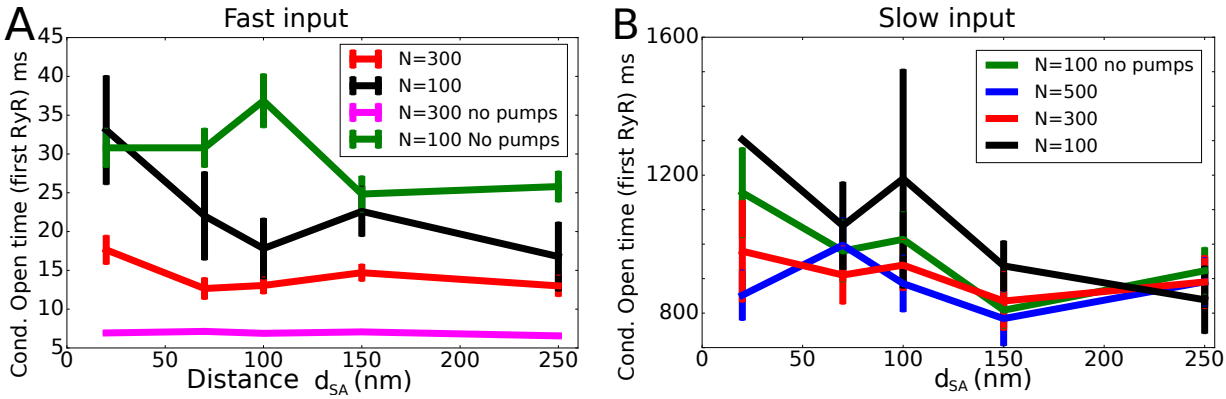

Figure 22: Conditional opening times of the first RyR after the first calcium entry in simulations. **(A)**. RyR opening after instantaneous calcium inputs. N=100 and 300 ions were initially injected (black and red curves), then the calcium pumps in the spine head were removed (purple and green). **(B)** Opening times same as A, but following slow calcium entry, with the numbers of ions N=100, 300 and 500 and the pumps removed during N=100.

Separation of depletion and replenishment conditions

The mean-field model and the stochastic simulations of the geometrical model confirmed that SOCE-like inputs are considerably more likely to refill stores safely without triggering a depletion event. In addition, calcium pumps also play the unexpected role of preventing and delaying the RyR activation by controlling the arrival of calcium ions at the base of the spine. Taken together, the calcium injection rate, SA-plasma membrane distance, along with the balance of SERCA and calcium pumps shape the SA-uptake and the CICR activation probability. These findings are summarized in Fig.23.

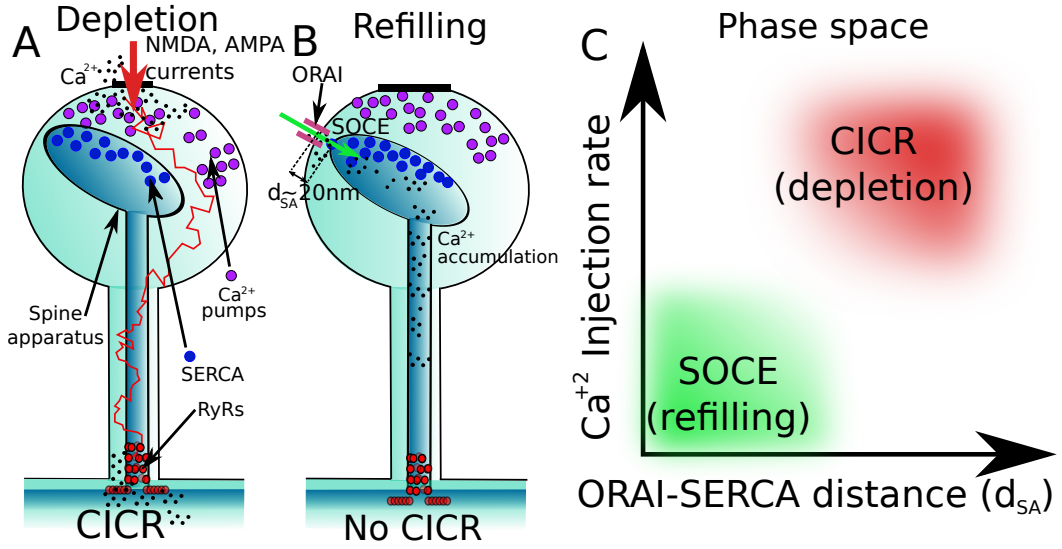

Figure 23: **Physiological conditions for SA depletion vs replenishment (A)** Synaptic currents entering dendritic spines through NMDA and AMPA receptors trigger CICR by activating RyRs at the base. **(B)** Weak calcium inputs with slow timescales through ORAI1 channels located near the SA membrane are insufficient to trigger a CICR at the base. These ions either replenish the SA calcium reservoir via the SOCE through SERCA pumps or they get absorbed into calcium pumps located in the spine head. **(C)** Phase space that consists of calcium injection rate and the distance d_{SA} between the ORAI and SERCA channels. Refilling and depletion conditions of calcium in spines are well separated, so that both do not occur at the same time.

Calcium dynamics during LTP and LTD protocols

Using the nanoscale organisation of the spine's calcium regulators revealed by the simulations and experiments, I evaluated the consequences of calcium dynamics on the induction protocols of synaptic long-term potentiation and depression (Fig.24 Top panels). Although these protocols have been used for a long time to induce LTP and LTD [43], the role of SA remains unknown. It is also known that only SP+ spines (which contain spine apparatus) increase their head sizes during LTP [44] thus the presence of SA could be a deciding factor in the plasticity of the synapse. The widely-accepted hypothesis in post-synaptic calcium levels is that LTP stimulations result in large calcium level elevations while LTD stimulations are associated to moderate calcium elevations.
The LTP protocol has a high frequency 100Hz stimulation phase for 1s followed by a silent phase of 30s. In terms of ionic inputs to spines, I simulated the stimulation phase starting with 300 ions followed by amplitudes reducing gradually with successive spikes as denoted by the Tsodyks-Markram model [45]. The 30s silent phase only includes a simulated STIM-ORAI entry, modeled with slow timescales as described above. The simulation confirmed that with LTP stimulations, calcium ions that reach the spine base lead

to several CICR events and thus increase the peak number of ions at the base to about 10 ions on average (Fig.24 middle left). Following these CICR events, the stored number of calcium ions in SA decays rapidly, leading to a full depletion in about 250ms (bottom left).

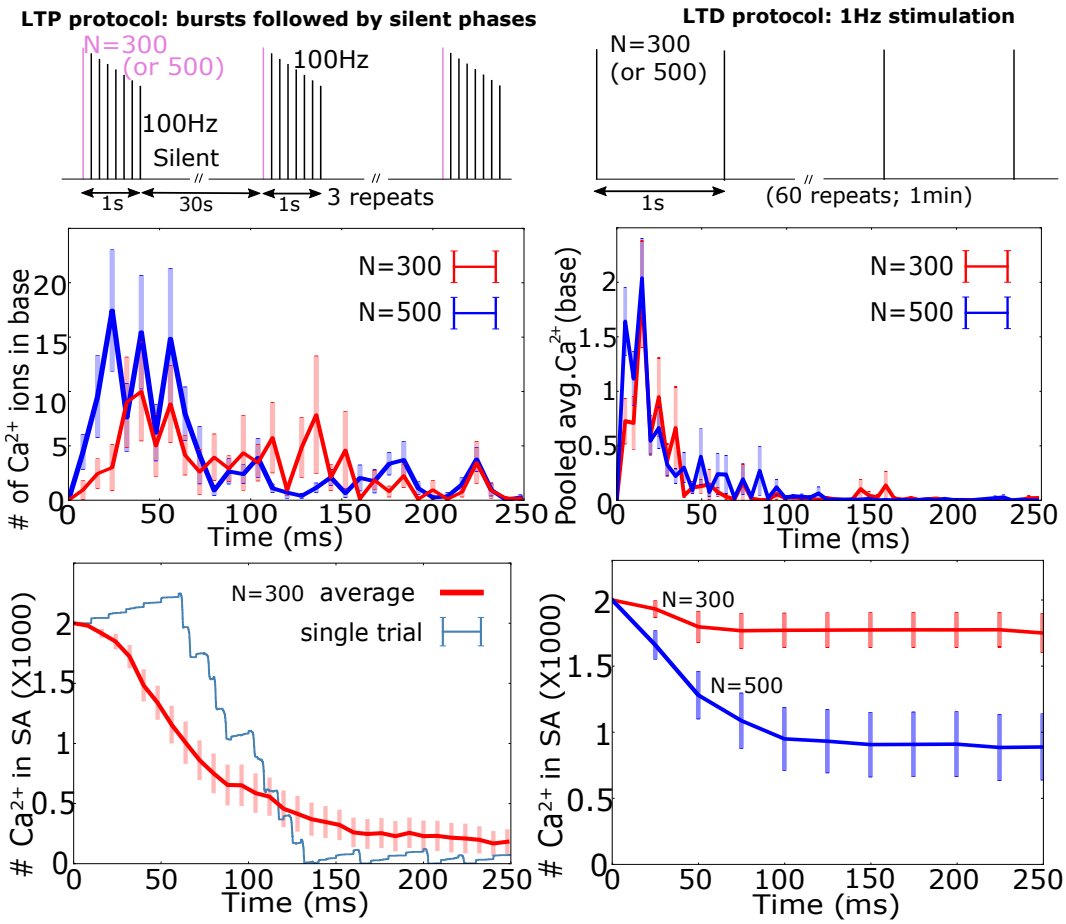

Figure 24: **Numerical simulations of dendritic spine's calcium transients during LTP (Left) and LTD (Right) induction protocols.** Top schematics show the postsynaptic induction protocols with the injected number of ions N per current stimulation. Middle plots compare the number of calcium ions in the base (pooled averages of the first 250 ms following the start of each injection). The bottom plots compare the SA depletion timescale. The mean and SEM values are calculated over 20 trials.

In comparison, during the LTD protocol, calcium is injected at a slower rate of 1Hz during one minute. The number of ions injected per stimulation is either 300 or 500. This input leads sometimes to CICR events of the spine that increase the concentration at the base and deplete SA calcium storage. The number of calcium ions at the base during the first 250ms here is only about one tenth of the LTP response for the injection protocols with

both N=300 and 500 ions (Fig. 24 right middle). In addition, calcium depletion in the SA during LTD is much slower and takes several seconds (Fig.24 right bottom) in contrast to the several hundred millisecond timescale during the LTP stimulation.
These results are counter-intuitive because we expect the calcium level at the spine base to be lower during the LTP protocol that rapidly depletes the SA stores. However, I found that the 30s silent periods in between LTP stimulations actually contribute to SA refilling via STIM-ORAI inputs, and thereby the spine is able to release sufficient calcium in the succeeding cycles of LTP stimulation. This recovery role of the silent periods in the LTP stimulation is the the key novel insight from my modeling and simulations. Therefore, I conclude that the SA depletion timescales are different in LTP and LTD induction protocols, resulting in a considerable difference in the calcium levels at the base of the spine. This difference could eventually be the underlying determinant of the spine's fate towards either synaptic potentiation or depression (See also discussion Section 8.1.1).

0.5 Organisation of the thesis

Part I, Chapters 1-3

Chapter 1 includes the computational results on extreme statistics of diffusion times in 1, 2 and 3 dimensional domains. This framework is further extended in Chapter 2, with the analysis of the fastest diffusing trajectories in domains including obstacles. In chapter 3, cusp-like domains with hidden targets are analysed. These findings will subsequently be applied to calcium diffusion in dendritic spines.

Part II, Chapters 4-5

In Chapters 4-5, I present my findings about fast calcium dynamics in dendrite spines. These results are based on the extreme statistics framework developed in the previous chapters. A major result about dendritic spines is the delineation of its nanoscale organisation in terms of calcium uptake and release that could explain the fast calcium transients with calcium-induced calcium release.

Part II, Chapters 6-7

In Chapters 6-7, I present the results about the calcium refilling mechanism of spine apparatus. I characterize the timescale of the SA-refilling STIM-ORAI pathway, in comparison to the synaptic inputs into spines that could deplete calcium stores. In addition, I show how the nanoscale geometry is critical also for the calcium refilling pathway as well as for regulating calcium towards long-term synaptic changes.

Part I: Analytical and simulation results on extreme statistics

Chapter 1

Asymptotic formulas for extreme statistics of escape times in 1,2 and 3-dimensions

Published as: **Basnayake, K.**, Schuss, Z., & Holcman, D. (2019). Asymptotic formulas for extreme statistics of escape times in 1, 2 and 3-dimensions. *Journal of Nonlinear Science*, 29(2), 461-499. https://doi.org/10.1007/s00332-018-9493-7

Abstract

The first of N identical independently distributed (i.i.d.) Brownian trajectories that arrives to a small target, sets the time scale of activation, which in general is much faster than the arrival to the target of a single trajectory only. Analytical asymptotic expressions for the minimal time is notoriously difficult to compute in general geometries. We derive here asymptotic laws for the probability density function of the first and second arrival times of a large number N of i.i.d. Brownian trajectories to a small target in 1,2, and 3 dimensions and study their range of validity by stochastic simulations. The results are applied to activation of biochemical pathways in cellular biology.

1.1 Introduction

Fast activation of biochemical pathways in cell biology is often initiated by the first arrival of a particle to a small target. This is the case of calcium activation in synapses of neuronal cells [46–48], fast photoresponse in rods, cones and fly photoreceptors [49–51], and many more. However, the time scale underlying these fast activations is not very well understood. We propose here that these generic molecular mechanisms are initiated by the first arrival of one or more of the many identical independently distributed (i.i.d.) Brownian particles to small receptors, such as the influx of many Brownian neurotransmitters inside a synaptic cleft to receptors [52, 53].
In general, one or several particles are required to initiate a cascade of chemical reactions,

such as the opening of a protein channel [54] of a cellular membrane, which amplifies the inflow of ions to an avalanche of thousands or more ions, resulting from the initial binding of few couple of ions or neurotransmitters. The statistic of the minimal arrival times are referred to in the statistical physics literature as extreme statistics [55]. Despite great efforts [55–62], there are no explicit expressions for the probability distributions of arrival times of the first trajectory, the second, and so on. Only general formulas are given, and they account for neither specific geometrical constraints of the bounding domains, where particles evolve, nor for the small targets that bind these particles.
The main example to keep in mind is the statistics of the escape time through a small window of the first of N particles. Asymptotic expressions for the mean escape time of a single Brownian path, the so called narrow escape time, computed in the narrow escape theory [37, 41, 63–65], depends on global and local geometric properties of the bound domain and its boundary, such as the surface area (in 2 dimensions or volume (in 3 dimensions), and the local geometry near the absorbing window (mean curvature of the boundary at the small window, the window's shape, and relative size). The number and distribution of absorbing windows can influence drastically the narrow escape time. As shown below, the escape of the fastest particles selects trajectories that are very different from the typical ones, which determine the mean narrow escape time (NET).
Moreover, asymptotic analysis of the expected first arrival time is not the same as of the mean first passage time (MFPT) of a single Brownian path to a small window. The analysis of the first one to arrive relies on the time-dependent solution of the Fokker-Planck equation and the short-time asymptotics of the survival probability density function (pdf). Previous studies of the short-time asymptotics of the diffusion equation concern the asymptotics of the trace of the heat kernel analysis [66, 67]. Here, an estimate is needed of the survival probability, which requires different analysis. Our method is based on the construction of the asymptotics from Green's function of the Helmholtz equation. The main results are explicit expressions for the statistics of the first arrival time, see attempt in [68] in 1,2, and 3 dimensions and a formula for the expected shortest exit time from a neuronal spine with and without returns. The manuscript is organized as follows. First we present the general framework for the computation of the pdf of the first arrival in a population of N Brownian particles in a ray and in an interval. We then compute the pdf of the extreme escape time in dimensions 2 and 3 through small windows. We then study the second arrival time. We further consider the case of a bulk domain with a window connected to a narrow cylinder (dendritic spine shape [37, 41]). Finally, we discuss applications to activation in cellular biology and neuroscience.

1.2 The pdf of the first escape time

The narrow escape problem (NEP) for the shortest arrival time of N non-interacting i.i.d. Brownian trajectories (ions) in a bounded domain Ω to a binding site is defined as follows.

Denote by t_i the arrival times and by τ^1 the shortest one,

$$\tau^1 = \min(t_1, \ldots, t_N), \tag{1.1}$$

where t_i are the i.i.d. arrival times of the N ions in the medium. The NEP is to find the pdf and the MFPT of τ^1. The complementary cumulative density function of τ^1 is given by

$$\Pr\{\tau^1 > t\} = \Pr^N\{t_1 > t\}, \tag{1.2}$$

where $\Pr\{t_1 > t\}$ is the survival probability of a single particle prior to binding at the target. This probability can be computed from the following boundary value problem. We will use the following notation for the pdf of the arrival time:

$$\Pr\{t_1 \in (t, t+dt)\} = \Pr\{t_1 = t\}dt. \tag{1.3}$$

Assuming that the boundary $\partial\Omega$ contains N_R binding sites $\partial\Omega_i \subset \partial\Omega$, we have

$$\partial\Omega_a = \bigcup_{i=1}^{N_R} \partial\Omega_i, \tag{1.4}$$

and $\partial\Omega_r = \partial\Omega - \partial\Omega_a$, the pdf of a Brownian trajectory is the solution of the initial boundary value problem (IBVP)

$$\begin{aligned}
\frac{\partial p(\boldsymbol{x},t)}{\partial t} &= D\Delta p(\boldsymbol{x},t) \quad \text{for } \boldsymbol{x} \in \Omega,\ t > 0 \\
p(\boldsymbol{x},0) &= p_0(\boldsymbol{x}) \quad \text{for } \boldsymbol{x} \in \Omega \ \text{(initial distribution)} \\
\frac{\partial p(\boldsymbol{x},t)}{\partial \boldsymbol{n}} &= 0 \quad \text{for } \boldsymbol{x} \in \partial\Omega_r \\
p(\boldsymbol{x},t) &= 0 \quad \text{for } \boldsymbol{x} \in \partial\Omega_a.
\end{aligned} \tag{1.5}$$

The survival probability is

$$\Pr\{t_1 > t\} = \int_\Omega p(\boldsymbol{x},t)\, d\boldsymbol{x}, \tag{1.6}$$

so that the pdf for the arrival of the first particle is

$$\Pr\{\tau^1 = t\} = \frac{d}{dt}\Pr\{\tau^1 < t\} = N(\Pr\{t_1 > t\})^{N-1}\Pr\{t_1 = t\}, \tag{1.7}$$

where

$$\Pr\{t_1 = t\} = \oint_{\partial\Omega_a} \frac{\partial p(\boldsymbol{x},t)}{\partial \boldsymbol{n}}\, dS_{\boldsymbol{x}}. \tag{1.8}$$

Since there are N_R well separated windows of the same size, using relation 1.4, we obtain [69] that the total flux over the boundary is the sum over individual fluxes:

$$\Pr\{t_1 = t\} = N_R \oint\limits_{\partial\Omega_1} \frac{\partial p(\boldsymbol{x}, t)}{\partial \boldsymbol{n}}\, dS_{\boldsymbol{x}}. \tag{1.9}$$

Putting all the above together results in the pdf

$$\Pr\{\tau^1 = t\} = NN_R \left[\int\limits_{\Omega} p(\boldsymbol{x}, t) d\boldsymbol{x}\right]^{N-1} \oint\limits_{\partial\Omega_1} \frac{\partial p(\boldsymbol{x}, t)}{\partial \boldsymbol{n}} dS_{\boldsymbol{x}}. \tag{1.10}$$

The first arrival time is computed from the survival probability of a particle and the flux through the target. Obtaining an explicit or asymptotic expression is not possible in general.

The pdf of the first arrival time in an interval

To obtain an analytic expression for the pdf of the first arrival time (1.10) of a particle inside a narrow neck that could represent the dendritic spine neck, we model the narrow spine neck as a segment of length L, with a reflecting boundary at $x = 0$ and absorbing boundary at $x = L$. Then the diffusion boundary value problem (1.5) becomes

$$\frac{\partial p}{\partial t} = D\frac{\partial^2 p}{\partial x^2} \quad \text{for } 0 < x < L,\ t > 0 \tag{1.11}$$

$$p(x, 0) = \delta(x) \quad \text{for } 0 < x < L \tag{1.12}$$

$$p(L, t) = \frac{\partial p(0, t)}{\partial x} = 0 \quad \text{for } t > 0, \tag{1.13}$$

where the initial condition corresponds to a particle initially at the origin. One possibility is to expand the solution on the eigenfunction basis:

$$p(x, t) = 2\sum_{n=0}^{\infty} e^{-D\lambda_n^2 t} \cos \lambda_n x, \tag{1.14}$$

where the eigenvalues are

$$\lambda_n = \frac{\pi}{L}\left(n + \frac{1}{2}\right). \tag{1.15}$$

The survival probability (1.6) of a particle is thus given by

$$\Pr\{t_1 > t\} = \int\limits_0^L p(x, t) dx = 2\sum_{n=0}^{\infty} \frac{(-1)^n}{\lambda_n} e^{-D\lambda_n^2 t}. \tag{1.16}$$

The pdf of the arrival time to L of a single Brownian trajectory is the probability efflux at the absorbing boundary $\partial\Omega_a$, given by

$$-\oint_{\Omega_a} \frac{\partial p(\boldsymbol{x},t)}{\partial \boldsymbol{n}}\, dS_{\boldsymbol{x}} = -\frac{\partial p(L,t)}{\partial x} = 2\sum_{n=0}^{\infty} (-1)^n \lambda_n e^{-D\lambda_n^2 t}. \tag{1.17}$$

Therefore, the pdf of the first arrival time in an ensemble of N particles to the absorbing end of the interval that started initially at the same location is given by

$$\Pr\{\tau^{(1)} = t\} = 2N \left(2\sum_{n=0}^{\infty} \frac{(-1)^n}{\lambda_n} e^{-D\lambda_n^2 t} \right)^{N-1} \sum_{n=0}^{\infty} (-1)^n \lambda_n e^{-D\lambda_n^2 t}. \tag{1.18}$$

For numerical purposes, we approximate (1.18) by truncating the sum after n_0 terms,

$$\Pr\{\tau^{(1)} = t\} \approx f_{n_0}(t) = N \left(\sum_{n=0}^{n_0} \frac{(-1)^n}{\lambda_n} e^{-D\lambda_n^2 t} \right)^{N-1} \sum_{n=0}^{n_0} (-1)^n \lambda_n e^{-D\lambda_n^2 t}. \tag{1.19}$$

Figs.1.1A-B show the pdfs of the first arrival time for $N = 5$ and $N = 500$ Brownian particles with diffusion coefficient $D = 1$, which start at $x = 0$ at time 0 and exit the interval at $x = 1$. These figures confirm the validity of the analytical approximation (1.18) with only $n_0 = 100$ terms in the slowly converging alternating series. We shall use later on (subsection 1.3) the short-term expansion of the diffusion equation.

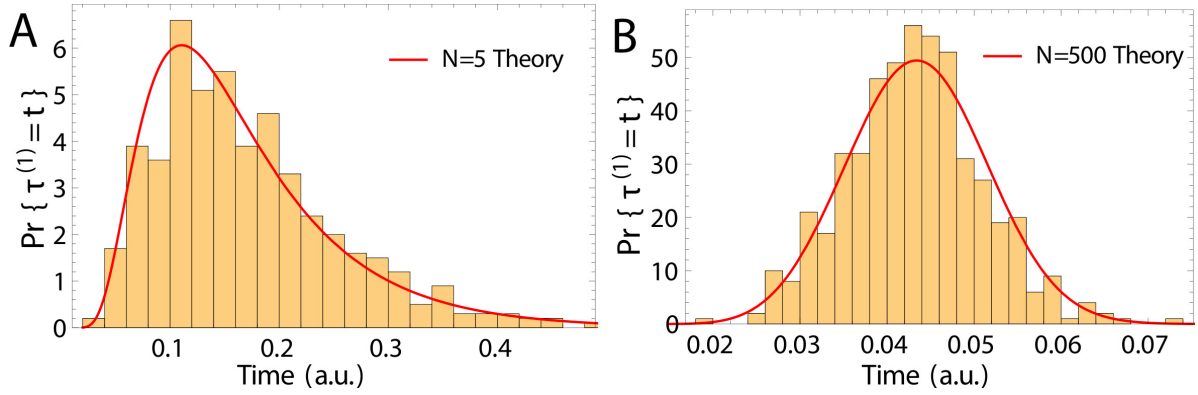

Figure 1.1: Histograms of the arrival times to the boundary of the fastest particle, obtained from Brownian simulations with Euler's scheme. The number of Brownian particles is $N = 5$ in **A** and $N = 500$ in **B**. The analytical solution (red curves) of equation (1.19) is obtained by truncating the series at $n_0 = 100$. Adding more term in the series does not change much the analytical curve. The time axes are in arbitrary units (a.u).

1.3 Asymptotics of the expected mean shortest time $\bar{\tau}^1$

In this section, we derive several asymptotic formulas for the expected mean shortest time $\bar{\tau}^1$ in dimension 1 before moving to dimension 2 and 3. Using relation 1.7 and integrating by part, the MFPT of the first among N i.i.d. Brownian paths is given by [41]

$$\bar{\tau}^1 = \int_0^\infty \Pr\{\tau^{(1)} > t\} dt = \int_0^\infty [\Pr\{t_1 > t\}]^N \, dt, \tag{1.20}$$

where t_1 is the arrival time of a single Brownian path. Writing the last integral in (1.20) as

$$\bar{\tau}^1 = \int_0^\infty e^{N \ln g(t)} dt, \tag{1.21}$$

it can be expanded for $N \gg 1$ by Laplace's method. Here

$$g(t) = \sum_{n=0}^{\infty} \frac{(-1)^n}{\lambda_n} e^{-D\lambda_n^2 t} \tag{1.22}$$

(see (1.16)).

Escape from a ray

Consider the case $L = \infty$ and the IBVP

$$\begin{aligned} \frac{\partial p(x,t)}{\partial t} &= D \frac{\partial^2 p(x,t)}{\partial x^2} \quad \text{for } x > 0,\ t > 0 \\ p(x,0) &= \delta(x-a) \quad \text{for } x > 0, \quad p(0,t) = 0 \quad \text{for } t > 0, \end{aligned} \tag{1.23}$$

whose solution is

$$p(x,t) = \frac{1}{\sqrt{4D\pi t}} \left[\exp\left\{ -\frac{(x-a)^2}{4Dt} \right\} - \exp\left\{ -\frac{(x+a)^2}{4Dt} \right\} \right]. \tag{1.24}$$

The survival probability with $D = 1$ is

$$\Pr\{t_1 > t\} = \int_0^\infty p(x,t)\, dx = 1 - \frac{2}{\sqrt{\pi}} \int_{a/\sqrt{4t}}^\infty e^{-u^2}\, du. \tag{1.25}$$

To compute the MFPT in (1.20), we use the expansion of the complementary error function

$$\frac{2}{\sqrt{\pi}} \int_x^\infty e^{-u^2}\, du = \frac{e^{-x^2}}{x\sqrt{\pi}} \left(1 - \frac{1}{2x^2} + O(x^{-4})\right) \quad \text{for } x \gg 1, \tag{1.26}$$

which gives

$$I_N \equiv \int_0^\infty \left[\Pr\{t_1 > t\}\right]^N dt \approx \int_0^\infty \exp\left\{N \ln\left(1 - \frac{e^{-(a/\sqrt{4t})^2}}{(a/\sqrt{4t})\sqrt{\pi}}\right)\right\} dt, \tag{1.27}$$

and with the approximation

$$I_N \approx \int_0^\infty \exp\left\{-N \frac{\sqrt{4t} e^{-\frac{a^2}{4t}}}{a\sqrt{\pi}}\right\} dt = \frac{a^2}{4} \int_0^\infty \exp\left\{-N \frac{\sqrt{u} e^{-\frac{1}{u}}}{\sqrt{\pi}}\right\} du. \tag{1.28}$$

To evaluate the integral (1.28), we make the monotone change of variable

$$w = w(t) = \sqrt{t} e^{-1/t}, \quad w'(t) = \sqrt{t} e^{-\frac{1}{t}} \left(\frac{1}{2t} + \frac{1}{t^2}\right). \tag{1.29}$$

Note that for small t,

$$w'(t) \approx w \frac{1}{t^2} \tag{1.30}$$

and $\ln w \approx -1/t$. Thus,

$$w'(t) \approx w(\ln w)^2. \tag{1.31}$$

Breaking with $N' = \frac{N}{\sqrt{\pi}}$

$$\begin{aligned} I_N &\approx \frac{a^2}{4} \int_0^\infty \exp\{-N'w\} \frac{1}{\frac{dw}{dt}}\, dw \\ &\approx \frac{a^2}{4} \left(\int_0^\delta \exp\{-N'w\} \frac{a^2}{w(\ln(w))^2}\, dw + \int_\delta^\infty \exp\{-N'w\} \frac{1}{\frac{dw}{dt}}\, dw \right) \end{aligned}$$

for some $0 < \delta < 1$, the second integral turns out to be exponentially small in N and is thus negligible relative to the first one. Integrating by parts,

$$\begin{aligned} I_N &\approx \frac{a^2}{4} \int_0^\delta \exp\{-N'w\} \frac{1}{w(\ln(w))^2} dw \\ &\approx O(\exp(-aN)) + \frac{a^2}{4} N' \int_0^\delta \exp\{-N'w\} \frac{1}{\ln|w|} dw \end{aligned}$$

and changing the variable to $u = N'w$, we obtain

$$N' \int_0^{\delta} \exp\{-N'w\} \frac{a^2}{4 \ln |w|}\, dw = \int_0^{N'\delta} \frac{a^2 \exp\{-u\}}{4 |\ln u/N'|}\, du.$$

Expanding

$$\frac{1}{|\ln u/N'|} = \frac{1}{\ln N'} \left(1 + \frac{|\ln u|}{\ln N} + O\left(\frac{|\ln u|}{\ln N'}\right)^2\right)$$

for $u > \varepsilon > 0$, we obtain,

$$N' \int_0^{\delta} \exp\{-N'w\} \frac{a^2}{4 \ln w} dw \approx \int_0^{N'\delta} \exp\{-u\} \frac{a^2}{4 |\ln N'|} \left(1 + \frac{|\ln u|}{\ln N'}\right) du.$$

Thus, breaking the integral into two parts, from $[0, \varepsilon]$ (which is negligible) and $[\varepsilon, \infty[$, we get

$$\bar{\tau}^1 \approx \frac{a^2}{4D \ln \frac{N}{\sqrt{\pi}}} \quad \text{for } N \gg 1. \tag{1.32}$$

Escape for the second fastest from half a line

Equation (1.144) and the approximation (1.141) give

$$\Pr\{\tau^{(2)} = t\} = \int_0^t f(t-s) f(s)\, ds, \tag{1.33}$$

where

$$f(s) = \Pr\{\tau^{(1)} = s\} = N g(t)^N h(t). \tag{1.34}$$

According to (1.25),

$$g(t) = \Pr\{t_1 > t\} = \int_0^{\infty} p(x,t)\, dx = 1 - \frac{2}{\sqrt{\pi}} \int_{a/\sqrt{4t}}^{\infty} e^{-u^2}\, du \tag{1.35}$$

$$= 1 - \frac{e^{-(a/\sqrt{4t})^2}}{(a/\sqrt{4t})\sqrt{\pi}} + O(t^{3/2} e^{-(a/\sqrt{4t})^2}), \tag{1.36}$$

and differentiating the first line, we get

$$h(t) = -\frac{d \Pr\{t_1 > t\}}{dt} = \frac{2}{\sqrt{\pi}} \frac{a}{4\sqrt{t^3}} e^{-(a/\sqrt{4t})^2}. \tag{1.37}$$

1.4 Escape from an interval $[0, a]$

We follow the steps of the previous section, where Green's function for the homogenous IBVP is now given by the infinite sum

$$p(x,t\,|\,y) = \frac{1}{\sqrt{4D\pi t}} \sum_{n=-\infty}^{\infty} \left[\exp\left\{ -\frac{(x-y+2na)^2}{4t} \right\} - \exp\left\{ -\frac{(x+y+2na)^2}{4t} \right\} \right]. \quad (1.38)$$

The conditional survival probability is

$$\begin{aligned} \Pr\{t_1 > t\,|\,y\} &= \int_0^a p(x,t\,|\,y)\,dx \qquad (1.39) \\ &= \frac{1}{\sqrt{4D\pi t}} \sum_{n=-\infty}^{\infty} \int_0^a \left[\exp\left\{ -\frac{(x-y+2na)^2}{4t} \right\} - \exp\left\{ -\frac{(x+y+2na)^2}{4t} \right\} \right] dx \\ &= \int_0^a \frac{1}{\sqrt{4D\pi t}} \left[\exp\left\{ -\frac{(x-y)^2}{4t} \right\} - \exp\left\{ -\frac{(x+y)^2}{4t} \right\} \right] dx + S_1(y,t) - S_2(y,t), \end{aligned}$$

where

$$\begin{aligned} S_1 &= \frac{1}{\sqrt{4D\pi t}} \sum_{n=1}^{\infty} \int_0^a \left[\exp\left\{ -\frac{(x+y+2na)^2}{4t} \right\} - \exp\left\{ -\frac{(x-y+2na)^2}{4t} \right\} \right] dx \\ S_2 &= \frac{1}{\sqrt{4D\pi t}} \sum_{n=1}^{\infty} \int_0^a \left[\exp\left\{ -\frac{(x+y-2na)^2}{4t} \right\} - \exp\left\{ -\frac{(x-y-2na)^2}{4t} \right\} \right] dx. \end{aligned}$$

Note that the integrand in the third line of (29), denoted $p_1(x,t\,|\,y)$, satisfies the initial condition $p_1(x,0\,|\,y) = \delta(x-y)$ and the boundary condition $p_1(0,t\,|\,y) = p_1(x,t\,|\,0) = 0$, but $p_1(a,t\,|\,y) \neq 0$ and $p_1(x,t\,|\,a) \neq 0$. However, with the first correction,

$$\begin{aligned} p_2(x,t\,|\,y) = \frac{1}{\sqrt{4D\pi t}} \Bigg[&\exp\left\{ -\frac{(x-y)^2}{4t} \right\} - \exp\left\{ -\frac{(x+y)^2}{4t} \right\} \qquad (1.40) \\ &+ \exp\left\{ -\frac{(x-y-2a)^2}{4t} \right\} - \exp\left\{ -\frac{(x+y-2a)^2}{4t} \right\} \\ &+ \exp\left\{ -\frac{(x-y+2a)^2}{4t} \right\} - \exp\left\{ -\frac{(x+y+2a)^2}{4t} \right\} \Bigg] \end{aligned}$$

it satisfies the same initial condition for x and y in the interval, and the boundary conditions

$$p_2(x,t\,|\,a) = 0, \quad p_2(x,t\,|\,0) = \frac{1}{\sqrt{4D\pi t}} \left[\exp\left\{ -\frac{(x+2a)^2}{4t} \right\} - \exp\left\{ -\frac{(x-2a)^2}{4t} \right\} \right]. \quad (1.41)$$

Higher-order approximations correct the one boundary condition and corrupt the other, though the error decreases at higher exponential rates.

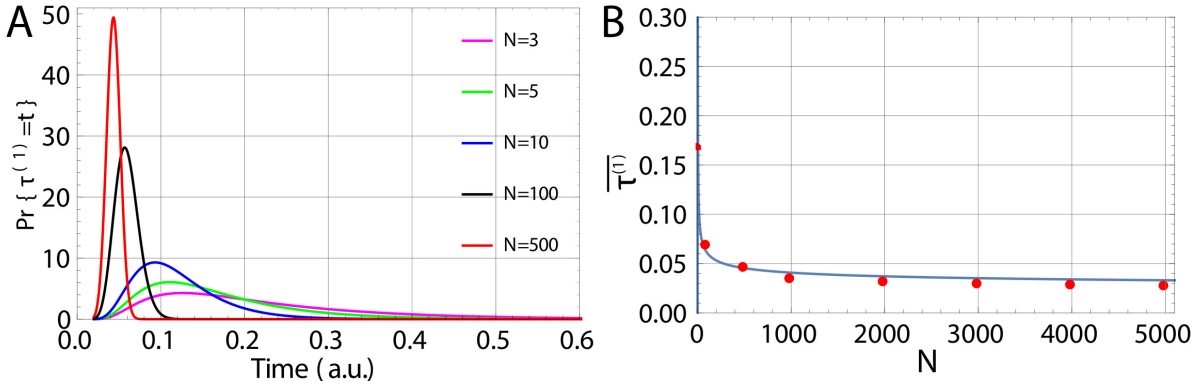

Figure 1.2: **A.** Plot of $\Pr\{\tau^{(1)} = t\}$ (escape from an interval) for $N = 3, 5, 10, 100$, and 500 with $n_0 = 100$ terms in the series of (1.19). **B.** Decay of the expected arrival time of the fastest particle vs N (red points). The plot of the asymptotic formula (1.48) is (blue) with parameter $\frac{0.282}{\log N}$. For the stochastic simulations, we used 500 runs.

The first line of (1.40) gives the approximation

$$\int_0^a \frac{1}{\sqrt{4\pi t}} \left[\exp\left\{ -\frac{(x+y)^2}{4t} \right\} - \exp\left\{ -\frac{(x-y)^2}{4t} \right\} \right] dx = \frac{1}{\sqrt{\pi}} \int_{(y-a)/2\sqrt{t}}^{y/2\sqrt{t}} e^{-u^2}\, du$$

$$\sim 1 - \max \frac{2\sqrt{t}}{\sqrt{\pi}} \left[\frac{e^{-y^2/4t}}{y}, \frac{e^{-(a-y)^2/4t}}{a-y} \right] \quad \text{as } t \to 0, \tag{1.42}$$

where the maximum occurs at $\min[y, a-y]$ for $0 < y < a$ (the shortest ray from y to the boundary). Starting at $x = a/2$, this gives

$$\Pr\{t_1 > t\} = \int_0^a \frac{1}{\sqrt{4\pi t}} \left[\exp\left\{ -\frac{(x-a/2)^2}{4t} \right\} - \exp\left\{ -\frac{(x+a/2)^2}{4t} \right\} \right] dx \quad \text{as } t \to 0,$$

so changing $x + a/2 = z\sqrt{4t}$ in the first integral and $x - a/2 = z\sqrt{4t}$ in the second, we get

$$\frac{1}{\sqrt{\pi}} \int_{-a/4\sqrt{t}}^{a/4\sqrt{t}} e^{-z^2}\, dz - \frac{1}{\sqrt{\pi}} \int_{a/4\sqrt{t}}^{3a/4\sqrt{t}} e^{-z^2}\, dz \approx 1 - \frac{4\sqrt{t}e^{-a^2/16t}}{a\sqrt{\pi}} - \frac{2\sqrt{t}e^{-a^2/16t}}{a\sqrt{\pi}} - \frac{4\sqrt{t}e^{-9a^2/16t}}{6a\sqrt{\pi}}$$

$$= 1 - \frac{6\sqrt{t}e^{-a^2/16t}}{a\sqrt{\pi}} - \frac{2\sqrt{t}e^{-9a^2/16t}}{3a\sqrt{\pi}}. \tag{1.43}$$

The second integral in the second line of (1.40) is

$$I_{3/2} = -\int_0^a \frac{1}{\sqrt{4\pi t}} \left[\exp\left\{-\frac{(x-3a/2)^2}{4t}\right\}\right] dx. \tag{1.44}$$

Set $x - 3a/2 = -z\sqrt{4t}$, then (1.44) becomes

$$I_{3/2} = -\frac{1}{\sqrt{\pi}} \int_{a/4\sqrt{t}}^{3a/4\sqrt{t}} \exp\left\{-z^2\right\} dz = -\frac{1}{\sqrt{\pi}} \int_{a/4\sqrt{t}}^{\infty} \exp\left\{-z^2\right\} dz + \frac{1}{\sqrt{\pi}} \int_{3a/4\sqrt{t}}^{\infty} \exp\left\{-z^2\right\} dz.$$

Thus the second line of (1.40) is

$$\begin{aligned} &-\int_0^a \frac{1}{\sqrt{4\pi t}} \left[\exp\left\{-\frac{(x-3a/2)^2}{4t}\right\} - \exp\left\{-\frac{(x-5a/2)^2}{4t}\right\}\right] dx \\ &\approx -\frac{2\sqrt{t}}{a\sqrt{\pi}} e^{-a^2/16t} + \frac{2\sqrt{t}}{5a\sqrt{\pi}} e^{-25a^2/16t}, \end{aligned} \tag{1.45}$$

and in the third line of (1.40), we get

$$\begin{aligned} &\int_0^a \frac{1}{\sqrt{4\pi t}} \left[\exp\left\{-\frac{(x+3a/2)^2}{4t}\right\} - \exp\left\{-\frac{(x+5a/2)^2}{4t}\right\}\right] dx \\ &\approx \frac{2\sqrt{t}}{3a\sqrt{\pi}} e^{-9a^2/16t} - \frac{2\sqrt{t}}{5a\sqrt{\pi}} e^{-49a^2/16t}, \end{aligned} \tag{1.46}$$

hence

$$\int_0^\infty \left[\Pr\{t_1 > t\}\right]^N dt \approx \int_0^\infty \exp\left\{N \ln\left(1 - \frac{8\sqrt{t}}{a\sqrt{\pi}} e^{-a^2/16t}\right)\right\} dt \tag{1.47}$$

and the expected time of the fastest particle that starts at the center of the interval is (1.32) with a replaced by $a/2$ and N replaced by $2N$. That is,

$$\bar{\tau}^1 \approx \frac{a^2}{16D \ln \frac{2N}{\sqrt{\pi}}} \quad \text{for } N \gg 1. \tag{1.48}$$

Figure 1.2A shows plot of the pdf analytical approximation of shortest arrival time (1.19) with $n_0 = 100$ terms, $D = 1$ and $L = 1$ for $N = 4, 6$, and 10. As the number of particles increases, the mean first arrival time decreases (Fig.1.2B) and according to equation (1.48), the asymptotic behavior is given by $C/\log N$, where C is a constant. We show below the pdf of the fastest Brownian particle.

1.5 The shortest NEP from a bounded domain in $\mathbb{R}^{2,3}$

To generalize the previous result to the case of N i.i.d. Brownian particles in a bounded domain $\Omega \subset \mathbb{R}^{2,3}$, we assume that the particles are initially injected at a point $\boldsymbol{y} \in \Omega$ and they can escape through a single small absorbing window $\partial\Omega_a$ in the boundary $\partial\Omega$ of the domain. The pdf of the fist passage time to $\partial\Omega_a$ is given by (1.10).

Asymptotics in dimension 3

To determine the short-time asymptotics of the pdf, we use the Laplace transform of the IBVP (1.5) and solve the resulting elliptic mixed Neumann-Dirichlet BVP [63]. The Dirichlet part of the boundary consists of N well-separated small absorbing windows, $\partial\Omega_a = \bigcup_{j=1}^{N} \partial\Omega_j$ and the reflecting (Neumann) part is $\partial\Omega_r = \partial\Omega - \partial\Omega_a$, so that the IBVP (1.5) has the form

$$\begin{aligned} \frac{\partial p(\boldsymbol{x}, t \,|\, \boldsymbol{y})}{\partial t} &= D\Delta p(\boldsymbol{x}, t \,|\, \boldsymbol{y}) \\ p(\boldsymbol{x}, 0 \,|\, \boldsymbol{y}) &= \delta(\boldsymbol{x} - \boldsymbol{y}) \quad \text{for} \quad \boldsymbol{x}, \boldsymbol{y} \in \Omega \\ \frac{\partial p(\boldsymbol{x}, t \,|\, \boldsymbol{y})}{\partial \boldsymbol{n}} &= 0 \quad \text{for} \quad \boldsymbol{x} \in \partial\Omega_r \\ p(\boldsymbol{x}, t \,|\, \boldsymbol{y}) &= 0 \quad \text{for} \quad t > 0, \ \boldsymbol{x} \in \partial\Omega_a. \end{aligned} \tag{1.49}$$

We consider the case $N = 1$. The Laplace transform of (1.5),

$$\hat{p}(\boldsymbol{x}, q \,|\, \boldsymbol{y}) = \int_0^\infty p(\boldsymbol{x}, t \,|\, \boldsymbol{y}) e^{-pt} \, dt, \tag{1.50}$$

gives the BVP

$$\begin{aligned} -\delta(\boldsymbol{x} - \boldsymbol{y}) + q\hat{p}(\boldsymbol{x}, q \,|\, \boldsymbol{y}) &= D\Delta\hat{p}(\boldsymbol{x}, q \,|\, \boldsymbol{y}) \ \text{ for } \boldsymbol{x}, \boldsymbol{y} \in \Omega \\ \frac{\partial \hat{p}(\boldsymbol{x}, q \,|\, \boldsymbol{y})}{\partial \boldsymbol{n}} &= 0 \ \text{ for } \ \boldsymbol{x} \in \partial\Omega_r \\ \hat{p}(\boldsymbol{x}, q \,|\, \boldsymbol{y}) &= 0 \quad \text{for} \quad \boldsymbol{x} \in \partial\Omega_a. \end{aligned} \tag{1.51}$$

Green's function for the Neumann problem in Ω is the solution of

$$\begin{aligned} -\Delta_{\boldsymbol{x}} \hat{G}(\boldsymbol{x}, q \,|\, \boldsymbol{y}) + q\hat{G}(\boldsymbol{x}, q \,|\, \boldsymbol{y}) &= \delta(\boldsymbol{x} - \boldsymbol{y}) \quad \text{for } \boldsymbol{x}, \boldsymbol{y} \in \Omega, \\ \frac{\partial \hat{G}_q(\boldsymbol{x}, q \,|\, \boldsymbol{y})}{\partial n_{\boldsymbol{x}}} &= 0 \quad \text{for } \boldsymbol{x}, \boldsymbol{y} \in \partial\Omega. \end{aligned} \tag{1.52}$$

The asymptotic solution of (1.52) in $\mathbb{R}^3$ is given by

$$\hat{G}(\boldsymbol{x}, q \,|\, \boldsymbol{y}) = \frac{e^{-\sqrt{q}|\boldsymbol{x}-\boldsymbol{y}|}}{4\pi||\boldsymbol{x} - \boldsymbol{y}||} + R_q(\boldsymbol{x}, \boldsymbol{y}), \tag{1.53}$$

where $R_q(\boldsymbol{x},\boldsymbol{y})$ is more regular than the first term. When $\boldsymbol{x}$ (or $\boldsymbol{y}$) is on the boundary,

$$\hat{G}(\boldsymbol{x},q\,|\,\boldsymbol{y}) = e^{-\sqrt{q}|\boldsymbol{x}-\boldsymbol{y}|}\left(\frac{1}{2\pi||\boldsymbol{x}-\boldsymbol{y}||}+\frac{H(\boldsymbol{x})}{2\pi}\log|\boldsymbol{x}-\boldsymbol{y}|+R(\boldsymbol{x},\boldsymbol{y})\right), \tag{1.54}$$

where $R(\boldsymbol{x},\boldsymbol{y})$ is more regular than the logarithmic term and $H(\boldsymbol{x})$ is a geometric factor [63]. We start with Green' identity,

$$\begin{aligned}&\int_{\Omega}\left[\hat{p}(\boldsymbol{x},q\,|\,\boldsymbol{y})\Delta_{\boldsymbol{x}}\hat{G}(\boldsymbol{x},q\,|\,\boldsymbol{y})-\Delta_{\boldsymbol{x}}\hat{p}(\boldsymbol{x},q\,|\,\boldsymbol{y})\hat{G}(\boldsymbol{x},q\,|\,\boldsymbol{y})\right]d\boldsymbol{y}\\ =&\int_{\partial\Omega}\left[\hat{p}(\boldsymbol{x},q\,|\,\boldsymbol{y})\frac{\partial\hat{G}(\boldsymbol{x},q\,|\,\boldsymbol{y})}{\partial n_{\boldsymbol{x}}}-\frac{\partial\hat{p}(\boldsymbol{x},q\,|\,\boldsymbol{y})}{\partial n_{\boldsymbol{x}}}\hat{G}(\boldsymbol{x},q\,|\,\boldsymbol{y})\right]dS_{\boldsymbol{y}},\end{aligned}$$

hence substituting with the solutions of equations (1.52) and (1.51), we get

$$\hat{p}(\boldsymbol{x},q\,|\,\boldsymbol{y}) = \hat{G}(\boldsymbol{x},q\,|\,\boldsymbol{y})-\int_{\partial\Omega_a}\frac{\partial\hat{p}(\boldsymbol{x},q\,|\,\boldsymbol{y}')}{\partial n_{\boldsymbol{x}}}\hat{G}(\boldsymbol{x},q\,|\,\boldsymbol{y}')\,dS_{\boldsymbol{y}'}. \tag{1.55}$$

If the absorbing window $\partial\Omega_a$ is centered at $\boldsymbol{x}=\boldsymbol{A}$, then, for $\boldsymbol{x}\in\partial\Omega_a$,

$$0 = \hat{G}(\boldsymbol{A},q\,|\,\boldsymbol{y})-\int_{\partial\Omega_a}\frac{\partial\hat{p}(\boldsymbol{A},q\,|\,\boldsymbol{y}')}{\partial n_{\boldsymbol{x}}}\hat{G}(\boldsymbol{A},q\,|\,\boldsymbol{y}')\,dS_{\boldsymbol{y}'}. \tag{1.56}$$

This is a Helmoltz equation and the solution has the following form (see [63]and [41])

$$\hat{p}(\boldsymbol{A},q\,|\,\boldsymbol{y}) = \frac{C}{\sqrt{a^2-r^2}}, \tag{1.57}$$

where $r=|\boldsymbol{A}-\boldsymbol{y}|$ and the constant $C>0$ is computed from

$$0 = G_q(\boldsymbol{A},\boldsymbol{y})-\int_{\partial\Omega_a}\frac{\partial\hat{p}(\boldsymbol{A},q,\boldsymbol{y}\,|\,\boldsymbol{y})}{\partial n_{\boldsymbol{x}}}G_q(\boldsymbol{A},\boldsymbol{y})dS_{\boldsymbol{y}} \tag{1.58}$$

and to leading order,

$$G_q(\boldsymbol{A},\boldsymbol{y}) = \int_{\partial\Omega_a}\frac{Ce^{-\sqrt{q}|\boldsymbol{y}-\boldsymbol{A}|}}{\sqrt{a^2-r^2}}\left(\frac{1}{2\pi||\boldsymbol{y}-\boldsymbol{A}||}+\frac{H(\boldsymbol{x})}{2\pi}\log|\boldsymbol{y}-\boldsymbol{A}|+R(\boldsymbol{y},\boldsymbol{A})\right)dS_{\boldsymbol{y}}. \tag{1.59}$$

If $\partial\Omega_a$ is a disk of radius a, then

$$G_q(\boldsymbol{A},\boldsymbol{y}) \approx C\int_{\partial\Omega_a}\frac{e^{-\sqrt{q}r}}{\sqrt{a^2-r^2}}\frac{1}{2\pi r}2\pi r dr = \frac{\pi}{2}\left(I_0(\sqrt{q}a)-L_0(\sqrt{q}a)\right)C, \tag{1.60}$$

where I_0 is the modified Bessel function of the first kind and L_0 the Struve function.

Thus,

$$\hat{p}(\boldsymbol{x}, q \,|\, \boldsymbol{y}) = G_q(\boldsymbol{x}, \boldsymbol{y}) - G_q(\boldsymbol{A}, \boldsymbol{y}) \frac{2}{\pi \left(I_0(\sqrt{q}a) - L_0(\sqrt{q}a) \right)} \int\limits_{\partial\Omega_a} \frac{G_q(\boldsymbol{x}, \boldsymbol{y}) dS_{\boldsymbol{y}}}{\sqrt{a^2 - r^2}}. \quad (1.61)$$

For $|\boldsymbol{A} - \boldsymbol{x}| \gg a$ and q large, the asymptotic expansion is given

$$I_0(\sqrt{q}a) - L_0(\sqrt{q}a) = 2 \frac{1}{\pi \, a\sqrt{q}} + 2 \frac{1}{\pi \, a^3 q^{3/2}} + O\left(q^{-9/4}\right) \quad (1.62)$$

Thus with

$$\frac{2}{\pi(I_0(\sqrt{q}a) - L_0(\sqrt{q}a))} = \sqrt{q}a(1 - \frac{1}{a^2 q} + O(\frac{1}{q^2})) \quad (1.63)$$

the expression

$$\hat{p}(\boldsymbol{x}, q \,|\, \boldsymbol{y}) \approx G_q(\boldsymbol{x}, \boldsymbol{y}) - G_q(\boldsymbol{A}, \boldsymbol{y}) G_q(\boldsymbol{A}, \boldsymbol{x}) \frac{2}{\pi(I_0(\sqrt{q}a) - L_0(\sqrt{q}a))} \int\limits_{\partial\Omega_a} \frac{dS_{\boldsymbol{y}}}{\sqrt{a^2 - r^2}}, \quad (1.64)$$

for a small circular window of radius a becomes,

$$\hat{p}(\boldsymbol{x}, q \,|\, \boldsymbol{y}) \approx G_q(\boldsymbol{x}, \boldsymbol{y}) - 2\pi\sqrt{q}a^2(1 - \frac{1}{a^2 q} + O(\frac{1}{q^2})) G_q(\boldsymbol{A}, \boldsymbol{y}) G_q(\boldsymbol{A}, \boldsymbol{x}) + o(a^2) \quad \text{for } a \ll 1 \quad (1.65)$$

To leading order in small t and $\boldsymbol{x}, \boldsymbol{y} \in \Omega$, we recall that the leading order term in expression 1.53 is the Green's function for diffusion equation:

$$\mathcal{L}^{-1}(G_q(\boldsymbol{x}, \boldsymbol{y})) \approx \frac{1}{(4\pi t)^{3/2}} e^{-\frac{|\boldsymbol{x} - \boldsymbol{y}|^2}{4t}}. \quad (1.66)$$

We will now use the inverse Laplace transform [70][p.1026; 29.3.87]

$$\mathcal{L}^{-1}(\sqrt{q} \frac{e^{-\sqrt{q}|\boldsymbol{x} - \boldsymbol{y}|}}{|\boldsymbol{x} - \boldsymbol{y}|}) = \frac{1}{4\sqrt{\pi t^3}} e^{-\frac{|\boldsymbol{x} - \boldsymbol{y}|^2}{4t}} H_2(\frac{|\boldsymbol{x} - \boldsymbol{y}|}{2\sqrt{t}}), \quad (1.67)$$

where $H_2(x) = 4x^2 - 2$ is the Hermite polynomial of degree 2. Note that the term in $\frac{1}{q^{1/2}}$ in (1.65) contributes for $t^{1/2}$, which can be neglected compared to the Hermite polynomial. With $\boldsymbol{A} \in \partial\Omega$, the image charge (for the Dirichlet boundary) leads to a factor 1/2 and we write

$$G_q(\boldsymbol{A}, \boldsymbol{y}) G_q(\boldsymbol{A}, \boldsymbol{x}) 2\pi\sqrt{q}a^2 = \sqrt{q}a^2 \frac{e^{-\sqrt{q}(|\boldsymbol{A} - \boldsymbol{y}| + |\boldsymbol{A} - \boldsymbol{x}|)}}{2\pi |\boldsymbol{A} - \boldsymbol{y}| |\boldsymbol{A} - \boldsymbol{x}|} \quad (1.68)$$

and

$$\mathcal{L}^{-1}(G_q(\boldsymbol{A},\boldsymbol{y})G_q(\boldsymbol{A},\boldsymbol{x})\sqrt{q}a^2) = \frac{a^2}{(4\pi t)^3}\frac{e^{-\frac{(|\boldsymbol{A}-\boldsymbol{y}|+|\boldsymbol{A}-\boldsymbol{x}|)^2}{4t}}}{|\boldsymbol{A}-\boldsymbol{y}||\boldsymbol{A}-\boldsymbol{x}|}H_2(\frac{|\boldsymbol{A}-\boldsymbol{y}|+|\boldsymbol{A}-\boldsymbol{x}|}{2\sqrt{t}}) \quad (1.69)$$

Finally,

$$\mathcal{L}^{-1}(\hat{p}(\boldsymbol{x},q\,|\,\boldsymbol{y})) = \frac{1}{\sqrt{(4\pi t)^3}}\left(e^{-\frac{|\boldsymbol{x}-\boldsymbol{y}|^2}{4t}} - \frac{a^2}{|\boldsymbol{A}-\boldsymbol{y}||\boldsymbol{A}-\boldsymbol{x}|}e^{-\frac{(|\boldsymbol{A}-\boldsymbol{y}|+|\boldsymbol{A}-\boldsymbol{x}|)^2}{4t}}H_2(\frac{|\boldsymbol{A}-\boldsymbol{y}|+|\boldsymbol{A}-\boldsymbol{x}|}{2\sqrt{t}})\right) \quad (1.70)$$

The short-time asymptotics of the survival probability with $\delta = |\boldsymbol{A}-\boldsymbol{y}|$ is

$$\begin{aligned} S(t) &\approx \int_\Omega p_t(\boldsymbol{x},\boldsymbol{y})d\boldsymbol{x} && (1.71)\\ &= \frac{1}{\sqrt{(4\pi t)^3}}\int_\Omega\left(e^{-\frac{|\boldsymbol{x}-\boldsymbol{y}|^2}{4t}} - \frac{a^2}{|\boldsymbol{A}-\boldsymbol{y}||\boldsymbol{A}-\boldsymbol{x}|}e^{-\frac{(|\boldsymbol{A}-\boldsymbol{y}|+|\boldsymbol{A}-\boldsymbol{x}|)^2}{4t}}H_2(\frac{|\boldsymbol{A}-\boldsymbol{y}|+|\boldsymbol{A}-\boldsymbol{x}|}{2\sqrt{t}})\right)d\boldsymbol{x} \\ &= I_1(t) - I_2(t) - I_3(t) - I_4(t), && (1.72)\end{aligned}$$

where for small t,

$$H_2(\frac{|\boldsymbol{A}-\boldsymbol{y}|+|\boldsymbol{A}-\boldsymbol{x}|}{2\sqrt{t}}) \approx \frac{(|\boldsymbol{A}-\boldsymbol{y}|+|\boldsymbol{A}-\boldsymbol{x}|)^2}{t}, \quad (1.73)$$

and

$$\begin{aligned} I_1(t) &= \frac{1}{\sqrt{(4\pi t)^3}}\int_\Omega e^{-\frac{|\boldsymbol{x}-\boldsymbol{y}|^2}{4t}}d\boldsymbol{x} && (1.74)\\ I_2(t) &= \frac{1}{\sqrt{(4\pi t)^3}}\frac{a^2\delta}{t}\int_\Omega\frac{1}{|\boldsymbol{A}-\boldsymbol{x}|}e^{-\frac{(\delta+|\boldsymbol{A}-\boldsymbol{x}|)^2}{4t}}d\boldsymbol{x} && (1.75)\\ I_3(t) &= \frac{1}{\sqrt{(4\pi t)^3}}\frac{2a^2}{t}\int_\Omega e^{-\frac{(\delta+|\boldsymbol{A}-\boldsymbol{x}|)^2}{4t}}d\boldsymbol{x}. && (1.76)\\ I_4(t) &= \frac{1}{\sqrt{(4\pi t)^3}}\frac{a^2}{\delta t}\int_\Omega|\boldsymbol{A}-\boldsymbol{x}|e^{-\frac{(\delta+|\boldsymbol{A}-\boldsymbol{x}|)^2}{4t}}d\boldsymbol{x}. && (1.77)\end{aligned}$$

Each integral is evaluated in the short-time limit.

$$I_1(t) = \frac{1}{\sqrt{(4\pi t)^3}} \int_\Omega e^{-\frac{|\boldsymbol{x}-\boldsymbol{y}|^2}{4t}} d\boldsymbol{x} \approx 1 - \frac{2}{\sqrt{\pi}} \int_{R_a/\sqrt{4t}}^{\infty} e^{-u^2} du \tag{1.78}$$

$$\approx 1 - \sqrt{4t}\frac{e^{-\left(R_a/\sqrt{4t}\right)^2}}{R_a\sqrt{\pi}} \left(1 + O\left(\left(R_a/\sqrt{4t}\right)^2\right)\right), \tag{1.79}$$

where R_a is the radius of the maximal ball inscribed in Ω. The integral I_2 is evaluated by the change of variables $\boldsymbol{z} = \boldsymbol{x} - \boldsymbol{A}$ and then $\eta = (\delta + r)/\sqrt{4t}$, where $r = |\boldsymbol{z}|$ (recall that $\boldsymbol{A}$ is in Ω_a),

$$I_2(t) = \frac{1}{\sqrt{(4\pi t)^3}} \frac{a^2\delta}{t} \int_\Omega \frac{1}{|\boldsymbol{A}-\boldsymbol{x}|} e^{-\frac{(\delta+|\boldsymbol{A}-\boldsymbol{x}|)^2}{4t}} d\boldsymbol{x} \tag{1.80}$$

$$= \frac{1}{\sqrt{(4\pi t)^3}} \frac{a^2\delta}{t} \int_{\Omega+\boldsymbol{A}} \frac{1}{|\boldsymbol{z}|} e^{-\frac{(\delta+|\boldsymbol{z}|)^2}{4t}} 2\pi|\boldsymbol{z}|^2 d|\boldsymbol{z}| \tag{1.81}$$

$$\approx \frac{2\pi}{\sqrt{(4\pi t)^3}} \frac{a^2\delta}{t} \int_{\frac{\delta}{\sqrt{4t}}}^{\frac{\delta+R}{\sqrt{4t}}} e^{-\eta^2} (\sqrt{4t}\eta - \delta)\sqrt{4t} d\eta, \tag{1.82}$$

where R is the radius of the largest half-ball centered at $\boldsymbol{A} \in \Omega_a$ and inscribed in Ω. For short time,

$$\int_{\frac{\delta}{\sqrt{4t}}}^{\frac{\delta+R}{\sqrt{4t}}} e^{-\eta^2} d\eta \approx \frac{1}{2}\left\{\frac{\sqrt{4t}}{\delta} e^{-\left(\frac{\delta}{\sqrt{4t}}\right)^2}\right\} \left(1 - \frac{4t}{2\delta^2} + 12\frac{t^2}{\delta^4}\right) \tag{1.83}$$

$$\int_{\frac{\delta}{\sqrt{4t}}}^{\frac{\delta+R}{\sqrt{4t}}} \eta e^{-\eta^2} d\eta = \frac{1}{2}\left(e^{-\left(\frac{\delta}{\sqrt{4t}}\right)^2} - e^{-\left(\frac{\delta+R}{\sqrt{4t}}\right)^2}\right) \approx \frac{1}{2} e^{-\left(\frac{\delta}{\sqrt{4t}}\right)^2}. \tag{1.84}$$

Therefore,

$$I_2(t) \approx \frac{1}{\sqrt{(4\pi t)^3}} \frac{2\pi a^2\delta}{t} \left(2te^{-\left(\frac{\delta}{\sqrt{4t}}\right)^2} - \delta\sqrt{4t}\frac{1}{2}\left(\frac{\sqrt{4t}}{\delta} e^{-(\frac{\delta}{\sqrt{4t}})^2}\right)(1 - \frac{4t}{2\delta^2} + 12\frac{t^2}{\delta^4})\right) \tag{1.85}$$

$$\approx \frac{4a^2}{\delta\sqrt{\pi}} \frac{1}{\sqrt{t}} (1 - \frac{6t}{\delta^2}) e^{-\left(\frac{\delta}{\sqrt{4t}}\right)^2}. \tag{1.86}$$

Now,

$$I_3(t) = \frac{1}{\sqrt{(4\pi t)^3}} \frac{2a^2}{t} \int_{\Omega} e^{-\frac{(\delta + |\boldsymbol{A} - \boldsymbol{x}|)^2}{4t}} d\boldsymbol{x} \tag{1.87}$$

$$= \frac{2\pi}{\sqrt{(4\pi t)^3}} \frac{2a^2}{t} \int_{\frac{\delta}{\sqrt{4t}}}^{\frac{\delta+R}{\sqrt{4t}}} e^{-\eta^2} (\sqrt{4t}\eta - \delta)^2 \sqrt{4t} d\eta \tag{1.88}$$

$$= \frac{2\pi}{\sqrt{(4\pi t)^3}} \frac{2a^2}{t} \int_{\frac{\delta}{\sqrt{4t}}}^{\frac{\delta+R}{\sqrt{4t}}} e^{-\eta^2} (4t\eta^2 - 2\sqrt{4t}\eta\delta + \delta^2) \sqrt{4t} d\eta, \tag{1.89}$$

that we write as $I_3(t) = I_3^{(1)}(t) + I_3^{(2)}(t) + I_3^{(3)}(t)$. The approximation

$$\int_{\frac{\delta}{\sqrt{4t}}}^{\frac{\delta+R}{\sqrt{4t}}} e^{-\eta^2} \eta^2 d\eta \approx \frac{\delta}{2\sqrt{4t}} e^{-\left(\frac{\delta}{\sqrt{4t}}\right)^2} + \frac{1}{4} \left(\frac{\sqrt{4t}}{\delta} e^{-\left(\frac{\delta}{\sqrt{4t}}\right)^2} \right) \left(1 - \frac{4t}{2\delta^2} + o(t) \right), \tag{1.90}$$

gives

$$I_3^{(1)}(t) = \frac{2\pi\delta}{\pi^{3/2}} \frac{a^2}{t\sqrt{4t}} e^{-\{\frac{\delta}{\sqrt{4t}}\}^2} + \frac{2a^2}{2t\pi^{3/2}} \frac{1}{\delta^2} \sqrt{4t} e^{-(\frac{\delta}{\sqrt{4t}})^2} \left(1 - \frac{4t}{2\delta^2} \right)$$

$$I_3^{(2)}(t) = -\frac{4\pi a^2 \delta}{t\sqrt{4t}\pi^{3/2}} e^{-(\frac{\delta}{\sqrt{4t}})^2}$$

$$I_3^{(3)}(t) = \frac{2\pi a^2 \delta}{t\sqrt{4t}\pi^{3/2}} e^{-\left(\frac{\delta}{\sqrt{4t}}\right)^2} \left(1 - \frac{4t}{2\delta^2} + o(t) \right).$$

Summing the three contributions, the leading order terms cancel and

$$I_3(t) = \frac{4a^2\sqrt{t}}{\pi^{1/2}\delta^3} e^{-\left(\frac{\delta}{\sqrt{4t}}\right)^2}. \tag{1.91}$$

To compute I_4, we decompose it into 4 pieces:

$$I_4(t) = \frac{1}{\sqrt{(4\pi t)^3}}\frac{a^2}{\delta t}\int\limits_{\Omega} |\boldsymbol{A}-\boldsymbol{x}| e^{-\frac{(\delta+|\boldsymbol{A}-\boldsymbol{x}|)^2}{4t}} d\boldsymbol{x}. \tag{1.92}$$

$$= \frac{2\pi}{\sqrt{(4\pi t)^3}}\frac{a^2}{\delta t}\int\limits_{\frac{\delta}{\sqrt{4t}}}^{\frac{\delta+R}{\sqrt{4t}}} e^{-\eta^2}(\sqrt{4t}\eta-\delta)^3\sqrt{4t}d\eta \tag{1.93}$$

$$= J_1(t)+J_2(t)+J_3(t)+J_4(t). \tag{1.94}$$

Direct computations give:

$$J_1(t) = \frac{2\pi(4t)^2}{\sqrt{(4\pi t)^3}}\frac{a^2}{\delta t}\int\limits_{\frac{\delta}{\sqrt{4t}}}^{\frac{\delta+R}{\sqrt{4t}}} e^{-\eta^2}\eta^3 d\eta = \frac{4a^2\delta}{\sqrt{\pi}(4t)^{3/2}}(1+\frac{4t}{\delta^2})e^{-\left(\frac{\delta}{\sqrt{4t}}\right)^2}, \tag{1.95}$$

where we used

$$\int\limits_{\frac{\delta}{\sqrt{4t}}}^{\frac{\delta+R}{\sqrt{4t}}} \eta^3 e^{-\eta^2} d\eta \approx \left(1+\frac{\delta^2}{4t}\right) e^{-\left(\frac{\delta}{\sqrt{4t}}\right)^2}. \tag{1.96}$$

Next,

$$J_2(t) = -\frac{2\pi}{\sqrt{(\pi)^3}}\frac{a^2}{\delta t}\int\limits_{\frac{\delta}{\sqrt{4t}}}^{\frac{\delta+R}{\sqrt{4t}}} e^{-\eta^2}3\eta^2\delta d\eta = -\frac{12a^2\delta}{\sqrt{\pi}(4t)^{3/2}}\left(1+\frac{2t}{\delta^2}(1-\frac{2t}{\delta^2}+\frac{12t^2}{\delta^4}+o(t^2))\right)e^{-\left(\frac{\delta}{\sqrt{4t}}\right)^2} \tag{1.97}$$

where we have used

$$\int\limits_{\frac{\delta}{\sqrt{4t}}}^{\frac{\delta+R}{\sqrt{4t}}} \eta^2 e^{-\eta^2} d\eta \approx \left(\frac{\delta}{2\sqrt{4t}}+\frac{\sqrt{4t}}{4\delta}\left(1-\frac{4t}{2\delta^2}+12\frac{t^2}{\delta^4}+o(t^2)\right)\right)e^{-\left(\frac{\delta}{\sqrt{4t}}\right)^2} \tag{1.98}$$

Using relation 1.83,

$$J_3(t) = \frac{2\pi}{\sqrt{(4t\pi^3)}}\frac{a^2}{\delta t}\int\limits_{\frac{\delta}{\sqrt{4t}}}^{\frac{\delta+R}{\sqrt{4t}}} e^{-\eta^2}3\eta\delta^2 d\eta = \frac{12a^2\delta}{\sqrt{\pi}(4t)^{3/2}}e^{-\frac{\delta^2}{4t}}. \tag{1.99}$$

Finally,

$$J_4(t) = -\frac{2\pi}{4t\sqrt{(\pi)^3}}\frac{a^2}{\delta t}\int\limits_{\frac{\delta}{\sqrt{4t}}}^{\frac{\delta+R}{\sqrt{4t}}} e^{-\eta^2}\delta^3 d\eta = -\frac{4a^2\delta}{(4t)^{3/2}\sqrt{\pi}}e^{-\frac{\delta^2}{4t}}\left(1-\frac{2t}{\delta^2}+\frac{12t^2}{\delta^4}+o(t^2)\right) \quad (1.100)$$

Direct computations show that the terms in $t^{-3/2}$ and $t^{-1/2}$ cancels out in the computation of I_4 from the four terms $J_1, ..J_4$ and it remains only the term in $t^{1/2}$

$$I_4(t) = -\frac{9a^2}{\sqrt{\pi}\delta^3}t^{1/2}e^{\{-\delta^2/4t\}}. \quad (1.101)$$

Summing (1.78)-(1.91)-(1.92), we get

$$\begin{aligned} S(t) &= \int\limits_{\Omega} p_t(\boldsymbol{x},\boldsymbol{y})d\boldsymbol{x} \\ &= 1-\sqrt{4t}\,\frac{e^{-\left(R_a/\sqrt{4t}\right)^2}}{R_a\sqrt{\pi}} - \frac{a^2}{\delta\pi^{1/2}\sqrt{t}}\,e^{-\delta^2/4t} + o\left(t^{1/2}e^{-\left(\frac{\delta}{\sqrt{4t}}\right)^2}\right) \\ &\approx 1-\frac{a^2}{\delta\pi^{1/2}\sqrt{t}}\,e^{-\delta^2/4t}. \end{aligned}$$

It follows that in three dimensions, the expected shortest arrival time to a small circular window of radius a, the expected shortest time $\bar{\tau}^3$ is given by

$$\begin{aligned} \bar{\tau}^3 = \int\limits_0^\infty \left[\Pr\{t_1 > t\}\right]^N dt &\approx \int\limits_0^\infty \exp N\log\left(1-\frac{a^2}{\delta\pi^{1/2}\sqrt{t}}\,e^{-\delta^2/4t}\right)dt \quad (1.102) \\ &\approx \int\limits_0^\infty \exp\left(-N\frac{4(a/\delta)}{\delta\pi^{3/2}\sqrt{t}}e^{-\delta^2/4t}\right)dt \quad (1.103) \\ &\approx \delta^2\int\limits_0^\infty \exp\left(-N'\frac{1}{\sqrt{u}}e^{-1/4u}\right)du, \quad (1.104) \end{aligned}$$

where $N' = N\frac{4a^2}{\pi^{1/2}\delta^2}$ Using the method develop in section 1.3 with the change of variable,

$$w = w(t) = \frac{1}{\sqrt{t}}e^{-1/t}, \quad w'(t) = \frac{1}{\sqrt{t}}e^{-\frac{1}{t}}\left(-\frac{1}{2t}+\frac{1}{4t^{3/2}}\right). \quad (1.105)$$

We have with $w' = 4w(\log(w))^{3/2}$

$$\bar{\tau}^3 \approx \delta^2\int\limits_0^\infty \frac{\exp(-N'w)}{4w(\log(w))^{3/2}}du$$

When the diffusion coefficient is D, the formula changes to

$$\bar{\tau}^3 \approx \frac{\delta^2}{2D\sqrt{\log\left(N\frac{4a^2}{\pi^{1/2}\delta^2}\right)}}. \tag{1.106}$$

The next term in the expansion can be obtained by accounting for the logarithmic singularity in the expansion of Green's function. When there are p windows, whose distances from the initial position of the Brownian particle are $d_k = dist(P_0, P_k)$, formula (1.106) changes to

$$\bar{\tau}^3 \approx \frac{\delta^2}{2D\sqrt{\log\left(N\frac{4a^2}{\pi^{1/2}\delta^2}\right)}}, \tag{1.107}$$

where $\delta^2 = \min(d_1^2, ..d_p^2)$. The asymptotic formula (1.106) is compared with results of Brownian simulations and shows very good agreement (Fig. 1.3). When absorbing windows are ellipses, the Green's function approach, based on Narrow Escape methodology, can be applied as well [41].

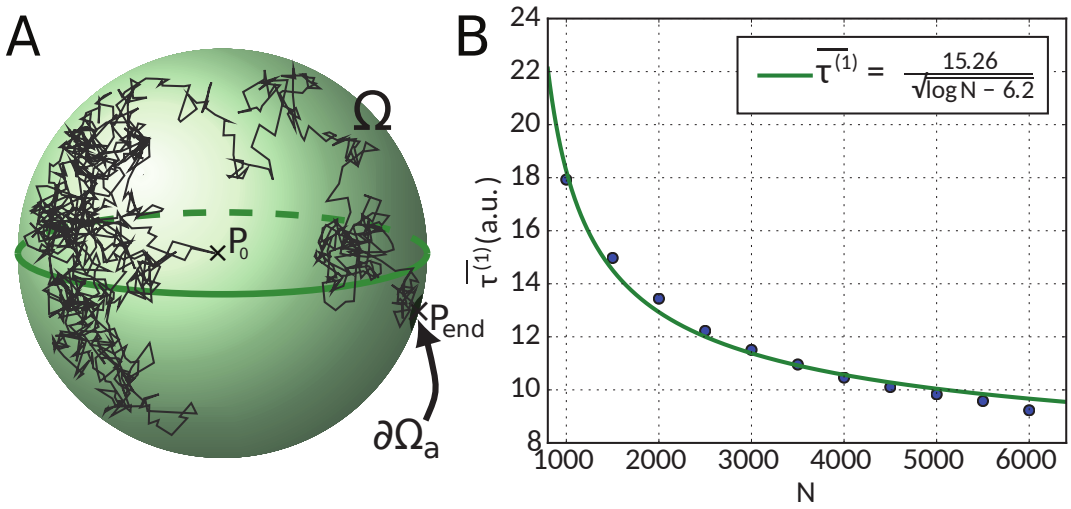

Figure 1.3: Extreme statistics of the narrow escape time through a small window in three dimensions. **A.** The geometry of the NEP for the fastest particle. In the simulation, the sphere has a radius 5 μm, the absorbing window $\partial\mathcal{S}_a$, has a radius $\varepsilon = 0.1\mu m$ and the diffusion coefficient is $D = 0.2\mu m^2 s^{-1}$. The trajectory starts at point P_0 (cross), and ends at point P_{end} . **B.** Plot of the MFPT of the fastest particle versus the number of particle N. We simulated 2000 runs. The asymptotic solution (red curve) is $A/\log(N + B)$.

Asymptotics in dimension 2

We consider the diffusion of N Brownian i.i.d. particles in a two-dimensional domain Ω with a small absorbing arc $\partial\Omega_a$ of length 2ε on the otherwise reflecting boundary $\partial\Omega$. To compute the pdf of the shortest arrival time to the arc, we follow the steps of the analysis in dimension 3, presented in the previous subsection 1.5.

The Neumann-Green function (1.52) in two dimensions is the solution of the BVP

$$-\Delta_{\boldsymbol{x}}\hat{G}(\boldsymbol{x},q\,|\,\boldsymbol{y})+q\hat{G}(\boldsymbol{x},q\,|\,\boldsymbol{y}) =\delta(\boldsymbol{x}-\boldsymbol{y}) \quad \text{for } \boldsymbol{x},\boldsymbol{y}\in\Omega, \tag{1.108}$$

$$\frac{\partial\hat{G}_q(\boldsymbol{x},q\,|\,\boldsymbol{y})}{\partial n_{\boldsymbol{x}}} =0 \quad \text{for } \boldsymbol{x},\boldsymbol{y}\in\partial\Omega, \tag{1.109}$$

is given for $\boldsymbol{x},\boldsymbol{y}\in\partial\Omega$ by [71, p.51]

$$\hat{G}(\boldsymbol{x},q\,|\,\boldsymbol{y})=\frac{1}{\pi}K_0(\sqrt{q}|\boldsymbol{x}-\boldsymbol{y}|)+R(\boldsymbol{x},\boldsymbol{y}), \tag{1.110}$$

where $R(\boldsymbol{x},\boldsymbol{y})$ is its regular part. For a disk, the analytical expression is given by the series

$$R(\boldsymbol{x},\boldsymbol{y})=\frac{1}{\pi}\sum_0^\infty \sigma_n\cos(n(\psi-\psi_0))\frac{K_n'(\sqrt{q})}{I_n'(\sqrt{q})}I_n(r\sqrt{q})I_n(r_0\sqrt{q}), \tag{1.111}$$

where $\sigma_0=1,\sigma_n=2$ for $n\geq 2$ and $\boldsymbol{x}=re^{i\psi},\boldsymbol{y}=r_0e^{i\psi_0}$. The integral representation (1.55) of the solution is

$$\hat{p}(\boldsymbol{x},q\,|\,\boldsymbol{y})=\hat{G}(\boldsymbol{x},q\,|\,\boldsymbol{y})-\int\limits_{\partial\Omega_a}\frac{\partial\hat{p}(\boldsymbol{x},q\,|\,\boldsymbol{y}')}{\partial n_{\boldsymbol{x}}}\hat{G}(\boldsymbol{x},q\,|\,\boldsymbol{y}')\,dS_{\boldsymbol{y}'}, \tag{1.112}$$

so choosing $\boldsymbol{x}\in\partial\Omega_a$,

$$0=\hat{G}(\boldsymbol{x},q\,|\,\boldsymbol{y})-\int\limits_{\partial\Omega_a}\frac{\partial\hat{p}(\boldsymbol{x},q\,|\,\boldsymbol{y}')}{\partial n_{\boldsymbol{x}}}\hat{G}(\boldsymbol{x},q\,|\,\boldsymbol{y}')\,dS_{\boldsymbol{y}'}. \tag{1.113}$$

This Helmholtz equation has the constant solution [41]

$$\frac{\partial\hat{p}(\boldsymbol{x},q\,|\,\boldsymbol{y}')}{\partial n_{\boldsymbol{x}}}=C \text{ for all } \boldsymbol{x}=\boldsymbol{A}\in\partial\Omega_a. \tag{1.114}$$

To leading order, we get

$$\hat{G}(\boldsymbol{A},q\,|\,\boldsymbol{y})=\frac{C}{\pi}\int\limits_{\partial\Omega_a}K_0(\sqrt{q}|\boldsymbol{A}-\boldsymbol{y}|)\,ds_{\boldsymbol{y}}, \tag{1.115}$$

where $ds_{\boldsymbol{y}}$ is arclength element in $\partial\Omega_a$. When $|\boldsymbol{x}-\boldsymbol{y}| \le 4\varepsilon$ and $\sqrt{q}\varepsilon \ll 1$ in the large q expansion of Green's function,

$$K_0(\sqrt{q}|\boldsymbol{x}-\boldsymbol{y}|) = -\log(\sqrt{q}|\boldsymbol{x}-\boldsymbol{y}|) + \log 2 - \gamma_0 + o(1), \tag{1.116}$$

we obtain

$$\hat{G}(\boldsymbol{A}, q \,|\, \boldsymbol{y}) = \frac{C}{\pi} \int\limits_{\partial\Omega_a} \left[-\log(\sqrt{q}|\boldsymbol{A}-\boldsymbol{y}|) + \log 2 - \gamma_0 + o(1)\right] ds_{\boldsymbol{y}}; \tag{1.117}$$

that is,

$$\hat{G}(\boldsymbol{A}, q \,|\, \boldsymbol{y}) = \frac{2C}{\pi} \int\limits_0^{\varepsilon} \left[-\log(\sqrt{q}r) + \log 2 - \gamma_0 + o(1)\right] dr. \tag{1.118}$$

Therefore the leading order approximation of C is

$$C = \frac{\pi \hat{G}(\boldsymbol{A}, q \,|\, \boldsymbol{y})}{2\varepsilon\left[-\log(\sqrt{q}\varepsilon) + O(\varepsilon)\right]}. \tag{1.119}$$

Finally, (1.112) gives for $|\boldsymbol{A}-\boldsymbol{x}| \gg \varepsilon$

$$\hat{p}(\boldsymbol{x}, q \,|\, \boldsymbol{y}) \approx \hat{G}(\boldsymbol{x}, q \,|\, \boldsymbol{y}) + \frac{\pi \hat{G}(\boldsymbol{A}, q \,|\, \boldsymbol{y}) \hat{G}(\boldsymbol{A}, q \,|\, \boldsymbol{x})}{\log(\sqrt{q}\varepsilon) + O(\varepsilon)}. \tag{1.120}$$

The inversion formula [70, p.1028] for $k > 0$

$$\mathcal{L}^{-1}(K_0(k\sqrt{q}) = \frac{1}{2t} e^{-\dfrac{k^2}{4t}}, \tag{1.121}$$

gives

$$\mathcal{L}^{-1}\left(\hat{G}(\boldsymbol{x}, q \,|\, \boldsymbol{y})\right) = \frac{1}{4\pi t} e^{-\dfrac{|\boldsymbol{x}-\boldsymbol{y}|^2}{4t}}. \tag{1.122}$$

For an initial point far from the boundary layer near the window, the expansion [70, p.378]

$$K_0(z) = \sqrt{\frac{\pi}{2z}} e^{-z}\left(1 + O\left(\frac{1}{z}\right)\right) \quad \text{for } z \gg 1, \tag{1.123}$$

gives in (1.110)

$$\hat{G}(\boldsymbol{A}, q \,|\, \boldsymbol{y}) \hat{G}(\boldsymbol{A}, q \,|\, \boldsymbol{x}) = \frac{1}{2\pi} \sqrt{\frac{1}{q s_1 s_2}} e^{-\sqrt{q}(s_1+s_2)} \left(1 + O(q^{-1/2})\right), \tag{1.124}$$

where $s_1 = |\boldsymbol{A} - \boldsymbol{y}|$ and $s_2 = |\boldsymbol{A} - \boldsymbol{x}|$,

$$\begin{aligned}\frac{\pi \hat{G}(\boldsymbol{A}, q \,|\, \boldsymbol{y}) \hat{G}(\boldsymbol{A}, q \,|\, \boldsymbol{x})}{-\log(\sqrt{q}\varepsilon) + O(\varepsilon)} &= \frac{1}{-2\log(\sqrt{q}\varepsilon)} \sqrt{\frac{1}{q s_1 s_2}} e^{-\sqrt{q}(s_1+s_2)} \left(1 + O(q^{-1/2})\right), \\ &\approx \frac{1}{-2\log(\varepsilon) + O(1)} \sqrt{\frac{1}{q s_1 s_2}} e^{-\sqrt{q}(s_1+s_2)} \left(1 + O(q^{-1/2})\right).\end{aligned}$$

The inversion formula

$$\mathcal{L}^{-1}\left(\frac{1}{\sqrt{q}} e^{-k\sqrt{q}}\right) = \frac{1}{\sqrt{\pi t}} e^{-\frac{k^2}{4t}} \tag{1.125}$$

gives

$$\frac{\pi \mathcal{L}^{-1}(\hat{G}(\boldsymbol{A}, q \,|\, \boldsymbol{y}) \hat{G}(\boldsymbol{A}, q \,|\, \boldsymbol{x})}{-\log(\sqrt{q}\varepsilon) + O(\varepsilon)}) = \frac{1}{-2\log(\varepsilon) + O(1)} \frac{1}{\sqrt{\pi t s_1 s_2}} e^{-\frac{(s_1+s_2)^2}{4t}}. \tag{1.126}$$

Hence, we obtain the short-time asymptotics of the survival probability

$$S(t) \approx \int_\Omega p_t(\boldsymbol{x}, \boldsymbol{y})\, d\boldsymbol{x} \tag{1.127}$$

$$= \frac{1}{4\pi t} \int_\Omega e^{-\frac{|\boldsymbol{x}-\boldsymbol{y}|^2}{4t}}\, d\boldsymbol{x} \tag{1.128}$$

$$- \frac{1}{-2\log(\varepsilon)\sqrt{s_2} + O(1)} \frac{1}{\sqrt{\pi t}} \int_\Omega \sqrt{\frac{1}{|\boldsymbol{A}-\boldsymbol{x}|}} e^{-\frac{(|\boldsymbol{A}-\boldsymbol{x}|+s_2)^2}{4t}}\, d\boldsymbol{x} \tag{1.129}$$

$$= R_1(t) + R_2(t) \tag{1.130}$$

where

$$R_1(t) = \frac{1}{4\pi t} \int_\Omega e^{-\frac{|\boldsymbol{x}-\boldsymbol{y}|^2}{4t}}\, d\boldsymbol{x} \approx 1 - e^{-\left(R_a/\sqrt{4t}\right)^2}, \tag{1.131}$$

and R_a is the radius of the maximal disk inscribed in Ω. The second term is

$$\begin{aligned}R_2(t) &= -\frac{1}{-2\log(\varepsilon)\sqrt{s_2} + O(1)} \frac{1}{\sqrt{\pi t}} \int_\Omega \sqrt{\frac{1}{|\boldsymbol{A}-\boldsymbol{x}|}}\, e^{-\frac{(|\boldsymbol{A}-\boldsymbol{x}|+s_2)^2}{4t}}\, d\boldsymbol{x} \\ &\approx -\frac{1}{-2\log(\varepsilon)\sqrt{s_2} + O(1)} \sqrt{\frac{\pi}{t}} \int_0^{R_a} e^{-\frac{(r+s_2)^2}{4t}} \sqrt{r}\, dr.\end{aligned} \tag{1.132}$$

The small t Laplace expansion and the two successive changes of variable $u = \frac{s_2}{2t} r$ and $v = u^{3/2}$ give

$$\int_0^{R_a} e^{-\frac{(r+s_2)^2}{4t}} \sqrt{r} dr \approx \frac{2}{3} \left(\frac{2t}{s_2}\right)^{3/2} e^{-\frac{s_2^2}{4t}} \int_0^{\infty} e^{-v^{3/2}} dv. \tag{1.133}$$

Thus, with

$$I = \int_0^{\infty} e^{-v^{2/3}} dv = \frac{3\sqrt{\pi}}{4}, \tag{1.134}$$

we obtain

$$R_2(t) - \frac{1}{-2\log(\varepsilon) + O(1)} \frac{\sqrt{2}\pi t}{s_2^2} e^{-\frac{s_2^2}{4t}}. \tag{1.135}$$

We conclude therefore that the survival probability (1.127) is approximately

$$S(t) \;\approx\; 1 - \frac{1}{2\log(\frac{1}{\varepsilon})} \frac{\sqrt{2}\pi t}{s_2^2} e^{-\frac{s_2^2}{4t}}, \tag{1.136}$$

where the contribution of (1.131) is negligible. Thus the MFPT of the fastest particle is given by

$$\begin{aligned} \bar{\tau}^2 = \int_0^{\infty} \left[\Pr\{t_1 > t\}\right]^N dt \;&\approx\; \int_0^{\infty} \exp\left\{ N \log\left(1 - \frac{1}{2\log(\frac{1}{\varepsilon})} \frac{\sqrt{2}\pi t}{s_2^2} e^{-\frac{s_2^2}{4t}} \right) \right\} dt \\ &\approx\; \int_0^{\infty} \exp\left\{ -N \frac{1}{2\log(\frac{1}{\varepsilon})} \frac{\sqrt{2}\pi t}{s_2^2} e^{-\frac{s_2^2}{4t}} \right\} dt. \end{aligned}$$

The computation of the last integral follows the steps described in subsection 1.4. The change of variable $w = te^{-\frac{s_2^2}{4t}}$ leads to the asymptotic formula with diffusion coefficient D

$$\bar{\tau}^2 \approx \frac{s_2^2}{4D \log\left(\frac{\pi\sqrt{2}N}{8\log\left(\frac{1}{\varepsilon}\right)} \right)}.$$

where $s_2 = |\boldsymbol{x} - \boldsymbol{A}|$ and $\boldsymbol{x}$ is the position of injection $\boldsymbol{A}$ the center of the absorbing window. This formula is compared with Brownian simulations in Fig. 1.4. However, the dependence on the window size is $\log(\frac{1}{\varepsilon})$.

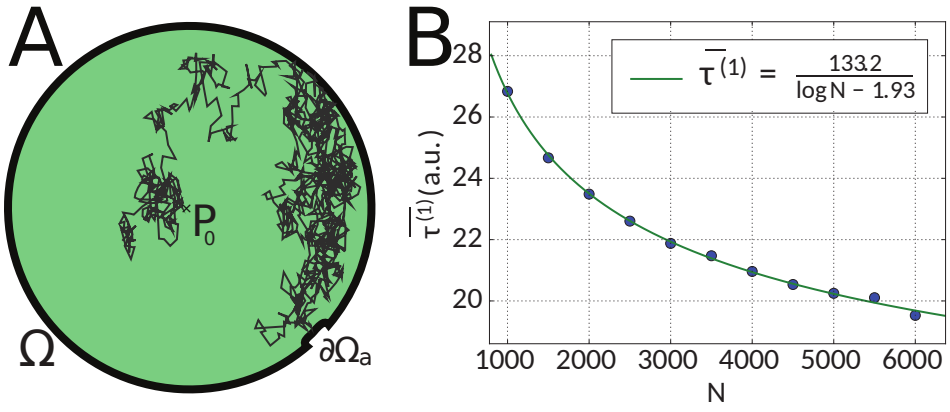

Figure 1.4: Escape through a narrow opening in a planar disk. **A.** The geometry of the NEP for the fastest particle. **B.** Plot of the MFPT of the fastest particle versus the number of particles N. The asymptotic solution (red curve) is of the form $\frac{\alpha}{\log(N)+\beta}$. The stochastic simulations are obtained with 500 runs.

1.6 Statistics of the arrival time of the second particle

Next, we turn to the computation of the conditional pdf of the arrival time $\tau^{(2)}$ of the second particle, which is that of the minimum of the shortest arrival time in the ensemble of $N-1$ trajectories after the first one has arrived, conditioned on their locations at time $\tau^{(1)}$:

$$\tau^{(2)} = \min\{t > 0 \text{ such that } X_2(t) \text{ or }, ..X_n(t) \in \partial\Omega_a | X_1(s) \in \partial\Omega_a, s < t\}. \quad (1.137)$$

The time $\tau^{(1)} + \tau^{(2)}$ is that of arrival of the first two particles at reach the target. The distribution of the arrival time $\tau^{(2)}$ of the second particle can be computed using the conditional probability of the positions $(x_2, \ldots, x_N)$ of the $N-1$ particles at time $\tau^{(1)}$ and the probability that the first particle has already arrived at time $\tau^{(1)} = s$,

$$\begin{aligned} & \Pr\{\tau^{(2)} = t\} \quad (1.138) \\ = & \int_0^t \int_\Omega .. \int_\Omega \Pr\{\tau^{(2)} = t, \tau^{(1)} = s, \boldsymbol{x}_2(s) = x_2, \ldots, \boldsymbol{x}_N(s) = x_N\}\, dx_1 \cdots dx_N\, ds. \end{aligned}$$

Since all particles are independent, the time of arrival of the fastest one is independent of the positions of the N-1 remaining particles that are located inside the domain, so that

$$\begin{aligned} & \Pr\{\tau^{(2)} = t, \tau^{(1)} = s, x_2(s) = x_2, \ldots, x_N(s) = x_N\} \\ = & \Pr\{\tau^{(2)} = t \,|\, \tau^{(1)} = s, x_2(s) = x_2, \ldots, x_N(s) = x_N\} \\ & \times \Pr\{\tau^{(1)} = s\} \Pr\{x_1(s) = x_2, \ldots, x_N(s) = x_N\}. \end{aligned}$$

Because all particles are independent,

$$\Pr\{\boldsymbol{x}_2(s) = x_2, \ldots, \boldsymbol{x}_N(s) = x_{N-1}\} = \prod_{i=2}^{N} \Pr\{\boldsymbol{x}_i(s) = x_i\},$$

where by definition $\Pr\{\boldsymbol{x}_i(s) = x_i\} = p(x_i, s)$ is the Survival pdf of a Brownian particle located at position x_i at time s that has not escaped the domain before time s: p is solution in the interval $[0, L]$ of equation (1.11) [72, page 203]. We recall that the pdf of the $N-1$ i.i.d particles, which are not absorbed when the first one reaches the boundary at time s, is the integral of the survival probability for the N-1 remaining i.i.d. particles [41, 73], which is given by

$$S^N(t) = \left(\int_0^L \Pr\{\boldsymbol{x}_2(s) = x_2\} dx_2 \right)^{N-1}, \tag{1.139}$$

so that for an interval $\Omega = [0, L]$, we obtain

$$\Pr\{\tau^{(2)} = t\} = \int_0^t \Pr\{\tau^{(2)} = t \,|\, \tau^{(1)} = s\} S^N(t) \Pr\{\tau^{(1)} = s\} ds. \tag{1.140}$$

We shall now study expression 1.140 when we neglect the weight function $S^N(t)$ induced by the survival distribution of the $N-1$ remaining particles at the time the first particle has reached the boundary. Later on, we will account for this weight.

The Poissonian-like approximation

The pdf (1.140) can be evaluated under some additional assumptions. For example, if the Brownian trajectories escape from a deep potential well, the escape process is well approximated by a Poisson process with rate equal the reciprocal of the mean escape time from the well [72]. Also, when Brownian particles escape a domain $\Omega = B \cup C$, which consists of a bulk B and a narrow cylindrical neck C, the escape process from Ω can be approximated by a Poisson process, according to the narrow scape theory [41]. Here the motion in the narrow cylinder C is approximated by one-dimensional Brownian motion in an interval of length L.

Consequently, under the Poisson approximation, the arrival of the first particle is much faster than the escape of the second one from the bulk compartment B, thus we can use the approximation that all particles are still in the bulk B after the arrival of the first one. The bulk is represented by the position $x = 0$ in an approximate one-dimensional model. For s small, this assumption simplifies relation (1.140), so that all remaining N-1 particles are frozen to their initial position so that

$$\left(\int_0^L \Pr\{\boldsymbol{x}_2(s) = x_2\} dx_2 \right)^N \approx 1, \tag{1.141}$$

(because the survival probability tends to one as s tends to zero), so that we make now the approximation

$$\Pr\{\tau^{(2)} = t\} \approx \int_0^t \Pr\{\tau^{(2)} = t|\tau^{(1)} = s\} \Pr\{\tau^{(1)} = s\} ds. \tag{1.142}$$

The Markovian property of the Poisson process gives

$$\Pr\{\tau^{(2)} = t|\tau^{(1)} = s\} = \Pr\{\tau^{(2)} = t - s, \tau^{(1)} = 0\} \tag{1.143}$$

so that after the first particle has arrived, the second arrival time $\tau^{(2)}$ has the same pdf as $\tau^{(1)}$ but with $N - 1$ particles, which we approximate to be the same for large N, that is,

$$\Pr\{\tau^{(2)} = t\} = \int_0^t f(t - s) f(s)\, ds. \tag{1.144}$$

We recall using (1.10) (for $N_R = 1$) that

$$f(s) = \Pr\{\tau^{(1)} = s\} = N g(t)^N h(t) \tag{1.145}$$

and by definition for a finite interval (see relation (1.18)), we have

$$g(t) = \sum_{n=0}^{N_t} \frac{(-1)^n}{\lambda_n} e^{-D\lambda_n^2 t} \tag{1.146}$$

and

$$h(t) = \sum_{n=0}^{N_t} (-1)^n \lambda_n e^{-D\lambda_n^2 t}. \tag{1.147}$$

It follows that, by neglecting for N large the difference between $N - 2$ and $N - 1$,

$$\Pr\{\tau^{(2)} = t\} = N^2 \int_0^t g(s)^{N-1} h(s) g(t - s)^{N-1} h(t - s) ds. \tag{1.148}$$

In Fig. 1.5 below, we compare this approximation (1.148) with the empirical distribution obtained from Brownian simulations.

$\Pr\{\tau^{(2)} = t\}$ of N Brownian i.i.d. trajectories in a segment

Following the development of the first paragraph of subsection 1.6, equations (1.138) and (1.140) are valid with Ω replaced by the segment $[0, L]$. That is,

$$\begin{aligned} &\Pr\{\tau^{(2)} = t\} \\ = &\int_0^t \int_0^L \cdots \int_0^L \Pr\{\tau^{(2)} = t, \tau^{(1)} = s, x_2(s) = x_2, \ldots, x_N(s) = x_N\}\, dx_2 \cdots dx_N\, ds. \end{aligned}$$

Hence, we start with

$$\Pr\{\tau^{(2)} = t\} = \int_0^t \Pr\{\tau^{(2)} = t | \tau^{(1)} = s\} \left(\int_0^L \Pr\{x_2(s) = x_2\} dx_2 \right)^{N-1} \Pr\{\tau^{(1)} = s\}\, ds \quad (1.149)$$

where we shall now account for the survival probability for any of the i.i. d remaining particles, by computing

$$S(s) = \int_0^L \Pr\{x_2(s) = x_2\}\, dx_2. \quad (1.150)$$

We shall use now the short-time asymptotics of the one-dimensional diffusion equation, for a diffusion particle starting at 0. The equation is

$$\begin{aligned} \frac{\partial p(x,t)}{\partial t} =& D \frac{\partial^2 p(x,t)}{\partial x^2} \quad \text{for } x > 0,\ t > 0 \\ p(x,0) =& \delta(x) \quad \text{for } x > 0, \quad p(L,t) = 0 \quad \text{for } t > 0 \end{aligned} \quad (1.151)$$

and $p(x,t)$ is the pdf of a Brownian particle located at position x at time t, when it started at position 0 and has not escape the domain before time t (see also [73]). The solution for short-time is well approximated by the fundamental solution (except at the boundary, where the error is exponentially small in $1/t$),

$$p(x,t) = \frac{1 + o(t)}{\sqrt{4D\pi t}} \exp\left\{ -\frac{x^2}{4Dt} \right\}. \quad (1.152)$$

Thus the survival probability at short time t is

$$S(t) = \int_0^L \frac{1 + o(t)}{\sqrt{4D\pi t}} \exp\left\{ -\frac{x^2}{4Dt} \right\} dx. \quad (1.153)$$

The short-time asymptotic expansion (1.26) (see below) and the change of variable $x = u\sqrt{4Dt}$ in the integral (1.153), give

$$S(t) = 1 - \frac{1}{\sqrt{\pi}} \int_{L/\sqrt{4Dt}}^{\infty} \left[\exp\left\{-u^2\right\}\right] du \tag{1.154}$$

$$= 1 - \sqrt{4Dt}\frac{\exp\left\{-(L/\sqrt{4Dt})^2\right\}}{\sqrt{\pi}L}\left(1 - 2\frac{Dt}{L^2} + O\left(\frac{t^2}{L^4}\right)\right). \tag{1.155}$$

It follows from (1.149) that the pdf of the second arrival time is

$$\Pr\{\tau^{(2)} = t\} \tag{1.156}$$

$$= [1 + o(1)] \int_0^t \Pr\{\tau^{(1)} = s\} \Pr\{\tau^{(1)} = t - s\} \left(1 - \sqrt{4Ds}\frac{\exp\left\{-(\frac{L}{\sqrt{4Ds}})^2\right\}}{\sqrt{\pi}L}\right)^{N-1} ds.$$

In figure 1.5, we compare results of the stochastic simulations with the analytical formula (1.148) for the second fastest arrival time $\tau^{(2)}$ to the boundary $x = 1$ of the interval $[0, 1]$ when there are $N = 20$ particles. We use the analytical formula (1.148) (no correction) and then (1.156), which contains the shift correction due to the distribution of the particles in the interval at time $\tau^{(1)}$, when the first particle arrives at $x = L$ been absorbed. The analytical formulas agree with the empirical histogram and the improvement can be seen in Fig 1.5.

We end this section by a remarkable results about the MFPT of the second fastest arrival among N particles, which can be directly linked to the MFPT of the first one, under the approximation that we neglect the contribution of the weight S^N . Indeed using (1.33), changing the order integration and putting $t - s = u$, we get

$$\bar{\tau}^{(2)} = \int_0^{\infty} t \Pr\{\tau^{(2)} = t\} dt = \int_0^{\infty} t \int_0^t f(t - s) f(s) ds dt \tag{1.157}$$

$$= \int_0^{\infty} \int_0^{\infty} (t + s) f(t) f(s) ds dt \tag{1.158}$$

$$= 2 \int_0^{\infty} s f(s) ds \left(\int_0^{\infty} f(t) dt\right) = 2\bar{\tau}^{(1)} \left(\int_0^{\infty} f(t) dt\right) = 2\bar{\tau}^{(1)}. \tag{1.159}$$

To conclude, this result is exactly the same as MFPT for the second particle for a Poisson process. We thus expect that the effect of accounting for the $N - 1$ particle distribution would in general not be significant, as we will see in section 1.8. Figure 1.5 shows how adding the corrected weight S^N in the distribution of arrival time for the second particle

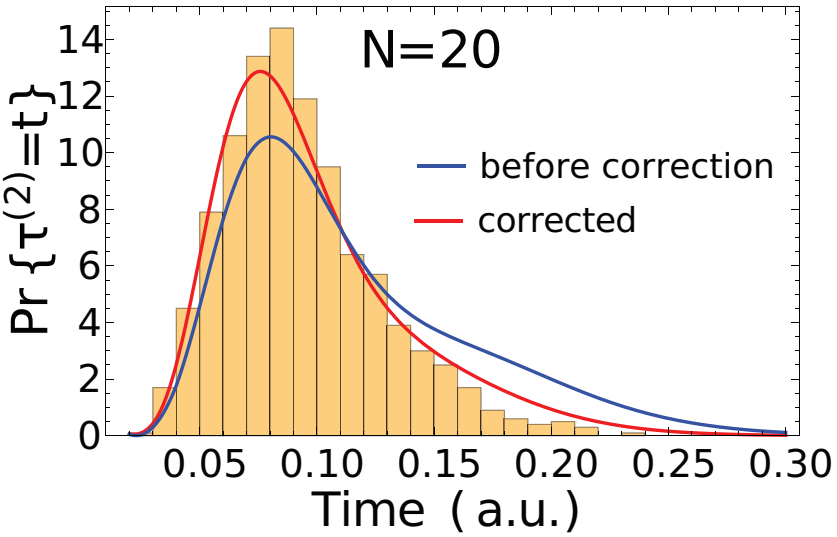

Figure 1.5: Histogram of the arrival time of the second fastest particle, obtained from Brownian simulations with the Euler's scheme. The fastest is computed for $N = 20$ in **B.** The analytical solution with no correction (no weight S^{N-1}) is given by (1.148) (blue) and compared to (1.156) with the pdf containing the weight (red). We used $n_0 = 6$ terms in the series (1.19) and 1000 runs for the stochastic simulations.

(expression (1.156)) improves the approximation of the empirical distribution generated by Brownian simulations, thus showing that the distribution of the remaining Brownian particles inside the interval contributes to the decrease of the arrival time of the second particle. The analytical curve (blue in fig. 1.5) was computed from the sum of eigenfunctions:

$$\Pr\{\tau^{(2)} = t\} = [1 + o(1)] \int_0^t \Pr\{\tau^{(1)} = s\} \Pr\{\tau^{(1)} = t - s\} \left(2 \sum_{n=0}^{\infty} \frac{(-1)^n}{\lambda_n} e^{-D\lambda_n^2 t} \right)^{N-1} ds, \tag{1.160}$$

which is equivalent to (1.156). Note that $\Pr\{\tau^{(1)} = s\}$ is computed directly from formula (1.145). The alternating series contains an even number of terms.
To conclude, the weight function which is survival probability of $N-1$ remaining particles at the time the first one has arrived, given by

$$S^{N-1}(s) = \left(1 - \sqrt{4Ds} \frac{\exp\left\{ -(\frac{L}{\sqrt{4Ds}})^2 \right\}}{\sqrt{\pi} L} \right)^{N-1} \tag{1.161}$$

account for a faster arrival of the second particle relative to the first one. Finally, it was hard to add more than 6 terms in the series of the eigenfunction, although this approximation is already quite good.

1.7 Application of extreme statistics in cell biology

The first arrival time of ions in a dendritic-spine geometry

The geometry of a dendritic spine (see Fig.1.6) is composed of a head with a small hole opening, connected to a cylindrical neck. Initially, all Brownian particles, which represent calcium ions that are uniformly distributed in the spine head at the time of their release. This geometry implies that the mean time τ to reach the base of the neck is the mean time τ_1 to reach the small window for the first time plus the mean time τ_2 spent in the spine neck, with no possible returns: we assume here that when a particle enters the neck cylinder, it cannot return to the head.

We compute now the distribution of the arrival time for the fastest and second fastest Brownian particle in a dendritic spine geometry. The pdf of a particle arriving at the base of the dendrite within the time $\tau = \tau_1 + \tau_2$ is computed as follows, when the escape time form the head is Poissonian:

$$\Pr\{\tau = \tau_1 + \tau_2 = t\} = \int_0^t \Pr\{\tau_2 = t - s | \tau_1 = s\} \Pr\{\tau_1 = s\} ds. \tag{1.162}$$

The Markovian property implies that

$$\Pr\{\tau_1 + \tau_2 = t\} = \int_0^t \Pr\{\tau_2 = t - s\} \Pr\{\tau_1 = s\} ds. \tag{1.163}$$

Using the narrow escape theory [41], the distribution of arrival time of a Brownian particle at the entrance of the dendritic neck is Poissonian,

$$\Pr\{\tau_1 = s\} = \gamma e^{-\gamma s}, \tag{1.164}$$

where

$$\gamma^{-1} = \frac{|\Omega|}{4aD\left[1 + \frac{L(\mathbf{0}) + N(\mathbf{0})}{2\pi} a \log a + o(a \log a)\right]},$$

with $|\Omega|$ the volume of the spherical head, while a is the radius of the cylindrical neck [41] and $L(0)$ and $N(0)$ are the principal mean curvature. After the first particles reaches the cylinder (spine neck), we approximate its Brownian motion in the cylindrical domain by one-dimensional motion (1D). By substituting $N = 1$ for the first arriving particle, this is given by (1.18):

$$\Pr\{\tau_2 = t - s\} = \sum_{n=0}^{\infty} (-1)^n \lambda_n e^{-D\lambda_n^2 (t-s)}. \tag{1.165}$$

Hence,

$$\Pr\{\tau_1+\tau_2=t\} = \gamma\int_0^t e^{-\gamma s}\sum_{n=0}^{\infty}(-1)^n\lambda_n e^{-D\lambda_n^2(t-s)}ds \quad (1.166)$$

$$= \gamma\sum_{n=0}^{\infty}(-1)^n\left[\frac{e^{-D\lambda_n^2 t}-e^{-\gamma t}}{\gamma-D\lambda_n^2}\right]. \quad (1.167)$$

This result represents the pdf of the arrival time of a Brownian particle at the base of a spine, or a process with two time scales: one dictated by diffusion and the other Poissonian. Relation (1.166) for the arrival time is derived for the study of the statistics of a single particle. The expression for the flux is given in terms of the probability

$$\Phi(t)=\Pr\{\tau_1+\tau_2=t\}, \quad (1.168)$$

gives

$$f_{min}(t)=\Pr\{\tau^{(1)}=\min(t_1,\ldots,t_N)=t\} = N\left(1-\int_0^t\Phi(s)ds\right)^{N-1}\Phi(t) \quad (1.169)$$

$$= N\left[J(t)\right]^{N-1}\Phi(t), \quad (1.170)$$

and using (1.166), we get

$$J(t)=1-\int_0^t\Phi(s)ds=1-\gamma\sum_{n=0}^{\infty}\frac{(-1)^n}{(\gamma-D\lambda_n^2)}\left[\frac{1-e^{-D\lambda_n^2 t}}{D\lambda_n^2}-\frac{1-e^{-\gamma t}}{\gamma}\right]. \quad (1.171)$$

At the stage, we shall make several remarks. The NET Poissonian approximation 1.164 for a Brownian particle to reach the entrance of the neck is not necessarily a good approximation for studying the arrival of the first one, which might be better described by the short-time asymptotic. To capture the rising phase, another approximation consists in approximating the entire spine as a single interval and by using the distribution of arrival times derived in section 1.2. This approximation works well for the first arriving particles because they use the straight line (geodesic to the exit). However, for longer arrival time, the effect of the narrow escape is not captured, leading to a poor approximation of the tail distribution.

Another improvement consists in using the ray solution of the diffusion equation, starting at the center of the ball and exiting at the entrance of the neck. The approximated solution is given by 1.64 and the first arrival probability is the flux through the neck of size a:

$$Pr\{\tau_1=t\} = \oint_{\partial\Omega_a}\frac{\partial p(\boldsymbol{x},t)}{\partial \boldsymbol{n}}\,dS_{\boldsymbol{x}} \quad (1.172)$$

$$= \pi a^2\frac{RD}{(4\pi tD)^{5/2}}e^{-R^2/(4Dt)}, \quad (1.173)$$

where R is the radius of the head. In that case, the first arrival time can be computed from 1.169 and we get

$$\Pr\{\tau_1+\tau_2=t\} \;=\; \int_0^t \pi a^2 \frac{RD}{(4\pi sD)^{5/2}} e^{-R^2/(4Ds)} \sum_{n=0}^{\infty} (-1)^n \lambda_n e^{-D\lambda_n^2(t-s)} ds. \quad (1.174)$$

The short and long time asymptotic, relation 1.174 shows that

$$\Pr\{\tau_1+\tau_2=t\} \;\sim_{t\sim 0}\; \frac{C}{t^{5/2}} e^{-R^2/(4Dt)} \quad (1.175)$$

$$\sim_{t\sim\infty}\; e^{-D\lambda_0^2 t}. \quad (1.176)$$

In the Poissonian approximation, the pdf of the arrival time $\tau^{(2)}$ of the second fastest particle is given by

$$\Pr\{\tau^{(2)}=t\} = N \int_0^t f_{min}(t-s) f_{min}(s) ds, \quad (1.177)$$

where $f_{min}(s) = J(s)^{N-1}\Phi(s)$. Thus,

$$\Pr\{\tau^{(2)}=t\} = \int_0^t [J(t-s)]^N \Phi(t-s) [J(s)]^N \Phi(s) ds. \quad (1.178)$$

Expressions (1.169) and (1.178) represent the distributions of arrival times of the first and second Brownian particles, initially injected in the spine head and escape at the end of the cylindrical neck . These expressions are computed under the assumption of no return: when a particle enters the neck cylinder, it cannot return to the head.

Escape times of Brownian particles with returns to the head

Consider Brownian particles that escape a dendritic spine (Fig. 1.6) into a dendrite with any number of returns to the head after crossing into the neck. Recrossing is defined to the stochastic separatrix [74], the position of which is not known exactly but is defined by the ensemble of points for which the probability to return to the head is 1/2. Recrossing is likely to impact the first arrival time. The pdf of the arrival time when no return is possible is given by (1.166). To compute the pdf of the shortest escape time τ^a with possible returns to the head, we use Bayes' law for the escape density, conditioned on any number of returns, that is

$$\Pr\{\tau^a=t\} = \sum_{k=0}^{\infty} \Pr\{\tau^a=t|k\} \Pr\{k\}, \quad (1.179)$$

where $\Pr\{k\} = \frac{1}{2^k}$ is the probability that the particle returns k times to the head. The particle hits the stochastic separatrix [72] and then returns to the head, before reaching the dendrite. The probability of the escape, conditioned on k returns, $\Pr\{\tau^a = t|k\}$, can be computed from the successive arrivals times $\tau_1, ..\tau_k$, to the stochastic separatrix, so that

$$\Pr\{\tau^a = t|k\} = \Pr\{\tau_1 + .. + \tau_k = t\}. \tag{1.180}$$

Assuming that the arrival time to the stochastic separatrix is Poissonian with rate λ_S [41], we obtain that

$$\Pr\{\tau_1 + .. + \tau_k = t\} = \lambda_S \int_0^t \frac{(\lambda_S s)^{n-1}}{(n-1)!} f(t-s)\, ds, \tag{1.181}$$

where $f(t)$ is the pdf of no return (1.166). Therefore

$$\Pr\{\tau^a = t\} = \frac{1}{2} f(t) + \sum_{n=1}^{\infty} \int_0^t \lambda_S \frac{(\lambda_S s)^{n-1}}{(n-1)!} f(t-s) ds \frac{1}{2^k}. \tag{1.182}$$

Finally,

$$\Pr\{\tau^a = t\} = \frac{1}{2} f(t) + \int_0^t \exp(-\lambda_S s/2) f(t-s) ds. \tag{1.183}$$

Expression (1.166) with $\lambda_S = \gamma$ is the pdf of the escape time

$$\begin{aligned} f_{return}(t) &= \Pr\{\tau^a = t\} \qquad (1.184)\\ &= \frac{1}{2} f(t) + \gamma N_R \sum_{n=0}^{\infty} (-1)^n \frac{\lambda_n \gamma^2}{4(\gamma - D\lambda_n^2)} \left[\frac{e^{-\gamma t/2} - e^{-\gamma t}}{\gamma/2} - \frac{e^{-\gamma/2 t} - e^{-D\lambda_n^2 t}}{D\lambda_n^2 - \gamma} \right]. \end{aligned}$$

The maximum of f_{return} is achieved at the point $t_{max} \approx \frac{2}{\gamma} \log 2$. The pdfs of the first and second arrivals are computed as

$$\begin{aligned} f_{min}^{(1)}(t) &= \Pr\{\tau^{(1)} = min(t_1, \ldots, t_N) = t\} \\ &= N \left(1 - \int_0^t f_{return}(s) ds \right)^{N-1} f_{return}(t), \end{aligned}$$

and following equation(1.177), we obtain

$$f_{min}^{(2)}(t) = \Pr\{\tau^{(2)} = t\} = N \int_0^t f_{min}^{(1)}(t-s) f_{min}^{(1)}(s) ds. \tag{1.185}$$

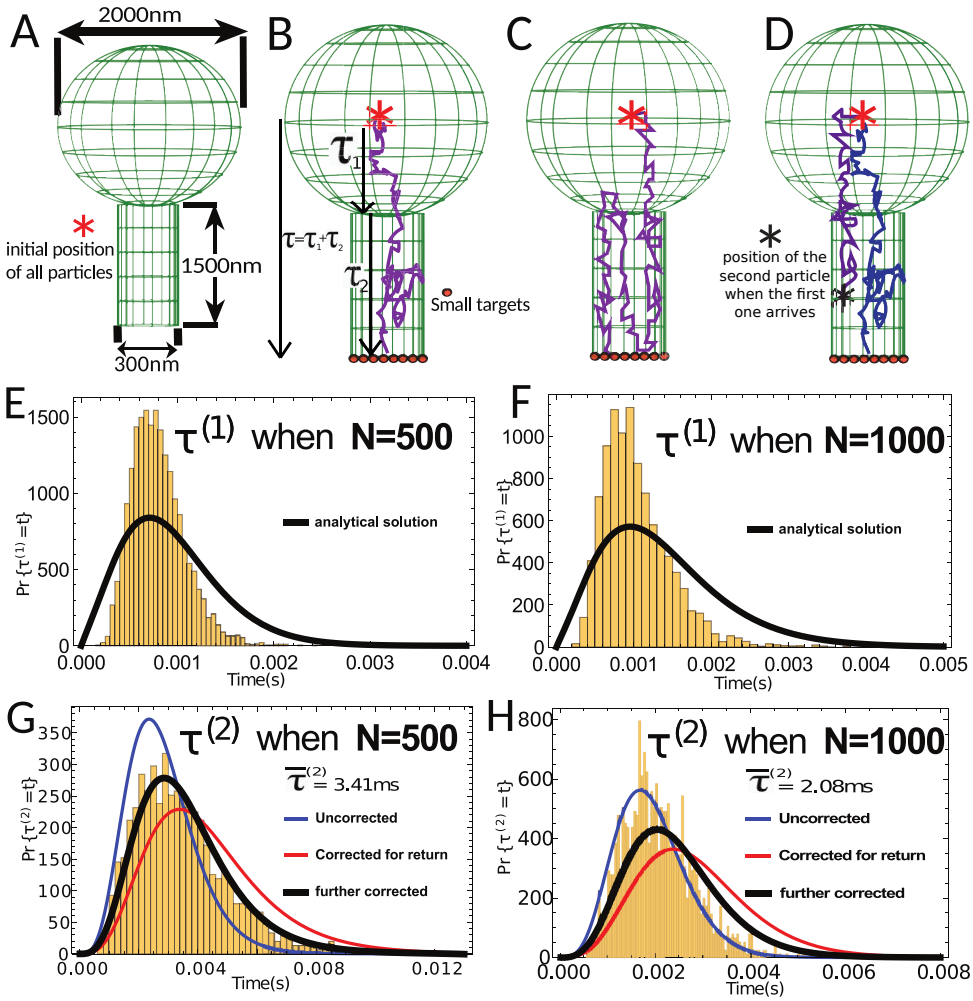

Figure 1.6: **A-B-C-D:** The geometry of the spine is a spherical head and cylindrical neck. **A-D** Brownian Particles are released at the center of the head and must first reach the top of the neck and then diffuse through the neck to reach the base. Time taken for each process is represented with the notation τ_1 and τ_2, making the total time to be $\tau = \tau_1 + \tau_2$. **C** shows a trajectory that can return to the head. Note that in **D**, when the first particle arrives, the second one, which could have return to the head, is now located inside the neck. **E-F.** Plot of $\Pr\{\tau^{(1)} = t\}$ for values $N = 500, 1000$ vs the approximation (1.169). **G-H.** Plot of $\Pr\{\tau^{(2)} = t\}$ for values $N = 500, 1000$. The analytical solution is that of (1.178). Returns are accounted for with (1.185). The further corrected curve (black) is given by 1.186. The diffusion coefficient is $D = 600\mu m^2/s$.

The pdfs of the fastest and second fastest arrival times are computed from (1.184), as in the previous sections. Fig. 1.6 shows the pdf of the arrival time $\tau^{(2)}$. Note that a correction is needed in (1.178), because the second particle is not necessarily located inside the head when the first one arrives at the base. Finally, the arrival time formula 1.185 can be further correct by adding the distribution of the particle inside the head. The correction is similar to the one we obtain in dimension one (formula 1.156 and 1.160). It can be written here using the survival probability 1.171 as

$$f^{(2)}_{further}(t) = \Pr\{\tau^{(2)} = t\} = N \int_0^t f^{(1)}_{min}(t-s) f^{(1)}_{min}(s) J(t)^{N-1} ds. \tag{1.186}$$

1.8 Conclusion and applications of extreme statistics to fast time scale activation in cell biology

We derived here new asymptotics for the expected arrival time of fastest Brownian particles in several geometries: half a line, a segment, a bounded domain in dimension two and three that contains a small window, and spine-shaped geometry (a ball connected to thin cylinder). We found that the geometry is involved and explored by the fastest particle and the pdf is defined by the shortest ray (with reflections if the is an obstacle [67]) from the source to the target, in contrast with the narrow escape problem [41], where the main geometrical feature is the size of the window and the surface or volume of the domain. We derived here new laws for the first arrival time of N (large) Brownian particles to a target, which can be summarized as

$$\bar{\tau}^{d1} = \frac{\delta^2_{min}}{4D \ln(\frac{N}{\sqrt{\pi}})}, \text{ in dim 1, valid for } N \gg 1 \tag{1.187}$$

$$\bar{\tau}^{d2} \approx \frac{\delta^2_{min}}{4D \log\left(\frac{\pi\sqrt{2}N}{8\log\left(\frac{1}{\varepsilon}\right)}\right)}, \text{ in dim 2, valid for } \frac{N}{\log(\frac{1}{\varepsilon})} \gg 1 \tag{1.188}$$

$$\bar{\tau}^{3d} \approx \frac{\delta^2_{min}}{2D\sqrt{\log\left(N\frac{4a^2}{\pi^{1/2}\delta^2_{min}}\right)}}, \text{ in dim 3, valid for } \frac{Na^2}{\delta^2_{min}} \gg 1, \tag{1.189}$$

where δ_{min} is the shortest ray from the source to the window, D is the diffusion coefficient and N is the number of particles, $\delta_{min} = |\boldsymbol{x} - \boldsymbol{A}|$ and $\boldsymbol{x}$ is the position of injection and the center of the window is $\boldsymbol{A}$. Formula (1.187) is very different from the classical NET, which involves volume or surface area and mean curvature (in dimension 3). When the window is located at the end of a cusp, the asymptotics for the fastest particle are yet unresolved.

We further found that the rate of arrival cannot be approximated as Poissonian, because the fastest particle can arrive at a time scale that can fall into the short-time asymptotic. We further studied here the arrival of a second particle. The mean arrival time of the second can be influence by the distribution of all particles, especially on a segment, because the distribution of particles at the time the first particle's arrival is not Dirac's delta function (see section 1.6). However, the case of a spine geometry is interesting, because the first particle may have already arrived, but all other particles can still be in the head (due to the narrow opening at the neck-head connection). We further computed the pdf of the arrival time when particle can return to the head after sojourn in the neck (see section 1.7).

The present asymptotics have several important applications: activation of molecular processes are often triggered by the arrival of the first particles (ions or molecules) to target-binding sites. The simplest model of the motion of calcium ions in cell biology, such as neurons or a dendritic spine (neglecting electrostatic interactions) is that of independent Brownian particles in a bounded domain. The first two calcium ions that arrive at channels (such as TRP) can trigger the first step of biochemical amplification leading to the photoresponse in fly photoreceptor. Another example is the activation of a Ryanodine receptor (RyaR), mediated by the arrival of two calcium ions to the receptor binding sites, which form small targets. Ryanodin receptors are located at the base of the dendritic spine. Computing the distribution of arrival times of Brownian particles at the base, when they are released at the center of the spine head, is a model of calcium release during synaptic activation. Computing the distribution of arrival time reveals that the fastest ions can generate a fast calcium response following synaptic activity. Thus the fastest two calcium ions can cross a sub-cellular structure, thus setting the time scale of activation, which can be much shorter than the time defined by the classical forward rate, usually computed as the steady-state Brownian flux into the target, or by the narrow escape time [41].

Acknowledgements

We thank C. Guerrier for her help in designing the two-dimensional simulations. This research was supported by the Foundation pour la Recherche Médicale - Équipes FRM 2016 grant DEQ20160334882.

Erratum: Asymptotic Formulas for Extreme Statistics of Escape Times in 1, 2 and 3-Dimensions

Published as: **Basnayake, K.**, Schuss,Z., and Holcman, D.(2020). "Correction to: Asymptotic Formulas for Extreme Statistics of Escape Times in 1, 2 and 3-Dimensions." *Journal of Nonlinear Science*: 30, 3443–3444 (2020). https://doi.org/10.1007/s00332-020-09636-7

In the section titled "The shortest NEP from a bounded domain in $\mathbb{R}^{2,3}$" for dimension 3, we found an error. This leads to the conclusion that also in three dimensions, the mean time for the fastest $\bar{\tau}^{(1)}$ depends on the reciprocal of $\log N$ and not on $1/\sqrt{\log N}$, as written previously. Here are the corrected computatio from Eq.102:

$$\bar{\tau}^{(3dim)} = \int_0^\infty \left[Pr\{t_1 > t\}\right]^N dt \approx \int_0^\infty exp\left\{Nlog\left(1 - \frac{a^2}{\delta\sqrt{\pi}} t^{-\frac{1}{2}} e^{-\left(\frac{\delta}{\sqrt{4t}}\right)^2}\right)\right\} dt \quad (1.190)$$

$$\approx \int_0^\infty exp\left\{-N\frac{a^2}{\delta\sqrt{\pi}} t^{-\frac{1}{2}} e^{-\left(\frac{\delta}{\sqrt{4t}}\right)^2}\right\} dt \approx \frac{\delta^2}{4}\int_0^\infty exp\left\{-N'\frac{1}{\sqrt{u}} e^{-\frac{1}{u}}\right\} du \quad (1.191)$$

where $N' = \frac{2Na^2}{\sqrt{\pi}\delta^2}$. Using the method developed in section "Escape from a Ray" with the change of variable,

$$w = w(t) = \frac{1}{\sqrt{t}} e^{-1/t}, \quad w'(t) = \frac{1}{\sqrt{t}} e^{-\frac{1}{t}}\left(-\frac{1}{2t} + \frac{1}{4t^2}\right). \quad (1.192)$$

We have with $w' = 4w(\log(w))^2$

$$\bar{\tau}^{(3dim)} \approx \delta^2 \int_0^\infty \frac{\exp(-N'w)}{4w(\log(w))^2} du.$$

We then follow the computation of section "escape from a ray". When the diffusion coefficient is D, we obtain the formula

$$\bar{\tau}^{3dim} \approx \frac{\delta^2}{4D\log\left(2N\frac{a^2}{\pi^{1/2}\delta^2}\right)}. \quad (1.193)$$

When there are p windows, whose distances from the initial position of the Brownian particles are $d_k = dist(P_0, P_k)$, formula (1.193) changes to

$$\bar{\tau}^3 \approx \frac{\delta^2}{4D\log\left(2N\frac{a^2}{\pi^{1/2}\delta^2}\right)}, \quad (1.194)$$

where $\delta^2 = \min(d_1^2, ..d_p^2)$. The asymptotic formula (1.193) is compared with results of Brownian simulations and shows very good agreement (Fig. 1.7). Fig.1.3). of this chapter has to be replaced by Fig.1.7, which fits the dependency of $\bar{\tau}^{(3dim)}$ with respect to the total number of particles N.

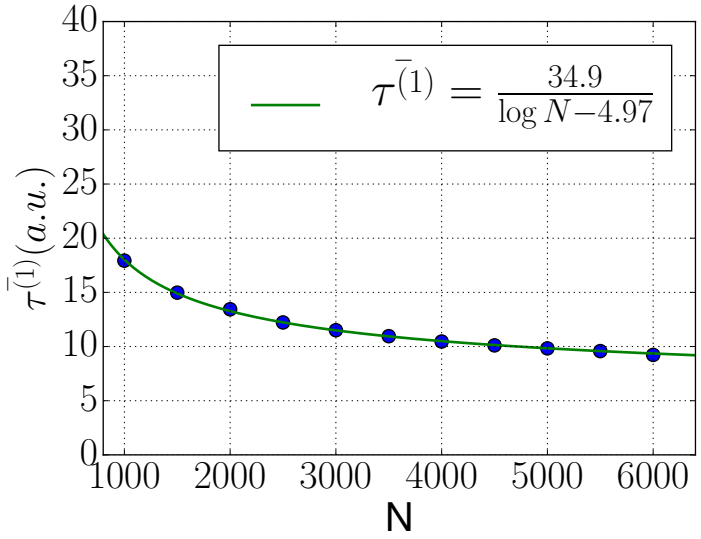

Figure 1.7: **B.** MFPT of the fastest particles vs the number of particles N. The asymptotic solution (green curve) $\frac{\alpha}{\log(N)+\beta}$ fitted the stochastic simulations, obtained with 2000 runs.

Chapter 2

Extreme Narrow Escape: shortest paths for the first particles among n to reach a target window

Published as: **Basnayake, K.**, Hubl, A., Schuss, Z. & Holcman, D. (2018). Extreme Narrow Escape: Shortest paths for the first particles among n to reach a target window. *Physics Letters A*, 382(48), pp.3449-3454. https://doi.org/10.1016/j.physleta.2018.09.040

Abstract

What are the paths associated with the fastest Brownian particles that reach a narrow window located on the boundary of a microdomain? Although the distribution of the fastest arrival times has been well studied in dimension 1, much less is known in higher dimensions. Based on the Wiener path-integral, we suggest that the paths of the fastest particle are concentrated near the shortest paths that minimize the energy-action. Stochastic simulations confirm the present result when an obstacle is positioned between the source point and a narrow window. To conclude paths associated with the fastest arrival times differ significantly from the ones of mean properties of Brownian motions, associated to mean first passage times of a single particle. These extreme properties should be considered instead of the classical Smoluchowski's rate of chemical reactions, because the statistics of the extreme for many copies of the same molecule changes the time scales of activation in cellular domain.

2.1 Introduction

Extreme statistics describe the properties of the shortest or longest arrival times in an ensemble of i.i.d. particles or their trajectories. The statistics of the shortest arrival time $\tau^{(n)}$ to a small target can be computed from the arrival times of a single particle [55, 57, 59, 60, 75, 76]. When there are n Brownian particles in a bounded domain Ω, the

shortest arrival time is defined by

$$\tau^{(n)} = \min(t_1, \ldots, t_n), \tag{2.1}$$

where t_i are the arrival times of the n paths in the ensemble. The first moments of $\langle \tau^{(n)} \rangle$ were computed in dimension one [77–79] and recently [80] in higher dimensions leading to the asymptotic formulas:

$$(\bar{\tau}^{(n)})^{dim1} \approx \frac{\delta^2}{4D \ln\left(\frac{n}{\sqrt{\pi}}\right)}, \tag{2.2}$$

$$(\bar{\tau}^{(n)})^{dim2} \approx \frac{\delta^2}{4D \log\left(\frac{\pi\sqrt{2}n}{8\log\left(\frac{1}{a}\right)}\right)}, \tag{2.3}$$

$$(\bar{\tau}^{(n)})^{dim3} \approx \frac{\delta^2}{2D\sqrt{\log\left(n\frac{4a^2}{\pi^{1/2}\delta^2}\right)}}, \tag{2.4}$$

where D is the diffusion coefficient, δ is the length of the shortest ray from the initial point to the small exiting window of size $a$and n is the number of particles.

Finding optimal paths for the fastest particles has many applications: spermatozoa are moving inside an uterus to find an ovule and the first one to arrive defines the success of the fertilization process: this process was recently modeled using a coarse-grained rectilinear model for the sperms motion inside a cusp-like domain [39]. Theory and simulations results showed that the empirical trajectories of the fastest sperms to arrive to a narrow target are concentrated near the optimal trajectories of a control problem, which consists in minimizing the energy along all admissible paths. The situation was not much studied in the context of Brownian motion or stochastic processes in bounded domains, especially when containing impenetrable obstacles.
We recall that the narrow escape problem (NEP) [41] for the shortest arrival time is to find the probability density function (PDF) and the MFPT of $\tau^{(n)}$ for $n = 1$. Here we focus on extreme trajectories associated with the fastest mean time $\langle \tau^{(n)} \rangle$ when n is large. We show that the paths used by the fastest particles to exit are concentrated near the optimal trajectories of a minimization problem, associated with the energy and are thus geodesics (see [81]).

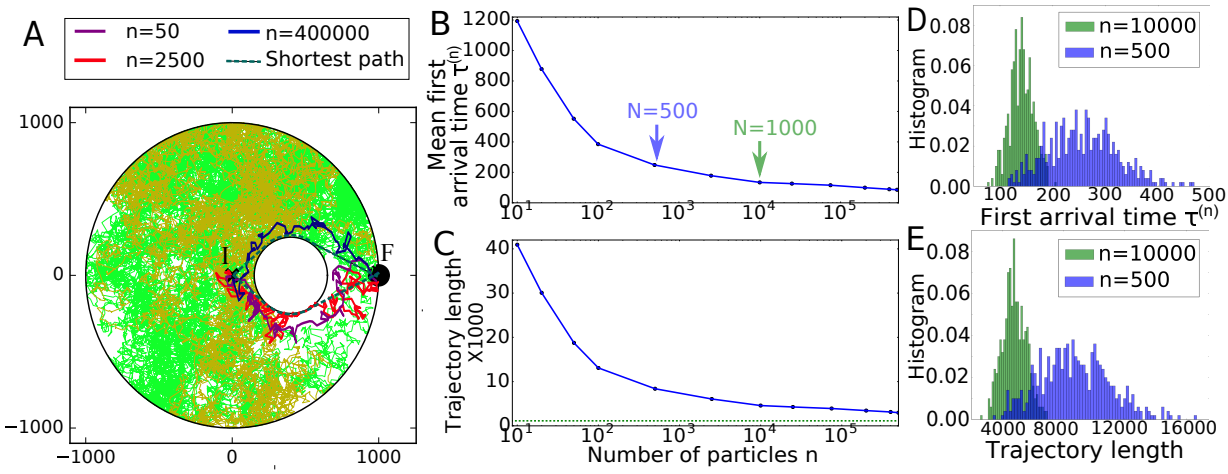

Figure 2.1: **Optimal paths associated to the fastest arrival time $\tau^{(n)}$ of n i.i.d. Brownian trajectories (A).**. Brownian trajectories are initially positioned at point I, where they move inside a domain avoiding a round impenetrable obstacle. They can escape in a small window of size $\varepsilon = 0.01 * R$ (R is the radius of the disk) located on the opposite side of point I. Classical escaping trajectories (green) are very different from the one associated to $\tau^{(n)}$ (bold face), concentrated as we shall see along shortest path (we just represented by symmetry the lower one). **(B).** MFPT associated to $\tau^{(n)}$ vs the number of particle n. **(C).** Trajectory length associated.**(D)-(E).** Distributions of times and lengths for $n = 500$ and 10^4. Parameters are: D=400 au, $\Delta t = 1$.

The present approach we develop here is a form WKB approximation to characterize extreme events. This approach should be put in parallel to the theory of random processes, where the small parameter is usually the diffusion coefficient. In the small diffusion limit, rare events correspond to escape events from the basin of attraction of an attractor. The Path-integral representation, the large deviation approach and the WKB method allowed to describe the most probable escape trajectory [82–86]. How the present results differ from this escape theory? First, the small parameter here is the narrow window located on the boundary of the domain, where the Brownian particles escape and not the diffusion coefficient. Second, the optimal trajectories are associated the fastest particles to escape, thus the number of initial particles n is a key parameter. Finally, although the most probable paths are associated to the extremal of the action, we propose here that a similar principle should apply. It also likely that when the domain has symmetries, several optimal paths are admissible, but it is not clear whether caustics or other singularities for the probability density function develops, as discussed for small diffusion in [87–89].
This letter is organized as follows. We first discuss a path-integral formulation [90, 91] for trajectories associated to the fastest arrival time. We then present a generic example of an extreme Narrow Escape Problem for the shortest arrival time among n trajectories in two dimensions where a disk obstacle is located exactly between the source position and the exiting window. Using numerical simulations, we estimate the splitting probability for the two possible optimal path out and show that the empirical paths to exit are concentrated

near the shortest paths. Finally, we discuss in the context of system and cellular biology how the statistics associated with the shortest paths define the time scale of activation and should be used instead of the classical Smoluchowski's rate constant.

2.2 Optimal paths associated to extreme statistics.

The mean time $\langle \tau^{(n)} \rangle$ for n i.i.d. Brownian particles can be expressed when n is large, as the complementary PDF of the time t_1,

$$\Pr\{\tau^{(n)} > t\} = \Pr^n\{t_1 > t\}, \tag{2.5}$$

so that

$$\langle \tau^{(n)} \rangle = \int_0^\infty \Pr\{\tau^{(n)} > t\} dt = \int_0^\infty [\Pr\{t_1 > t\}]^n \, dt. \tag{2.6}$$

Here $\Pr\{t_1 > t\}$ is the survival probability of a single particle prior to exiting at a target window (Fig. 2.1A). The survival probability is

$$[\Pr\{t_1 > t\}]^n = \exp\{n \log \Pr\{t_1 > t\}\}, \tag{2.7}$$

where the survival probability for one particle is [72]

$$S(t) = \Pr\{t_1 > t\} = \int_\Omega p(\boldsymbol{x}, t) \, d\boldsymbol{x}. \tag{2.8}$$

The transition probability density $p(\boldsymbol{x}, t \,|\, \boldsymbol{y})$ is the solution of

$$\begin{aligned} \frac{\partial p(\boldsymbol{x}, t \,|\, \boldsymbol{y})}{\partial t} &= D \Delta p(\boldsymbol{x}, t \,|\, \boldsymbol{y}) \quad \text{for } \boldsymbol{x}, \boldsymbol{y} \in \Omega, \\ p(\boldsymbol{x}, 0 \,|\, \boldsymbol{y}) &= \delta(\boldsymbol{x} - \boldsymbol{y}) \quad \text{for } \boldsymbol{x}, \boldsymbol{y} \in \Omega \\ \frac{\partial p(\boldsymbol{x}, t \,|\, \boldsymbol{y})}{\partial \boldsymbol{n}} &= 0 \quad \text{for } \boldsymbol{x} \in \partial\Omega_r, \boldsymbol{y} \in \Omega \\ p(\boldsymbol{x}, t \,|\, \boldsymbol{y}) &= 0 \quad \text{for } \boldsymbol{x} \in \partial\Omega_a, \boldsymbol{y} \in \Omega, \end{aligned} \tag{2.9}$$

where the boundary $\partial\Omega$ contains a small absorbing window $\partial\Omega_a$ and $\partial\Omega_r = \partial\Omega - \partial\Omega_a$. Finally,

$$\langle \tau^{(n)} \rangle = \int_0^\infty \exp\left\{ n \log \int_\Omega p(\boldsymbol{x}, t|\boldsymbol{y}) \, d\boldsymbol{x} \right\} dt = \int_0^\infty \tau_\sigma Pr\{ \text{ Path } \sigma \in S_n(\boldsymbol{y}), \tau_\sigma = t\} dt \tag{2.10}$$

where the ensemble $S_n(\boldsymbol{y})$ is the ensemble of shortest paths selected among n Brownian paths, starting at point $\boldsymbol{y}$ and exiting between time t and $t + dt$ from the domain Ω.

Our goal is to study the probability $Pr\{$ Path $\sigma \in S_n\}$ and in particular, to see whether or not the empirical stochastic trajectories of S_n concentrate near the shortest paths starting from $\boldsymbol{y}$ and ending at the small absorbing window $\partial\Omega_a$, under the condition that $\varepsilon = \frac{|\partial\Omega_a|}{|\partial\Omega|} \ll 1$. To further describe the ensemble $S_n(\boldsymbol{y})$, we approximate all paths as discrete broken lines among a finite number of points and we denote the associated ensemble by $\tilde{S}_n(\boldsymbol{y})$. Using Bayes'rule, we get

$$Pr\{ \text{ Path } \sigma \in \tilde{S}_n(\boldsymbol{y}) | t < \tau_\sigma < t + dt\} = \sum_{m=0}^{\infty} Pr\{ \text{ Path } \sigma \in \tilde{S}_n(\boldsymbol{y}) | m, t < \tau_\sigma < t + dt\} Pr\{m \text{ steps}\}$$

where $Pr\{m \text{ steps}\} = \Pr\{$the paths of $\tilde{S}_n(\boldsymbol{y})$ exit in m steps $\}$ is the probability that a path of $\tilde{S}_n(\boldsymbol{y})$ exits in $m-$discrete time steps. A path made of broken lines (random walk with a time step Δt) can be expressed using Wiener path-integral. Indeed, for a stochastic process

$$d\boldsymbol{x} = \boldsymbol{a}(\boldsymbol{x})dt + \boldsymbol{b}(\boldsymbol{x})d\boldsymbol{w} \tag{2.11}$$

the probability density function for a path to arrive at point $\boldsymbol{x}, t$ and exiting at time T is given by

$$\Pr\Big\{\boldsymbol{x}(t_{0,N}) = \boldsymbol{y}, \boldsymbol{x}_N(t_{1,N}) \in \Omega, \ldots, \boldsymbol{x}_N(t) = \boldsymbol{x}, t \le T \le t + \Delta t \,|\, \boldsymbol{x}(0) = \boldsymbol{y}\Big\} \tag{2.12}$$

$$\approx \Bigg[\int_\Omega \cdots \int_\Omega \prod_{j=1}^{N} \frac{d\boldsymbol{y}_j}{\sqrt{(2\pi\Delta t)^n \det \boldsymbol{\sigma}(\boldsymbol{x})(t_{j-1,N}))}}$$

$$\exp\left\{ -\frac{1}{2\Delta t} \left[\boldsymbol{y}_j - \boldsymbol{x}(t_{j-1,N}) - \boldsymbol{a}(\boldsymbol{x}(t_{j-1,N}))\Delta t\right]^T \boldsymbol{\sigma}^{-1}(\boldsymbol{x}(t_{j-1,N})) \left[\boldsymbol{y}_j - \boldsymbol{x}(t_{j-1,N}) - \boldsymbol{a}(\boldsymbol{x}(t_{j-1,N}))\Delta t\right] \right\} \tag{2.13}$$

where $\boldsymbol{\sigma} = \frac{\boldsymbol{b}^t\boldsymbol{b}}{2}$, $\Delta t = t/N,\ t_{j,N} = j\Delta t,\ \boldsymbol{x}(t_{0,N}) = \boldsymbol{y}$ and $\boldsymbol{y}_j = \boldsymbol{x}(t_{j,N})$ (N is the number of time steps) in the product and T is the exit time in the narrow absorbing window $\partial\Omega_a$. For a pure Brownian motion, where $\boldsymbol{\sigma} = D$ is a constant and $\boldsymbol{a} = 0$. We recall the identity

$$\prod_{j=1}^{N} \frac{1}{\sqrt{(2\pi D\Delta t)}} \exp\left\{ -\frac{1}{2\Delta t} \left[|\boldsymbol{y}_j - \boldsymbol{y}_{j-1}|^2\right] \right\} = \frac{1}{\sqrt{(2\pi D\Delta t)^N}} \exp\left\{ -\Delta t \sum_i \frac{\left[|\boldsymbol{y}_j - \boldsymbol{y}_{j-1})|^2\right]}{2(\Delta t)^2} \right\}$$

and that the probability of a Brownian path $\boldsymbol{x}(s)$ can be expressed in the limit of a path-integral with the functional:

$$Pr\{\boldsymbol{x}(s) | s \in [0,t]\} \approx \exp\left(-\int_0^t |\dot{\boldsymbol{x}}|^2 ds \right). \tag{2.14}$$

The Survival probability conditioned on starting at $\boldsymbol{y}$ is given by the Wiener representation:

$$S(t|\boldsymbol{x}_0) = \int_{\boldsymbol{x}\in\Omega} d\boldsymbol{x} \int_{\boldsymbol{x}(0)}^{\boldsymbol{x}(t)=\boldsymbol{x}} \mathcal{D}(\boldsymbol{x}) \exp\left(-\int_0^t |\dot{\boldsymbol{x}}|^2 ds \right),$$

where $\mathcal{D}(\boldsymbol{x})$ is the limit Wiener measure [91]: the exterior integral is taken over all end points $\boldsymbol{x}$ and the path integral is over all paths starting from $\boldsymbol{x}(0)$ [59]. When we consider n-independent paths $(\sigma_1, ..\sigma_n)$ (made of points with a time step Δt) that exit in m-steps, the probability of such an event is

$$Pr\{\sigma_1, ..\sigma_n \in S_n(\boldsymbol{y})|m, \tau_\sigma = m\Delta t\} = \left(\int_{\boldsymbol{y}_0=\boldsymbol{y}} \cdots \int_{\boldsymbol{y}_j \in \Omega} \int_{\boldsymbol{y}_n \in \partial\Omega_a} \frac{1}{(4D\Delta t)^{dm/2}} \prod_{j=1}^{m} \exp\left\{ -\frac{1}{4D\Delta t} \left[|\boldsymbol{y}_j - \boldsymbol{y}_{j-1})|^2 \right] \right\} \right)^n \quad (2.15)$$

Indeed, when the are n paths of m steps, and the fastest one escapes in m-steps, they should all exit in m steps. Using the limit of path integral, we get heuristically using (2.15), the representation

$$Pr\{ \text{ Path } \sigma \in \tilde{S}_n(\boldsymbol{y})|m, \tau_\sigma = m\Delta t\} \approx \int_{\boldsymbol{x}\in\Omega} d\boldsymbol{x} \int_{\boldsymbol{x}(0)=\boldsymbol{y}}^{\boldsymbol{x}(t)=\boldsymbol{x}} \mathcal{D}(\boldsymbol{x}) \exp\left\{ -n \int_0^{m\Delta t} \dot{\boldsymbol{x}}^2 ds \right\},$$

where the integral are over all paths starting at $\boldsymbol{y}_0$ and exiting in time $m\Delta t$. This formula suggests that when n is large, only the paths that minimize the integrant will contribute. Thus, we can rewrite the first moment of $\tau^{(n)}$ by conditioning on the number of steps before exit

$$\begin{aligned} \langle \tau^{(n)} \rangle &= \sum_0^\infty (m\Delta t) Pr\{ \text{ shortest path among } n|m \text{ steps } \} Pr\{m \text{ steps}\} \quad (2.16) \\ &\approx \sum_0^\infty (m\Delta t) \int_{\boldsymbol{x}\in\Omega} d\boldsymbol{x} \int_{\boldsymbol{x}(0)=\boldsymbol{y}}^{\boldsymbol{x}(t)=\boldsymbol{x}} \mathcal{D}(\boldsymbol{x}) \exp\left\{ -n \int_0^{m\Delta t} \dot{\boldsymbol{x}}^2 ds \right\} Pr\{ \text{ shortest path escape in } m \text{ steps}\}. \end{aligned}$$

For large n, this formula suggests that paths that will contribute the most are the ones that will minimize the exponent in eq. 2.16, which allows selecting the paths for which the energy functional is minimal, that is

$$E = \min_{X\in\mathcal{P}_t} \int_0^T \dot{\boldsymbol{x}}^2 ds, \quad (2.17)$$

where the integration is taken over the ensemble of regular paths $\mathcal{P}_t$ inside Ω starting at $\boldsymbol{y}$ and exiting in $\partial\Omega_a$, defined as

$$\mathcal{P}_T = \{P(0) = \boldsymbol{y}, P(T) \in \partial\Omega_a \text{ and } P(s) \in \Omega \text{ and } 0 \le s \le T\}.$$

This formal argument shows that the random paths associated to the fastest exit time are concentrated near the shortest paths. Indeed the Euler-Lagrange equations for the extremal problem 2.17 are the classical geodesics between $\boldsymbol{y}$ and a point in the narrow window $\partial\Omega_a$.

To conclude, in the limit of large n, the Brownian paths contributing to the first moment of $\langle \tau^{(n)} \rangle$ are concentrated on the shortest paths, solution of the variational problem 2.17 (Fig. 2.1A shows the paths for increasing values of n, where the empirical paths concentrated around the shortest paths). Fig. 2.1B-C show how the mean first arrival time for the fastest and the associated length of the paths decay with n. Finally, as n increases, the associated distribution concentrates (Fig. 2.1B-C): for the case of the first arrival time, the distribution is $P_n(t) = nPr\{\tau > t\}^{n-1} Pr\{\tau = t\}$, where τ is the arrival time for a Brownian path. The distribution of lengths for the fastest particles is more difficult to describe as it involves integrating over the history of paths under the constraint that the length is a given number. We shall now focus on an asymmetric example of Brownian escape, where the initial point is positioned above a round obstacle and the narrow escaping window is fixed (fig. 2.2). In the absence of such an obstacle, the optimal path is the straight line, as shown in [80] in the construction of the asymptotic solution by the ray method.

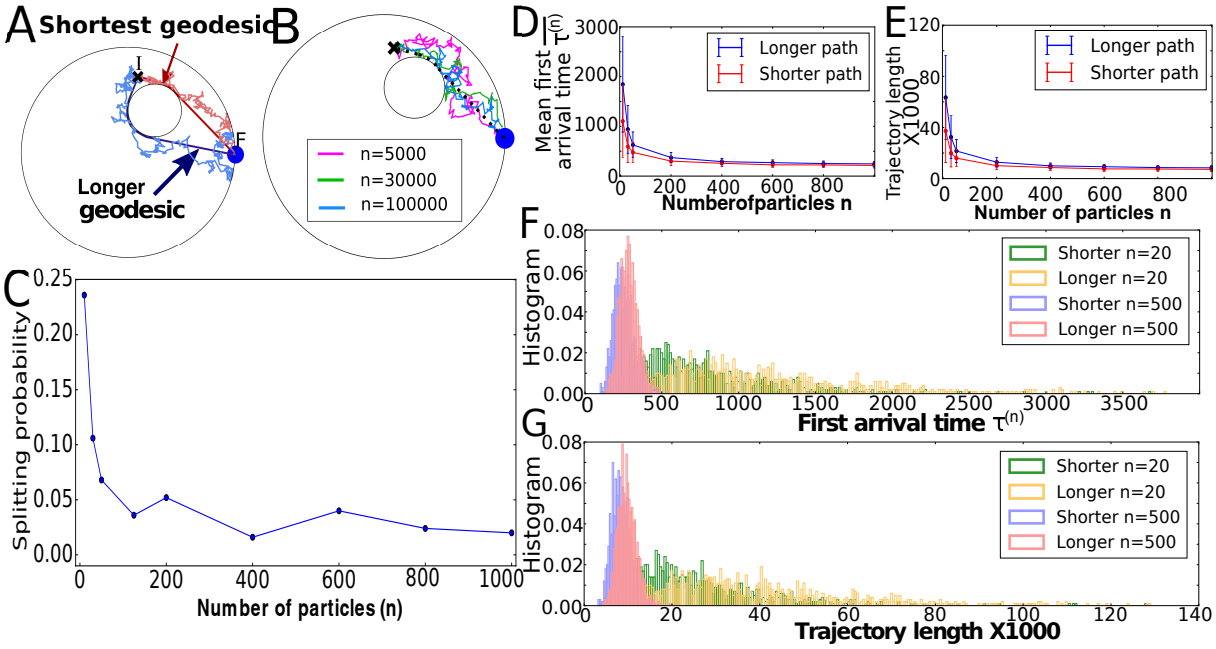

Figure 2.2: **Optimal paths associated to the fastest arrival time of Brownian trajectories starting with an asymmetric initial point (A)-(B).** Empirical shortest paths are concentrated for increasing n. **(C).** Splitting probability computed empirically as the ratio of arrival times from above and below. **(D)-(F).** Mean arrival time and mean length of the trajectories for the fastest for the short and longer optimal paths. **(G)-(H).** histogram of the arrival time and the length for $n = 20$ and 500.

2.3 Optimal paths for an asymmetric escape between $\boldsymbol{y}$ and $\partial\Omega_a$.

We run stochastic simulations to determine the path associated with fastest arrival time among n trajectories (Fig. 2.2) when the domain Ω contains an obstacle positioned between the asymmetric initial $\boldsymbol{y}$ and the narrow absorbing window $\partial\Omega_a$. We recall that as n increases, the trajectories associated with $\langle\tau^{(n)}\rangle$ concentrate near the optimal paths: in the symmetric case (Fig. 2.1), there are two identical shortest paths which consists of straight lines from $\boldsymbol{y}$ to the tangent of the disk, followed by an arc along the disk and finally a straight line from the tangent of the disk to the center of $\partial\Omega_a$. When the initial point $\boldsymbol{y}$ is not on the axis of symmetry, the two optimal paths consist of one shorter than the other (Fig. 2.2A). In that case, the splitting probability between trajectories associated with $\tau^{(n)}$, can be estimated using stochastic simulations (Fig. 2.2C): it is given empirically by the ratio of the mean first arrival time from above $\tau_a^{(n)}$ to the sum of the mean time above and below $\tau_b^{(n)}$ (Fig. 2.2A-B): $P_1 = \frac{\langle\tau_a^{(n)}\rangle}{\langle\tau_a^{(n)}\rangle+\langle\tau_b^{(n)}\rangle}$.
The distribution and the mean associated with the arrival times and the lengths of the shortest Brownian paths near the longer and shorter optimal paths show that the statistics is not very different when we considered the upper and lower trajectories. The main effect that we report from these simulations is the concentration of the pdfs as n increases (Fig. 2.2D-H).
Finally, to confirm that the fastest trajectory $l(t)$ is located near the optimal path $\gamma(t)$ (Fig. 2.3A, we estimated the distance $dist(l(t),\gamma(t))$ along the path and the average distance $\frac{1}{T}\int_0^T dist(l(t),\gamma(t))dt$ (Fig. 2.3B), which is decreasing as n increases (Fig. 2.3C). We note that since the mean arrival time of the fastest among n decreases to zero with $\frac{1}{\log n}$, the path associated to the fastest arrival time cannot be compared to the geodesic of speed 1 (diagonal curve), but we had to renormalize the time before comparing it to a optimal path, see also Fig. 2.3D-F), where we computed the speed along the path. Finally, we observe that the mean displacement or velocity (here $\Delta t = 1$) is very close to the one computed analytically using the displacement of the Brownian motion: indeed, we computed $\mu = \langle|X(t+\Delta t) - X(t)|\rangle = 20\sqrt{\pi} = 35.44$ and $\sigma = \langle|X(t+\Delta t) - X(t)|^2\rangle = 20\sqrt{4-\pi} \approx 18.53$, which are very close to the empirical value we found in Fig. 2.3D-F (lower panel). This result confirms that the extreme trajectory do not jump directly to the escape target. To conclude, the paths of the fastest particle among n concentrate along the geometrical shortest optimal path.

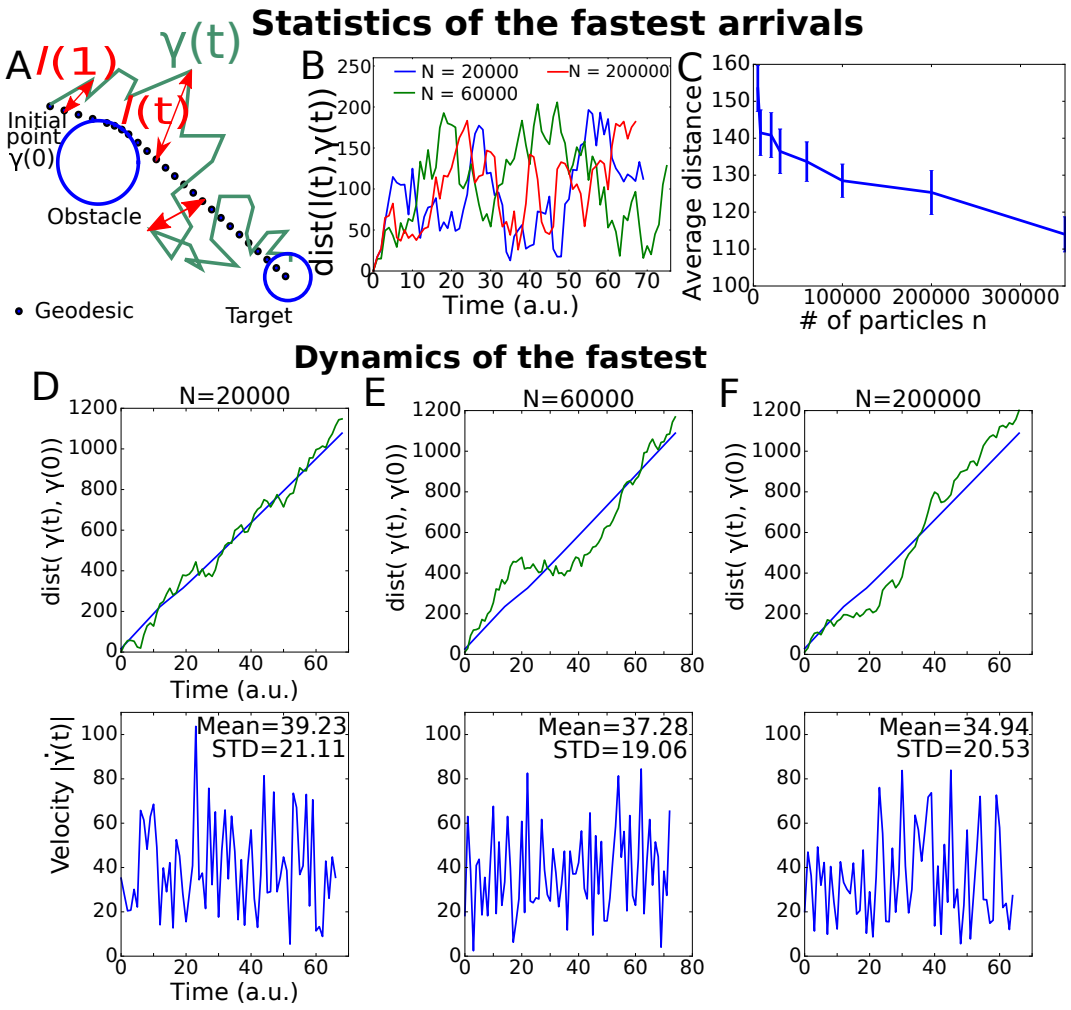

Figure 2.3: **Geometrical properties of the paths associated to the fastest arrival times between n Brownian motions. (A).** Shortest path (green) $l(t)$ and shortest path (doted line) $\gamma(t)$. **(B).** Distance $dist(l(t), \gamma(t))$ computed between t=0 and T, the arrival time to the target for $N = (20, 60, 200) * 10^3$ particles. **(C).** Empirical average distance $\frac{1}{T}\int_0^T dist(l(t), \gamma(t))dt$ vs n (Number of particles). **(D).** Upper: Distance of the shortest path to the initial point $dist(\gamma(t), \gamma(0))$ for various n, showing that it is average proportional to At, where A is a constant. Lower: amplitude of the velocity $|\dot{\gamma}(t)|$.

2.4 Computing the mean shortest path associated to $\langle \tau_a^{(n)} \rangle$ at a resolution Δt

How to construct a mean path at resolution Δt associated to the mean arrival time for the mean fastest arrival time $\langle \tau_a^{(n)} \rangle$? To address this question, we shall consider the empirical paths and define a piecewise segment path connecting two neighboring points separated

by a finite time step Δt. For each realization, we select the optimal path γ_n^1. After we repeat the procedure p times, we obtain the ensemble of paths $\Gamma_p = (\gamma_n^1, ..\gamma_n^p)$ associated with the shortest arrival times $\tau_n^1, ..\tau_n^p$, each are selected as the fastest time among n Brownian walks. We recall that the mean time is computed empirically from the limit of the sum

$$\langle \tau_a^{(n)} \rangle \approx \lim_{p\to\infty} \frac{1}{p} \sum_{k=1}^{p} \tau_N^k. \tag{2.18}$$

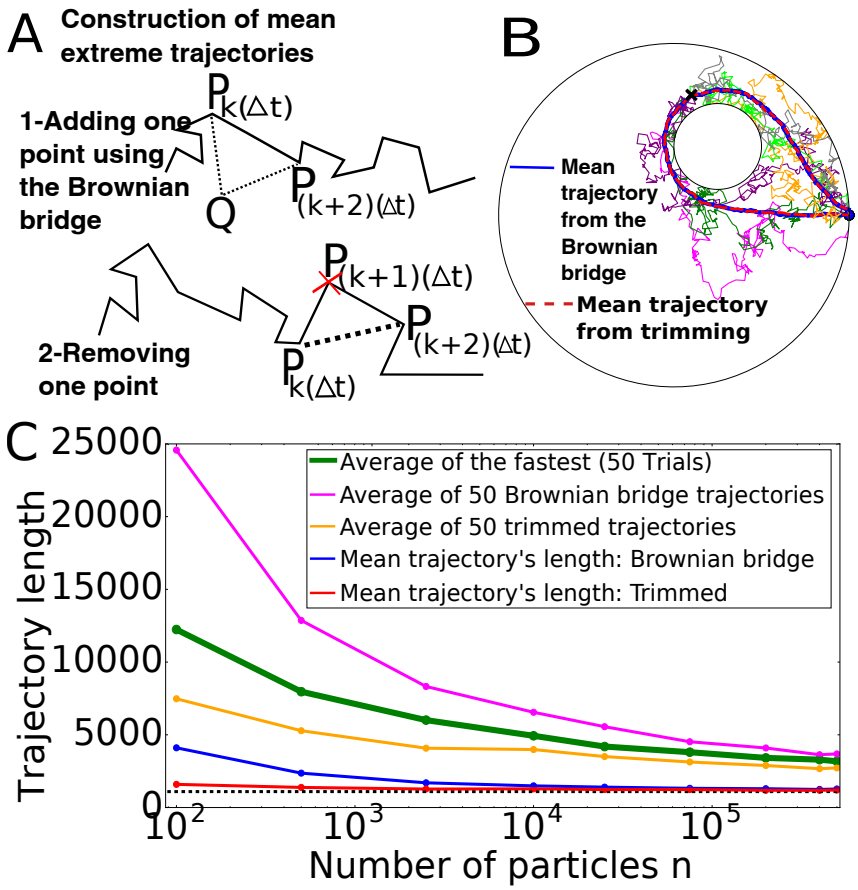

Figure 2.4: **Computing the mean escape paths. (A).** Schematic procedure to add or eliminate one point from a trajectory arriving with the fastest time among n particles. **(B).** Computing the mean maximum and minimum length trajectories (thick line) from the ensemble of fastest trajectories. **(C).** Mean average, longest and shortest trajectories for increasing n.

However, constructing an average path is not straightforward. Indeed, the number of points for each individual trajectory in Γ_p are different, but we can construct the mean shortest trajectory by selecting the path with the minimum number of points n_{min} and then for any other longer trajectories, we remove points chosen uniformly along the

path, so that all resulting trajectories will have the same number of points. The mean shortest trajectory Γ_{min} will then be computed by averaging the position at each time step $k\Delta t, k = 1..$:

$$\Gamma_m(k\Delta t) = \frac{1}{p}\sum_1^p \tilde{\gamma}_N^k(k\Delta t). \tag{2.19}$$

The path Γ_m contains exactly n_{min} points. It is associated to the mean of the fastest time $\langle \tau_a^{(n)} \rangle$. The trajectory is obtained by joining any two neighboring points by a straight line (Fig. 2.4A-B).
It is also possible to compute other averaged trajectories associated to mean fastest arrival time $\langle \tau_a^{(n)} \rangle$, which are not necessarily shortest paths. Indeed, to construct such a longer path, we can start with a mean trajectory that has exactly $n_{min} + 1$ points. for that purpose, we apply the procedure mentioned above to remove points for all longer paths that contained more than $n_{min} + 2$ points. However, we need to add one point for the shortest path that contains n_{min} points only. For that purpose, we use the discrete Brownian bridge at step Δt. We chose a point $P(k_s\Delta t)$ uniformly distributed in the sequence of points $(P(\Delta t), ..P((n_{min})\Delta t)$. Then we insert a point Q_b between $P(k_s\Delta t)$ and $P((k_s + 1)\Delta t)$ (Fig. 2.4A), so that the jump from $P(k_s\Delta t)$ to Q_b is conditioned on the next jump to be at $P((k_s + 1)\Delta t)$ during the time step Δt. The Brownian bridge is defined by

$$\boldsymbol{Q}_b = \frac{\boldsymbol{P}(k_s\Delta t) + \boldsymbol{P}((k_s + 1)\Delta t)}{2} + \sqrt{2D\frac{\Delta t}{2}}\boldsymbol{\eta},$$

where $\boldsymbol{\eta}$ is a Gaussian variable of variance one and mean zero. We end-up with a path containing $n_{min} + 1$ points $(P(\Delta t), ..P((n_{min} + 1)\Delta t)$, that can be used to generate any statistics with the ensemble of other paths, that have been shorten to the same length $n_{min} + 1$. This procedure can be iterated to any number of points, thus we can generate a piecewise constant path with any given number of points n_p between the minimum n_{min} and the maximum n_{max} number for trajectories in the ensemble Γ_p. Examples are shown in (Fig. 2.4B-C).

2.5 Conclusion

To conclude, we have studied here the possible paths associated with the shortest time $\langle \tau_a^{(n)} \rangle$ for n independent Brownian particles to arrive to a small target in the presence of an obstacle. In the first part of the manuscript, using the heuristic of Wiener path-integral and Brownian simulations, we have shown that in the large n limit, the path associated to the first arrived particle concentrates near the shortest path, so that the Euclidean distance between the empirical and shortest path decreases as n increases. In the second part, we studied numerically the splitting probability when there is one

short and long optimal path: we showed that the empirical path is concentrated near the shortest optimal path. Finally, we studied the properties of paths at a resolution Δt by introducing a procedure to average these discrete paths after removing or adding points. The present numerical simulations confirm the decay of the mean arrival time of the fastest with $\frac{1}{logn}$ (in dimension 2), thus we conjecture that even with obstacles, the mean first exit time for the fastest will be given by

$$\bar{\tau}_N^{d2} \approx \frac{\min(l_{g1}^2, ..l_{gn}^2)}{4D \log\left(\frac{\pi\sqrt{2}N}{8\log\left(\frac{1}{\varepsilon}\right)}\right)}, \tag{2.20}$$

where the l_g are the length of the shortest geodesic.
The present approach could be generalized to the exit of n i.i.d stochastic processes 2.11 and in that case, the optimal trajectory could be associated with the control problem $\min \int_0^T |\dot{\boldsymbol{x}}(s) - \boldsymbol{b}(\boldsymbol{x}(s))|^2 ds$ [86]. An other perspective is to use a large deviation approach to further characterize optimal path.
The present results have several consequences and applications to cellular transduction. First, they show that redundancy (having many copies of the same signaling molecule) defines the time of activation as the shortest arrival time using the shortest path from a source of production to the target(s), that can be located at a certain distance away of the source: The mean activation time is not anymore given by the Narrow escape time [41], but it depends (formula 2.20) on the shortest distance between the source and the target and on the number of particle through $1/\log n$. The redundancy can counterbalance the time lost by avoiding the obstacles. This principle is likely to be generic due to the organization of many organelles that constitute impenetrable obstacles.
Finally, in the absence of a steady-state concentration of activator molecules, the present approach revealed that the rate of activation cannot be computed from the forward rate of the Smoluchowski formula [92], showing that the classical chemical reaction theory based on the mass-action law or the Gillespie'algorithm using the forward rate are not appropriate to study transient activations with small targets.
Another consequence is that the effective diffusion coefficient computed from homogenization in the presence of large obstacles, which could be based on the narrow escape theory [41], is not relevant to characterize fast activation from the fastest among n Brownian particles. Rather the arrival time should be computed directly from the molecular scale by accounting for the shortest paths, as we have shown here. Applications range from gene activation by transcription factors in the cell nucleus [93] to cellular transduction [7].

Chapter 3

Extreme escape from a cusp: when geometry does matter for the fastest Brownian particle moving in crowded cellular environment

Published as: **Basnayake, K.**, & Holcman D. (2020). Extreme escape from a cusp: When does geometry matter for the fastest Brownian particles moving in crowded cellular environments? *The Journal of Chemical Physics* 152.13: 134104.
https://doi.org/10.1063/5.0002030 [94]

Abstract

We study here the extreme statistics of Brownian particles escaping from a cusp funnel: the fastest Brownian particles among n follow an ensemble of optimal trajectories located near the shortest path from the source to the target. For the time of such first arrivers, we derive an asymptotic formula, which differs from the mean first passage times obtained for classical narrow escape and dire strait. When particles are initially distributed at a given distance from a cusp, the time of the fastest ones depends on the cusp geometry. Therefore, when many particles diffuse around impermeable obstacles, the geometry plays a role in the time to reach a target. In the context of cellular transduction with signalling molecules, having to escape from such cusp-like domains slows down signaling pathways. Consequently, generating multiple copies of the same molecule enables molecular signals to be delivered through crowded environments in sufficient times.

3.1 Introduction

The redundancy principle describes the need to generate many copies of the same object to guarantee the successful execution of a biological function within a certain time constraint.

Recently, it was shown that the time scale of biological signal transduction, such as the activation of a channel, a cascade of secondary messengers as well as gene activation by a transcription factor are mediated by first among many copies of particles (molecules, ions, transcription factors, etc.) that arrive at a small target [42,95]. In this scenario, the classical Smoluchowski rate, which is extended in narrow escape theory [65, 96–98] only provides the statistics of the mean and becomes irrelevant for estimating the activation time. The mean time taken by the fastest particles to find a small window (i.e. the binding site), has been computed for regular domains [41].

In the probabilistic formulation, for n i.i.d. Brownian particles in a bounded domain Ω with the boundary that is reflecting (except at a narrow window), the shortest arrival time is defined by $\tau^{(n)} = \min(t_1, \ldots, t_n)$, where t_i are the arrival times of the n paths in the ensemble. Extreme statistics and first moments of $\langle \tau^{(n)} \rangle$ were computed previously in [55, 57, 59, 75–79, 99] and recently in higher dimensions [80] leading to the following asymptotic formulas:

$$(\bar{\tau}^{(n)})^{dim1} \approx \frac{\delta^2}{4D \ln\left(\frac{n}{\sqrt{\pi}}\right)}, \tag{3.1}$$

$$(\bar{\tau}^{(n)})^{dim2} \approx \frac{\delta^2}{4D \log\left(\frac{\pi\sqrt{2}n}{8\log\left(\frac{1}{a}\right)}\right)}, \tag{3.2}$$

where D is the diffusion coefficient, δ is the length of the shortest path from the initial point to the small absorbing exiting window, n is the number of particles that were initially injected and a is the radius of the exiting window. Interestingly, the fastest particles use a trajectory close to the optimal path, showing the major contrast with the statistics of a typical brownian particle [100].

In the present study, we focus on the escape of n Brownian particles from a two-dimensional domain with a funnel cusp, for various initial distributions. This is a ubiquitous modality of cellular signaling, where stochastic molecules should find their way across a crowded environment paved with many impermeable obstacles. Here the generic geometrical shape of a two dimensional region between round obstacles is a cusp funnel (Fig. 3.1). We recall that the formula for the mean time of a single Brownian particle to escape from such region Ω, to the leading order [40] is

$$\bar{\tau} = \frac{\pi |\,\Omega|}{2D\sqrt{\varepsilon/R}} \left(1 + O(\sqrt{\varepsilon/R})\right) \quad \text{for } \varepsilon \ll 1, \tag{3.3}$$

where its surface area is $|\Omega|$ while the cusp has a size ϵ in the opening and a curvature R. The diffusion coefficient is D. We shall also use the notation $|\partial\Omega|$ for the boundary of the domain Ω.

For the shortest arrival time, we derive here a new asymptotic formula valid for large n,

when the remaining geometric quantities are fixed:

$$\tau^{(n)} \approx \frac{\pi^2 R^3}{4\varepsilon D(\frac{1-\cos(c\sqrt{\tilde{\varepsilon}})}{\tilde{\varepsilon}})^2 \log(\frac{2n}{\sqrt{\pi}})}. \tag{3.4}$$

Here $\tilde{\varepsilon} = \frac{\varepsilon}{R}$ and c is a constant that depends on the diameter of the domain. When the region outside the cusp has approximately a shape of a disk, (Figs. 3.1 and 3.2 below), it could be shown that $c = \frac{2}{D_{iam}}$, where D_{iam} is the diameter of the domain.
Our new formula presented in Eq.3.4 shows that the time taken by the first arrivers is proportional to the reciprocal to the size of the narrow target ε. This formula is derived for fixed geometry and large n and not in the opposite limit of large n and small ε.
. This new formula has several consequences for studying the time scale of molecular transduction occurring in crowded cellular membranes. First, as anticipated also in [101], the time scale of cellular activation should be described by the statistics of the fastest particles, which notably differ from the mean statistical properties of diffusion. Second, the formula indicates that the time to reach a distant target by the fastest depends on geometrical features that are not the ones taken into account in the effective diffusion coefficient [40] and Eq. 3.3.

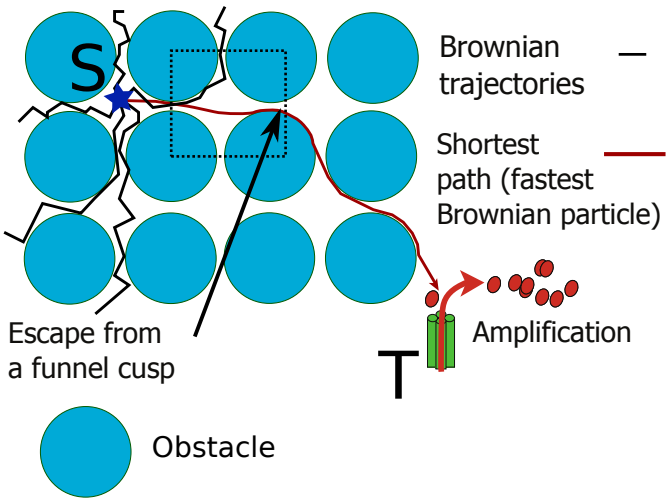

Figure 3.1: **Schematic representation of signaling activation using the fastest Brownian messenger.** When the initial position of the source (S) of particles is distant from the cusp funnel of the obstacles, the trajectory of the fastest particles is an optimal path from the source to the target passing through several cusps. The many trajectories (black) have to avoid many impermeable obstacles (blue). At the target site (T), the first arriving particles activate a secondary messenger pathway, leading to an amplification of the signal.

3.2 Computing the mean escape time from a funnel for the fastest Brownian particle.

The distribution of exit times for the first Brownian particles to escape is

$$\Pr\{\tau^1 > t\} = [\Pr\{t_1 > t\}]^n = \left[\int_\Omega p(\boldsymbol{x}, t)\right]^n,$$

and the mean is

$$\bar{\tau}^{(n)} = \int_0^\infty \left[\int_\Omega p(\boldsymbol{x}, t)\right]^n dt. \tag{3.5}$$

The probability density function p satisfies the Fokker-Planck equation (FPE):

$$\begin{aligned}
\frac{\partial p(\boldsymbol{x}, t \,|\, \boldsymbol{y})}{\partial t} &= D\Delta p(\boldsymbol{x}, t \,|\, \boldsymbol{y}) \quad \text{for } \boldsymbol{x}, \boldsymbol{y} \in \Omega, \\
p(\boldsymbol{x}, 0 \,|\, \boldsymbol{y}) &= \delta(\boldsymbol{x} - \boldsymbol{y}) \quad \text{for } \boldsymbol{x}, \boldsymbol{y} \in \Omega \\
\frac{\partial p(\boldsymbol{x}, t \,|\, \boldsymbol{y})}{\partial \boldsymbol{n}} &= 0 \quad \text{for } \boldsymbol{x} \in \partial\Omega_r, \boldsymbol{y} \in \Omega \\
p(\boldsymbol{x}, t \,|\, \boldsymbol{y}) &= 0 \quad \text{for } \boldsymbol{x} \in \partial\Omega_a, \boldsymbol{y} \in \Omega,
\end{aligned} \tag{3.6}$$

where Ω is a domain with a cusp funnel so that the boundary $\partial\Omega$ contains a small absorbing window $\partial\Omega_a$ of length ε at the cusp opening while the rest of the boundary is reflecting $\partial\Omega_r = \partial\Omega - \partial\Omega_a$ (Fig. 3.1). We will focus here on the case where the initial condition is a function $p(\boldsymbol{x}, 0 \,|\, \boldsymbol{y}) = p_0(\boldsymbol{x})$ concentrated inside the bulk at a certain distance from the cusp.

The domain Ω is generic for studying the effect of escape from narrow passages [40,98,102] . To remove the cusp-singularity, we first normalize the domain by changing variable $z = x/R$, where R is the curvature at the symmetric cusp (Fig. 3.2). The normalized length is $\tilde{\varepsilon} = \frac{\varepsilon}{R}$. In the z-plan, we use the Möbius conformal mapping

$$w = w(z) = \frac{z - \alpha}{1 - \alpha z},, \tag{3.7}$$

where $\alpha = -1 - \sqrt{\tilde{\varepsilon}}$, to map the cusp domain into the banana shape [102, 103] (see Fig. 3.3). Setting $p(z, t) = v(w, t)$, and using the polar coordinates as $w = Re^{i\theta}$, the system (3.6) is converted to:

$$\begin{aligned}
\frac{\partial v(w,t)}{\partial t} &= \frac{D|w(1-\sqrt{\tilde{\varepsilon}}) - 1|^4}{(4\tilde{\varepsilon} + O(\tilde{\varepsilon}^{3/2}))R^2} \frac{\partial^2 v(w,t)}{\partial \theta^2} \quad \text{for } \boldsymbol{w} \in \Omega_w \\
\frac{\partial v(w)}{\partial n} &= 0 \quad \text{for } w \in \partial\Omega_w - \partial\Omega_{w,a} \\
v(w) &= 0 \ \text{ for } w \in \partial\Omega_{w,a}.
\end{aligned} \tag{3.8}$$

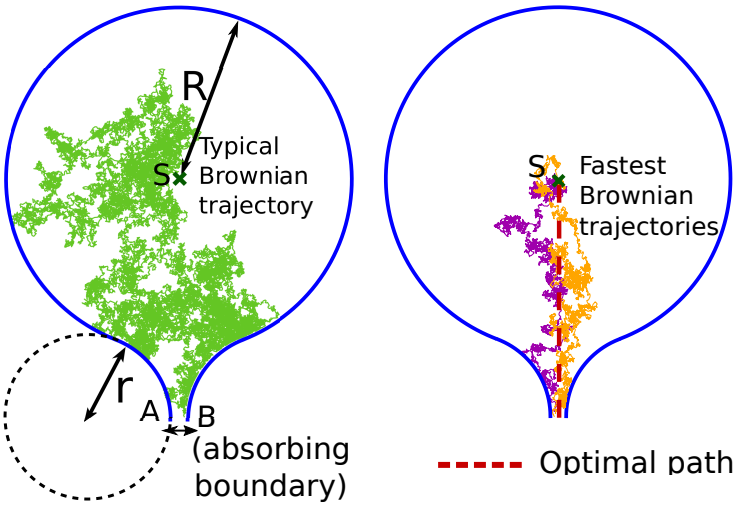

Figure 3.2: **Escape path for a typical and the fastest of n i.i.d. Brownian trajectories Left.** A Brownian trajectory starts initially at position S and escapes into a narrow cusp opening ($2\epsilon = |AB|$). R is the radius of curvature. **Right.** Examples of two trajectories for the fastest among $n = 100$, starting at S.

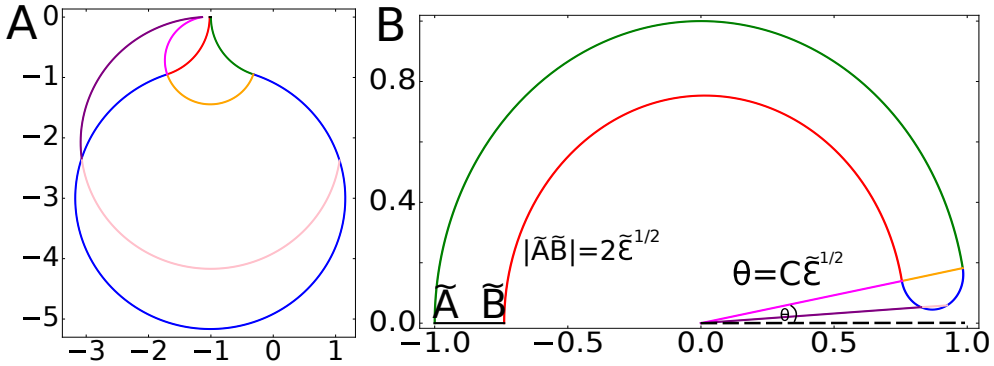

Figure 3.3: **Mapping of the cusp-domain into a banana-shaped domain. Left.** Domain containing a cusp funnel. **Right.** Mapped domain $w(\Omega)$. The yellow arc (left) is mapped in the end of the banana at an angle $c\sqrt{\tilde{\varepsilon}}$, while the cusp is mapped into the red and green arcs.

The asymptotic solution of equation (3.8) is independent of R to the leading order. The reflecting boundary condition is given at the angle $\theta_r = c\sqrt{\tilde{\varepsilon}}$, where $c = O(1)$ is a constant independent of $\tilde{\varepsilon}$ to the leading order. The boundary conditions are [102]

$$\frac{\partial v(c\sqrt{\varepsilon}, t)}{\partial \theta} = 0, \quad v(\pi, t) = 0. \tag{3.9}$$

The diffusion equation, therefore, simplifies to:

$$\frac{\partial v(\theta, t)}{\partial t} = \tilde{\varepsilon} a(\theta) \frac{\partial^2 v(\theta, t)}{\partial \theta^2}, \tag{3.10}$$

where the diffusion tensor $a(\theta)$, which accounts for the cusp geometry, is given by

$$\begin{aligned} a(\theta) &= \frac{D}{R^2}\left(\frac{|e^{i\theta} - 1 - e^{i\theta}\sqrt{\tilde{\varepsilon}}|^4}{\tilde{\varepsilon}^2}\right) \\ &= \frac{D}{R^2}(1 - \sqrt{\tilde{\varepsilon}} + O(\tilde{\varepsilon}))^2 (\frac{1 - \cos(\theta)}{\tilde{\varepsilon}})^2. \end{aligned}$$

The initial condition is such that $v(c\sqrt{\varepsilon}, t)$ tends to $\delta_{c\sqrt{\varepsilon}}$, as t tends to zero. We search for a WKB-type solution [72] of the form (see appendix): we obtain the solution, that does not satisfy the boundary conditions,

$$v(\theta, t, c\sqrt{\tilde{\varepsilon}}) = \frac{1}{\sqrt{4\tilde{\varepsilon}\pi\tilde{D}t}} \exp(-\frac{(\theta - c\sqrt{\tilde{\varepsilon}})^2}{4\tilde{\varepsilon}\tilde{D}t}), \tag{3.11}$$

where $\tilde{D} = \frac{D}{R^2}(1 - \sqrt{\tilde{\varepsilon}} + O(\tilde{\varepsilon}))^2 (\frac{1-\cos(c\sqrt{\tilde{\varepsilon}})}{\tilde{\varepsilon}})^2$.
We construct the entire solution v_{ent} that accounts for the boundary condition, using the reflection principle in the interval of length $L = 2l = 2(\pi - \sqrt{\tilde{\varepsilon}})$,

$$v_{ent}(\theta, t, \theta_0) = \frac{K_0}{\sqrt{4\tilde{\varepsilon}\pi\tilde{D}t}} \sum_n \left(e^{(-\frac{(\theta - \theta_0 + 2Ln)^2}{4\varepsilon\tilde{D}t})} - e^{(-\frac{(\theta + \theta_0 + 2Ln)^2}{4\varepsilon\tilde{D}t})} \right).$$

Here K_0 is a normalization constant computed using the survival probability $S(t) = \int_\Omega p(\boldsymbol{x}, t) d\boldsymbol{x}$ when the particles start inside the bulk, yielding:

$$S(t) = \frac{2}{R^2}\sqrt{\tilde{\varepsilon}} \int_{\tilde{\Omega}} v_{ent}(\theta, t, c\tilde{\varepsilon}) |w'(e^{i\theta})|^2 d\theta. \tag{3.12}$$

and $|w'(e^{i\theta})|^2 = \frac{2\tilde{\varepsilon}}{(1-\cos(\theta))}$. We recall that the diffusion solution $v_{ent}(\theta, t, c\tilde{\varepsilon})$ should be normalized such that $S(t) \to 1$ as $t \to 0$. The Laplace's method applied to Eq.3.12 for large values of n, when $\tilde{\varepsilon} \ll 1$ shows that the weight $|w'(e^{i\theta})|^2$ does not matter in the leading order.
Using computations developed in [80], we obtain for an initial point at $\theta_0 = c\sqrt{\tilde{\varepsilon}}$, integrating from 0 to $\pi - c\sqrt{\tilde{\varepsilon}}$

$$S(t) \approx \frac{K_0}{\sqrt{4\tilde{\varepsilon}\pi\tilde{D}t}} \int \left(\frac{e^{(-\frac{(\theta - \pi + c\sqrt{\tilde{\varepsilon}})^2}{4\varepsilon\tilde{D}t})} - e^{(-\frac{(\theta + \pi - c\sqrt{\tilde{\varepsilon}})^2}{4\varepsilon\tilde{D}t})}}{(1 + \cos(\theta + 2c\sqrt{\tilde{\varepsilon}}))^2} \right) d\theta.$$

Thus $S(t)^n \approx \exp n\left(\ln(1-\frac{8\sqrt{\tilde{\varepsilon}\tilde{D}t}}{L\sqrt{\pi}}e^{-L^2/(16(\tilde{\varepsilon}\tilde{D})t)})\right)$ [80] and the mean escape time for the fastest among n is

$$\tau^{(n)} \approx \frac{(\pi-\sqrt{\tilde{\varepsilon}})^2}{4\tilde{\varepsilon}\tilde{D}\log(\frac{2n}{\sqrt{\pi}})} \approx \frac{\pi^2 R^3}{4\varepsilon D(\frac{1-\cos(c\sqrt{\tilde{\varepsilon}})}{\tilde{\varepsilon}})^2\log(\frac{2n}{\sqrt{\pi}})}. \tag{3.13}$$

This result is obtained for an initial position where a Brownian particle starts inside the bulk [100].

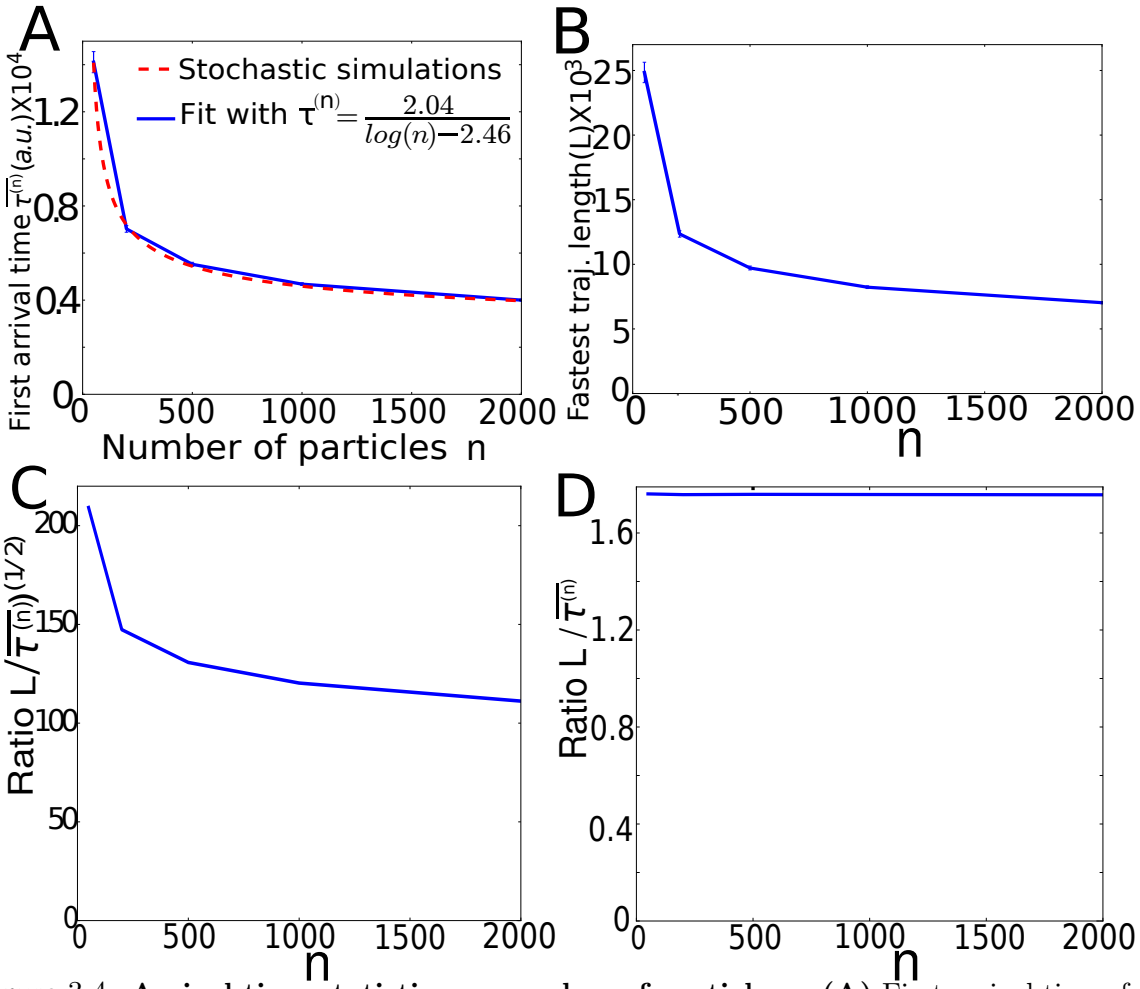

Figure 3.4: **Arrival time statistics vs number of particles n (A)** First arrival times from stochastic simulations (blue) fitted with Eq. 3.13 (red). Parameters are $r = 200$, $R = 100$ and ε=10 in the geometry of Fig. 3.2 computed over 350 trials. **(B)** Approximated lengths of the trajectories. Ratios $\frac{L_n}{(\bar{\tau}^{(n)})^{1/2}}$ **(C)** and $\frac{L_n}{\bar{\tau}^{(n)}}$ **(D)** vs n.

3.3 Comparison with stochastic simulations

To test the predictions of this formula, we performed numerical simulations of 2D-Brownian motion of particles inside a cusp funnel geometry (Fig. 3.2). The particles follow the Langevin's equation at the Smoluchowski's limit (Brownian motion) $\dot{X} = \sqrt{2D}\dot{w}$, where w is the Wiener noise. The discretized form is simulated using the Euler's scheme: $X_m = X_{m-1} + \sqrt{2D\Delta t} \cdot \eta$, where X_m is the position of the Brownian particle at the m^{th} time step while η is a two-dimensional normal random variable. In all realisations, the diffusion coefficient D and the width of the time step Δt were chosen as one.
We find a good agreement of the log-dependency of $\tau^{(n)}$ with respect to the target size ε (Fig.3.4A), predicted analytically in Eq. 3.13. Indeed, we fitted to stochastic simulations $\bar{\tau}^{(n)}$ with the function $A/[log(n) - B]$, where B is a constant representing the second order term expansion in formula 3.4. We obtain the values for these two parameters $A = 2.04$ and $B = 2.46$, confirming the wide range of agreement $n \in [10 - 2000]$ between the analytical formula and the stochastic simulations. Moreover, we notice that the ratio between the mean time $\tau^{(n)}$ and the trajectory length L_n of the fastest particles is constant with respect to n, showing that trajectories are concentrated along the geodesic, but behave as random walks: indeed the ratio $\frac{L_n}{(\bar{\tau}^{(n)})}$ is almost constant (Fig. 3.4C & D).
We recall that during the simulation results (Fig.3.4), all particles were initially positioned at the center S (Fig. 3.2). Next we varied the initial conditions (Fig.3.5). One way to study this is to use the Möbius transformation, that mapped the domain inner arcs into straight line segments in the banana-shaped transformed domain (Fig. 3.3) Orange & Pink). Setting initial conditions on one of the arcs in the large circular domain of the bulk (Fig. 3.5A) is equivalent in the mapped domain to an initial positions located on a small straight segment.
Using these different initial conditions, we confirm the agreement of the log-dependency of $\tau^{(n)}$ with respect to the size ε of the target (Fig.3.5B Left: fits in dotted lines). Although we predicted that $\tau^{(n)}$ increases proportional to R^3 (Eq.3.13), numerical simulations show some deviations that depend on the initial position. In the case of a long diameter, analytical computations predict a local dependency in R^2. We confirmed again in these simulations that the ratios between the mean time $\tau^{(n)}$ and the trajectory length L_n of the fastest particles is constant with respect to both ε and R, while the ratio $\frac{L_n}{(\bar{\tau}^{(n)})^{(1/2)}}$ is not constant, confirming that the fastest arrivers remain Brownian along the neighborhood of the shortest path.

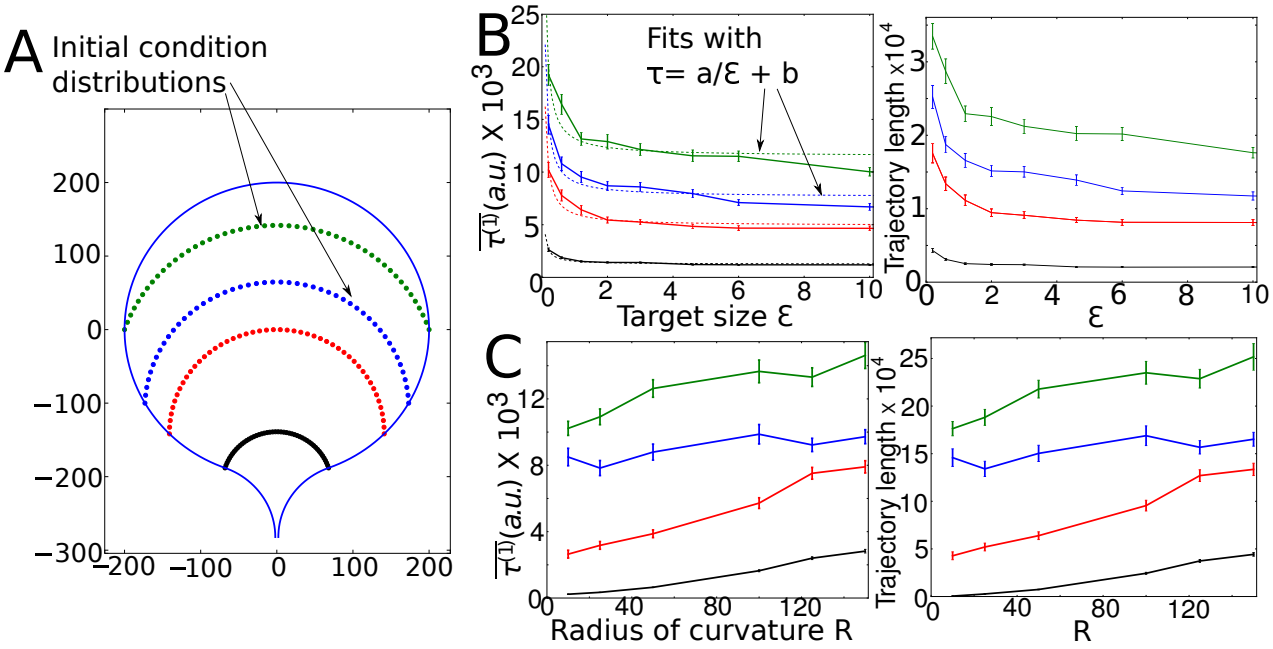

Figure 3.5: **First arrival times vs the approximated lengths of the fastest trajectories on the cusp geometry for various initial conditions. A.** 1000 particles were initially released simultaneously from each of the 50 points (dots) located on the arcs and simulated until the first one arrives to the target site. **B.** Time $\tau^{(n)}$ (Left) and approximated trajectory lengths of the fastest (Right) vs target size ϵ in the range 0.1-10.0. Individual fits are obtained with Eq. 3.13. **C.** Time $\tau^{(n)}$ (Left) and approximated trajectory lengths L_n of the fastest (Right) vs the cusp radius (R). Different initial conditions (colors) are used in correspondence between panel A, B and C. The error bars indicate $\pm$ standard error of the mean over 50 realisations.

3.4 Concluding remarks

We showed here that n independent Brownian particles initially located away from a generic cusp funnel would escape following an ensemble of shortest paths. The parameters characterizing the cusp such as the curvature or the width of the window determine the mean time of the fastest, showing that the cusp geometry influences the escape time to leading order. When the initial locations of the particles are distributed far from the target, the dependency of $\tau^{(n)}$ with respect to the geometrical features remains an interesting question to further explore.

In the context of cell biology, the present modeling and results suggest that fast molecular signaling using the fastest Brownian particles between a source and target occurs along the shortest paths. The time to find the target depends on the shortest distance between obstacles creating funnel cusps especially on the membrane surface of living cells. This process of finding a target by the fastest arrivers defines rapid molecular activation in signal transduction with ubiquitous manifestations in biology such as in phototransduc-

tion, activation of G potein-coupled receptors, and many more. The present results show that the properties of extreme statistics could be used to estimate activation times in molecular biology without computing the effective diffusion coefficient.

Acknowledgments: K.B. is supported by the Programme "Espoirs de la Recherche", Fondation pour la Recherche Médicale (FRM) grant number FDT201904008192. D.H. thanks ANR-18-NEUC-0001-01.

Appendix. We use WKB asymptotics to find a solution of equation 3.10. We search for a solution of the form

$$v(\theta,t) = \frac{K_{\tilde{\varepsilon}}(\theta,t)}{\sqrt{\tilde{\varepsilon}}} \exp(-\frac{\Psi(\theta,t)}{\tilde{\varepsilon}}). \tag{3.14}$$

Here the function Ψ satisfies the eikonal equation

$$-\frac{\partial \Psi}{\partial t} = a(\theta)\left(\frac{\partial \Psi}{\partial \theta}\right)^2. \tag{3.15}$$

The Taylor's expansion along the optimal trajectory gives

$$\Psi(\tilde{\theta}(t),t,\theta_0) \approx \Psi(\tilde{\theta}(t),0,\theta_0) + \frac{1}{2}\Psi_{\theta\theta}(\tilde{\theta}(t),0,\theta_0)(\tilde{\theta}(t)-\theta)^2 + ..,$$

where $\theta_0 = c\sqrt{\tilde{\varepsilon}}$. Due to the normalization condition of WKB-type solution, the zeroth order can be chosen $\Psi(\theta,0,\theta_0) = 0$. Since $\Psi(\theta,t)$ is minimal along the optimal path $\tilde{\theta}(t)$, $\frac{\partial \Psi}{\partial x}(\tilde{\theta}(t),t) = 0$. Thus the optimal solution satisfies:

$$\dot{\tilde{\theta}} = 0 \tag{3.16}$$

$$\tilde{\theta}(0) = c\sqrt{\varepsilon}, \tag{3.17}$$

leading to $\tilde{\theta}(t) = c\sqrt{\varepsilon}$.For computing the second-order term of the expansion, we note that $P(t,\theta_0) = \frac{2}{\Psi_{\theta\theta}(\tilde{\theta}(t),0,\theta_0)}$ is a solution of

$$\frac{\partial P(t,\theta_0)}{\partial t} = 2a(\tilde{\theta}(t,\theta_0)), \tag{3.18}$$

leading to

$$\begin{aligned} P(t,\theta_0) &= 2\int_0^t a(\theta(u,\theta_0))du = 2ta(c\sqrt{\tilde{\varepsilon}}) \\ &= 2t\frac{D}{4R^2}(1-\sqrt{\tilde{\varepsilon}}+O(\tilde{\varepsilon}))^2(\frac{1-\cos(c\sqrt{\tilde{\varepsilon}})}{\tilde{\varepsilon}})^2. \end{aligned} \tag{3.19}$$

For computing the remaining function $K_{\tilde{\varepsilon}}$ in Eq. 3.14, we note that $K_{\tilde{\varepsilon}}(t,\theta_0)$ is a solution of the transport equation [72]:

$$\frac{\partial K_{\tilde{\varepsilon}}(t,\theta_0)}{\partial t} = -\left(\frac{a(\tilde{\theta}(t))}{P(t,\theta_0)}\right) K_{\tilde{\varepsilon}}(\tilde{\theta}(t,\theta_0)). \tag{3.20}$$

The solution is

$$K_{\tilde{\varepsilon}}(\tilde{\theta}(t),\theta_0) = \frac{K_0(\theta, c\sqrt{\tilde{\varepsilon}})}{\sqrt{P(t,\theta_0)}}. \tag{3.21}$$

Finally, using the normalization condition in the transformed domain, we obtain the outer-solution (that does not satisfy the boundary conditions) to the leading order:

$$v(\theta,t,c\sqrt{\tilde{\varepsilon}}) = \frac{1}{\sqrt{4\tilde{\varepsilon}\pi\tilde{D}t}} \exp(-\frac{(\theta - c\sqrt{\tilde{\varepsilon}})^2}{4\tilde{\varepsilon}\tilde{D}t}), \tag{3.22}$$

where

$$\tilde{D} = \frac{D}{R^2}\left(1 - \sqrt{\tilde{\varepsilon}} + O(\tilde{\varepsilon})\right)^2 (\frac{1-\cos(c\sqrt{\tilde{\varepsilon}})}{\tilde{\varepsilon}})^2. \tag{3.23}$$

Part II: Applications of diffusion theory and extreme statistics to calcium signalling in spines

Chapter 4

Fast calcium transients in dendritic spines driven by extreme statistics

Published as: **Basnayake, K.**, Mazaud, D., Bemelmans, A., Rouach, N., Korkotian, E. & Holcman, D. (2019). Fast calcium transients in neuronal spines driven by extreme statistics. *PLOS Biology* 17.6: e2006202. https://doi.org/10.1371/journal.pbio.2006202

Significance statement: We investigate here the mechanism and consequences of fast calcium transients lasting few milliseconds in dendritic spines. We show that these transients are generated by the diffusion of the fastest calcium ions to receptors located on the spine apparatus, which is an extension of the endoplasmic reticulum. Furthermore, these transients are possible due to the asymmetric distribution of Ryanodyne receptors that are present only at the base of a spine, while SERCA pumps are present mostly in the spine head, as revealed here by immunostaining and STED microscopy. Diffusing calcium ions activate the calcium-induced-calcium release pathway, which is modulated by the initial number of calcium ions located in the spine head. To conclude, instead of the classical forward rate of chemical reactions, the activation time scale is defined by the arrival rate of the fastest messenger to a small target receptor followed by an amplification step. Investigations of similar mechanisms are likely to be generic across fast transients present in many other cells such as astrocytes and protrusions, and could lead to predictions of the molecular organization at a nanometer resolution.

Abstract

Fast calcium transients (<10ms) remain difficult to analyse in cellular microdomains, yet they can modulate key cellular events such as trafficking, local ATP production by ER-mitochondria complex or spontaneous activity in astrocytes. In dendritic spines receiving synaptic inputs, we show here that in the presence of a spine apparatus (SA), which is an extension of the smooth ER, a calcium-induced calcium release is triggered at the base of the spine by the fastest calcium ions arriving at a Ryanodine receptor. The mechanism relies on the asymmetric distributions of Ryanodine receptors and SERCA pumps that we predict using a computational

model and further confirm experimentally in culture and slice hippocampal neurons. The present mechanism where the statistics of the fastest particles arriving at a small target followed by an amplification is likely to be generic in molecular transduction across cellular micro-compartments such as thin neuronal processes, astrocytes, endfeets or protrusions.

4.1 Introduction

Extreme statistics describes the distribution of rare events such as the first ions to find a small target [39, 77], which are difficult to detect experimentally in biological microdomains. However, indirect signatures can be derived from their statistical properties. We examine here the role of rare events associated to calcium dynamics in dendritic spines that are local microdomains located on the dendrites of neuronal cells. Spines can form synaptic connections that transmit neural activity [104, 105]. Here we describe specifically how the fastest calcium ions define the time scale of calcium transduction when it is followed by an amplification step. Regulating this fast event has many consequences in the induction of plastic changes. Indeed, calcium increase can be restricted to the spine head isolated from the dendrite, enabling the induction of local synapse-specific calcium-dependent plasticity leading to AMPA receptor accumulations [43, 106]. A fast and localized amount of calcium ions is necessary to induce ATP production from mitochondria to supply the energy required to maintain homeostasis [107–109].
Spines are characterized by the diversity of their shapes, sizes, and the presence or absence of different structural components and organelles such as an endoplasmic reticulum. During synaptic plasticity, spine morphology [16, 110, 111] can change, leading to an increase/decrease of the head size [112] or an elongation/retraction of their neck. Neck elongation can further lead to electrical and biochemical isolation from their parent dendrites [113–120]. Spines can contain a smooth endoplasmic reticulum (ER), fragmented in a compartment called the spine apparatus (SA), that can regulate calcium ions by storing or releasing them [121, 122] and modulate synaptic inputs [14, 123]. The SA is monitored by the actin-associated protein synaptopodin (SP) that can modulate calcium kinetics [18, 124, 125].
After calcium ions enter into dendritic spines, they can bind to endogeneous buffers, get extruded by pumps into the extracellular medium or be pumped into the SA by the sarco/endoplasmic reticulum calcium-ATPase pumps (SERCA3). Calcium ions can also induce calcium release (denoted calcium induced calcium release CICR) from internal SA stores through the ryanodine receptors (RyR) [122, 126]. However, the specific calcium regulation by SA remains unclear due to the fast dynamics and the spine nanometer-scale organization. We recall that the time scale of calcium diffusion transient during long-term plasticity [127] induction is of the order of hundreds of milliseconds [104, 128] but not faster. However, back-propagating action potential can also elicit fast calcium transients leading to long-term enhancement of the back-propagating calcium transients in dendritic spines [129].

We show here that the mechanism involved in fast calcium transient (faster than tens of milliseconds) relies on a new mechanism associated to the extreme statistics of the fastest ions that we describe here. For that purpose, we develop a computational model for calcium ion dynamics and use stochastic simulations to interpret uncaging and fluorescent imaging. To simulate calcium dynamics in synapses and dendritic spines, there are two possible approaches: deterministic reaction-diffusion equations [46, 130] or stochastic modeling [41, 47, 131–133] that we use here. With our approach based on stochastic modeling, we will show here that obtain a new understanding of fast calcium transients: after calcium ions are released inside the spine head using flash photolysis of caged calcium, the concentration increase at the dendrite is faster in spines containing a SA compared to those where it is absent. This is a paradox as the SA should obstruct the passage from the spine head to the dendrite and prevent calcium ions from diffusing. To address the paradox, we use stochastic simulations to show that after calcium release in the spine head, under the hypothesis that RyRs are located at the base and SERCA in the head of spine, the fastest ions arriving at the base determine the time scale of calcium transients due to an amplification step. We further confirm this hypothesis experimentally using imaging in culture and slice hippocampal neuron.

Furthermore, we find that the distribution of arrival times of the fastest ions depends on the initial number of calcium ions, which is a signature of extreme statistics and rare events. Finally, we suggest that molecular activation initiated by the fastest particles is a generic mechanism in molecular transduction that can occurs in cellular micro-compartments such as protrusions or astrocytic endfeets. This mechanism is likely to define the time scale of biochemical activation in nano- and micro-domains, when the source of diffusing particles and the binding targets are spatially separated.

4.2 Materials and Methods

Ethics statement

Animal handling was done in accordance with the guidelines of the Institutional Animal Care and Use Committee (IACUC) of the Weizmann Institute of Science, and the appropriate Israeli law. The Weizmann Institute is accredited by AAALAC. The Weizmann Institutional Animal Care and Use Committee approved this study, conducted with cultured hippocampal neurons.

Animals statement

Experiments were carried out according to the guidelines of the European Community Council Directives of January 1st 2013 (2010/63/EU) and of the local animal welfare committee (certificate A751901, Ministere de l'Agriculture et de l'Alimentation). All

efforts were made to minimize the number of animals used and their suffering. Mice (Mus musculus) were group housed on a 12h light/dark cycle.

Experimental procedure

Calcium uncaging and immunostaining procedure in cultured hippocampal neurons

Cultured hippocampal neurons were transfected with DsRed and loaded with NP-EGTA AM (caged calcium buffer) after which several specific cells were microinjected with Fluo-4 calcium sensor. We expect no more than 50 μ M Fluo-4 after sharp pipette unicellular microinjection. Pipette resistance was 30-50MΩ, the dye concentration in the pipette 1mM and the duration of injection is about 1s. Calcium imaging was done at 30^oC.

UV laser was directed to either spine heads or the basal dendritic shafts. Following the flashes of ND-YAG UV laser (4ns, 330nm) focused into a region of about 0.5 μm in diameter, the released calcium signals could be detected and line-scanned using confocal microscope at the rate of 0.7ms/line. Other sources of calcium fluctuations were blocked using TTX ($1\mu M$), DNQX ($10\mu M$) and APV ($20\mu M$). No special image processing has been applied. Confocal offset function has been used to adjust the background levels for immunostaining. Each recording channel has been adjusted independently, using range indicator. The "optimal signal" imaging mode has been used, in which each separate imaging track is illuminated with its specific wavelength one by one, without mixing the excitation lines.

Following the experiment, cultures were fixed in 4% paraformaldehyde and immunostained for synaptopodin (green staining). The same cell regions, containing recorded spines, were identified and imaged. For immunostaining, cover glasses bearing transfected primary hippocampal cells were washed briefly with standard extracellular solution (NaCl 129mM, KCl 4mM, MgCl 21mM, CaCl 22mM, glucose 10mM and HEPES 10mM). Cultures were then fixed with 4% paraformaldehyde and 4% sucrose in 0.1MPBS, pH 7.4, for 20min, and washed with PBS thoroughly. Cultures were incubated for 1 hwith 10% normal goat serum (NGS) in 0.1% Triton X-100 containing PBS to reduce unspecific staining and subsequently incubated for 24 h at 4C in rabbit anti-SP antibody (SE-19, Sigma; 1:1000, 10%bovine serumalbumin, 0.1% Triton X-100 in PBS) and/or rabbit anti-RYR1antibody (gift from Dr. Shoshan-Barmatz BGU, Israel, 1:250, 10% goatserum in PBS) (Shoshan-Barmatz et al., 2007). Anti-SERCA2 N-19 and anti-SERCA3 PL/IM430 were from Santa Cruz Biotechnology. Cultures were incubated for 1 h with Alexa 568-labeled or Alexa 633-labeled goat anti-rabbit antibody (Invitrogen; 1:200, 10% bovine serum albumin, 0.1% TritonX-100). Cover slips were washed again, transferred onto glass slides and mounted for visualization with anti-fading mounting medium.

For double or triple-immunolabeling cultures were incubated in a mixture of rabbit anti-synaptopodin antibody and other antibodies visualized at appropriate wavelengths. After washing, sections were incubated first with anti-rabbit secondary antibody, washed again, and then incubated with anti-mouse secondary antibody. In all cases, secondary

and tertiary dendritic segments were visualized. Confocal image stacks were recorded using a Zeiss LSM510 laser-scanning microscope, or Zeiss 880 LSM airy scan confocal using a 40 oil-immersion objective lens [1.4 numerical aperture (NA)] and 4 scan zoom. Detector gain and amplifier were initially set to obtain pixel densities within a linear range. Up to 25 images were recorded per stack. All images in this study were sampled at a rate more than two times the ideal Nyquist rate.

Finally, immunostained cells were visualized using two confocal systems: 1. Inverted LSM 510 Zeiss, 100x, 1.4 NA, oil immersion objective, zoom 4-6, z-stacks of 0.7 um thin optical sections, 4-8x average, 2000x2000 pixel window, range indicator used for optimized illumination, 488, 543, 633 laser lines used for excitation. 2. Upright, LSM 880 Zeiss, 63x 1.4 NA, oil immersion objective, GaSP PMT, Airyscan, 0.7μm optical sections, 405, 488, 543 wavelengths. For the statistical analysis, 18 SP-positive and 26 SP-negative spines were analyzed.

Glutamate uncaging

Cultured hippocampal neurons have been transfected with DsRed (1 μg/well) plasmid was using Lipofectamine 2000, at the age of 6-7 d in vitro (DIV). Transfected cells displayed no apparent differences in morphology, spine density, and survival compared with GFP transfected cells. Cells were left to grow in the incubator at 37^{o}C, 5% CO2 and were used for experimentation at 14-17 DIV.

Cultures were placed in the imaging chamber, controlled by an automated X-Y stage (Luigs and Neumann). Neurons were imaged on the stage of an upright Zeiss PASCAL confocal microscope using an Olympus 63X water-immersion objective (0.9NA) and 4X scan zoom. Temperature in the recording chamber was adjusted to 30C. Standard recording medium contained (in mM): 129 NaCl, 4 KCl, 1 $MgCl_2$, 2 $CaCl_2$, 10 glucose, 10 HEPES, pH adjusted to 7.4 with NaOH, and osmolarity to 310 mOsm with sucrose. K+ Fluo-4 solution (200μM, Invitrogen) was injected into neurons with sharp micropipettes with resistance of about 5 MOhm during 3s and allowed to diffuse for 1h before imaging. Flash photolysis of caged molecules has been described elsewhere in more details [116]. A UV laser (New Wave, air-cooled ND:YAG), emitting 355 nm, 4ns single light pulses, was focused through the objective lens (63X, 0.9NA Olympus, water-immersion) into a spot of $< 1\mu m^3$. The UV spot is localized using a parallel red laser light (633 nm), directed through the sane optical axis. Single UV pulses could be applied repeatedly without noticeable tissue damage. MNI-caged glutamate, Tocris Bioscience, 0.5mM was used for uncaging procedure. The laser was pointed to the area adjacent to a randomly chosen dendritic spine with relatively long (0.8-1μm) neck length to minimize the uncaged glutamate effect on the shaft due to diffusion towards the parent dendrite. Line scans through the spine head and the dendrite were recorded at the rate of 0.7 ms/line with pinhole adjusted to 1.5μm optical section. No bleaching or photo-damage was seen during the recording. Note that we did calibrate the uncaging pulse to obtain physiological synaptic responses, which we recorded with electrophysiology together with the uncaging. Thus

the glutamate uncaging procedure induces currents similar to synaptic events (See also results).

After the experiment, cover glasses with transfected hippocampal cells were washed briefly with standard extracellular solution. Cultures were then fixed with 4% PFA and 4% sucrose in 0.1MPBS, pH7.4, for 20 min, and washed with PBS thoroughly. Cultures were incubated for 1 h with 10% normal goat serum in 0.1% Triton X-100 containing PBS and subsequently incubated for 24h at 4^oC in rabbit anti-synaptopodin (SP) antibody (SE-19, Sigma; 1:1000, 10% BSA in PBS). Then cultures were incubated for 1 h with Alexa-488-labeled goat anti-rabbit secondary antibody (Invitrogen; 1:200). Coverslips were washed again, transferred onto glass slides, and mounted for visualization with antifading mounting medium. Same transfected neurons and same dendritic spines as imaged during the live experiment were identified and the spines were classified as SP+ or SP- depending on the presence of immunostaining in the heads and/or necks of the analyzed spines.

AAV production and injection

One GFP cassette was placed under the control of a hSynapsin-specific promoter in an AAV shuttle plasmid containing the inverted terminal repeats (ITR) of AAV2. Pseudotype serotype 9 AAV particles were produced by transient co-transfection of HEK-293T cells. Viral titers were determined by quantitative PCR amplification of the ITR on DNase-resistant particles and expressed as vector genomes per mL (vg/mL).
2-month old C57Bl6 mice were anesthetized with a mixture of ketamine (95 mg/kg; Merial) and xylazine (10 mg/kg; Bayer) in 0.9% NaCl and placed on a stereotaxic frame under body temperature monitoring. AAVs were diluted in PBS at a concentration of AAV-hSynapsin-GFP $1.02 * 10^{13}$ vg/ml, and $1\mu l$ of virus was stereotaxically injected unilaterally into the hippocampal region at a rate of $0.2\mu l$/min, using a 29-gauge blunt-tip needle linked to a $2\mu l$ Hamilton syringe (Phymep). The stereotaxic coordinates to Bregma were: antero-posterior: +2 mm; lateral: -1.5 mm; dorso-ventral: -2 mm. At the end of the injection, the needle was left in place for 5min before being slowly removed. The skin was sutured and mice recovery was checked for the next 24 h. After two weeks, the mice were sacrificed and the brains were extracted after 2% paraformaldehyde/PBS intracardiac perfusion.

Immunoshistochemistry

40 μm thick brain slices were cut with a Leica microtome. Brain slices were permeabilized and blocked for 2h in 0.25%Triton/0.2%Gelatine in PBS (blocking solution) at room temperature. Primary and secondary antibodies were diluted in blocking solution and incubated overnight at 4^oC and mounted in Fluoromount-G mounting medium. The following primary antibodies were used (anti-synaptopodin (Rabbit, 1/100, Sigma-Aldrich SE-19), anti-Ryanodin Receptor (Mouse, 1/100, Abcam ab2827), anti-Serca3 (Mouse, 1/100, Sigma-Aldrich WH0000489M1), anti-GFP (chicken, 1/600, Aves 1020)) in combination with the following secondary antibodies (anti-chicken 488 (Goat, 1/300, Invitrogen,

A11039), anti-rabbit 555 (Goat, 1/300, Invitrogen, A21439), anti-mouse 647 (Goat, 1/300, Invitrogen, A21235)). Z-stacks images were taken using a super resolution STED microscope (Abberior Instruments GmbH) and analyzed using ImageJ software. Identification and localization of punctae was done when the brightest punctae staining in the Z-axis was within the dendritic spine to limit the analysis of punctae located below or above the spine. Images were taken using a STED microscope (Abberior Instruments GmbH) and analyzed using ImageJ software.

Super-resolution STED imaging in brain slices

STED imaging was performed using a custom upright STED microscope (Abberior Instruments). The microscope is based upon a Scientifica microscope body (Slice Scope, Scientifica) with an Olympus 100X/1.4NA ULSAPO objective lens. It comprises a scanner design featuring four mirrors (Quad Scanner, Abberior Instruments). 488nm, 561nm and 640nm excitation lasers are available (Abberior Instruments, pulsed @40/80 Mhz). Two STED-lasers at 595nm (MPB-C, cw) and 775nm (MPB-C, pulsed @40/80 MHz) are at disposal. The conventional laser excitation and STED laser beams are superimposed using a beam-splitter (HC BS R785 lambda/10 PV flat, AHF Analysetechnik).

Common excitation power with pulsed excitation ranges from 10-20uW with STED power intensities of up to 200 mW in the focal plane. Gated STED is possible where STED at 595nm is always gated STED due to the cw-laser (typical gate delay of 1ns to 2ns depending on desired signal level and resolution).

Statistics

All data are expressed as mean ± SEM. Statistical significance for within-group comparisons was determined by one-way ANOVAs (followed by Tukey's post-test), whereas unpaired t-tests were used for between-group comparisons.

Stochastic simulations of calcium ions in a dendritic spine

We model a dendritic spine with a spherical head connected to a narrow, cylindrical neck, as described in [47, 116, 134]. The SA present in SP+ spines are modeled also with a similar geometry with a neck and a head positioned inside the spine. Calcium ions are described as Brownian particles following the Smoluchowski limit of the Langevin equation $\dot{X} = \sqrt{2D}\dot{w}$, where w is the Wiener white noise. This motion of particles in the spine is simulated using the Euler's scheme: $\boldsymbol{X}_n = \boldsymbol{X}_{n-1} + \sqrt{2D\Delta t} \cdot \eta$, where $X_t = \{X, Y, Z\}$ is the position of a particle at time t, while η is a three-dimensional normal random variable. D is the diffusion coefficient of calcium ions in the cytoplasm and Δt is the time step. (All parameter values are summarized in S1 Table). We neglected here the baseline of free calcium concentration and we released $N = 1000$ particles (leading to an initial calcium concentration of 0.4μM in the spine head). Ions can diffuse inside the cytoplasm, and they are reflected at the surfaces of the spine and the SA (Snell-Descartes

reflection). To replicate the uncaging experiments, we use either the center of the ball or the base of the cylindrical neck as the initial positions of particles. Ions arriving at the dendritic shaft located at the base are considered to be lost and do not return to the spine during the time scale of the simulations (absorbing boundary). The inner surface of the spine head contains absorbing circular disks with a $10nm$ radius, which models calcium pumps. In all simulations, we kept the number of pumps in the head fixed at the value 50, as calibrated from a pure diffusion model (see S1 Fig). The number of trials for each simulation is shown in S2 Table. Our code is written in Python 2.7 and are available at http://bionewmetrics.org/simulations-of-spine-calcium-transients-with-er/

Ryanodine receptors

RyRs are activated upon the arrival of the first two ions to a small absorbing disk of size $a_{RyR} = 10nm$ (see S2 Fig). We positioned $n_R = 36$ receptors for the simulations organized in four rings in the SA neck, each containing six receptors. The other 12 are located on the SA component parallel to the dendritic shaft. After a receptor opens, it releases instantaneously a fixed number of calcium ions n_{Ca}, which are positioned at the center of the receptors. Following this release, a RyR enters into a refractory period that lasts 3 to $6ms$, during which it is modeled as a reflective boundary for free diffusing ions. After calibration, we find that calcium ions should be released with a delay of 0.25ms after the arrival of a second ion to the RyR binding site.

SERCA Pumps

We model SERCA pumps as absorbing disks of size $a_{SERCA} = 10nm$. When a calcium ion arrives to the disk, it is bound indefinitely. If a second ion arrives, both are absorbed immediately and the transporter is frozen in an inactive state. (see S3 Fig) We positioned 36 SERCA pumps uniformly distributed on the upper hemisphere of the spine head.

Mean first passage time of ions to the base of a spine

For a Brownian particle released in the spine head, the mean arrival time to the base of a spine has been computed asymptotically [41]

$$\bar{\tau} = \frac{V}{4Da}[1 + \frac{a}{\pi R}\log(\frac{R}{a})] + \frac{L^2}{2D} + \frac{VL}{\pi Da^2}, \tag{4.1}$$

where D is the diffusion coefficient, V, a, R and L are the volume of the head, spine neck radius, head radius and the total length of the neck respectively. We refer to S1 Table for the parameter values, from which we estimated $\bar{\tau} \approx 120ms$.

4.3 Results

4.3.1 Fast calcium transient in spines with and without a SA are not due to classical diffusion

To investigate the role of the SA, we first released calcium following the flashes of ND-YAG UV laser to uncage calcium in dendritic spines from hippocampal neurons (Fig 4.1A). After the experiment, the cultures were fixed using 4% paraformaldehyde and immunostained for SP to identify spines containing SA (see Materials and Methods). About 25% of total mushroom spines contained synaptopodin puncta (SP +) while in the others (SP -) clear puncta could not be seen. Note that medium spines (of about 1-1.5 μm in length) are studied. The transient fluorescence signal reveals the influence of the SA on calcium dynamics as shown in Fig 4.1B-C (see also S4 Fig). The calcium decay time in the head is well approximated by a single exponential [41] with a time constant $\tau = 5.28ms$ in $SP+$ compared to $\tau = 6.97ms$ for $SP-$, showing that the SA does not influence the extrusion rate from the spine head, probably because its obstruction is not completely occluding the passage from the head through the head-neck junction. However, the elevation of calcium at the base was much different, leading to high and very fast elevation in the case of SP+, a phenomena that is the focus on the present study. Finally, uncaging at the base of the spine leads to the same response in the head for SP+ and SP-, suggesting that the privileged calcium response occurs only in the head-neck direction when a SA is present. The asymmetry found here between releasing either in the spine head or at in the dendrite is specific to calcium, as shown in S4 Fig). We confirm that similar calcium transients can be induced by caged glutamate only in SP+ dendritic spines, as classified by the presence of immunostaining in the heads and/or necks, as shown in Fig 4.2A-D. Note that the glutamate evoked responses are similar to one induced by a synaptic event Fig 4.2E-G. Thus we conclude that fast calcium transients at the base of the SP+ spines did not depend on the mode of induction, as they could be induced by calcium and glutamate uncaging with similar time scale.

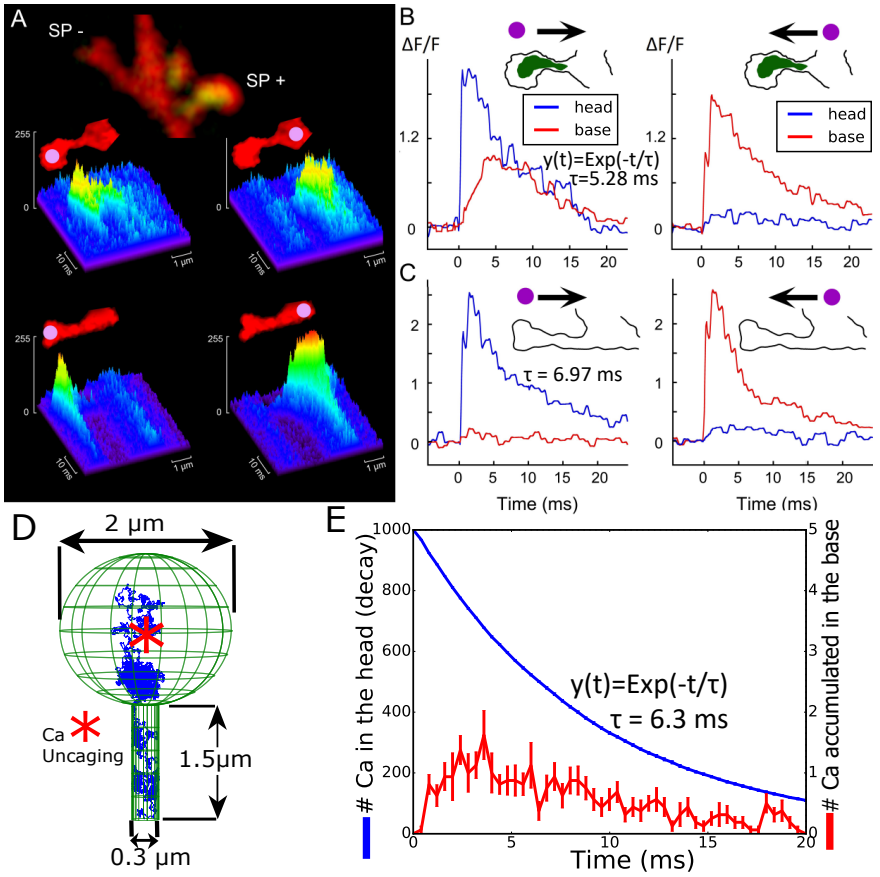

Figure 4.1: **Calcium transient in dendritic spines with and without a SA. (A).** Examples of line scans in two neighboring spines of about same length, following flash photolysis of NP-EGTA in spine heads (left) and the parent dendrite (right). At the end of the experiment, the cultures were immuno-stained for SP (green staining). The same cell regions, containing recorded spines, were identified and imaged. Some spines (about 25%) of total mushroom spines contained synaptopodin puncta (SP+) while in the others (SP-) a clear puncta could not be seen. **(B) and (C)** Individual traces of calcium transients for the same spine heads (blue) and the parent dendrites (red) are shown on panel A. Schematic contours of two spines, containing (SP+) and not containing (SP-) synaptopodin puncta are shown on the top of the graphs. The arrows indicate the possible direction of calcium diffusion from the focus of uncaging (purple dots). There is a clear signal transfer from the spine head to the parent dendrite in the SP-positive spine and such signaling is absent if the focus of uncaging is set in the dendrite (B). For the SP-negative spine, calcium signaling in both directions looks the same (C). The decay times $\exp(-t/\tau)$ for calcium in the head were fitted for 19 (for SP+) and 27 (for SP-) experiments. **(D)** Stochastic simulations of calcium ions in a dendritic spine without a SA: initial position of calcium ions (red star) and a trajectory (blue) are shown. The surface of the head contains 50 absorbing circular calcium pumps with a $10nm$ radius (not shown). **(E)** Simulated calcium transient following the model in (D). Calcium ions propagate from the head to the neck.

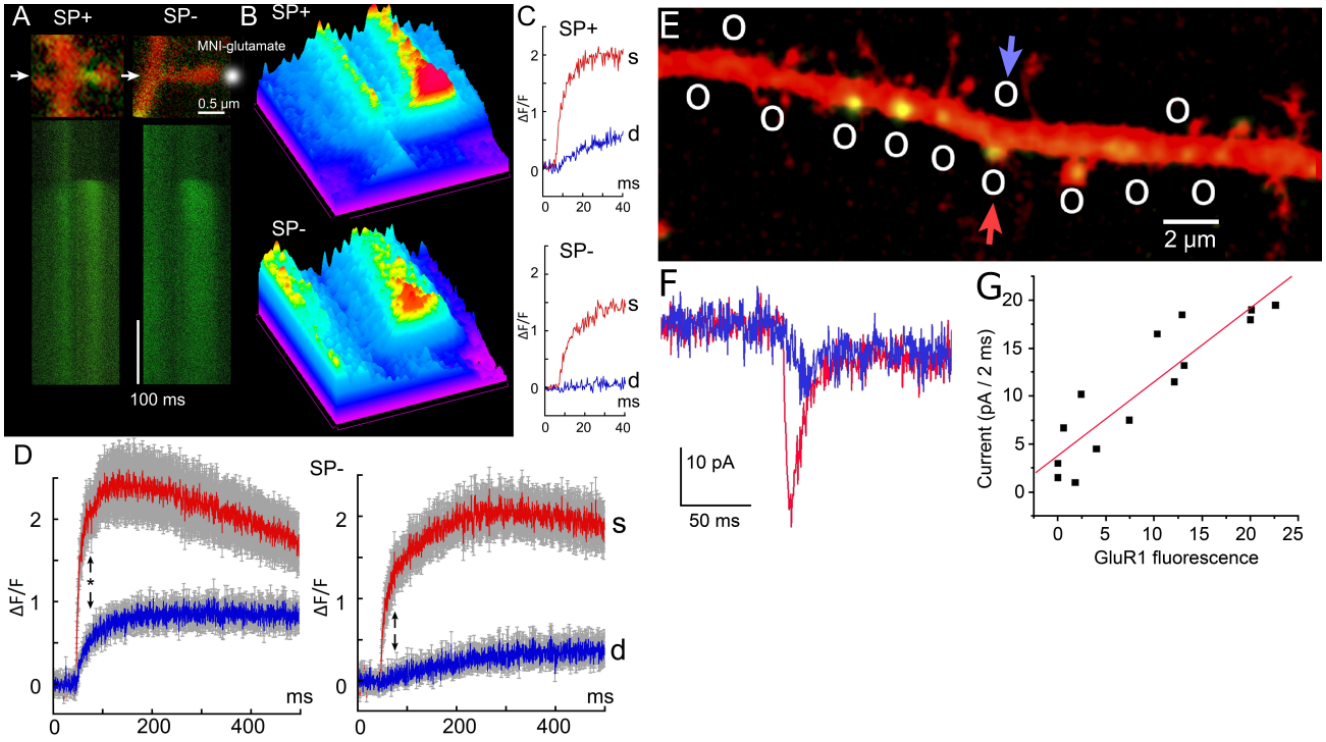

Figure 4.2

Figure 4.2: Effect of MNI-caged glutamate photolysis on spine-dendrite coupling in synaptopodin (SP) positive and negative spines. (A top) Examples of two SP+ and SP- spines as revealed by immunocytochemical analysis, done after the recording experiments. Transfected cultured hippocampal cells were microinjected with 200 μM K+ Fluo-4 and calcium transients as fast 0.35ms/ line line-scans (A bottom) were recorded following single 4ns 355nm Nd:YAG laser ash(third harmonic of 1064nm). B, same line-scans, presented as spectrum-colored surface plots, oriented from bottom right to top left with magenta-blue corresponding to low fluorescence and yellow-red to high Fluo-4 fluorescence. (C) Examples of the initial stage of calcium transients (during first 30 ms) from SP+ and SP- spines. (D) Summarized graphs presenting 23 SP+ spine/ dendrite pairs and 22 SP- spine/ dendrite pairs. Averaged spine lengths were 1.1 $\pm$ 0.13 μm for SP+ and 1.15 $\pm$ 0.15μm for SP- spines. Note faster and higher calcium rise in the dendrites SP+ versus SP- parent dendrites and faster decay time in the SP+ spine heads. Black arrows indicate 80 ms: P-values based on ANOVA for (SP+/SP-) spines is 0.011 while for (SP+ / SP-) dendrites is 0.038 respectively. (E) Multiple uncaging locations (circles) of glutamate along the dendrite (transfected with glutamate receptor 1 (GluR-1, AMPA) marked in green, to visualize the accumulation of GluR1 and transfected with DsRed for visualiazng dendrite morphology), from typical cultured pyramidal neurons. Glutamate is uncaged at several GluR-positive and GluR-negative locations. (F) Patch clamp responses to glutamate uncaging located by the arrows (in panel E) at a dendritic spine (red) and on the dendritic shaft (blue). (G) Overall correlation between GluR1 fluorescence and recorded current following uncaging [135]. Data used for generating D and G is available in S1 Data.

For analysing the calcium transient further, we used stochastic simulations, where ions are treated as Brownian particles (see Materials and Methods) and released at the center of the spine head (Fig 4.1D-E). Using a single exponential approximation, we obtained a decay time in the head $\tau = 6.3ms$, comparable to the one obtained experimentally (see S1 Fig for the calibration of calcium pumps in the absence of RyRs and SERCAs). To conclude, fast calcium transient of less than $20ms$ in spines with no SP is well reproduced by stochastic simulations, but the calcium increase at the dendrite base for spines with a SA is much faster than the mean arrival time of calcium ions. This effect is surprising because it occurs despite the serious SA obstruction that should prevent calcium ions from passing easily through the neck. We shall now investigate the mechanism for this fast increase.

4.3.2 The fast calcium transient is generated by calcium induced calcium released and the asymmetric distribution of RyR on the SA

To gain intuition and clarify how the SA could affect the calcium transient, we first run stochastic simulations similar to the ones we used in Fig 4.1F. Ions are released initially in the spine head (red star Fig 4.3A). But now we introduce a SA type compartment, where we added 36 SERCA pumps (blue) located on the surface of the SA (head) and 36 RyRs located on the SA at the base (red). While SERCA pumps can uptake calcium ions from the cytoplasm to the ER, RyRs generate a calcium flux from the SA to the cytoplasm when two calcium ions are bound (Materials and Methods, S2 Fig, S3 Fig and S1 Table). Interestingly, and in contrast to the results of Fig 4.1E, after 1000 ions are released in the spine head, a significant calcium increase can be observed at the base of the spine in less than $2ms$. This effect is already present when 3 calcium ions per RyR are released (Fig 4.3B), and further amplified with 5 ions, compared to spines with no SA (green curve). Interestingly, this calcium amplification does not depend on the distances between RyRs within the range below 150nm (see S5 Fig).

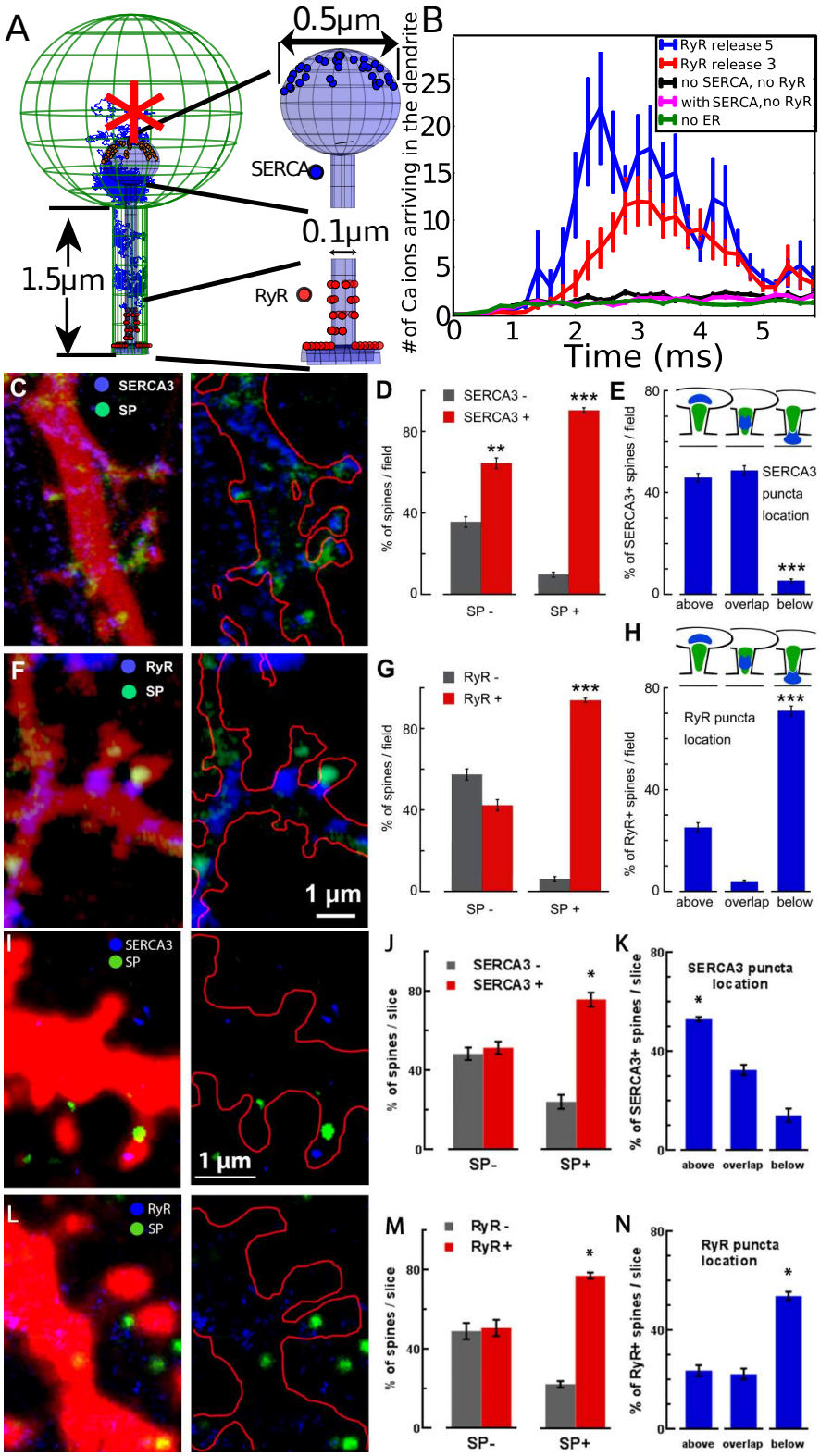
A
0.5µm
SERCA
0.1µm
1.5µm
RyR
B
RyR release 5
RyR release 3
no SERCA, no RyR
with SERCA,no RyR
no ER
# of Ca ions arriving in the dendrite
Time (ms)
C
SERCA3
SP
D
SERCA3 -
SERCA3 +
% of spines / field
SP -
SP +
E
% of SERCA3+ spines / field
SERCA3 puncta location
above
overlap
below
F
RyR
SP
1 µm
G
RyR -
RyR +
H
RyR puncta location
I
J
SERCA3 -
SERCA3 +
% of spines / slice
SP-
SP+
K
SERCA3 puncta location
L
M
RyR -
RyR +
N
RyR puncta location

Figure 4.3: **(A)-(B)** Stochastic simulations of calcium ions: (G) Model of a spine containing a SA with SERCA pumps and RyRs (right: magnifications show the distribution of 36 SERCA pumps in the upper hemisphere of the SA head and 36 RyRs located on the SA at the base, 12 on the shaft and 24 in the neck organized in four rings containing six randomly distributed receptors). Ions are initially released at the center of the head (red star). **(B)** Calcium ions arriving at the base of the dendrite following released in the head and released from RyRs (3 and 5 ions per activated receptors). **(C-H)**: Distributions of SERCA 3 and RyRs in dendritic spines depend on the presence of synaptopodin (SP) puncta. (A) and **(F)**- cultured rat hippocampal neurons were co-transfected with DsRed (red color on the right panels and red contour on the left panel) and SP (green puncta) and immunstained against SERCA3 and RyR. In SP occupied dendritic spines top head locations of SERCA3 (blue staining in (D)) and basal locations of RyR (blue staining in (F)) are confirmed. Gray columns versus red columns compares the presence of SERCA3 immunostaining **(D)** and RyR immunostaining **(G)** in SP-negative (left bars) and SP-positive (right bars) spines. Both the number of SERCA3- versus SERCA3+ as well as RyR- versus RyR+ spines is given in % per standard field (N=41 fields for (D) and 67 fields for (G)). Higher percentage of SERCA3+ and RyR+ spines in the SP+ groups (t-probability ¡0.01 for (D) and ¡0.001 for (G)). **(E)** Specific location of SERCA3 in SP+ dendritic spines. Number of spines is given as percentages of total SP+ and SERCA3+ spines per standard field, which is taken as 100%. Fields are the same as in (D). Schematic representations of SERCA3 and SP puncta "typical" locations are shown on the top of the panel (E). Prevalence of SERCA3 puncta location above the SP puncta or overlapping with it (left and middle bars). **(H)** Location of RyR in SP+ dendritic spines. Again the number of spines is given as percentages when the total SP+ and RyR+ spines per standard field is taken as 100%. Fields are the same as in (G). Schematic representations are shown on the top of the panel (H). Prevalence of RyR puncta located below the SP puncta (right bar). **(I)-(N)**: Distributions of SERCA3 and RyR puncta in dendritic spines of hippocampal neurons from adult mouse brain slices also depend on the presence of synaptopodin puncta. **(I)** and **(L)** C57Bl6 mouse hippocampal neurons infected with AAV-hSynapsin-GFP virus (red color on the left panels and red contour on the right panels) and immunostained against SERCA3 or RyR and Synaptopodin (SP). Representative images show the top head locations of SERCA3 (blue staining in (I)) and basal locations of RyR (blue staining in (L)) in SP occupied dendritic spines (green staining in both (I) and (L)). **(J)** and **(M)** Gray versus red columns compare the presence of SERCA3 or RyR immunostainings in SP-negative (left bars) and SP-positive (right bars) spines. Both numbers of SERCA3- vs SERCA3+ and RyR- vs RyR+ spines are given in % of spines per brain slice (between 7 to 17 fields are analyzed for each sample for a total of 548 and 376 spines analyzed for SERCA3 and RyR conditions respectively). There is significant higher percentage of SERCA3+ and RyR+ spines in the SP+ groups ($p< 0.05$ for both conditions). **(K)** and **(N)** There is a significant prevalence of SERCA3 puncta location above SP puncta and RyR puncta location below SP puncta (One-way ANOVA test with multiple comparison, p¡0.05,). The number of spines is given as percentages of the total SP+ and SERCA3/RyR+ spines. The fields of (K) and (N) are the same as in (J) and (M) respectively. Data of the panels DEGHJKMN are available in S1 Data.

At this stage, we proposed to test the prediction of the model and decided to study the distributions of SERCA3 and RyRs located on dendritic spines containing a synaptopodin puncta revealed by immunostaining (Fig 4.3C-N). We found that SERCA pumps are present in $SP+$ spines and are located predominantly above the SA inside the spine head (Fig 4.3C-E). This is in contrast with the distribution of the RyRs, present in the $SP+$ and mostly located below the SA at the base of the spine neck (Fig 4.3F-H).
In order to confirm these results obtained in vitro, we also analyzed the distributions of SERCA3, RyR and SP in dendritic spines of adult mouse hippocampi. We performed STED super-resolution imaging in immunostained brain sections from mice injected unilaterally in the hippocampus with the AAV-hSynapsin-GFP virus. We confirmed that SERCA pumps and RyRs are enriched in SP+ spines, similar to the observations made in neuronal culture: RyR puncta are preferentially located below SP puncta (Fig 4.3 I-K), while the distribution of SERCA3 puncta revealed that they are mostly positioned above SP (Fig 4.3K-N).
We thus conclude that fast calcium increase at the base of the spine is due to the calcium release from the SA. This release is induced by the opening of RyRs and triggered by the fastest calcium ions traveling from the head to the neck inside the cytoplasm. Finally, this amplification is possible only when RyRs are mostly located at the base of the spine head and the SERCA pumps in the head (see below for the confirmation, when calcium ions are released in the dendrite instead of the head).

4.3.3 Extreme statistic for the fastest ions as a mechanism for activating Ryanodine receptors during calcium transients

To clarify the origin of the fast calcium transient observed at the base of a spine, we studied using modeling and simulations the dynamics of RyR opening when ions are released inside the head (Fig 4.4A). In this stochastic model, a RyR opens when two ions are bound (Fig 4.4B, see also Materials and Methods) and releases calcium ions from SA to the cytoplasm (Fig 4.4B). Stochastic simulations reveal that in the presence of RyRs, the calcium released in the spine head induces a calcium increase at the base within the first $5ms$ (Fig 4.4C). This effect is modulated by the distribution of SERCA pumps, but was clearly due to the presence of RyRs. This result confirms the role of RyRs in generating the fast calcium transient at the base of a spine.

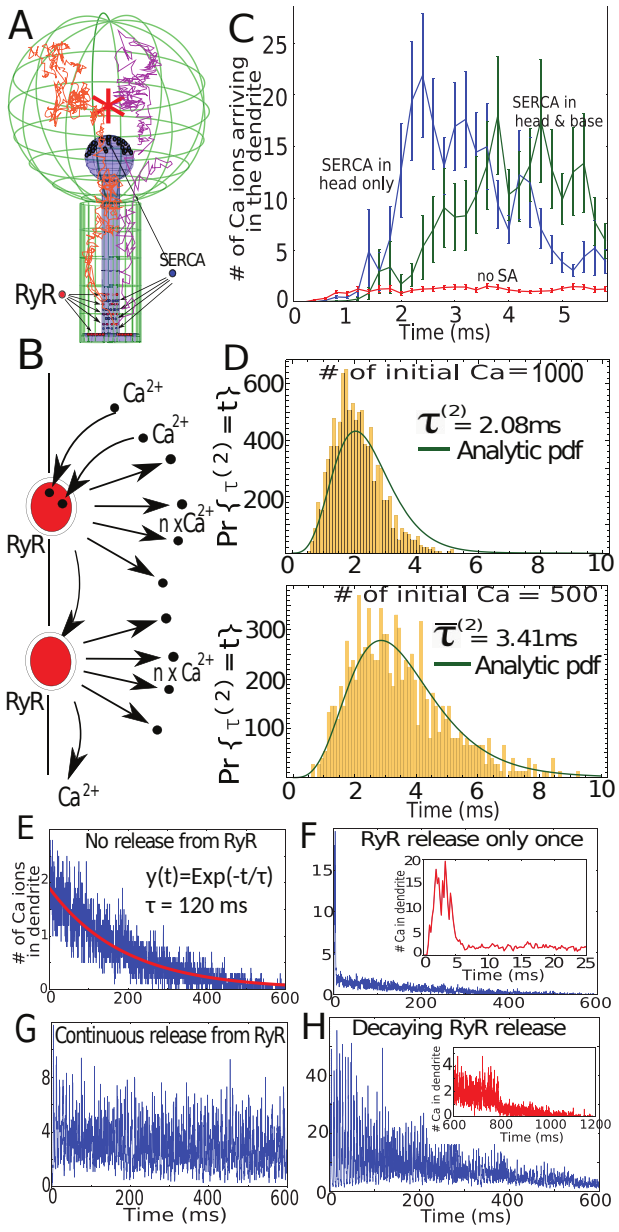

Figure 4.4: **(A)**Representation of calcium trajectories in a spine with ER, where SERCA (blue) are in the head and at the base. Arrangement in four separated layers containing nine of them. RyRs arrangement is described in Fig 4.1H. **(B)** Schematic release of calcium ions from RyR opening, triggered by two calcium ions. **(C)** Dynamics of calcium accumulation in the dendrite in the presence (green) or absence (blue) of SERCA pumps at the base vs dynamics in a spine with no SA (red). **(D)** Arrival times of the two fastest calcium ions that open the first RyR when the initial numbers are $N = 1000$ and $N = 500$, super-imposed with the analytical solution (not a fit) of Eq. 4.5 (see S1 Text). **(E)** Transient calcium ions arriving at the base of the dendrite when no RyRs are present, but with SERCA and calcium pumps. **(F)** Similar to (G) but all RyRs open and release Calcium ions for only once and then deactivated (magnified in the inset). **(G)** Continuous calcium release following two bound ions at RyR (with a refractory period of 6ms). **(H)** Same dynamics as in (G), but the number of calcium released from RyRs is reduced exponentially with time: when RyRs open, n_{Ca} ions are released and the receptor is desensitized for $6ms$. Initially $n_{Ca} = 8$ and decreases exponentially with a time constant of $360ms$.

To assess the time scale of RyR activation, we constructed histograms of the first time $\tau^{(2)}$ to activate RyRs by the binding of two consecutive calcium ions. The distribution of $\tau^{(2)}$ is shown in Fig 4.4D. Interestingly, this distribution depends on the initial number of calcium ions. We computed numerically from the histogram the mean time for the first RyR by the first calcium ions, which is 3.4ms (resp 2.1ms) when 1000 (resp. 500) ions are initially placed in the head. These times are much faster than the mean time for an ion to arrive at the base of a spine, which is of the order of $120ms$ (see Eq 4.1) or the peak distribution of the arrival for a single ion (around 15ms). To conclude, we can now understand that the fast calcium transient at the base of a spine containing an SA can be generated by the fast ion arrival, located in the tail of statistical distribution, which therefore selects the fastest among many Brownian particles.

4.3.4 General theory of extreme statistics for Brownian calcium ions in a cellular microdomain

To further validate the results of stochastic simulations described in the previous section, we computed from the distribution of arrival time for N independent Brownian trajectories (ions) at a small binding site inside a bounded domain Ω. This time is defined by $\tau^1 = \min(t_1, \ldots, t_N)$, where t_i are the arrival times of the N ions. The arrival probability can be computed when the boundary $\partial\Omega$ contains N_R binding sites $\partial\Omega_i \subset \partial\Omega$ so that the total absorbing boundary is $\partial\Omega_a = \bigcup_{i=1}^{N_R} \partial\Omega_i$, and the reflecting part is $\partial\Omega_r = \partial\Omega - \partial\Omega_a$. The probability density function of a Brownian motion is the solution of

$$\begin{aligned} \frac{\partial p(\boldsymbol{x},t)}{\partial t} &= D\Delta p(\boldsymbol{x},t) \quad \text{for } \boldsymbol{x} \in \Omega,\ t > 0 \\ p(\boldsymbol{x},0) &= p_0(\boldsymbol{x}) \quad \text{for } \boldsymbol{x} \in \Omega \\ \frac{\partial p(\boldsymbol{x},t)}{\partial \boldsymbol{n}} &= 0 \quad \text{for } \boldsymbol{x} \in \partial\Omega_r \\ p(\boldsymbol{x},t) &= 0 \quad \text{for } \boldsymbol{x} \in \partial\Omega_a. \end{aligned} \tag{4.2}$$

The survival probability, which is the probability that an ion is still not absorbed at time t is given by

$$\Pr\{t_1 > t\} = \int_\Omega p(\boldsymbol{x},t)\, d\boldsymbol{x}, \tag{4.3}$$

so that $\Pr\{\tau^1 = t\} = \frac{d}{dt}\Pr\{\tau^1 < t\} = N(\Pr\{t_1 > t\})^{N-1}\Pr\{t_1 = t\}$, where $\Pr\{t_1 = t\} = \oint_{\partial\Omega_a} \frac{\partial p(\boldsymbol{x},t)}{\partial \boldsymbol{n}}\, dS_{\boldsymbol{x}}$ and $\Pr\{t_1 = t\} = N_R \oint_{\partial\Omega_1} \frac{\partial p(\boldsymbol{x},t)}{\partial \boldsymbol{n}}\, dS_{\boldsymbol{x}}$. Putting all the above formula

together, we obtain that the distribution for the first particle to arrive is

$$\Pr\{\tau^1 = t\} = NN_R \left[\int_\Omega p(\boldsymbol{x}, t) d\boldsymbol{x} \right]^{N-1} \oint_{\partial\Omega_1} \frac{\partial p(\boldsymbol{x}, t)}{\partial \boldsymbol{n}} dS_{\boldsymbol{x}}, \tag{4.4}$$

and the arrival time $\tau^{(2)}$ for the second ion, which modeled the activation of a RyR, is that of the minimum of the shortest arrival time in the ensemble of $N-1$ trajectories after the first one has arrived and is given by

$$\Pr\{\tau^{(2)} = t\} = \int_0^t \Pr\{\tau^{(2)} = t \,|\, \tau^1 = s\} \left(\int_0^L \Pr\{\boldsymbol{x}_1(s) = x_1\} dx_1 \right)^N \Pr\{\tau^1 = s\} ds. \tag{4.5}$$

We plotted in Fig 4.4D the solution of equation 4.5 where the distribution of arrival time for the first ion $\Pr\{\tau^1 = s\}$ also accounts for the return of the ion located in the neck back to the head (see S1 Text for the complete mathematical derivation). We find that the solution superimposes with the stochastic simulations, confirming the consistency of the stochastic simulations and the theory of the extreme statistics. To conclude, this analytical approach further confirms the role of the fastest ions in setting the time scale of CICR by RyR activation. We observe that the typical shortest path is very close to the shortest geodesic going from the initial position to the RyRs, which is much different compared to the paths associated with the mean arrival time.

4.3.5 Long-time dynamics of calcium induced calcium-release

To further confirm the role of the fastest ions in triggering calcium release, we generated much longer simulations over 600ms (Fig 4.4E-H). In the absence of an SA, we simulate the flux of ions arriving at the dendrite, showing an exponential decay of $\tau = 120ms$ (Fig 4.4E), indeed in agreement with equation 4.1. We note that here there are no extrusion mechanisms such as calcium pumps. To evaluate the impact of the SA, we simulated in Fig 4.4F, a single release event of calcium ions, following RyR activation (5 ions are released per receptors). This release is local and affects only the global decay during the first few milliseconds (insets).

When RyRs are releasing a minimum number of two calcium ions with a refractory period of $6ms$, after a fast transient regime, the ensemble of RyR self-entertains (Fig 4.4G). Indeed, when the SA contains a sufficiently large amount of calcium, the locally released calcium binds to RyRs that open, but the ions disappearing at the base of the spine are not sufficient to prevent this positive feedback loop between calcium and RyRs.

Finally, to account for a local SA calcium depletion, we simulated a decrease in calcium release from the SA, starting from 8 ions per RyR. The decay followed an exponential with a decay time of $360ms$. After $600ms$, the transient regime was completely abolished (Fig 4.4H).

To conclude, the two fastest ions arriving at a single RyR trigger the release of calcium from SA that induces a local calcium release. The time scale of activation depends on the initial number of released calcium ions in the head, which is the signature of an extreme statistics mechanism. This avalanche mechanism is responsible for the fast and large calcium increase at the base of the spine, when ions are diffusing from the head. Thus a release of local calcium ions from RyRs amplify the calcium signal. Furthermore, the calcium transient termination can be attributed to the local SA depletion over a few hundred milliseconds (see S7 Fig).

4.3.6 Asymmetric calcium dynamics between spine and dendrite

To investigate the consequences of RyR distribution on calcium transients, we replicate the experimental protocol described in Fig 4.1B-C with numerical simulations. We ran simulations using the numerical scheme as the one described in Fig 4.1D, with SERCA pumps located on head of the SA, while calcium ions are released at the base of the spine (red star in Fig 4.5A). We tested two RyR distributions: (1) RyRs are only at the base of the neck, as suggested from Fig 4.3F (2) RyRs are located also in the spine head.

We find that adding RyRs only at the base already increases significantly the calcium transient in the spine head (blue vs green, Fig 4.5A). If in addition, RyRs are added in the head, the calcium transient in the head is further increased (red versus blue). However when calcium ions are released at the base and measured in the head, calcium transient in the head is not amplified as showed by our experimental findings (Fig 4.1B-C). Therefore, these stochastic simulations agree with the immunostaining results of Fig 4.3F, suggesting that there should be no RyRs in the spine head. We note however that there is a small difference between the result of our simulations (small increase in the calcium in the head) and the calcium uncaging experiments inside the dendrite, which show in the absence and the presence of a SA, only a slight increase of calcium in the head. This difference suggests that removal mechanisms, such as calcium pumps could be located at the base of the spine, leading to a removal of the fraction of the calcium ions entering the spine versus the one flowing directly. To conclude, the asymmetric distributions of the RyRs contribute to the asymmetry of calcium transmission.

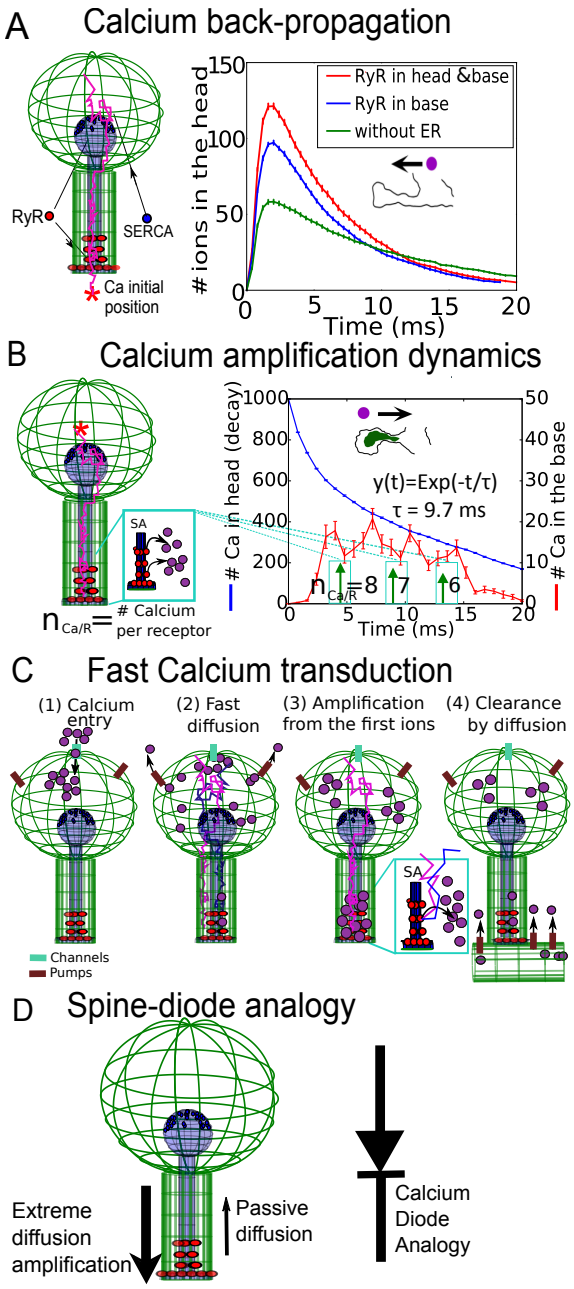

Figure 4.5: **(A) Left:** Schematic representation of spine with SERCA pumps in the head and 36 RyRs placed in the head (18) and the neck (18). Calcium ions are released in the dendrite (red star). **Right:** Simulation of calcium transient in the head in the absence of a SA (green), when RyRs are present in both neck and head (red) and only in the neck (blue). **(B)** Stochastic simulations of calcium transient when taking into account SA depletion: RyRs are releasing with a delay of $0.25ms$, initially 8, 7 and finally 6 ions with an averaged time indicated by the green arrows. The RyR refractory period is 3ms. (see also S6 Fig) **(C)** Summary of the calcium diffusion-amplification in a dendritic spine with a SA. **(D)** Diode representation of a spine with an SA.

At this stage, we could not access the calcium dynamics inside the ER. However, it could have a drastic consequence on the calcium transient, as shown in Fig 4.4E-H (see also S7 Fig, where we varied the RyR cluster location and restricted calcium concentration in the ER). We thus decided to use the calcium transient signal (Fig 4.1B red curve) to recover the local SA depletion at a time scale of $20ms$ following calcium release. We had to slightly modify the values of the parameters as now described: we released consecutively 8, 7 and then 6 ions per RyR with a refractory period of 3ms between each release (see also S6 Fig). In that case, we could recover the transient kinetics observed experimentally (Fig 4.5B red). We remark that the decay from 8, 7 to 6 ions accounts for the limited amount of available calcium in the ER, which is slowly depleting following consecutive release. The calcium ions were released with a delay of 0.25ms after the arrival of a second ion to the RyR binding site. This delay was introduced to account for the reduction of the increase during CICR. We calibrated this delay to account for the experimental time scale. Finally, the refractory period of 3ms after each release was estimated based on the experimental CICR transient (Fig 4.1B, Left). To conclude, each one of the RyR parameter was optimized using the physiological condition of the calcium transient. This adjustment of parameters reveals a small calcium depletion inside the SA during calcium transient before the SA is depleted in calcium ions. This effect should be considered as a possible prediction of the model.
We also found here that calcium release from the RyRs is delayed by $0.25ms$ following the binding of two calcium ions. These results give us an indication of the SA depletion time scale, which is probably at a few tens of milliseconds. Putting the present results together, we describe a novel diffusion-amplification calcium transduction in spine containing a SA (see Fig 4.5C) and that the SA plays the role of a diode, amplifying ion transmission from the head to the dendrite, but not in the opposite direction (Fig 4.5C).

4.4 Discussion

In the present study, we investigated how SA influences calcium transient inside dendritic spines. We found that calcium increases at the dendrite following uncaging in the head occurs in a few millisecond time scale. As shown here, this property can be explained by the statistics of the fastest calcium ions, without the need of considering electro-diffusion [118, 136, 137]. The fastest arriving ions open RyRs located at the base of the spine neck, which generate an avalanche through a CICR from SA. This local avalanche leads to an accelerated amplification of the calcium signal before the remaining ions diffuse from the head. Previously, RyRs were shown to contribute to calcium transients in the spine's cytosol [129] in the context of back-propagating action potentials.
Furthermore, the comparison of stochastic simulations with the experimental calcium transient constraints the number of ions released by the opening of RyRs: indeed we find that releasing a 3 to 8 ions each time one of the 36 RyRs opens gives us a range of concentrations for experimental observations. Interestingly, we could recapitulate the decrease of released calcium by decreasing the released number from 8 to 6 one-by-one, occurring

once in a few milliseconds (Fig 4.5B). The distribution of RyRs has little influence on the calcium transient, as long as their inter-distances are less than few tens of nanometers (see also S5 Fig). Note that we used here a minimum number of released calcium per RyR, but it is conceivable that more ions are indeed released. It would be quite interesting to obtain a direct measurement for the number of RyRs and the concentration of calcium release from RyRs located on the SA, but also estimations of other parameters predicted by the present model such as the delay of calcium flux after activation and refractory periods.

Role of extreme statistics in molecular transduction in nanodomains

As RyRs are activated by the two fastest ions that arrive to the binding sites, the physical separation of the initial calcium release in the spine head and the location of RyRs in the base is compensated by the redundancy based on the large initial number of released ions. The time scale induced by the fastest ions depends on the logarithm of initial ion number and the length of the direct ray starting from the source and ending at the target [80].
The time scale generated by the fastest particle or ions is generic and can occur in many molecular transduction pathways where there is a separation between the initial source and a second step that consists of amplifying the signal [95]. This is the case for second messengers such as IP3 [138], G-protein coupled receptors [7] and modulation of the inner hair cell voltage by CICR [139]. This time scale is very different from the Narrow Escape Time [41] phenomena, where the time scale depends on the volume of the domain. We conclude that the statistics of the fastest particle compensates for long distances (limiting the importance of the neck length in calcium transmission, see S8 Fig) and the key modulating parameter is the number of initial ions.

Can Voltage-Gated-Calcium-Channels contribute to fast calcium transient at the spine base?

Neuronal depolarization activates Voltage-Gated-calcium-channels (VGCCs) that results in calcium entry. In principle, calcium ions could enter in dendritic spines through VGCCs. However, little is known about their localization and whether or not they are present in the head of spines, despite some studies reporting 1 to 20 channels [13]. No significant local effect of VGCCs was found to contribute to synaptic depolarization and the amplitude of Ca2+transients induced by excitatory postsynaptic potential seems to be regulated independent of VGCCs, as discussed in [140].
Under the hypothesis that VCGGs are located in the spine head, they would simply increase the number of initial calcium ions in the head, but will not be implicated in accelerating a local transient at the base of the spine. If VGCCs are positioned on the membrane opposed to the RyRs located at the base, then a sufficient depolarization in the spine head would be needed, first to pass the high neck voltage drop and second

to activate VGCCs during synaptic activity. This scenario is unlikely, but it can exist independently of the extreme statistics diffusion that we have studied here. However our glutamate and calcium uncaging experiments indicate that fast calcium increase at the base of a spine is unlikely to result from VGCC activation upon synaptic depolarization as there would be no time delay compared to the calcium appearance in spine head, contrary to what we observe. To conclude, at this stage, we cannot rule out that in short spines, characterized by a low neck resistance, RyRs open due to a sufficiently high membrane depolarization generated in the spine head. This scenario should be further investigated and may be relevant for short spines.

Spontaneous calcium release from residual calcium

In dendrites, many buffers, ER-mitochondria interaction, calcium pumps, maintain the intracellular calcium at low concentration [105], but this concentration is subject to constant fluctuations. Small local fluctuations in the intracellular calcium concentration could result in spontaneous regenerative release events at the ER. In the model developed here, we wanted to estimate the rate of spontaneous regenerative release events. We use that two calcium ions are necessary to trigger off a regenerative release from the surrounding cluster of RyRs, as long as the ER contains a sufficient among of calcium ions. We recall that the distribution of residual calcium concentrations was found in neurons to be heterogenous varying in the range [10-60]nM [141].

How residual calcium activates CICR from RYRs? In a well mixed dendritic subcompartment, the distribution of arrival time of an ion to a small channel site is Poissonian, described by $P_1(t) = \lambda e^{-\lambda t}$, where the rate λ is the reciprocal of the mean first arrival time of a diffusing ion to a channel site [41]. The distribution of arrival times for two ions is computed as the convolution of the arrival time of the first with the second ion, leading to $P_2(t) = \lambda^2 t e^{-\lambda t}$.

The mean time for the residual calcium to activate RyRs is equal to the mean time for two ions to find a target site, given by $\bar{\tau} = \int_0^\infty t P_2(t) dt = \frac{2}{\lambda}$. When there are N ions uniformly distributed in a subdendritic compartment, the mean duration between two calcium fluctuation events is thus the mean arrival time for two ions, chosen among N, that is $N(N-1)/2$. We conclude that the mean time between two calcium release events when there are N ions is approximated by $\bar{\tau}_N = [2/N(N-1)]\bar{\tau}$, where $1/\lambda = 100/(4Da) = 500s$, where $V = 100\mu m^3$, $D = 20\mu m^2/s$ [142] and $a = 10nm$. For a residual calcium concentration of $50nM$, the residual number of calcium is $N \approx 30$ calcium and a mean duration between two consecutive calcium release events of the order of $\bar{\tau}_N \approx 1s$. This calcium increase is due to CICR from RyRs induced from the diffusion of residual calcium ions in the dendrite. When RyRs are hidden, this time between two spontaneous events could be exponentially longer [41], of the order of tens of seconds. To conclude, we found a time scale of calcium fluctuation of the order of few seconds when calcium ions are uniformly distributed at low concentration in dendrites $< 50nM$ [141]. If calcium ions are not uniformly distributed (out of equilibrium), a different approach should be considered.

The residual calcium concentration is maintained low due to various types of calcium buffers, the presence of mitochondria below the spine neck, that could also regulate calcium concentration. How these processes do maintain calcium locally low should certainly be further investigated.

Consequences of amplifying calcium concentration at the base of a dendritic spine

What could be the role of calcium signal amplification induced by SA release at the base of a dendritic spine and not in the head? The asymmetry of RyR localization is a key feature in this difference, leaving the head compartment separated from the rest of the dendrite. Amplifying calcium at the base could favor receptor trafficking by influencing the delivery of AMPA receptors to dendritic spines. Successive calcium accumulative events leading to SA refilling could trigger a massive release, while a depleted SA would only lead to a small release, suggesting an integrating role of the SA. Experimental evidences [143] further suggest that gating of the RyRs is also modulated by the luminal calcium concentration fluctuations while the release can diminish when calcium is bound to buffers such as calsequestrin [144]. Another consequence of amplifying locally the calcium concentration at the ER is to trigger the production of ATP from nearby mitochondria [108]. Indeed, inducing ATP production requires that the calcium concentration reaches a threshold of $10\mu M$.
We studied here a time scale of a few to 20 milliseconds. For longer durations, other mechanisms such as secondary messenger involving IP3 receptors [138] or the ORAI1 pathways [31] involved in SA replenishment can contribute to calcium concentration regulation. Future models should also incorporate the cycle of SA calcium, depletion using the ORAI1 pathways and the calcium uptake at the base of the spine by mitochondria [145].

Acknowledgements

We thank P. Ezan for excellent technical assistance.

Chapter 5

Supplementary information: Fast calcium transients in dendritic spines driven by extreme statistics

Mathematical derivations of arrival times of the first and second ions

In this section, we derive the distribution of the first and second arrival time of the calcium ions released from the head and arriving to a single RyR. These expressions are then used in Fig 3D (main text) to compare the PDFs obtained analytically against Brownian simulation results.

During the Brownian motion inside a dendritic spine, calcium ions can be absorbed at the dendritic shaft, or they can return to the head after crossing into the neck any number of times. The pdf of no return can be computed by decomposing the total time (τ) as the sum of the time to reach the small window at the head-neck junction (τ^1) and the time spent in the spine neck (τ^2). The pdf of both times can be computed separately. According to the narrow escape theory [41], the distribution of arrival time of a Brownian particle at the entrance of the dendritic neck is Poissonian,

$$\Pr\{\tau^1 = s\} = \gamma e^{-\gamma s}, \tag{5.1}$$

where

$$\gamma^{-1} = \frac{|\Omega|}{4aD\left[1 + \frac{L(\mathbf{0}) + N(\mathbf{0})}{2\pi}\, a\log a + o(a\log a)\right]},$$

with $|\Omega|$ the volume of the spherical head, while a is the radius of the cylindrical neck [41] and $L(0)$ and $N(0)$ are the principal mean curvatures.
After the first particles reaches the cylinder (spine neck), we approximate its Brownian

motion in the cylindrical domain by one-dimensional motion (1D). The pdf of arrival time of a Brownian particle to the end of an interval of length L is

$$\Pr\{\tau_2 = t - s\} = \sum_{n=0}^{\infty} (-1)^n \lambda_n e^{-D\lambda_n^2 (t-s)}, \tag{5.2}$$

where the eigenvalues are

$$\lambda_n = \frac{\pi}{L}\left(n + \frac{1}{2}\right). \tag{5.3}$$

We can now compute the pdf of the total time τ:

$$\begin{aligned}
\Pr\{\tau_1 + \tau_2 = t\} &= \int_0^t \Pr\{\tau_2 = t - s | \tau_1 = s\} \Pr\{\tau_1 = s\} ds & (5.4)\\
&= \gamma \int_0^t e^{-\gamma s} \sum_{n=0}^{\infty} (-1)^n \lambda_n e^{-D\lambda_n^2 (t-s)} ds & (5.5)\\
&= \gamma \sum_{n=0}^{\infty} (-1)^n \left[\frac{e^{-D\lambda_n^2 t} - e^{-\gamma t}}{\gamma - D\lambda_n^2}\right]. & (5.6)
\end{aligned}$$

This is the pdf of a Brownian particle's the arrival time at the base of a spine. This is a process with two timescales: one is dictated by diffusion and the other is Poissonian.
To compute the pdf of the shortest escape time τ^a with returns, that is the when a particle can return inside the head, we use Bayes' law for the escape density, conditioned on any number of returns, given by

$$\Pr\{\tau^a = t\} = \sum_{k=0}^{\infty} \Pr\{\tau^a = t | k\} \Pr\{k\}, \tag{5.7}$$

where $\Pr\{k\} = \frac{1}{2^k}$ is the probability that the particle returns k times to the head. The particle hits the stochastic separatrix [72] and then returns to the head, before reaching the dendrite. The probability of the escape, conditioned on k returns, $\Pr\{\tau^a = t|k\}$, can be computed from the successive arrivals times to the stochastic separatrix, $\tau_1, ..\tau_k$, so that

$$\Pr\{\tau^a = t|k\} = \Pr\{\tau_1 + .. + \tau_k = t\}. \tag{5.8}$$

Assuming that the arrival time to the stochastic separatrix is Poissonian with rate λ_S [41], we obtain that

$$\Pr\{\tau_1 + .. + \tau_k = t\} = \lambda_S \int_0^t \frac{(\lambda_S s)^{n-1}}{(n-1)!} f(t-s)\, ds, \tag{5.9}$$

where $f(t)$ is the pdf of the time to escape the head entering the neck and returning to the head which we approximated by 5.4. Therefore,

$$\Pr\{\tau^a = t\} = \frac{1}{2}f(t) + \sum_{n=1}^{\infty} \int_0^t \lambda_S \frac{(\lambda_S s)^{n-1}}{(n-1)!} f(t-s)ds \frac{1}{2^k}. \tag{5.10}$$

Finally,

$$\Pr\{\tau^a = t\} = \frac{1}{2}f(t) + \int_0^t \exp(-\lambda_S s/2) f(t-s)ds, \tag{5.11}$$

Expression (5.4) with $\lambda_S = \gamma$ gives the final expression for the pdf of the escape time

$$\begin{aligned} f_{return}(t) &= \Pr\{\tau^a = t\} \qquad (5.12) \\ &= \frac{1}{2}f(t) + \gamma \sum_{n=0}^{\infty} (-1)^n \frac{\lambda_n \gamma^2}{4(\gamma - D\lambda_n^2)} \left[\frac{e^{-\gamma t/2} - e^{-\gamma t}}{\gamma/2} - \frac{e^{-\gamma/2t} - e^{-D\lambda_n^2 t}}{D\lambda_n^2 - \gamma} \right]. \end{aligned}$$

The maximum of f_{return} is achieved at the point $t_{max} \approx \frac{2}{\gamma}\log 2$. The pdfs of the first and second arrivals are thus given by

$$\begin{aligned} f_{min}^{(1)}(t) &= \Pr\{\tau = min(t_1, \ldots, t_N) = t\} \\ &= N \left(1 - \int_0^t f_{return}(s)ds \right)^{N-1} f_{return}(t). \end{aligned}$$

In the Poissonian approximation, the pdf of the arrival time $\tau^{(2)}$ of the second fastest particle is given by

$$f_{min}^{(2)}(t) = \Pr\{\tau^{(2)} = t\} = N \int_0^t f_{min}^{(1)}(t-s) f_{min}^{(1)}(s)ds. \tag{5.13}$$

The pdfs of the fastest and second fastest arrival times are computed from equation (5.12). We used expression 5.13 to compare this analytical result and the Brownian simulations in Fig 4B of the main text.

Calibrating the model for the number of Calcium pumps located in the spine head.

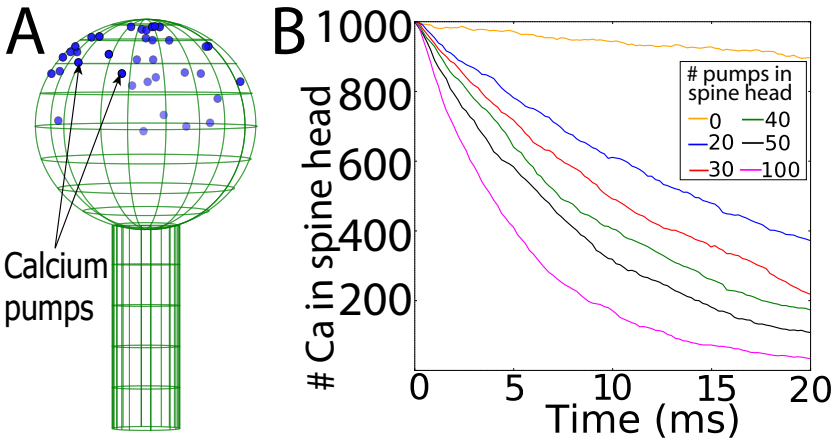

Figure S1: **(A)** Simulation with calcium pumps uniformly distributed on the upper hemisphere of the spine surface. No SA is present (no contributions from RyRs and SERCA pumps). **(B)** Transient decay of the calcium number in the spine head (pumps are arranged as in (A)) when the number of pumps varies between N=0 to N=100 (the initial number of calcium ions is 1000). We confirmed that N=50 provides a matching approximation to the timescales that were obtained from calcium transient experiments. Therefore, we chose the value N=50 for the remaining simulations.

Calcium-dependent operation of RyRs

RyRs have been modeled in the past in the continuum limit description, as a boundary condition of the reaction-diffusion equation [146]. However this condition cannot be used here in a stochastic approach. Instead, RyR opens in our stochastic simulations when 2 ions arrives at the catchment area of the receptor, which is a disk of radius $a = 10nm$. This radius is comparable to the size revealed by crystallography studies [147, 148]. Fluctuations in the radius $a = 10nm$ are not expected to affect much the arrival time as shown by the formula for the first arrival, where the dependency in the radius a occurs through a log term, as shown analytically [80].

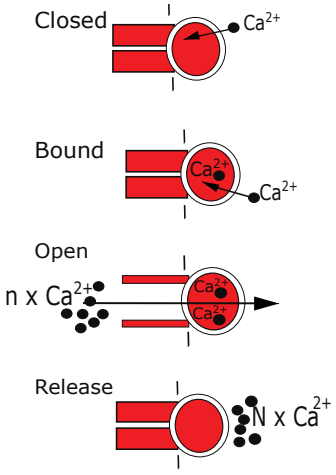

Figure S2: For simulating the RyR activity, we implemented the stochastic model [149]: when a first ion arrives from the cytoplasm, it is indefinitely bound to the RyR. When the second ion arrives at the same receptor, it opens the RyR, resulting an outflux of fixed number of calcium ions n_{Ca} (typically, n_{Ca}=2 to 8, as mentioned in the figures of the main text) from the SA calcium stores to the cytosolic side of the spine.

The number of released ions depends on the calcium concentration of ER and cytoplasm. Due to the unavailability of these values in literature, we used a total number of released ions from tens to few hundreds. These numbers are compatible with classical experiments where CICR leads to a fluctuation of calcium concentration with a magnitude of 100nM [150]. A change of 100nM is equivalent to 250 calcium ions in a volume of the size of the spine head. We assumed here that ER contains a sufficiently large amount of calcium ions and thus when around 300 ions are released though 36 receptors, we release around 8 ions per receptor. This number can decrease to zero when the ER does not contain calcium ions. Future research should investigate these predictions.

RyR release is instantaneous, except in Fig 4B where we found upon testing several delays that a 0.25ms delay is necessary for the simulations to agree with experimental calcium transient. The released calcium ions are placed at the center of the RyRs. This release is followed by a refractory period of a few milliseconds, as shown in each figure. If further ions arrive during this period, the receptor can bind maximum to one more (third) calcium ion. This situation corresponds to the third binding site proposed in [151]. For subsequent arrivals ($n > 3$), the receptor acts as a reflecting boundary.

We arrange 36 RyRs at the base of the SA such that a third (12) of receptors is present on the top of the shaft, while the remaining two thirds (24) are distributed in four layers, each containing randomly-distributed six channels (Fig 2G).

Calcium-dependent operation of SERCA pumps

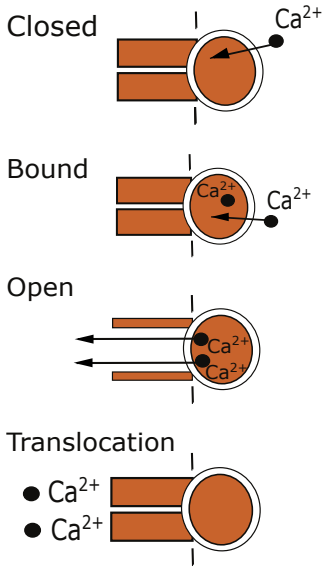

Figure S3: We considered that calcium flow through SERCA pumps is unidirectional from the cytoplasmic side to the SA [152]. The pumps are opened by the arrival of two calcium ions to its binding sites from the cytoplasmic side [153]. Such opening event can translocate both calcium ions into the ER (luminal side). We modeled SERCA pumps as absorbing disks with a radius of 10nm [54] with the precise operation as follows:

1. When the first calcium ion arrives at the circular disk of a pump from the cytoplasmic side, it is bound and retained for an indefinite time.

2. When a second ion arrives at the SERCA pump from the cytoplasmic side, after binding of the first ion, the pump opens and both ions are moved into the SA.

3. SERCA translocation time $\tau_{SER,TL} \approx 100ms$ is in the range of several hundred milliseconds [154], much longer than the total duration of our simulations which ran $\approx$ 20ms. Therefore, we consider the two ions to be indefinitely bound to the SERCA pump during the remaining duration of the simulation and no longer able to return to the spine.

4. A SERCA pump is prevented from uptaking ions after the second ions is bound (step 2) and it is modeled in the simulation as a reflecting disk.

Comparison of calcium transmission rates between SP+ve and SP−ve spines

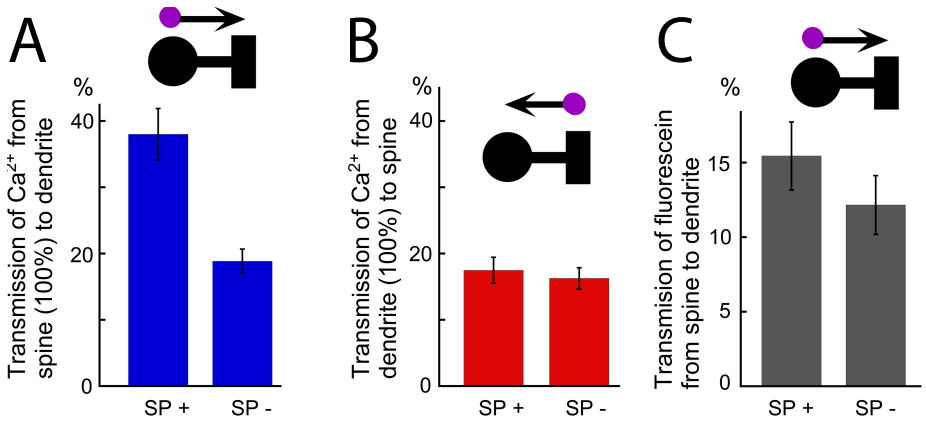

Figure S4: The Calcium signal transmissions during uncaging experiments were compared as measurements from the focus of uncaging to the neighboring compartment, and the peak signal at uncaging is taken as 100%. **(A)** Transmission from the spine head to the dendrite and **(B)** from dendrite to the spine head. Left and right bars are the averaged transmission measures of SP+ and SP− spines. The focus of uncaging is marked with purple dot and the arrow indicates the possible signaling direction between the two compartments. Note much higher transmission rate from the head of SP+ spines to the dendrite, compared to dendrite to spine transmission (A: t probability ¡ 0.0001). The rate of transmission in both directions for the SP- spine is the same (B: t-probability 0.6). Here the number of spines is $N = 3$ for SP+ and 7 for SP−. This result confirms that the presence of a spine apparatus is critical for an effective uni-directional calcium flow in the spine. **(C)** In a set of control experiments, NP-EGTA was replaced with caged fluorescein, a biologically neutral molecule that becomes fluorescent only after its flash photolysis. The rate of transmission from spine head of SP+ and SP- spines to their parent dendrites in this case had no significant statistical difference, while the lengths of the spines were approximately the same length as in A & B. The slightly smaller percentages found for fluorescein here (compared to calcium in A & B) can probably be attributed to the larger mass of fluorescein molecules.

Impact of inter-RyR distance on calcium induced calcium release.

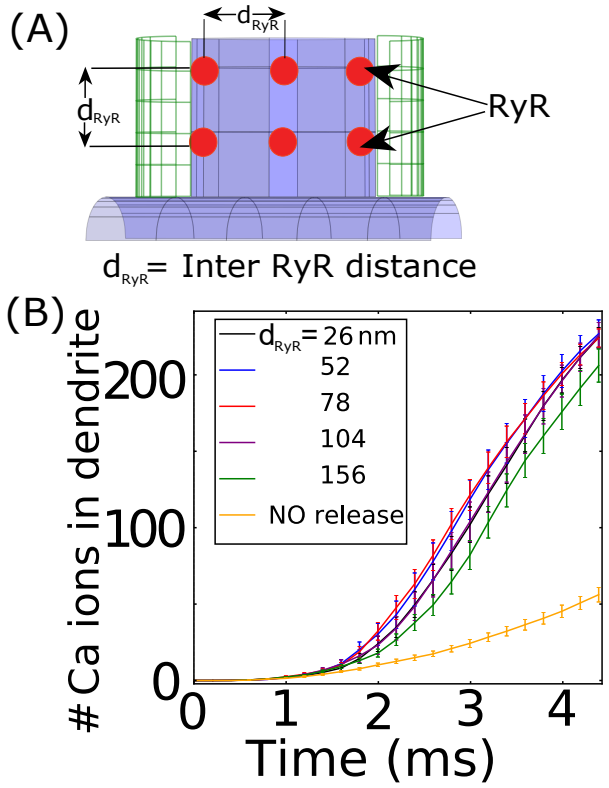

Figure S5: **(A)** 20 RyRs are positioned at the base of the ER neck surface and arranged in a grid with an inter-RyR distance (d_{RyR}), between 26 to 156nm. **(B)** 1000 calcium ions are released from the center of the spine head and we estimated from numerical simulations the cumulative sum of calcium ions arriving in the base of the dendrite (similar to Fig 2A & B), compared to the control (orange), where no calcium ions are released from the RyRs, but can only arrive from the head. There is a slight reduction in the number of calcium arriving at the base only when the inter-RyR distance d_{RyR} was increased to 156nm. Therefore, we confirm that in the range of the present simulations, the reported amplifications of calcium signal do not depend on the distance among neighboring RyRs.

Dependency of CICR on ER calcium concentration

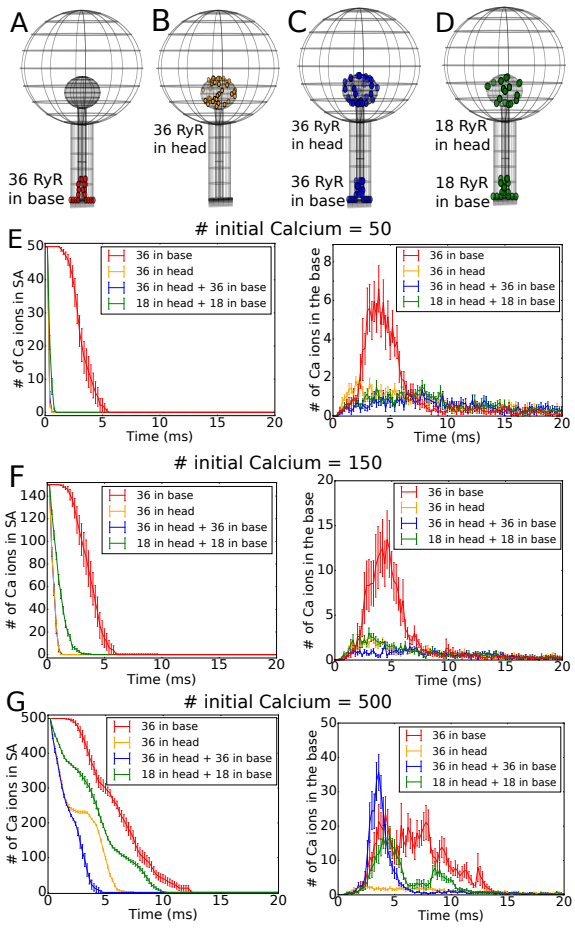

Figure S6: Calcium concentration in the SA decays with each RyR opening. We tested four configurations of RyR positioning (**(A)-(D)** and three different initial # of calcium in the SA N=50, 150 and 500 (**(E)-(G)**. (Initially calcium is at the center of the spine head, similar to Fig 1D and each curve was obtained using 20 runs). When there is a smaller number of calcium (50 or 150), the increase at the base is limited to the case when RyRs are only at the base of the SA (Red curves). Calcium decay in the SA (left plots) shows that this is due to the RyRs located in the SA head being triggered too quickly by the calcium ions arriving from the nearby uncaging spot, leading to a fast drop in calcium concentration in the SA. This release leaves SA with insufficient calcium to generate a large CICR response when ions arrive at the base, therefore calcium at the base is limited to the few ions arriving from the head. In that case, the amplification is almost abolished (flat curves). This confirm our experimental and simulation results (Fig 3 Main Text) showing that the calcium response is amplified at the base only when RyRs are located at this particular place. When there is enough calcium (N=500 ions in G), having RyRs lead to ER calcium depletion, but there is still enough calcium in the SA to elicit a response at the base (blue and green). However, the optimal positioning of RyRs to trigger the strongest response is at the base (red curve). We conclude that for the compatibility between glutamate & calcium uncaging experiments and stochastic simulations with limited and unlimited calcium an enriched RyR distribution is required at the base of spines.

Release dynamics from RyRs induced by cytoplasmic calcium ions

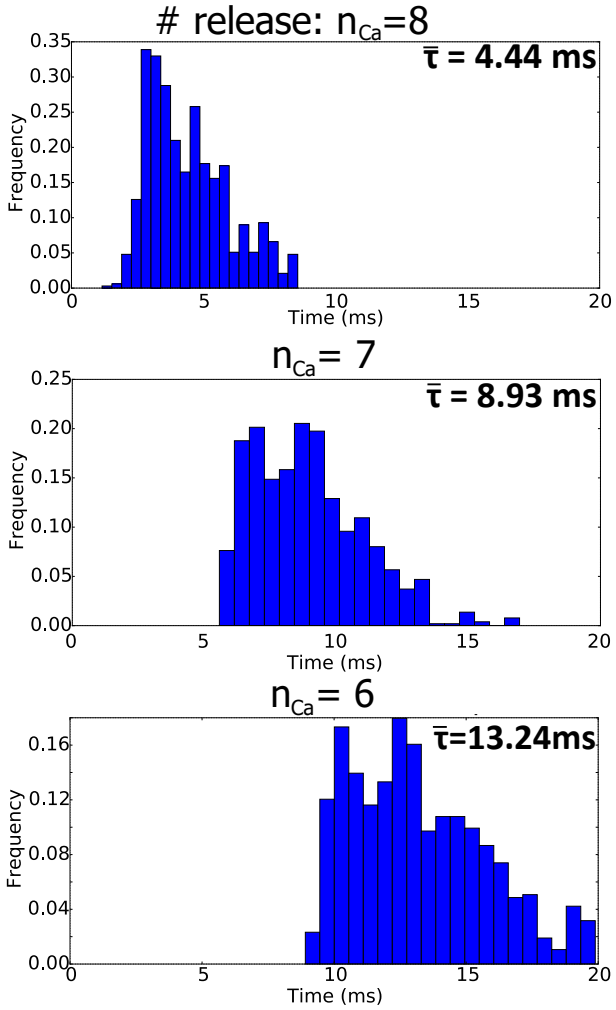

Figure S7: Histograms of the release times of RyRs in the three consecutive release events shown in Fig 4B. The number of release ions decrease starting from N_{Ca} =8, then to 7 and finally to 6. (36 RyR receptors are positioned on the SA and 25 trials were run). The interval between each release is 3ms, and after two calcium ions have arrived, it takes 0.25ms for a RyR to open and release RyR. We conclude that calcium release occurs in wave packets, with each release leading to the release of new ions that can open the neighbouring RyRs and thus leading to calcium-induced calcium release. Moreover, this simulation confirmed that all RyRs do participate to this process, regardless of the distances among them. The mean release times $\bar{\tau}$ shown in Fig 4B (green arrows) were evaluated using these three histograms.

Dependence of Extreme statistics mechanism on the length of spine necks.

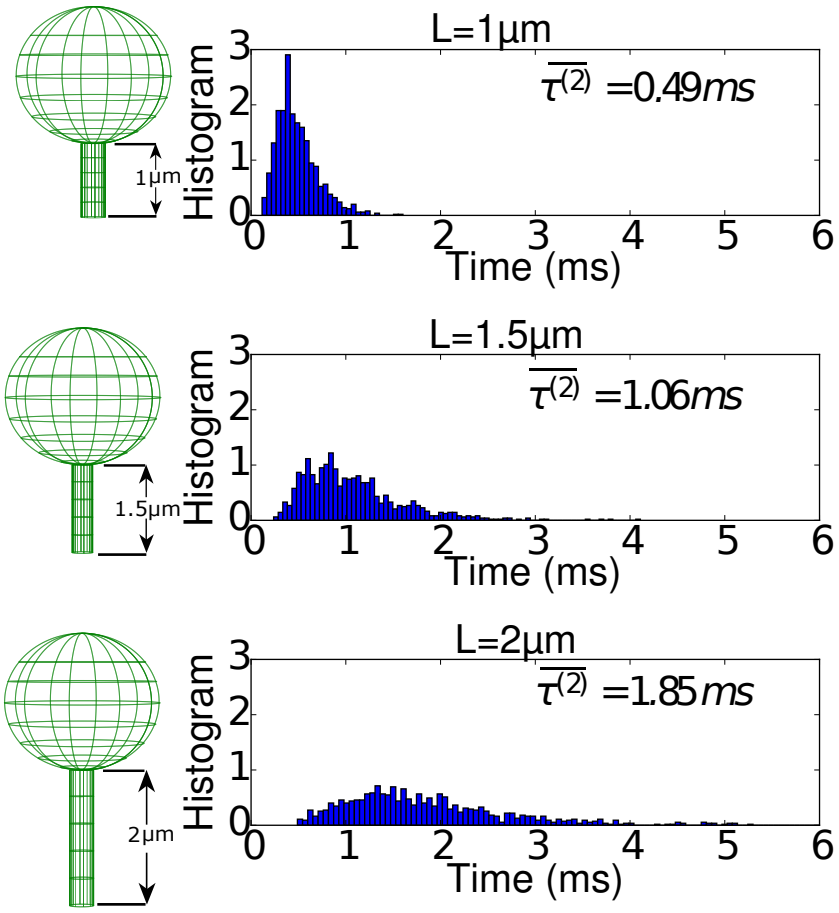

Figure S8: Arrival time distributions for three different spine neck lengths (L=1μm, 1.5μm and 2μm), modeled as a one dimensional segment with a reflecting boundary at the origin x=0 and absorption at x=L. Here N=5 ions were used to match the very small number of ions that escapes the spine head and remains in the neck during the first few milliseconds. The mean arrival times for the first two ions in the three neck lengths are 0.49ms, 1.06ms and 1.85ms, confirming that uncaging location and the spine neck length have little impact on the time course of calcium release from the ER. These simulations confirm the associated experimental results in dendritic spine, based on glutamate uncaging [44]. In general three dimensional geometry, trajectories associated to the fastest particles are concentrated near the shortest path, therefore changing the initial calcium injection location within the spine head does not change much the delay of calcium induced calcium release [100]

Table S1: **Parameters for calcium transient**

Parameters	Symbols	Values
Time step	Δt	10^{-7} s
Diffusion	D	600 $\mu m^2 s^{-1}$ [37]
Initial number of calcium ions	N	1000
Spine head radius	R	1 μm
Spine neck radius	a	0.15 μm
Spine neck length	L	1.5 μm
SA head radius	R_{SA}	0.25 μm
SA neck length	L_{SA}	1.5 μm
SA neck radius	a_{SA}	0.05 μm
Spine head-SA head center distance	l	0.5 μm
Radius (RyR and SERCA)	a_{RyR}, a_{SERCA}	10 nm
# SERCA pumps in the SA head		36
# ions absorbed by one SERCA		2
# RyR in the SA base		36
# ions to activate one RyR		2
# calcium released from one RyR	n_{Ca}	varies (2-8)
# calcium released from one RyR	$\tau_{SER,TL}$	∞

Table S2: **Number of trials for numerical simulation results**

Figure	Values
Fig 1E	16
Fig 2B	25
Fig 3C	25
Fig 3D N=500 & N=1000	750 & 1500
Fig 3E	10
Fig 3F	25
Fig 3G	10
Fig 3H	15
Fig 4A	20
Fig 4B	25
Fig S4B	25

Chapter 6

Nanoscale molecular architecture controls calcium diffusion and ER replenishment in dendritic spines

Published as: **Basnayake, K.**, Mazaud, D., Kushnivera, L., Rouach, N., Korkotian, E. & Holcman, D. (2021) Nanoscale molecular architecture controls calcium diffusion and ER replenishment in dendritic spines. *Science Advances*, 7(38): eabh1376 https://doi.org/10.1126/sciadv.abh1376

Abstract: Dendritic spines are critical components of neuronal synapses as they receive and transform synaptic inputs into a succession of calcium-regulated biochemical events. The spine apparatus (SA), an extension of smooth endoplasmic reticulum, regulates slow and fast calcium dynamics in spines. Calcium release events deplete SA calcium ion reservoir rapidly, yet the next cycle of signaling requires its replenishment. How spines achieve this replenishment without triggering calcium release remains unclear. Using computational modeling, calcium and STED superresolution imaging, we show that the SA replenishment involves the store-operated calcium entry pathway during spontaneous calcium transients. We identified two main conditions for SA replenishment without depletion: a small amplitude and a slow timescale for calcium influx, and a close proximity between SA and plasma membranes. Thereby, spine's nanoscale organization separates SA replenishment from depletion. We further conclude that spine's receptor organization also determines the calcium dynamics during the induction of long-term synaptic changes.

Introduction

Dendritic spines are cellular protrusions found on the surface of dendrites that function as a postsynaptic component of the neuronal synapse. Morphologically, spines commonly include two distinct features, a spine head and a spine neck, with the head engaging the presynaptic axon and the neck connecting the head with the postsynaptic dendrite.

The size and shape of a spine (as well as the number of spines on a dendrite) are dynamic, plastic, and change in response to repeated synaptic activity, which directly affects synaptic plasticity and is therefore critical for processes such as learning and memory [104,105,155,156]. Moreover, changes in shape, distribution, loss, and gain of dendritic spines have been associated with a range of human diseases, although the mechanisms remain incompletely understood [157,158]. Functionally, dendritic spines are sites of intense biochemical activity, whereby signals received from the synapse via glutamate receptors [such as N-methyl-D-aspartate receptors (NMDARs) and AMPA receptors (AMPARs)] lead to influx of the main second messenger, calcium ions (Ca^{2+}). Although a single receptor activation event produces transient calcium influx, repeated activation of the receptor leads to rapid build-up of calcium concentration, resulting in calcium binding to buffers such as calmodulin (CaM), a calcium sensor protein, and subsequent biochemical activation of CaM-dependent protein kinase II (CaMKII) and subsequent downstream signaling [159]. In general, high calcium concentrations in spines are associated with long-term potentiation (LTP), while low calcium is associated with long term depression (LTD) [43]. Thus, calcium dynamics in dendritic spines emerged as a key mechanism for the induction of synaptic plasticity in neurons. Calcium concentration in dendritic spines is tightly regulated [115,126,160] by the amplitude and timing of the influx through the receptors, binding and unbinding with proteins, buffers and pumps, and also by organelles that could sequester or release calcium, such as endoplasmic reticulum (ER) and an extension of smooth ER called spine apparatus (SA) that spans spine head and neck [13, 105, 123, 125].

The SA is involved in multiple signaling functions such as calcium regulation, protein synthesis and cell apoptosis, and the absence of the SA results in a reduction of hippocampal LTP in the CA1 region and an impairment of spatial learning [18]. In addition, SA facilitates calcium-induced calcium release (CICR) process through which calcium ions that entered dendritic spine due to synaptic activity cause release of additional calcium from intracellular calcium stores. The timing of CICR activation, on the order of a few tens of milliseconds, is governed by the fastest calcium ions arriving by diffusion at a ryanodine receptor (RyR) present mostly as clusters at the base of spines [42] and also involves sarco/ER Ca^{2+}-Adenosine triphospate (SERCA) [44]. Therefore, calcium concentration increase in a spine head due to a synaptic stimulation is followed by a pronounced depletion of SA calcium reservoir within less than tens of milliseconds due to this avalanche phenomenon at the base of the spine. Whereas CICR calcium dynamics and flux in spines have been extensively studied, mechanisms that govern calcium store replenishment in SA are still imperfectly understood.

Recently, store-operated calcium entry (SOCE), mediated by STIM1 (stromal interaction molecule 1)-ORAI1 (Calcium Release-Activated Calcium Modulator 1) channel complex, has been implicated as important for the replenishment process in SA [122,161]. Calcium concentration inside the SA is sensed by ER membrane-anchored STIM1 regulatory protein that interacts with ORAI1 channel present at the plasma membrane [31]. As the first step, the ORAI1 channels pump calcium into cytoplasm, followed by calcium entrance into

the SA through SERCA pumps mostly located in the SA head [42]. However, it remains unclear how SOCE could function to replenish calcium stores without triggering CICR activation. Here we investigate the release and replenishment pathways that are both activated by calcium but could operate without interfering with each other. Resolving this enigma is crucial, not only to determine the computational power of dendritic spines based on calcium signaling, but also for characterizing calcium dynamics underlying the induction of LTP and LTD. To study these processes under different calcium influx conditions (large and small, fast and slow), we used a combination of calcium imaging, computational modeling and simulations, and STED (Stimulated Emission Depletion) microscopy. Our stochastic model predicted and our measurements confirmed that SA-amplified CICR occurs only under strong and fast calcium influx conditions, whereas slow and small amplitude calcium influx triggers SA replenishment via STIM1-ORAI1 pathway and SERCA pumps located proximal to the plasma membrane. Furthermore, we also examined using numerical simulations calcium dynamics at the base of spines, during LTP and LTD and observed that the SA depletion timescale varies between LTP and LTD, resulting in a strong difference in the calcium levels at the base, which may determine the spine's fate towards the direction of either enhancement or depression of synaptic efficacy. Together, our study reveals that nanoscale molecular architecture plays a critical role in controlling calcium diffusion and ER replenishment. Moreover, contrary to the view that calcium concentration inside the whole spine dictates potentiation or depression, the work presented here suggests that calcium concentration at the spine base is the main determinant of LTP versus LTD induction.

Results

SOCE is associated with SA replenishment but not depletion

To investigate the mechanism of SA replenishment, following the methods developed in [116] and [162], we blocked synaptic activity [calcium voltage channels and synaptic inputs using APV [(2R)-amino-5-phosphonovaleric acid]/DNQX (6,7-dinitroquinoxaline-2,3-dione)/tetrodotoxin (TTX)] in cultured hippocampal neurons cotransfected with blue fluorescent protein and synaptopodin (SP), an actin-associated protein found in SA [125]. The only known source of calcium under these conditions remains the SOCE mechanism associated with the STIM1-ORAI1 pathway [31]. To monitor calcium fluctuations in spines containing SA, we used Fluo-4, a high-affinity calcium sensor (see also Materials and Methods). With this setup, we observed fluctuations that were restricted to spines and were not present in dendrites (Fig. 6.1A and B top panels). In addition, these calcium activity patterns associated with the STIM1-ORAI1 complex were much slower (on the order of seconds) and exhibited smaller amplitudes compared to the ones triggered by synaptic inputs (on the order of a few hundred milliseconds; figs. S1 and S2).

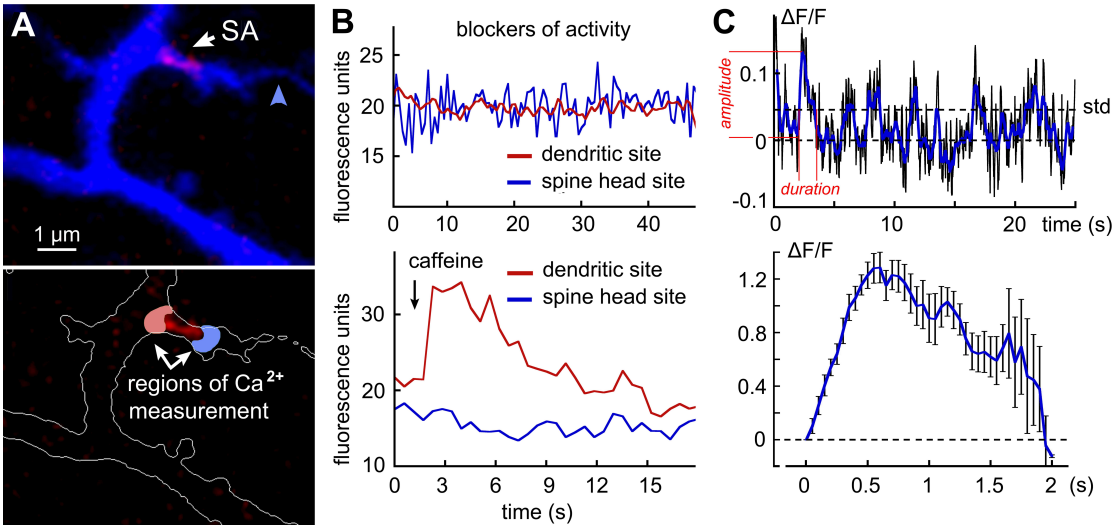

Figure 6.1: **Refilling or depleting the SA in dendritic spines with slow versus fast calcium transients (A).** Top: Blue fluorescent protein (blue) and SP (red) co-transfected in hippocampal neurons, cultured 3 weeks and loaded with the Fluo2 high affinity calcium sensor. A large SP+ spine attached to an axon (blue arrowhead) and several SP- spines can be seen. Bottom: Same region, with a white contour and two regions of interest: behind (red) and in front of (blue) the SP-labeled SA are shown. Synaptic activity was blocked using tetrodotoxin (1μM), APV (50μM) and DNQX (20μM). Following a caffeine addition of 5 mM, release of calcium is observed towards the base of the spine, but not in the spine head. **(B)** Top: Spontaneous calcium activity due to SOCE, only located in the spine head. Bottom: Time course of calcium activity in the head versus base following caffeine addition. Both are typical single realizations of the recordings. **(C)** Top: Segmented recording of spontaneous calcium activity in the spine head. Bottom: Overlapped average of the fluctuation segments larger than a pre-defined threshold of 1 SD (SD=0.0457 in the example trial shown in the top). Bottom shows the average of 18 such sequences.

To confirm that the SOCE pathway leads to calcium accumulation in the SA, we depleted the SA calcium stores with caffeine [125] and found an asymmetric calcium release, mostly toward the base of the spine (Fig. 6.1B bottom panel). This result is in agreement with the timescale of CICR activation and the underlying heterogeneous distribution of RyRs that are mostly located at the base of the spine [42]. To further study calcium transients and develop numerical simulations, we needed to obtain a stereotypical response. For that goal, we segmented the calcium time series, which was recorded in the spine head over a timescale of a few minutes. We defined a threshold which is one standard deviation (std) to differentiate between calcium transient and background fluctuations (Fig. 6.1C top). We collected events and averaged them (Fig. 6.1C bottom), resulting in a stereotypical response that we fitted with a difference of two exponentials (Fig. S3). The calcium concentration in the spine head has a correlation time of approximately 1s, as revealed by the autocorrelation function (Fig. S4), compatible with previous analysis on calcium transients in [141].

We then used this fit to determine the conditions that favor calcium accumulation in the SA by developing stochastic computational simulations for calcium diffusion inside a dendritic spine (Fig. 6.2A). For calcium inputs to the spine head, we simulated two distinct conditions: **(i)** a fast entry from synaptic inputs through NMDARs, which we modeled with an instantaneous calcium injection, and **(ii)** the SOCE activity (as observed in Fig. 6.1C bottom), which we model with a slow calcium injection to the spine head.

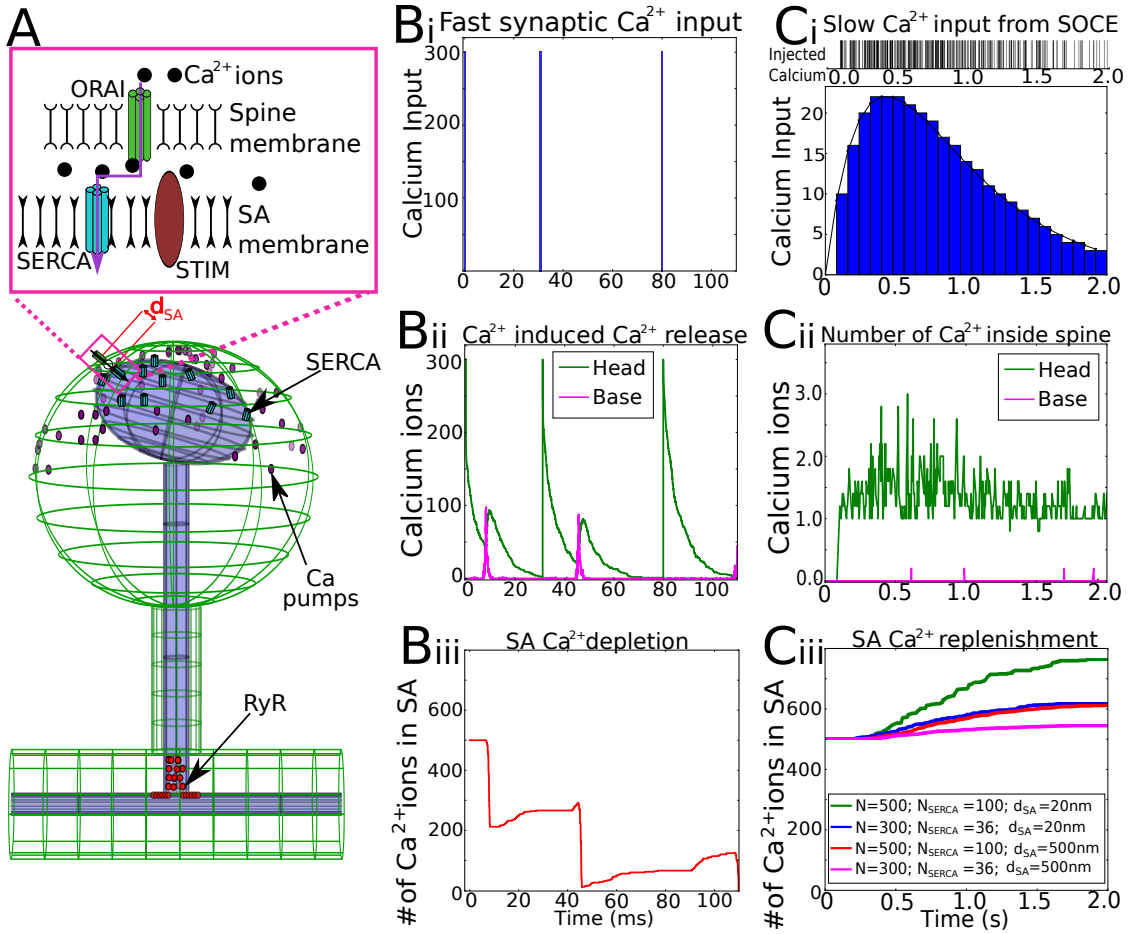

Figure 6.2: **Modeling SA depletion and refilling with slow versus fast calcium inputs.** **(A)** Schematic of the spine domain (green) with its calcium inputs and regulators (see Materials and Methods for channel models). **[B(i)]** Simulated synaptic inputs with an instantaneous injection amplitude of N=300 ions, repeated each time when the calcium in the spine reaches zero [B(ii) green curve at t=0, t=30.9, and t=80.1s]. [B(ii)] Calcium dynamics in the spine head (green) versus base (magenta) following fast inputs. [B(iii)] SA reservoir of 500 ions depleted during fast inputs upon three CICR events. **[C**(i)] Slow calcium input to spine head with SOCE, fitted with a difference of two exponentials over 2s (black curve, accounting for 94.5% of the distribution), and discretized into 25 bins (blue histogram: $R^2 = 0.9986$). The barcode represents the injection times of single ions. [C(ii)] Simulated calcium levels in the spine head and base during the slow input of C(i) (total injection N=300; 5 trials averaged). [C(iii)] SA reservoir always increase without depletion under slow SOCE conditions with different numbers of SERCA pumps N_{SERCA} and SA-plasma membrane distances d_{SA}.

Our results revealed that: **(i).** A fast synaptic input is associated with store depletion events through RyR-induced CICR. In the numerical simulations [Fig. 6.2B (i)], we verified this prediction by injecting 300 ions into the spine head to mimic fast synaptic inputs, then waiting until the spine head was completely depleted of calcium before injecting another batch of 300 ions. In all, we thus simulated three injections, at t=0, 30.9, and 80.1s and observed a sharp increase in calcium due to CICR occurring at the base a few milliseconds following each calcium injection into the spine head [Fig. 6.2B(ii)]. Calcium decay in the head is due to the uptake through SERCA pumps, the diffusion toward the base and the absorption by pumps. A few milliseconds after each injection into spine head, we also observed a smaller second calcium peak due to the headward diffusion of calcium ions "generated" by CICR in the base region. When we started with 500 ions in the SA, after three stimulations, SA became totally depleted of calcium ions due to CICR [Fig. 6.2B(iii)] as predicted under these conditions [80]. Note that the small increases in between the fast depletion events here are due to uptake of ions into SA through SERCA pumps.

(ii). In contrast, when we injected calcium ions into the spine head at a slower rate, the SA was refilled by calcium without triggering CICR, despite the much smaller number of calcium ions present in the head [Fig. 6.2C(i), C(ii) and C(iii)]. By accounting for the spontaneous activity above the threshold SD (Fig. 6.1C), we model here the slow calcium inputs as a difference of two exponentials [black curve in Fig. 6.2C(i)] over a duration of 2s, discretized into 25 bins and normalized to the total number N of calcium ions injected throughout the duration [histogram in Fig. 6.2C(i)]. Injection times of single ions are obtained from a uniform random distribution of input ion numbers corresponding to each bin [Barcode representation in Fig. 6.2C(i)]. In contrast to synaptic inputs, the number of calcium ions in the spine base during slow inputs was extremely low, thus no calcium release events could be triggered through RyRs [Fig. 6.2C(ii), magenta].

For this mechanism of refilling to occur, we hypothesized that the distance d_{SA} between the SA and the plasma membrane is in the order of a few tens of nanometers. Therefore, for the simulations, we positioned SERCA and ORAI1 in close proximity inside the spine head. We then explored the impact of d_{SA} on the refilling of SA by changing this distance from 20 to 500nm [Fig. 6.2C(iii)]. We found that the reduction of refilling due to the increased distance can be compensated with an increase in the number of SERCA pumps or by amplifying the calcium input. Therefore, these results suggest that the distance d_{SA}, the number of SERCA pumps N_{SERCA}, and the slow influx rate of calcium are key parameters favoring SA calcium refilling.

To further characterize the distribution of calcium fluxes in the SA, i.e. extrusion from the head or the arrival at the base of the spine, we followed the fate of each ion during numerical simulations. We simulated 300 injected ions each time over a slow input lasting 2s [similar to Fig. 6.2C(i)], keeping the distance d_{SA} at a constant value of 20nm. In an ensemble of 210 trials that we simulated, we analysed the 161 in which a CICR did not occur. We observed that most ions (236 of 300) were bound to calcium extrusion pumps, while the number of ions that refilled the SA through SERCA pumps was 46 of 300.

Around 14 of 300 remained in the spine domain or stayed as single-occupants in SERCA or RyRs without triggering an opening within the simulated 2s; only the remaining 4 of 300 ions reached the base and disappeared from the absorbing boundary. Therefore, under these conditions, calcium concentration at the base of the spine remained too low to trigger a CICR, safely eliminating the possibility of triggering a depletion.
To characterize the spatiotemporal conditions of calcium dynamics leading to SA replenishment, we also developed a mean-field computational model (section S4 and figs. S5 to S7), accounting for the mean number of calcium ions m_{ca} in the spine, the fraction n_1 of RyRs bound by one calcium ion and the probability p_2 to trigger CICR by activating at least one RyR when two calcium ions are bound. The complete system of equations are

$$\begin{aligned} \dot{n}_1 &= -\mu n_1 + \lambda m_{ca}(n_R - 2n_1) \\ \dot{m}_{ca} &= J_{inj}(t) - \nu m_{ca} - \lambda m_{ca}(n_R - n_1) + \mu n_1 \\ \dot{p}_2 &= \lambda n_1 m_{ca}(1 - p_2), \end{aligned} \tag{6.1}$$

where μ is the unbinding rate of calcium binding to RyR, ν is the calcium extrusion rate from a spine, and λ is the forward rate of calcium binding to RyR. To study the fast synaptic inputs and SOCE, we used the two different initial conditions:
(i) instantaneous injection of ions, modeled with a Dirac's δ function at $t = 0$ (or equivalently with the initial condition $m_{ca}(0) = N_0$, $n_1(0) = 0$, $p_2(0) = 0$), and **(ii)** a slow injection, modeled by $J_{inj}(t) = A(e^{-\lambda_1 t} - e^{-\lambda_2 t})$ (fitted in fig. S3) with the initial conditions of $m_{ca}(0) = 0$, $n_1(0) = 0$ and $p_2(0) = 0$.
The probability to activate a RyR by two ions is

$$P_2 = Pr\{n_2(\infty) = 1\} = 1 - e^{-\lambda \int_0^\infty n_1(u) m_{ca}(u) du}. \tag{6.2}$$

We also evaluated numerically this activation probability P_2 (fig. S8), and confirmed its agreement with the results of the stochastic simulations in Fig. 6.2: Even with a small (<500) number of ions, an instantaneous calcium influx $J_{inj}(t)$ leads to a higher probability of SA calcium release, whereas a slower influx with such a number leads to CICR events at a much low probability. The solution of the system of Eq. (6.1) shows how the probability P_2 depends on the number N of fast synaptic inputs and on the amplitude A of the slow SOCE inputs (fig. S5 and sections S4.2 and S4.3). Therefore, both our mean-field model and the stochastic simulations strongly indicate that a slow calcium transient from the STIM1-ORAI1 pathway does not induce calcium release at the base of a dendritic spine, but leads to SA refilling. Thus we conclude that the biophysical conditions for SA replenishment and depletion are well separated (fig. S6). Collectively, our calcium imaging-based observations and our computational modeling suggest that SOCE plays role in replenishment exclusively, and that spatial co-localization (proximity) of key molecular regulators in this process (SERCA and ORAI1) is critical for ensuring fidelity of replenishment while not triggering CICR.

Calcium redistribution in dendritic spines: Replenishment without release

To test the predictions generated using our computational modeling of SA replenishment, we explored the conditions for calcium replenishment in dendritic spines containing SA using calcium imaging of hippocampal cultured neurons. To identify spines containing SA, we used SP as a marker for SA (red puncta in Fig. 6.3A and B). To demonstrate that the SA is refilled in the absence of any activity, we blocked both voltage-gated channels and glutamatergic receptors by adding TTX (1μM), APV (50μM) and DNQX (20μM). In the absence of extracellular calcium, spines do not show any calcium transients regardless of whether they contain SA or not (Fig. 6.3C). By blocking the SOCE pathway (fig. S1), we confirmed that STIM1-ORAI1 is responsible for SA calcium replenishment. Moreover, we observed that the replenishment of calcium in SA through SOCE increases with duration of refilling (fig. S2).

In contrast, when presented with extracellular calcium, notable transients occur only in the heads of SP+ spines [Fig. 6.3 D(i) and D(ii)]. Calcium entry did not lead to any calcium transient at the bases of both SP+ and SP- spines, confirming our predictions (Fig. 6.2) that a slow calcium entry leading to SOCE does not activate RyRs. However to confirm that RyRs were functional, we activated them using caffeine. This activation led to substantial transient increases in calcium at the base of SP+ spines only, where RyRs are mostly located [Fig. 6.3 E(i), E(ii) and F(iii)]. In these experiments, caffeine is present in the extracellular medium and trigger CICR with a slower time scale compared to our simulations where calcium ions are directly available in the spine head. To quantify the spontaneous calcium activity further (Fig. 6.3 Di and Dii), we also confirm that both the amplitudes [2.2 versus 1.54 arbitrary units (a.u.)] and the durations (1.4 versus 0.8s) are significantly larger in SP+ spines compared to SP- ones [Fig. 6.3F(i)]. In addition, the frequencies of activation [Fig. 6.3F(ii)] were higher in the spine head of SP+ (gray, 0.5 Hz) compared to SP- spines (purple, 0.2 Hz) or dendrites (black, 0.1 Hz) [n=16, $P<0.0001$, analysis of variances (ANOVA)]. Therefore we conclude that SOCE occurs preferentially in the heads of SP+ spines and requires the presence of SA. In summary, these results confirm our initial theoretical predictions that in the absence of synaptic activity, calcium ions enter the spine through SOCE and are stored inside the SA stores.

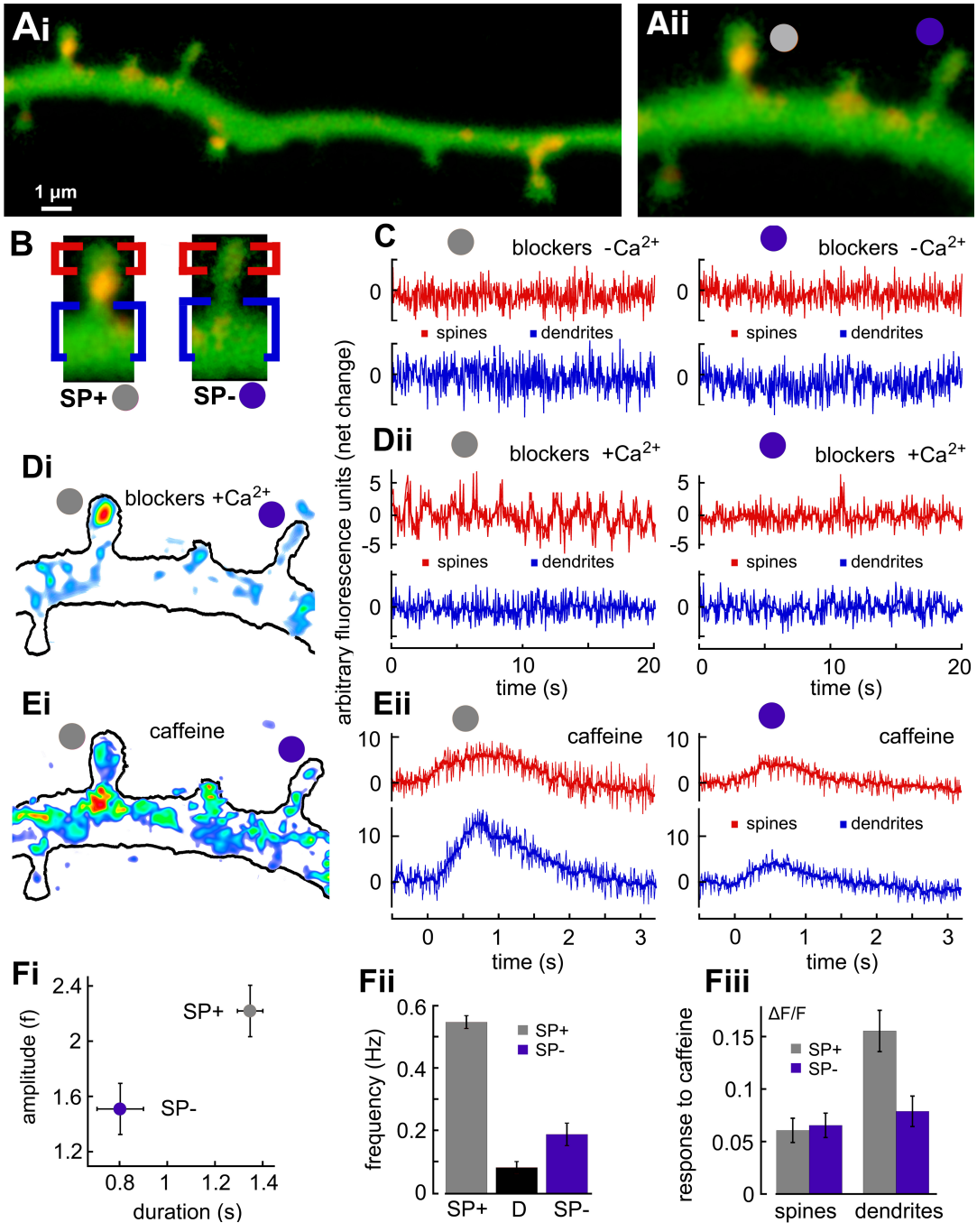
Ai
1 µm
Aii
B
SP+
SP-
C
blockers -Ca2+
spines
dendrites
Di
blockers +Ca2+
Dii
blockers +Ca2+
arbitrary fluorescence units (net change)
time (s)
Ei
caffeine
Eii
caffeine
Fi
amplitude (f)
duration (s)
SP+
SP-
Fii
frequency (Hz)
SP+
D
SP-
Fiii
ΔF/F
response to caffeine
spines
dendrites

Figure 6.3: **Local calcium storage in dendritic spines. A(i)** Dendrite of a rat hippocampal cultured neuron, transfected with synaptopodin (SP) (red puncta), and loaded with Fluo-2. [A(ii)] Magnification of (A) with two spines with similar lengths $\approx 1.2\ \mu m$: left = SP+ (gray circle); right = SP- (purple). **(B)** Labeling of SP+/- spines with head (red) and base (blue) regions. **(C)** Recordings in calcium-free medium with activity blockers. Sustaining these conditions for 15 mins partially depleted calcium stores, and initiated store-operated calcium entry (not shown). [**D(i)**] Colored representation of the background-subtracted calcium transient (low calcium = blue/cyan; higher levels = red>yellow>green). [D(ii)] Recordings from the same regions with activity blockers and extracellular calcium (2 mM). [**E(i)**] Examples of caffeine-induced calcium transient {background levels subtracted, same colors as [D(i)]}. [E(ii)] Calcium release from internal stores due to caffeine bath application (5 mM) uniquely observed in the SP+ spine bases. [**F(i)**] Amplitudes and durations of calcium fluctuations in SP+ (gray dot) and SP- spine heads (purple) (n=16 for both, P<0.0001, t test). [F(ii)] Frequency of calcium fluctuations in SP+ heads (gray), dendrites (black) and in SP- spines (purple). [F(iii)] Caffeine responses in SP+ spine heads, SP- dendrites, and SP- heads were approximately the same, but significantly weaker than in the SP+ dendritic sites (all groups: n=16, P<0.001, ANOVA).

STED microscopy reveals the colocalization of ORAI1 in plasma membrane and SERCA pumps in spines containing SA

Our stochastic simulations predicted that SOCE is the main source of calcium ions for the SA calcium replenishment process. We thus hypothesized that ORAI1 channels, which allow slow calcium entry from the plasma membrane should be closely colocalized with SERCA pumps that refill the SA. In addition, we predicted that this colocalization should predominately occur in the heads of spines containing SA. To determine the association between SERCA and ORAI1 localization, we used super-resolution STED imaging of immunostained hippocampal tissues (see Materials and Methods).

We confirmed that the colocalization frequency of ORAI1 and SERCA3 is significantly higher (Fig. 6.4A and B) when SP is present (ORAI1+SERCA3+SP: 88.9±0.73%, n=19, P<0.001) than when SP is absent (ORAI1+SERCA3: 0.99±0.24%, n=19, P<0.001). The colocalization of SP with ORAI1 or SERCA3 only is weak (ORAI1+SP: 7.75±0.61%, n=19, P<0.001; SERCA3+SP: 0.45±0.16%, n=16, P<0.001) similar to spines with SP alone (1.88±0.33%, n=19, P<0.001). Moreover, the average colocalization distance of SERCA and ORAI1 in SP+ spine heads is around 100nm, (106±4 nm, n=378), with a substantial population of SERCA and ORAI1 localized as closely as 30nm, while their average distance is more than doubled to around 200nm in the neck (221±14 nm, n=159, P=0.0067) or at the base (210±8 nm, n=290, p=0.0034) of a spine (Fig. 6.4C to D). To conclude, these results reveal the short distance between SERCA and ORAI1 in spine heads containing SA, confirming the predictions of the stochastic simulations about SOCE-associated SA refilling.

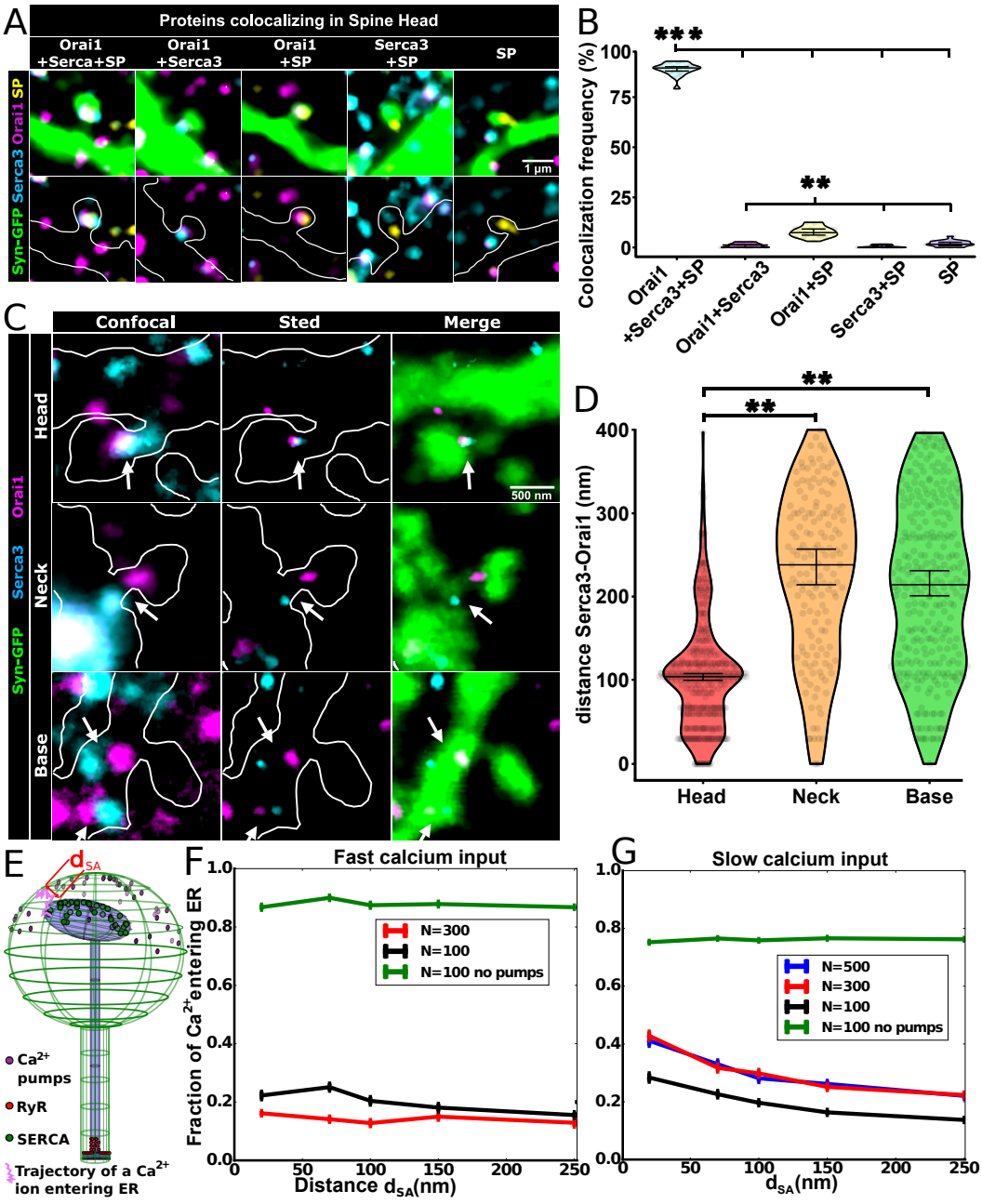
A
Proteins colocalizing in Spine Head
Orai1 +Serca+SP
Orai1 +Serca3
Orai1 +SP
Serca3 +SP
SP
Syn-GFP Serca3 Orai1 SP
1 µm
B
***
**
Colocalization frequency (%)
100
75
50
25
0
Orai1 +Serca3+SP
Orai1+Serca3
Orai1+SP
Serca3+SP
SP
C
Confocal
Sted
Merge
Syn-GFP Serca3 Orai1
Head
Neck
Base
500 nm
D
**
**
distance Serca3-Orai1 (nm)
400
300
200
100
0
Head
Neck
Base
E
d_{SA}
Ca^{2+} pumps
RyR
SERCA
Trajectory of a Ca^{2+} ion entering ER
F
Fast calcium input
Fraction of Ca^{2+} entering ER
1.0
0.8
0.6
0.4
0.2
0.0
N=300
N=100
N=100 no pumps
0
50
100
150
200
250
Distance d_{SA}(nm)
G
Slow calcium input
N=500
N=300
N=100
N=100 no pumps
d_{SA}(nm)

Figure 6.4: **SERCA-ORAI1 distributions and consequences. (A–D)** Distances between SERCA3 and ORAI1 puncta in dendritic spines of hippocampal neurons from adult mouse brain slices. **(A)** Green florescent protein (GFP)-labeled neurons (green), immunostained for ORAI1 (magenta), SERCA3 (cyan) and SP (yellow). Representative images show the five conditions analyzed in (B). **(B)** Quantified colocalization between ORAI1, SERCA3 and SP proteins. Four slices, each with 279-364 spine heads were analyzed. **(C).** The three conditions analyzed in (D), with the same colors as in (A). **(D)** Quantified SERCA3-ORAI1 distances in spine head, neck, and base. Statistical analysis involved one-way ANOVA and Tukey's multiple comparisons tests. (B) and (D) significances: ** $P<0.01$, *** $P<0.001$. **(E)** Schematic of calcium regulators in the simulated spine model, also showing the distance d_{SA} between the plasma and SA membranes. **(F)** Normalized fractions of calcium entering SA under instantaneous inputs to spine heads for different amplitudes N, with (black and red) and without (green) calcium pumps. Of the 100 trials, we chose here the ones without a RyR activation until there were no more ions to simulate. **(G)** Same fractions as in (F), during slow calcium influx with the previously shown 2-s protocol under different N values, and when pumps were removed for N=100. Error bars in (F) and (G) represent SEM.

To examine the colocalization requirement further, we used our numerical strategy to evaluate how SERCA-ORAI1 distance d_{SA} (Fig. 6.4E) influences the number of ions entering the SA during fast synaptic inputs (Fig. 6.4F) and slow SOCE currents [Fig. 6.4G]. Following a fast input with 100 or 300 injected calcium ions, we found that the fraction of calcium entering the SA is stable around 15 to 20% when d_{SA} varies from 0 to 250nm (Fig. 6.4F black and red curves). We found that a majority of remaining ions were extruded by calcium pumps. To evaluate the influence of the extrusion pumps on the calcium uptake, we repeated the same simulations after removing all extrusion pumps. In that case, the fraction of SA calcium uptake increases to $\approx 90\%$ (Fig. 6.4F green curve) as expected, because more ions remain in the cytoplasm.
For simulating SOCE conditions (Fig. 6.4G), we placed calcium ions at the top of the spine head with dynamics following the fit with a difference of exponentials lasting 2s [6.2C(i)] with different numbers of ions. By comparing the numbers of calcium ions entering SA divided by the total number N, we noted that slow inputs with N=300 ions are much more successful in refilling the SA than the corresponding fast inputs [red curves in Fig. 6.4, F versus G]. However, when there were no calcium pumps with N=100 (green curves), this fraction was slightly lower under slow input conditions, compared to what we saw with the fast inputs. This is likely due to longer RyR activation times during slow calcium inputs (fig. S7 and S8), resulting in a larger ion loss by diffusion. In all cases N=100, 300 and 500 with calcium pumps during slow inputs (black, red and blue curves in Fig. 6.4G), the ratio of calcium ions entering the SA to the total N decreases gradually when d_{SA} increases. This is in contrast to the stable behavior observed under the fast calcium input conditions and to the slow inputs when SA calcium pumps are absent (green curve in Fig. 6.4G). Moreover, we found that the probability P_2 of SA calcium depletion via

CICR is extremely low during a slow calcium input, compared to a fast injection (fig. S8). The probability P_2 increased gradually with d_{SA}, and the conditional time to trigger such events was governed by the presence of calcium pumps in the head.
Therefore, calcium pumps play an unexpected role in preventing and delaying the RyR activation by controlling the arrival of calcium ions at the base of the spine. Together, the calcium injection rate and the distance between the SA and plasma membrane, along with the balance of SERCA and calcium pumps shape the SA calcium uptake and the CICR activation probability.

Calcium dynamics in spines and SA during LTP versus LTD protocols

We next evaluated the consequences of calcium dynamics by the induction protocols of long-term synaptic potentiation and depression (Fig. 6.5A to C). Although the role of calcium dynamics in LTP and LTD has been known for some time [43], the role of SA calcium stores in these processes remains unclear. It has been previously observed that only the SP+ spines increase their head sizes during LTP [44], suggesting that the presence of SA could be a critical factor in the plasticity of the synapse. To examine this possibility further, we used numerical simulations to investigate calcium dynamics during the LTP and LTD induction at a single spine level based on the molecular organization we delineated heretofore.
We simulated spine calcium dynamics during LTP in two phases: (i) stimulation phase, and (ii) silent phase. The first phase involves a 100Hz calcium spike train that we started with N=300 (or 500) calcium ions per spike. In this range of N, the increase in calcium concentration falls into the physiological range of $\approx 0.15\mu$M following a synaptic input [163]. Afterward, the injection was allowed to decay slowly with successive events, accounting for synaptic depression [45]. (See Materials and Methods for the numerical implementation). Both phases included a repetition of slow background input of calcium similar to the STIM1-ORAI1 pathway [N=300 for 2s; profile shown in Fig. 6.2C(i)]. We only simulated the first 250ms (25 injections) of calcium dynamics of the stimulation phase and 30s of the silent phase.
In the stimulation phase, we found that on average, the number of calcium ions in the spine head peaks around 50ms (fig. S9, blue curve), and then decays with weakened inputs. During this time, less than 20 calcium ions reached the spine base [Fig. 6.5D(i)]; nonetheless they led to several CICR events (green spikes in fig. S9). Increasing the number of initial calcium ions from 300 [Fig. 6.5D(i) red] to 500 (blue) reduces the onset time of these RyR responses. Because of these CICR events, the stored number of calcium ions in the SA decayed rapidly, leading to a nearly total SA depletion in about 250ms [Fig. 6.5D(ii)].
During the second phase that only included slow inputs, we found that on average, a few hundreds of calcium ions replenish the SA through SERCA pumps [Fig. 6.5D(iii), red curve]. In some cases, SA calcium level could go up to more than 1500 ions and

sometimes diminish to a very low level due to intermittent CICR events [blue curves in Fig. 6.5D(iii)]. We conclude that such variability in SA refilling is compensated by the repetitiveness of the LTP protocol, applying multiple high-frequency stimulations intermitted by silent periods. We also repeated the refilling phase of the LTP protocol by adding ectopic vesicular release events that introduce small amplitude calcium spikes (fig. S10). We found that the presence or absence of ectopic release did not considerably alter SA refilling.

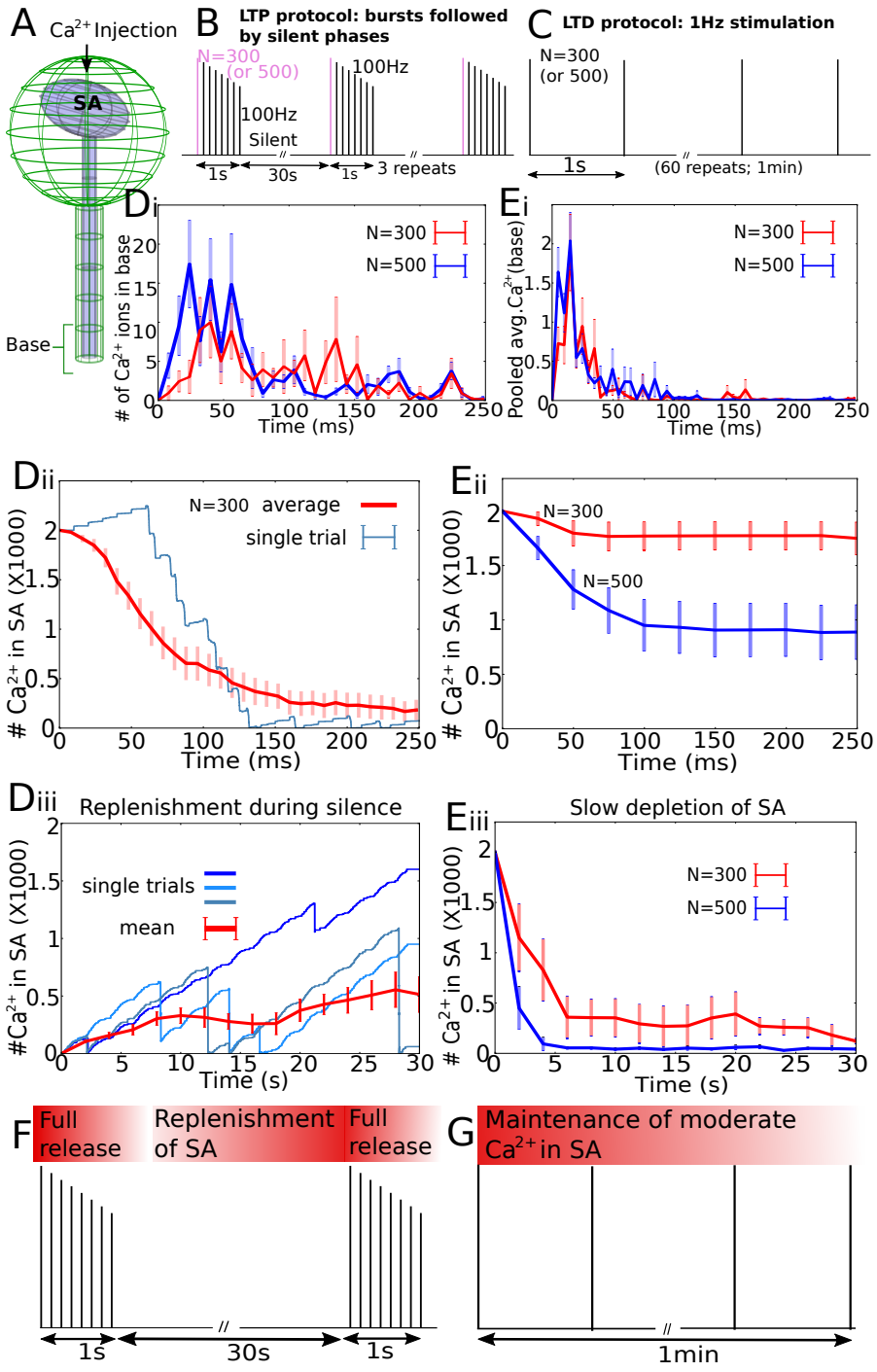
A
Ca2+ Injection
SA
Base
B
LTP protocol: bursts followed by silent phases
N=300 (or 500)
100Hz
100Hz
Silent
1s
30s
1s
3 repeats
C
LTD protocol: 1Hz stimulation
N=300 (or 500)
1s
(60 repeats; 1min)
Di
# of Ca2+ ions in base
N=300
N=500
Time (ms)
Ei
Pooled avg.Ca2+(base)
N=300
N=500
Time (ms)
Dii
# Ca2+ in SA (X1000)
N=300 average
single trial
Time (ms)
Eii
# Ca2+ in SA (X1000)
N=300
N=500
Time (ms)
Diii
Replenishment during silence
#Ca2+ in SA (X1000)
single trials
mean
Time (s)
Eiii
Slow depletion of SA
# Ca2+ in SA (X1000)
N=300
N=500
Time (s)
F
Full release
Replenishment of SA
Full release
1s
30s
1s
G
Maintenance of moderate Ca2+ in SA
1min

Figure 6.5: **Simulations of calcium transients in spines during LTP and LTD induction protocols. (A).** Schematic of a spine with SA and injected calcium. **(B).** Postsynaptic LTP protocol with 100-Hz stimulations followed by 30s silences (SOCE only). The injection starts from N=300 (or 500) and decays according to the model in [45]. **(C).** LTD protocol is induced by injecting a calcium spike every 1s. **D(i).** Average number of calcium at the spine base during the first 250ms of LTP induction. (Mean & SEM are from 20 trials). **D(ii).** Number of calcium ions in SA at the beginning of the LTP protocol (20 trials averaged). **D(iii).** Simulated SA refilling during the silent phase of LTP. Calcium input into spine head is a succession of the slow entry described in Fig. 6.2C(i). Time courses of SA calcium refilling (blue) that reach high, low and medium values. Mean (red) and SEM are from 10 trials. **E(i).** Calcium response at the spine base after each 1Hz spike of the LTD protocol over 300 time courses (30s simulations x 10). E(ii) & E(iii). Number of calcium ions in the SA during the first 250ms and the total 30s of the LTD protocol. **(F) & (G)**. Interpretation of the LTP protocol as CICR at the base followed by SA replenishment, while during LTD the calcium is maintained at low level.

We then investigated calcium dynamics during the LTD protocol (Fig. 6.5C): Calcium ions were injected at a slow rate of 1Hz during 1 min. As we confirmed that the transient is much shorter, we decided to simulate calcium dynamics for the first 30s. We first injected N=300 ions to use ion concentrations identical to those used in the LTP protocol. We then increased the number of ions to N=500, and confirmed that the results did not change. We observed that this input to spine head could trigger CICR events at the base of the spine and thereby increase the calcium at very low levels of 10 ions or less when averaged (orange curves in fig. S11, axis on the right).
To compare the LTD responses at the base with the ones generated by the LTP protocol, we averaged the number of calcium ions during the first 250ms after each 1-Hz stimulation pulse [Fig. 6.5E(i)]. The number of calcium ions at the base during LTD simulations is only about one tenth of the corresponding LTP simulation response [Fig. 6.5D(i)]. Moreover, the calcium release response at the base during the onset of each stimulation lasted shorter than the corresponding LTP response. In addition, the calcium depletion in the SA is slower during LTD stimulations and takes several seconds [Fig. 6.5E(ii)-E(iii)], compared to the timescale of several hundred milliseconds observed during the LTP stimulation [Fig. 6.5D(i)].
We conclude that the SA depletion timescale varies between LTP versus LTD induction protocols, resulting in a strong difference in the calcium levels at the base of the spine (Fig. 6.5F and G). Overall, we propose that this difference could represent the underlying determinant of the spine's fate toward either enhancement or depression of synaptic efficacy.

Discussion

Despite being widely acknowledged as a critical factor of dendritic spine physiology, regulation of the calcium ion dynamics, especially the mechanisms that exert spatiotemporal control over the calcium release and replenishment, remain less clear. We focused on

the role of SA in these processes, and found that only strong and fast calcium influxes are amplified by the presence of SA in the spine, resulting in CICR at the spine base (Fig. 6.6A). In contrast, a slow and small amplitude calcium influx through the STIM1-ORAI1 pathway leads to SA replenishment through SERCA pumps located proximal to the plasma membrane (Fig. 6.6B). From our observations, we can conclude that calcium influx timescales, their amplitudes, and the spatial distance between ORAI1 and SERCA pumps guarantee that the two pathways (rapid depletion and slow replenishment) are not triggered at the same time (Fig. 6.6C).

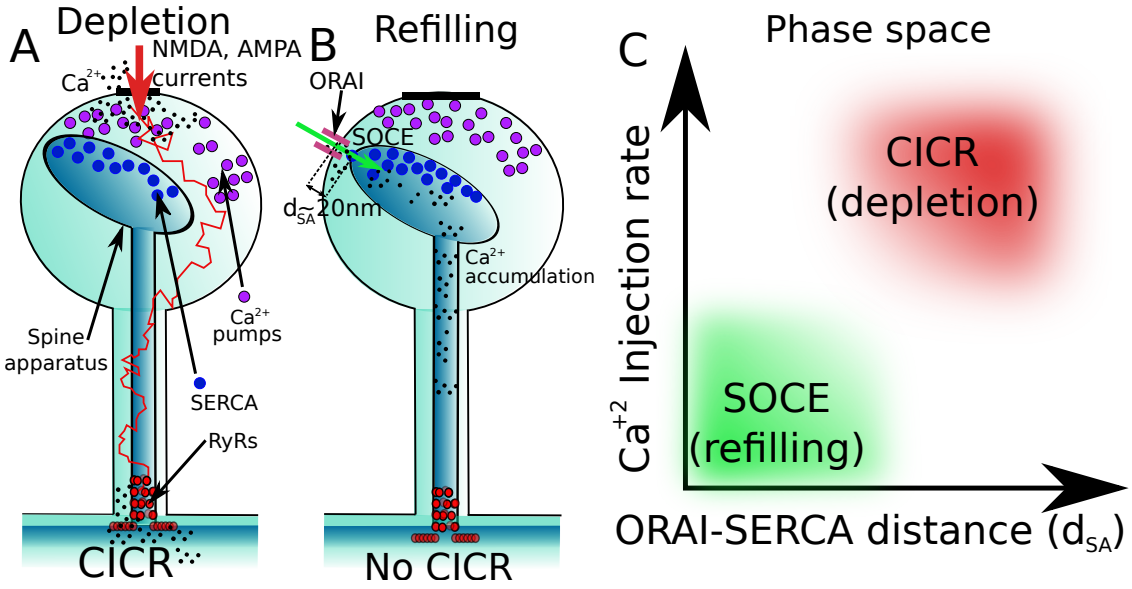

Figure 6.6: **Physiological conditions for SA depletion vs replenishment. (A).** Synaptic currents entering the dendritic spines through NMDAR and AMPAR trigger CICR by activating RyRs at the base. **(B)** Small calcium inputs with slow timescales through ORAI1 channels located near the SA membrane are insufficient to trigger a CICR at the base. These ions are either absorbed into calcium pumps located in the spine head, or replenish the SA calcium reservoir via the SOCE through SERCA pumps. **(C)** Phase space described by the main axes: calcium injection rate and the distance d_{SA} between the ORAI1 and SERCA channels. Refilling and depletion conditions of calcium in spines are well separated, so that both do not occur at the same time.

Perhaps the most prominent result of our analysis is the insight that nanoscale molecular architecture plays an essential role in regulating calcium ion release and replenishment. We observed evidence that the distance between the SA and the plasma membrane (d_{SA}) plays a major role, whereby calcium replenishment stops as d_{SA} increases past a certain point. More specifically, we propose that proximity of the two channels ORAI1 and SERCA is required for an optimal SA replenishment, an increase in this distance reduces the chance for the diffusing calcium ions to hit one of the SERCA located in the SA head and thus they could escape to activate RyRs located at the base. We did observe that

adding more SERCA pumps could partially compensate for a longer distance, suggesting that the effect also depends on SERCA density and distribution. Other key players in these processes are calcium pumps as we show that they restrict small calcium inputs. Their presence increases the temporal separation of the calcium transient between the head and the base, generating an additional delay in CICR activation.

Although suggested to play in regulating calcium dynamics [164], we do not model here calcium buffers because: **(i)** for a fast CICR onset within a 5 ms, an ion bound to a slow buffer would not contribute, thus a simple reduction in the available free ions is equivalent to calcium buffering [95]. **(ii)** In the case of ORAI1 channel influxes through the plasma membrane, we do not expect buffers to affect SA replenishment due to the short distance d_{SA} in the range of 20 to 100nm, which can contain only very few buffers. Nevertheless, similar to surface pumps, buffers could also help separating the depletion from the replenishment regime, as they introduce an asynchrony to the calcium arrival times to the spine base by absorbing calcium ions followed by delayed release. Overall, the present numerical simulations give an upper estimate of the calcium release probability, and therefore, SA replenishment that compensate such depletion events could be possible even with weaker (N<300) SOCE inputs than what we simulated here.

At this stage, we conclude that a few molecular players such as SERCA, RyR and surface pumps seem sufficient to guarantee the interplay between calcium SA refilling and depletion. In the broader context, we propose that these insights could be used to explain the proposed role of the dendritic spines as biochemical computation units [105]. From this perspective, given that we observe that the SA depletion is achieved only during synaptic inputs and is unlikely during SOCE, the spine can function in an almost deterministic regime.

The main methodological development that enabled our analysis is the construction of the stochastic model that, unlike the models based on average reaction-diffusion equations, which usually ignore molecular details [46,114,130,133,142,152,163,165,166], integrates local binding, and organization of molecules, channels and transporters [167,168]. Therefore, the stochastic modeling allows monitoring of diffusion trajectory of each ion separately, thus providing insights into the level of single molecules usually at the expense of high computational cost.

The ability to analyze a system at the single molecule (stochastic) manner is especially important for a system like dendritic spines, given that many of spine processes occur at low copy numbers. For example, AMPARs are of the order of few tens; NMDARs could be less than 10 [43,169]. SERCA pumps and RyR are less than hundreds [170,171], and the residual level of calcium in spines also ranges below 100 ions. Here, stochastic modeling allows us to estimate relevant statistics to quantify the fluctuations due to low copy numbers.

Thus in the present modeling and simulations of the spine with a SA, we accounted for the spatial organizations of RyR, ORAI1 and SERCA, which allowed us to obtain accurate nanophysiological predictions about the geometrical organization required for calcium store replenishment versus depletion. We were also able to model and examine

how calcium ion release and replenishment affects two fundamental processes essential for synaptic plasticity, learning, and memory: LTP and LTD.

Synaptic plasticity is classically thought to result from calcium elevation in spines, activating a variety of molecular pathways. During this process, both spine head volume and the number of AMPARs increase rapidly within a few minutes [172]. Spines with SA predominantly undergo LTP [18, 23, 44]. Chemical LTP preferentially enlarges and enhances volume of the head and the surface of the post-synaptic density of dendritic spines containing SA [173]. The need of local calcium increase at the base could lead to protein synthesis, as several machineries such as ribosomes and mitochondria [145] are located near the base of the spine neck [174]. Thus, if local protein synthesis near SA is regulated by calcium ions due to CICR, then the products could directly be delivered to the stimulated spines to achieve the postsynaptic changes underlying LTP [175] or LTD [176].

Our analysis of calcium dynamics during the LTP-LTD protocols revealed the store depletion level, the total duration, the overall strength and the initial height of the calcium response at the spine base. At this stage, it remains unclear whether there is a molecular mechanism that compares calcium transients between spine head and base during synaptic plasticity. However, we showed that the number of calcium ions at the base during LTD is only about 10% of the calcium concentration during LTP. This increased calcium concentration at the base during potentiation has been previously shown to regulate trafficking of AMPAR and NMDAR [43, 177–179]. It would therefore be interesting to investigate how these receptors could be selected by local calcium elevation. In addition, this elevation at the spine base could also restrict receptor diffusion and interactions, result in potential well nanodomain trapping [180, 181] or phase separation [182], and create an asymmetric receptor influx in spines. Last, calcium elevation at the base of spines could trigger ER-mitochondria calcium communication [145, 183] to produce the adenosine 5'-triphosphate required for the spine homeostasis, and for the remodeling of spine shape and volume [184].

We also identified a key difference in SA depletion timescales between LTP and LTD, suggesting that this is also a key determinant of whether a given dendritic spine enhances or depresses synaptic signal. Moreover, in our simulations of the LTD protocol, failure to induce CICR prevents SA depletion and leads to a larger calcium accumulation. Thereby subsequent inputs could trigger a large calcium increase at the base of the spine. This scenario could explain the instability of LTD induction that could accidentally result in LTP, especially in the presence of secondary calcium sources such as voltage-gated channels.

Although these additional aspects of calcium dynamics in dendritic spines remain to be examined in future studies, our current work found the critical role that molecular architecture plays in regulating calcium ion release and replenishment in dendritic spines. The architecture imposes constraints on the two opposing processes, thus ensuring fidelity and spatiotemporal control which ensures that calcium stores within SA are replenished without triggering calcium release.

Materials and Methods

Ethics statement

Animal handling was done in accordance with the guidelines of the Institutional Animal Care and Use Committee of the Weizmann Institute of Science (approval number: 00650120-3 from 20 January 2020 for 3 years), Collège de France and the appropriate Israeli and French laws and national guidelines. Experiments were carried out according to the guidelines of the European Community Council Directives of 1 January 2013 (2010/63/EU) and of the local Animal Welfare Committee. All efforts were made to minimize the number of used animals and their suffering.

Calcium imaging experiments

Culture preparation

Cultures were prepared as detailed elsewhere [185]. Briefly, rat pups were decapitated on the day of birth (P_0), and their brains were removed and placed in a chilled oxygenated Leibovitz L-15 medium (Gibco) enriched with 0.6% glucose and gentamicin (Sigma-Aldrich; 20 μg/ml). Hippocampal tissue was dissociated after incubation with trypsin and deoxyribonuclease, and passed to the plating medium consisting of 5% horse serum and 5% fetal calf serum prepared in minimum essential medium (MEM; Gibco), and enriched with 0.6% glucose, gentamicin and 2 mM GlutaMAX (Gibco). Approximately 10,000 cells in 1 ml of medium were plated in each well of a 24-well plate, onto a glial layer which has been grown for a week before the plating of the neurons. Cells were left to grow in the incubator at 37°C, 5% CO_2 for 3 days, following which the medium was switched to 10% horse serum in enriched MEM, and in addition of 5´fluoro-2-deoxyuridine + uridine (20 μg and 50 μg/ml, respectively; Sigma-Aldrich), to block glial proliferation. The medium was replaced 4 days later by 10% horse serum in MEM. The same medium was used after the transfection and no further changes were made until cultures were used for experimentation.

Transfection

Transfection was conducted at 7 to 8 days in vitro. A Lipofectamine 2000 (Invitrogen) mix was prepared at 1 μl per well with 50 μl per well OptiMEM (Invitrogen) and incubated for 5 min at room temperature in the hood. Separately, a mix of 2 μg per well total DNA in 50 μl per well OptiMEM was prepared and also incubated for 5 min. Then, two preparations were co-incubated for 15 min at room temperature in the hood. This mix was then added to the each culture well at the amount of 100 μl per well, and allowed to induce the transfection during 3 hours before a final change of medium. In most cases, at least 20 neurons/well were transfected. In these experiments SP-short subcloned into pEGFP-C1 (BD Biosciences, Clontech) [19] or into mCherry were used. For morpholog-

ical analysis, a blue fluorescent protein (BFP) plasmid was cotransfected with the SP construct. Co-transfected cells displayed no apparent differences in spontaneous calcium activity, morphology, spine density and survival compared with BFP-only transfected cells or non-transfected cells. The distribution and pattern of the expression of the SP plasmid were similar to those of the endogenous SP [125]. Co-transfection efficiency for the plasmids using this method is nearly 90%. Experiments were conducted routinely at 7 to 10 days after transfection. Cultures were used at the same age for comparisons.

Imaging and drug application

Cultures were incubated for 1 hour in high affinity Fluo-2 acetoxymethyl (AM) (2 μM; ; Invitrogen, Carlsbad, CA, USA) containing recording medium containing 129mM NaCl , 4mM KCl, 1 mM $MgCl_2$, 2 mM $CaCl_2$, 4.2 mM glucose, and 10 mM Hepes; pH was adjusted to 7.4 with NaOH, and osmolality to 320 mosm with sucrose. Alternatively, K+ Fluo-4 salt solution was injected into transfected neurons with sharp micropipettes and allowed to diffuse for 0.5 hours before imaging. In the latter case, no BFP transfection was required and cell morphology could be detected based on Fluo-4 basal fluorescence. After loading of calcium sensor cells were imaged using and LSM 880 Zeiss (Germany) upright confocal microscope equipped with 40x1 numerical aperature (NA) water-immersion objective. Spontaneous calcium transients were detected in both SP and BFP co-transfected and non-transfected neurons using fast scan mode (10 to 20 Hz per frame). Bath application of the blockers TTX (1 μM), APV (50 μM) and DNQX (20 μM) (all from Sigma-Aldrich) was used to eliminate action potentials, postsynaptic potentials, neurotransmitter release and activity-induced calcium transients. Caffeine (5 mM) was added using quick bath perfusion and then washed out rapidly, while fast calcium transients from dendritic segments with SP+ and SP- spines of cotransfected cells were recorded. In some cases, a caffeine-containing patch pipette (diameter 1 to 2 μm, 15 mM) was positioned close to individually identified dendritic segments of a SP-transfected neuron and responses to local pressure application of caffeine in neighboring SP+ and SP- spines of the same dendritic segment were imaged. Images were obtained at high speed for detecting rapid changes in $[Ca^{2+}]_i$ (10 to 20 Hz, restricted, horizontally oriented scan region). In latter case, distance between the caffeine containing pipette and individual dendritic spines was chosen carefully to be similar for all cases.

Data analysis

Fluorescence intensity was calculated using ZEN (Zeiss, Germany), ImageJ (National Institutes of Health, Bethesda, MD, USA) and MATLAB software (MathWorks Inc., Natick, MA, USA). Dendritic protrusions were categorized into spine types based on their morphological measurements. SP+ and SP- dendritic spines that were used for calcium imaging were identified in BFP-transfected of Fluo-4-microinjected neurons and analyzed independently. Statistical comparisons were made with t tests or ANOVA, as appropriate, using MATLAB and KaleidaGraph (Synergy Software, Reading, PA,USA).

Experiments using STED

AAV production and injection

This was performed as previously described in [42]. Briefly, a green fluorescent protein (GFP) cassette was placed under the control of a hSynapsin promoter in a serotype 9 adeno-associated virus (AAV). Two-month old C57Bl6 mice were anesthetized under ketamine/xylazine in 0.9% NaCl. AAVs were diluted in phosphate-buffered saline (PBS) to 1.02 $\times$ 1013 vg/ml, and 1 μl of virus was injected into the hippocampal region. After 2 weeks, the mice were euthanized and the brains extracted after 2% paraformaldehyde/PBS intracardiac perfusion.

Immunohistochemistry and STED microscopy

This was also performed as previously described in [42]. Briefly, 40-μm thick brain slices were permeabilized and blocked for 2 hours in 0.25% Triton X-100/0.2% gelatin in PBS at room temperature. Primary and secondary antibodies were diluted in the same solution and incubated for 2 hours at room temperature followed by overnight at 4°C. In addition to the primary and secondary antibodies used in [42], anti-ORAI1 (mouse, 1:100; Abcam ab244352), anti-SP (guinea pig, 1:100; Synaptic Systems, 163004), anti-chicken Star Green (goat, 1:200, Abberior STGREEN-1005) and anti-guinea pig Alexa Fluor 405 (goat, 1:500; Abcam, ab175678) were used in this study.
For the distance measurements between SERCA3 and ORAI1, Z-stacks of 100 nm steps images were taken using a three color superresolution three-dimentional (3D) STED microscope [Abberior Instruments GmbH; as also described in [42]]. Note that the distances that are measured below 100nm are located in the same Z plane, as the Z step of our stack acquisition is 100nm. Thus, the errors in the distance measurements are minimized compared to 2D microscopy systems.
Superresolution was used for SERCA3 and ORAI1 channels. All channels were then deconvolved using Huygens software and analyzed using an in-house–developed plugin on ImageJ to measure the distance between two maximas in 3D (maximum distance of 400 nm as a cutoff threshold). Between 83 and 120 interactions (distance from ORAI1 to SERCA3 less than 400 nm) per slice were analyzed in the spine head, between 27 and 52 in the neck and between 45 and 88 at the base. Four slices were analyzed. The violin plots represent all the dots analyzed (378 in the head, 159 in the neck and 290 at the base).
For the presence of SP, images were taken with another set of immunostained slices with an additional 405 nm laser for the excitation of the SP-Alexa Fluor 405, using a Zeiss Axio Observer Z1 with a CSUW11 Spinning-disk scan head (Yokogawa 63 $\times$ /1.4-NA objective lens). Z stacks of 150-nm steps were taken and analyzed with ImageJ software. Colocalization frequencies were calculated over the total number of spine head analysed.

Nineteen field of views from four animals were analyzed. Sixty to 80 spine heads were analysed per field of view. Each interaction type was assigned to one of the five categories of colocalization type.

Statistical analysis

All data are expressed as means ± SEM. Statistical significance for within-group comparisons was determined by one-way ANOVAs (followed by Tukey's post-test) on GraphPad Prism.

Stochastic model of calcium dynamics and numerical simulations

Modeling and simulation of calcium diffusion in a dendritic spine

To simulate calcium transients in a spine, we use the following model: The dendritic spine geometry is made of a large spherical head connecting the dendrite by a cylindrical neck [47, 116]. We added an SA as a "spine inside a spine" with a similar geometry (Fig. 6.2A). The parameter for radii of the spine head, spine neck, SA head, and SA neck is summarized in table S2.

The motion of calcium ions are modeled with Brownian diffusion described by the stochastic equation $\dot{X} = \sqrt{2D}\dot{w}$, where w represents Wiener white noise, δ-correlated in both space and time: For distinct time and space coordinates X, X' and t, t' therefore, $\langle w(X,t)w(X',t')\rangle = \delta(X-X')\delta(t-t')$, where $\delta(.)$ is Dirac's δ function. We simulate a discretized form of this motion using the Euler's scheme: $X_n = X_{n-1} + \sqrt{2D\Delta t}\cdot\eta$. Here, $X_t = \{X, Y, Z\}$ is the position of a particle at time t, and η is a normal random variable with three independent components generated by the NumPy library of Python. The diffusion coefficient of calcium in the medium is D, while Δt is the width of a single time step (values in table S2). We chose the largest Δt such that reducing it further neither alters the calcium fluxes through SERCA pumps nor the RyR activation times.

We consider the small baseline concentration of free initial calcium in the medium to be zero, thus we introduce calcium in two ways: either we position instantaneously a total of N calcium ions at single point at the top of the spine head (fast synaptic inputs) or we introduce calcium ions one after the other according to a distribution, which follows a difference of two exponentials (the STIM1-ORAI1 pathway is described below).

After entering the spine, ions can diffuse within the spine domain until it reaches the bottom of the neck. Spine base is modeled as an absorbing boundary; thus, ions arriving at the base of the spine do not appear again in the simulation. In our model, we neglected any electrostatic interactions between the ions and the membranes of the spine or the SA, from which ions are reflected with the classical Snell-Descartes law.

Moreover, calcium ions have two valence charges that can create an electric interaction with the surface charge density located on the dendrite membrane. However, in the pres-

ence of a small calcium influx, the possible interaction of the ion with the rest of the medium is described by the Debye length in an order of a few nanometers [137, 186]. Therefore, as there is a minimum distance of 20nm between the two membranes in our model, we neglected the electro-diffusion of calcium ions.

Modeling calcium channels and pumps

Calcium extrusion pumps

Calcium extrusion pumps are located on the inner surface of the spine head, and are modeled as absorbing circular disks having a catchment radius of 10nm as previously calibrated in [47]. To match a decay time scale of 6ms recorded for calcium fluorescence in the spine head, we calibrated the number of pumps to be 50 [42]. If we increase this catchment area, we would need to reduce the number of pumps to keep this calcium decay time fixed.

Ryanodine receptors

We model RyRs as circular disks located on the surface of SA with a catchment radius of 10nm where calcium ions are bound. There are n_R=36 RyRs located at the base (Fig. 6.2A). Of these, 12 are located on the segment of the SA parallel to the dendrite. The remaining 24 form four rings (six receptors in each ring) in the SA neck. Opening of a RyR is triggered by the arrival of two calcium ions into the receptor site. When a first calcium ion arrives at a receptor, it stays bound for 10ms and then unbinds to diffuse to a distance of one Brownian step. The RyR is opened only if the second one arrives within this 10ms window. We confirmed that results in RyR opening times and probabilities are largely independent of this window size, when varied from 10ms to ∞. After the arrival of a second ion to the RyR, calcium ions are released with a delay of 0.25 ms. The number of calcium ions released per RyR starts from 8 and decays to 6 and 7, followed by another cycle of 8-7-6 as reported in [42]. After each release, RyRs are inactivated for 3 ms, during which they do not bind to calcium ions.

SERCA pumps

Classical models of SERCA pumps are based on a four-state Markov chain model, where most of the parameters are unknown (p.43, after equation 2.47 in [152]). We model here SERCA pumps using the same formulation as we previously implemented in [42] with a stochastic model of four states: 0 ions bound; 1 ion bound; 2 ions bound; and refractory state. A pump is opened by the arrival of two successive ions within a 100ms window. If a second ion does not arrive within this time, then the first ion is released at a distance given by one Brownian step. In case of an opening event, the two ions get translocated into the SA, and the pump remains inactive for its refractory period. Hence, our model uses only two parameters: the first ion's waiting time of 100ms and the refractory time of

10ms. The catchment radius of SERCA pumps R=10nm is justified by the atomic-level description given in [153]. The positioning of SERCA pumps are on the top hemisphere of the SA head, according to a uniform random distribution (Fig. 6.2A).

Influx through the STIM1-ORAI1 pathway

We do not model here explicitly the transfer of ions from the extracellular to the intracellular medium upon the activation of ORAI1 channels that form complexes with STIM1 molecules. Instead, to simulate the SOCE inputs through ORAI1 channels, we use the time course extracted from the calcium fluorescence signal of the spine head (Fig. 6.1C and fig. S3). In addition, we vary the distance d_{SA} between the plasma membrane and the SA membrane that governs the proximity between ORAI1 channels and SERCA pumps.

Simulation of LTP and LTD protocols for calcium injection

1. **LTP protocol:** The 1-s high-frequency stimulation during the LTP protocol is simulated as a series of calcium spikes into the top of the spine head. The amplitude of this spike is a decreasing number of ions proportional to the fraction E of synaptic resources in the effective state that we compute using the facilitation-depression model [45] described by

$$\frac{dR}{dt} = \frac{I}{\tau_{\mathrm{rec}}} - U_{se} R f(t) \tag{6.3}$$

$$\frac{dE}{dt} = -\frac{E}{\tau_{\mathrm{inac}}} + U_{se} R f(t) \tag{6.4}$$

$$I = 1 - R - E \tag{6.5}$$

   Here I and R are the inactive and recovered fractions of synaptic resources that add up to the normalized amount of total resources with value 1. The two time constants τ_{rec}=0.3s and τ_{inac}=0.2s govern the recovery and the inactivation of the resources, respectively [187]. The stimulation protocol is modeled by the function $f(t)$ made of 100Hz train of $\delta-$Dirac impulses during 1s: $f(t) = \sum_{\lambda=1}^{100} \delta(t - 0.01\lambda)$. Last, U_{se} is the fraction of synaptic resources in the recovered state getting activated by each instantaneous input. During the first 250ms that we simulated, the value of E decayed from 1 to 0.47, and depended weakly on U_{se}. This decay mimics the gradual reduction of the synaptic input amplitude into spines.
   In addition to these injections of fast calcium spikes, we also maintain the model of slow input of calcium through ORAI1 channels [similar to Fig. 6.2C (i) with N=300 ions during 2s]. During the simulation of the refilling phase of the LTP protocol [Fig. 6.5D (ii)], the high-frequency stimulation is absent; hence, only this slow calcium influx was available.

2. **LTD protocol:** For each stimulation pulse of LTD, we injected calcium ions instantaneously every 1 s over a duration of 1 min (we only simulate the first 30s of the protocol to investigate the SA calcium dynamics). We predetermined the number of ions contained in injected pulse to be constant at N=300 or 500. In addition to these fast injections, throughout all LTP simulations we also inject a repetition of the slow calcium influx as mentioned before.

Chapter 7

Supplementary information: Nanoscale molecular architecture controls calcium diffusion and ER replenishment in dendritic spines

7.1 Asymmetric calcium dynamics between SOCE and synaptic transients

We compare in Fig. 7.1 calcium transients during synaptic inputs (solid lines) and SOCE (dashed) in the head (red) versus base (blue) of a dendritic spine. The synaptic input transient peaks about 0.25s after the stimulation, while the SOCE increase is very shallow with a maximum around 0.6s. Interestingly, this difference is even more prominent in the base area, suggesting that during SOCE, only a small amount of calcium could reach the base.

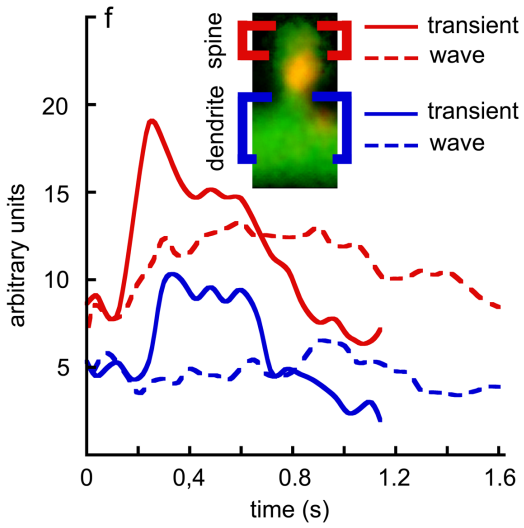

Figure 7.1: **Comparison of synaptic activity-related calcium transient to store-operated calcium entry (calcium wave).** Cultured hippocampal neuron was transfected with synaptopodin-cherry (SP) plasmid at the age of 1 day after plating. At the age of 3 weeks the neuron was loaded with Fluo-2 calcium sensor and spontaneous activity was recorded using fast scan of Zeiss-880 confocal microscope. A randomly selected area contains a typical SP+ mushroom spine with post synaptic density (PSD) area (marked in red) and adjacent dendritic shaft (blue). A typical single spontaneous event in both compartments is shown using solid lines. Afterwards, calcium was removed from extracellular medium for 15 minutes in the presence of DNQX (7μM), APV (20μM) and TTX (1 μM) which depleted calcium stores and did not allow new calcium ions to enter the spine as a result of synaptic activity. Then initial calcium concentration (1.5 mM) was recovered in the presence of blockers, following which slow and low amplitude calcium waves were observed in the PSD area, but not in the shaft, indicating the activity of store-operated calcium entry (SOCE) mechanism. A typical waves are shown with dotted lines. The timescale is twice longer and the SOCE amplitude is smaller compared to the synaptic activity.

7.2 Time-dependent calcium refilling in SA in the presence of activity blockers

To investigate the time course of SOCE and SA refilling, we develop a timelapse protocol after depleting the SA with a caffeine application at time t=0. Afterwards, at different time points of t = 1, 2, 5 and 10 minutes, we find that for SP+, the amount of released calcium is proportional to the time we waited until the second application (Fig. 7.2A). This result was specific to SP+ spines. In addition, when SOCE is completely abolished in the presence of 50 μM 2-aminoethoxydiphenylborane: 2-APB (Fig. 7.2B-C), calcium is not released from the SA at a significant amount. These results confirm that SOCE refills the SA with a timescale of a few minutes and the refilling dominates any possible calcium leakage.

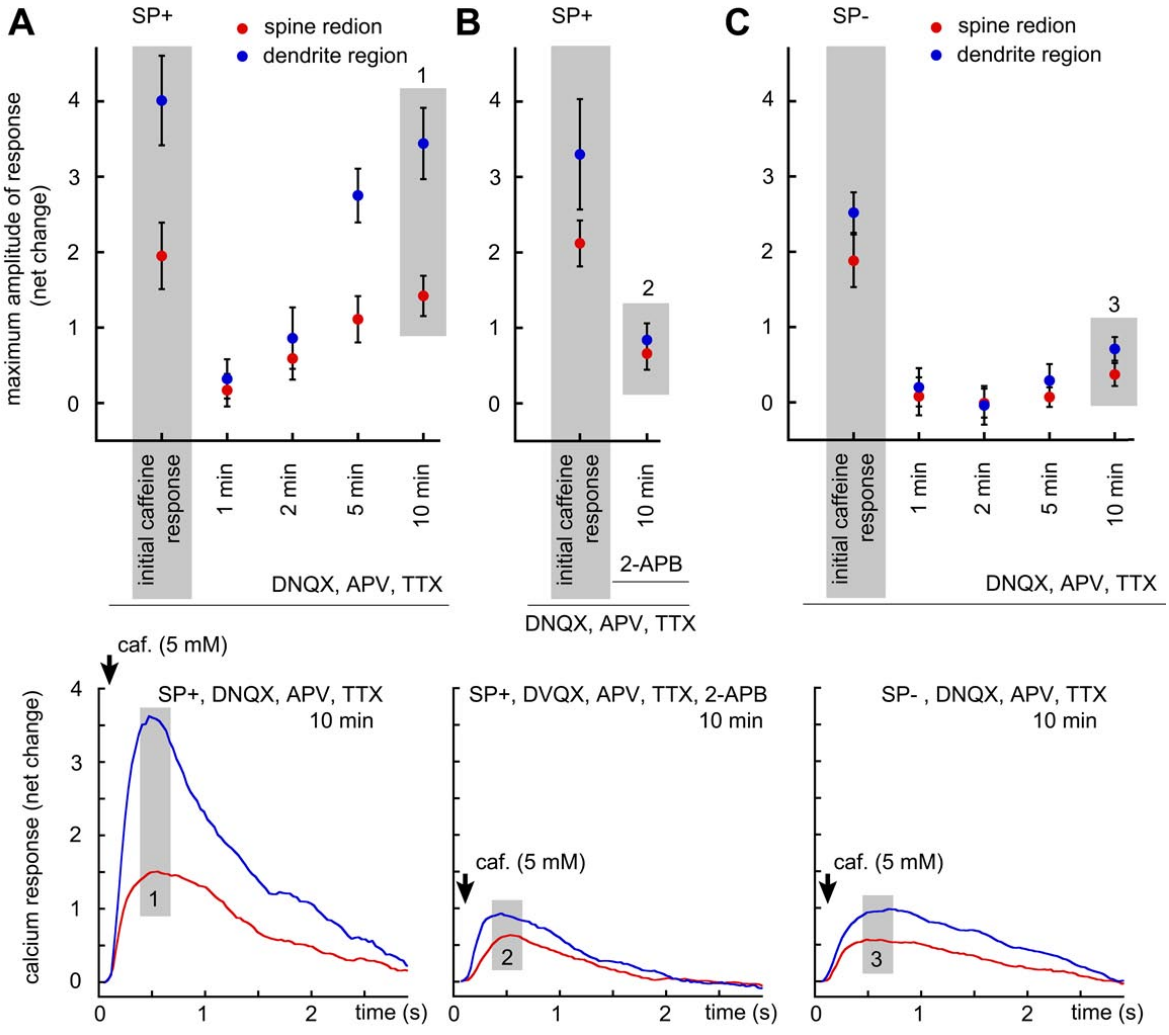

Figure 7.2: **Synaptopodin-associated local calcium storage of dendritic spines reveals time-dependent refilling ability in the presence of activity blockers.** Hippocampal neurons were transfected with synaptopodin-cherry (SP) and blue fluorescent protein (BFP) as a morphological marker. At the age of 3 weeks after plating, cultures were used in acute experiments. The channels/receptors serving a source of calcium entry into the neurons during normal cell activity were suppressed using a mixture of the following blockers: AMPAR was blocked using DNQX (7 μM), NMDAR was blocked with APV (20 μM) and voltage-gated channels were disabled using TTX (1 uM). After 10 minutes of preincubation with blockers, bath application of caffeine (5 mM) was performed to deplete SP-associated, ryanodine-dependent calcium stores and the responses were recorded form the spine head and the adjacent dendritic shaft local areas (as shown in Fig. 1). According to the presence of SP puncta, the spines were divided into SP-positive (SP+) and SP-negative (SP-). Ten neighboring spines of about the same sizes and shapes were recorded in each group (3 experiments). Following the initial caffeine application and extensive wash (during about 30 s), caffeine was applied again at the time points of 1, 2 5 and 10 minutes after the initial application, all in the presence of blockers. The results are presented in A for SP+ and C for SP- spine/dendrite pairs. Panel B represents a similar experiment with 5 SP+ spines in the presence of 2-aminoethoxydiphenylborane (2-APB, 50 μM), which is a store-operated calcium (SOC) blocker at the given high concentration. In this case, only 10 minutes time point was tested.

7.3 Quantifying the SOCE transient signal

For the slow transients, by fitting with a difference of two exponentials $J_{in}(t) = \frac{A}{1/a-1/b}(e^{-at} - e^{-bt})$, we obtained the parameter values $a = 1.53s$ and $b = 1.43s$.

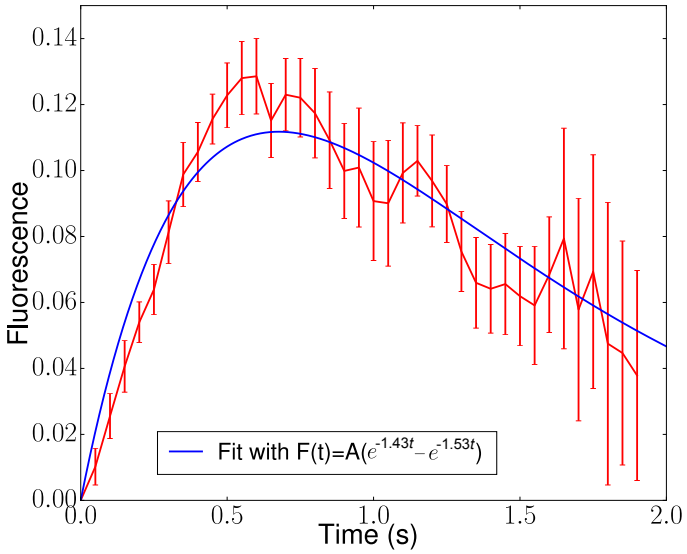

Figure 7.3: **Quantification of slow calcium transient timescales from store-operated calcium entry activation.** The slow calcium fluctuations is induced by the application of neuron activity blockers in synaptopodin-positive spines (data presented in Fig. 1C bottom). Average dataset with 18 trials (mean in red) fitted by the difference of two exponentials (blue).

We also computed the autocorrelation functions of the two time series recorded in the spine head and the base shown in Fig. 1C for lags up to 10s:

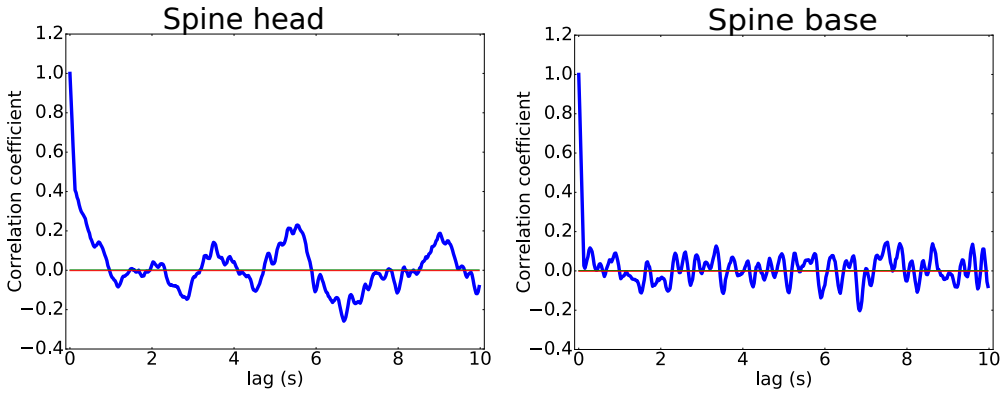

Figure 7.4: **The auto-correlation of the calcium activity signals in spine head and base.** The two signals start to de-correlate (first zeros) at 0.96s and 0.56s.

7.4 Mean-field model to compute the probability to activate CICR through RyRs

We present here a mean-field model to compute the release probability of calcium from RyRs located at the base of a spine containing a SA, triggered by a calcium influx to the head. The model disregards the geometry by considering the spine as a homogeneous compartment, but leads to explicit formulas. The influx of calcium ions into the spine head is modeled by the function $J(t)$.
The probability P_2 to initiate CICR is the probability that at least one RyR is activated during a calcium transient. This activation is induced by the binding of two calcium ions to a single RyR among a total of N_R receptors. We derive below an equation for the number $n_2(t)$ of RyRs containing 2 ions for the first time. In this approach, we approximate the arrival of a single ion to a single receptor by a Poissonian rate constant λ. When there are $n_1(t)$ RyRs bound to one calcium ion, the rate of arrival of single calcium ion to one of the RyRs is:

$$\lambda(t) = \lambda n_1(t). \tag{7.1}$$

When one of the $n_1(t)$ RyRs is bound to a second calcium ion, this event leads to RyR activation. For the first times of such activation t_a, the number of RyR bound to two ions $n_2(t_a)$ jumps to 1. Therefore, we have the following conservation conditions before the termination step:

$$\begin{aligned} n_1(t) + n_0(t) &= n_R & (7.2)\\ n_2(t) &= 0 \text{ for } t < t_a. & (7.3) \end{aligned}$$

The first identity is based on the pre-activation condition where a RyR either contains zero or one ion. The second constraint ensures that before any activation events, the number of RyRs containing 2 ions is zero. To compute the probability of a RyR activation, we consider the probability $\tilde{p}_2(t) = Pr\{n_2(t) = 0\}$ that there are no RyRs bound to two calcium ions at time t. During an interval between t and $t + \Delta t$, when we assume that that no ions out of the total $m_{ca}(t)$ calcium ions leave the spine, the probability of a second ion binding to one of the $n_1(t)$ single-bound RyRs is:

$$Pr\{n_2(t + \Delta t) = 0\} = Pr\{n_2(t) = 0\}(1 - \lambda n(t) n_1(t) \Delta t). \tag{7.4}$$

That is

$$\dot{\tilde{p}}_2 = -\lambda n_1 m_{ca} \tilde{p}_2. \tag{7.5}$$

Thus integrating with the initial condition that there are no RyRs bound to two calcium ions, we obtain for the probability $Pr\{n_2(0) = 0\} = 1$

$$\tilde{p}_2(t) = e^{-\lambda \int_0^t n_1(u) m_{ca}(u)} du. \tag{7.6}$$

Taking the first time that two calcium ions binding to one RyR as τ_2, we can now compute the probability $p_2(t) = Pr\{n_2(t) = 1\} = Pr\{\tau_2 < t\}$ that a second binding event occurs before time t. Using the identity

$$Pr\{n_2(t) = 0\} + Pr\{n_2(t) = 1\} = 1, \tag{7.7}$$

we obtain the expression for the probability

$$Pr\{n_2(t) = 1\} = 1 - e^{-\lambda \int_0^t n_1(u) m_{ca}(u) du}. \tag{7.8}$$

We shall now use a mean-field approximation to derive a coupled system of equations governing $m_{ca}(t)$, $n_1(t)$ and $p_2(t)$. By using the rate μ for the unbinding of calcium to RyRs, we obtain the relation for the number of RyRs bound to one calcium ion (prior to any RyR binds to two ions):

$$\dot{n}_1 = -\mu n_1(t) + \lambda m_{ca}(t) n_0(t) - \lambda m_{ca}(t) n_1(t). \tag{7.9}$$

Here the first term measures unbinding events while the second term measures the binding events proportional to the number of available sites $n_0(t)$ and the number of calcium $m_{ca}(t)$. The third term corresponds to the binding of the second ion to one of the $n_1(t)$ RyRs containing one calcium ion. By eliminating n_0 with Eq.7.2 we obtain:

$$\dot{n}_1 = -\mu n_1 + \lambda m_{ca}(n_R - 2n_1). \tag{7.10}$$

The mass-action law for calcium is

$$\dot{m}_{ca} = J(t) - \nu m_{ca} - \lambda m_{ca}(n_R - n_1) + \mu n_1, \tag{7.11}$$

where $J(t)$ is the calcium influx rate into the spine. The extrusion rate of calcium from the spine (by calcium pumps and arrivals at the absorbing boundary in the base) is ν, thus the total extrusion (which is proportional to the mean number of calcium ions in the spine) is given by the second term νm_{ca}. The third term accounts for the binding of calcium to one of the unoccupied RyRs. This binding also has the rate constant λ, and is also proportional to the number $n_0 = n_R - n_1$ of unoccupied receptors as well as to m_{ca}. The final term measures the unbinding of calcium ions from some of the n_1 RyR-calcium bindings with the rate μ. In summary, we obtain the system of equations:

$$\begin{aligned} \dot{n}_1 &= -\mu n_1 + \lambda m_{ca}(n_R - 2n_1) \\ \dot{m}_{ca} &= J(t) - \nu m_{ca} - \lambda m_{ca}(n_R - n_1) + \mu n_1 \\ \dot{p}_2 &= \lambda n_1 m_{ca}(1 - p_2). \end{aligned} \tag{7.12}$$

We now explore the solution under the two conditions:

1. the ions are injected instantaneously, modeled with a Dirac's delta function in time, or equivalently with the initial condition $m_{ca}(0) = N_0, n_1(0) = 0, p_2(0) = 0$,

2. a slow injection rate, modeled by $J_{inj}(t) = A(e^{-\lambda_1 t} - e^{-\lambda_2 t})$ with the initial condition $m_{ca}(0) = 0, n_1(0) = 0, p_2(0) = 0$.

Parameters λ_1, λ_2 and A can be calibrated to account for empirical data. Our goal is to compute the probability to ever activate a RyR by two ions, which is obtained by taking the limit $t \to \infty$ in Eq. 7.8:

$$P_2 = Pr\{n_2(\infty) = 1\} = 1 - e^{-\lambda \int_0^\infty n_1(u) m_{ca}(u) du}. \tag{7.13}$$

We are also interested in the relation between this probability P_2 and the parameters such as the flux $J_{inj}(t)$, the initial condition and the rate constants μ, ν and λ.

7.4.1 Parameters of the mean-field model and the numerical analysis

We solve system 7.12 numerically for the three variables $m_{ca}(t)$, $n_1(t)$ and $p_2(t)$ under the two input conditions (Fig. 7.5). Here we scaled the total number of RyRs to one (N_R=1), as a representation of a possible cluster of receptors. We use the forward rate $\lambda = 6s^{-1}$, which is the reciprocal of the mean first passage time of a calcium ion to a target receptor at the spine base (approximated as $166ms$ in [188]). For the unbinding rate constant, we use the value $\mu = 38s^{-1}$ [189]. Finally, we model calcium clearance with an exponential rate constant of $\nu = 1000s^{-1}$ when there are pumps, and $\nu = 100s^{-1}$ when there are no pumps. We summarize these parameters in Table 7.1.
The numerical values obtained for the probability p_2 (Fig. 7.5 two bottom plots) show that the approximations from the mean-field model are in excellent agreement with the stochastic simulations of the biophysical model (Fig. 7.8 Top plots).

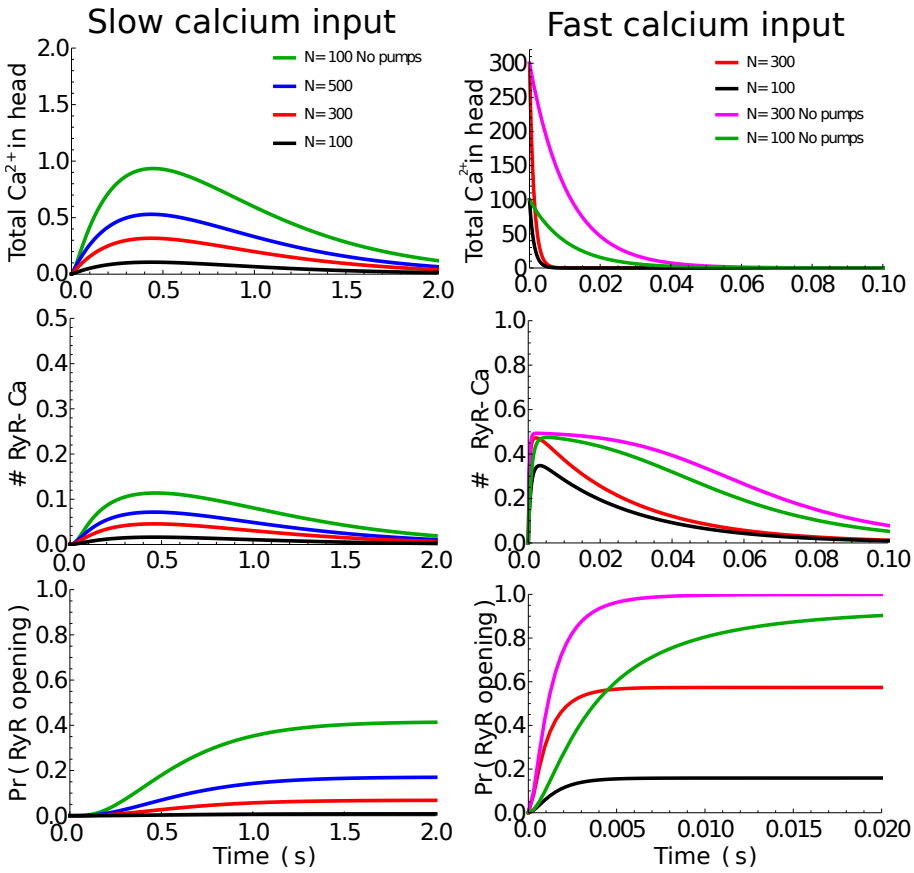

Figure 7.5: **Consequences of slow (A) and fast (B) calcium inputs in a homogeneous model of a dendritic spine.** The total number of calcium $m_{ca}(t)$, the number of RyRs occupied by a single RyR $n_1(t)$ and the probability of opening one RyR $p_2(t)$ are shown in Top, Middle and Bottom plots, respectively. Slow injection rate modeling the STIM1-ORAI1 inputs is similar to Fig. 2Ci, while the fast, synaptic inputs are modeled with a Dirac's Delta functions at t=0. Presence and absence of pumps are modeled with different extrusion rates ν (see Table 7.1 for parameter values).

Finally, SOCE-based refilling is associated to a low probability of RyR release with a small number of injected ions (<600), in contrast to the higher number of calcium ions (>600) entering with synaptic activation that almost surely results in a SA transient depletion by RyR-triggered CICR (Fig. 7.6). Therefore, the RyR opening probability for the slow and fast injection regimes has a clear separation with the difference in the total number of injected ions.

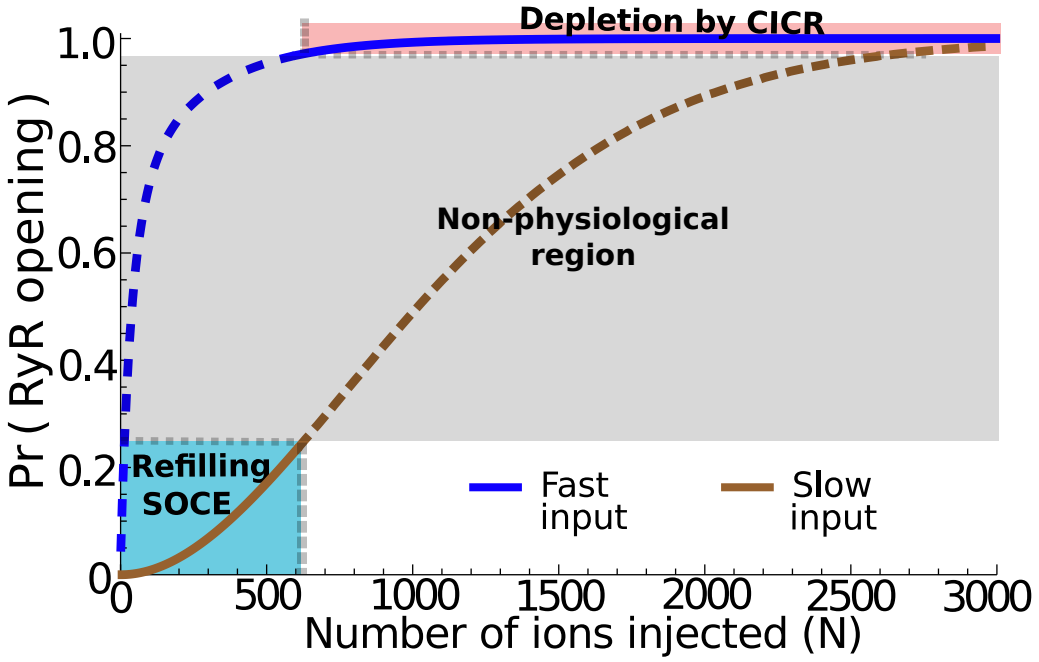

Figure 7.6: **Distinct physiological separation of the two pathways through the modulation of RyR opening probability**. In the conditions of slow inputs with 0-600 ions in 2s, RyR opening probability remains below 0.25, thus the refilling of SA is dominant (light blue area, solid brown curve). During fast, synaptic inputs with more than 600 ions, RyR probability guarantees CICR and SA depletion that increases calcium level at the spine base (pink area, solid blue curve).

Table 7.1: Parameters of the mean-field model

Parameter name	**Symbol**	**Value**
Arrival rate of calcium to a RyR	λ	$6s^{-1}$
Calcium unbinding rate from RyR	μ	$38s^{-1}$
Clearance rate by calcium pumps	ν	$1000s^{-1}$
Clearance rate (without calcium pumps)	ν	$100s^{-1}$

7.4.2 Analytical exploration of the fast injection regime $J(t) = N\delta_0(t)$

We now derive an analytical expression for the probability of having 2 ions bound to one RyR during a fast calcium transient activation

$$P_2 = 1 - e^{-\lambda \int_0^\infty n_1(u) m_{ca}(u) du}. \tag{7.14}$$

We shall now consider the limit of a large number $N \gg 1$ of calcium ions. In that case, since the fraction of bound calcium ions is small compared to the total number, we neglect this bound fraction and approximate the solution for the free calcium ion in system 7.12, $m_{ca}(t) \approx Ne^{-\nu t}$. Thus the approximation for the second equation is

$$\dot{n}_1 + \mu n_1 = \lambda m_{ca} N_R. \tag{7.15}$$

A direct integration leads to

$$n_1(t) \approx \lambda N_R N \frac{e^{-\mu t} - e^{-\nu t}}{\nu - \mu}. \tag{7.16}$$

The probability to ever activate a single RyR is computed from

$$\int_0^\infty n_1(u) m_{ca}(u) du = \lambda N_R N^2 \int_0^\infty e^{-\nu t} \frac{e^{-\mu t} - e^{-\nu t}}{\nu - \mu} dt = \frac{\lambda N_R N^2}{2\nu(\nu + \mu)}. \tag{7.17}$$

Finally, we obtain

$$P_2 = 1 - e^{-\frac{\lambda N_R N^2}{2\nu(\nu+\mu)}}, \tag{7.18}$$

which tends asymptotically to 1, as the number N of calcium ions increases. Moreover, as the extrusion rate ν increases, $P_2 \approx \frac{\lambda n_R N^2}{2\nu^2}$ tends to zero.

7.4.3 Analysis of the slow calcium injection rate during STIM1-ORAI1 activation

We derive here an analytical formula for the probability P_2 during the slow calcium input from the SOCE that we approximate as the difference of two exponentials

$$J_{inj}(t) = A(e^{-at} - e^{-bt}). \tag{7.19}$$

First we consider the total number of calcium ions in the compartment that can be approximated by the equation

$$\dot{m}_{ca} = J(t) - \nu m_{ca}, \tag{7.20}$$

leading to

$$m_{ca}(t) \approx A(\frac{e^{-\nu t} - e^{-at}}{\nu - a} - \frac{e^{-\nu t} - e^{-bt}}{\nu - b}). \tag{7.21}$$

We are left with estimating the number of bound RyRs given by Eq.7.15:

$$\dot{n}_1 + \mu n_1 = \lambda N_R A(\frac{e^{-\nu t} - e^{-at}}{\nu - a} - \frac{e^{-\nu t} - e^{-bt}}{\nu - b}). \tag{7.22}$$

Thus

$$n_1(t) = \lambda N_R A \left(\frac{1}{a-\nu} \left(\frac{e^{-\mu t} - e^{-\nu t}}{\nu - \mu} - \frac{e^{-\mu t} - e^{-at}}{\mu - a} \right) - \frac{1}{b-\nu} \left(\frac{e^{-\mu t} - e^{-\nu t}}{\nu - \mu} - \frac{e^{-\mu t} - e^{-bt}}{\mu - b} \right) \right).$$

After integrating,

$$\int_0^\infty n_1(u) m_{ca}(u) du = \frac{\lambda N_R A^2}{2} \frac{(b-a)\left((\mu+b+2\,\nu)\,a^2 + (\mu+b+2\,\nu)\,(b+\nu+\mu)\,a + (\mu+\nu)\,(b+\nu)\,(b+\mu)\right)}{a\nu\ (\mu+\nu)\,(b+\nu)\,(b+\mu)\,(a+\nu)\,(a+\mu)\,(b+a)} \tag{7.23}$$

We find an expression for the RyR activation probability

$$P_2 = 1 - e^{-\frac{\lambda N_R A^2}{2} \frac{(b-a)\left((\mu+b+2\,\nu)\,a^2 + (\mu+b+2\,\nu)\,(b+\nu+\mu)\,a + (\mu+\nu)\,(b+\nu)\,(b+\mu)\right)}{a\nu\ (\mu+\nu)\,(b+\nu)\,(b+\mu)\,(a+\nu)\,(a+\mu)\,(b+a)}}. \tag{7.24}$$

7.4.4 Conditional time $\bar{\tau}_2$ for RyR activation when ions can be expelled from the spine head

We compute here formally the mean time for RyR to be activated starting from the moment when calcium ions are injected. This activation time τ_2 can be computed from model 7.12. Indeed,

$$\begin{aligned} \bar{\tau}_2 &= \int_0^\infty t \frac{d}{dt} Pr\{\tau_2 < t | \tau_2 < \infty\} dt \\ &= \int_0^\infty t \frac{d}{dt} \frac{Pr\{\tau_2 < t, \tau_2 < \infty\}}{Pr\{\tau_2 < \infty\}} dt \\ &= \int_0^\infty \frac{Pr\{\tau_2 < \infty\} - Pr\{\tau_2 < t\}}{Pr\{\tau_2 < \infty\}} dt. \end{aligned} \tag{7.25}$$

$$\tag{7.26}$$

Using relation 7.13, we obtain

$$\bar{\tau}_2 = \frac{\int_0^\infty (e^{-\lambda \int_0^t n_1(u) m_{ca}(u) du} - e^{-\lambda \int_0^\infty n_1(u) m_{ca}(u) du}) dt}{1 - e^{-\lambda \int_0^\infty n_1(u) m_{ca}(u) du}}. \tag{7.27}$$

We approximate this mean time by rewriting relation 7.27 using that

$$e^{-\lambda \int_0^t n_1(u)m_{ca}(u)du} - e^{-\lambda \int_0^\infty n_1(u)m_{ca}(u)du} = e^{-\lambda \int_0^t n_1(u)m_{ca}(u)du}(1 - e^{-\lambda \int_t^\infty n_1(u)m_{ca}(u)du}) \quad (7.28)$$

and Taylor's expansion, $1 - e^{-X} = X + o(X)$ for small X, thus

$$\bar{\tau}_2 \approx \lambda \int_0^\infty \left(\int_t^\infty n_1(u)m_{ca}(u)du \right) e^{-\lambda \int_0^t n_1(u)m_{ca}(u)du} dt. \quad (7.29)$$

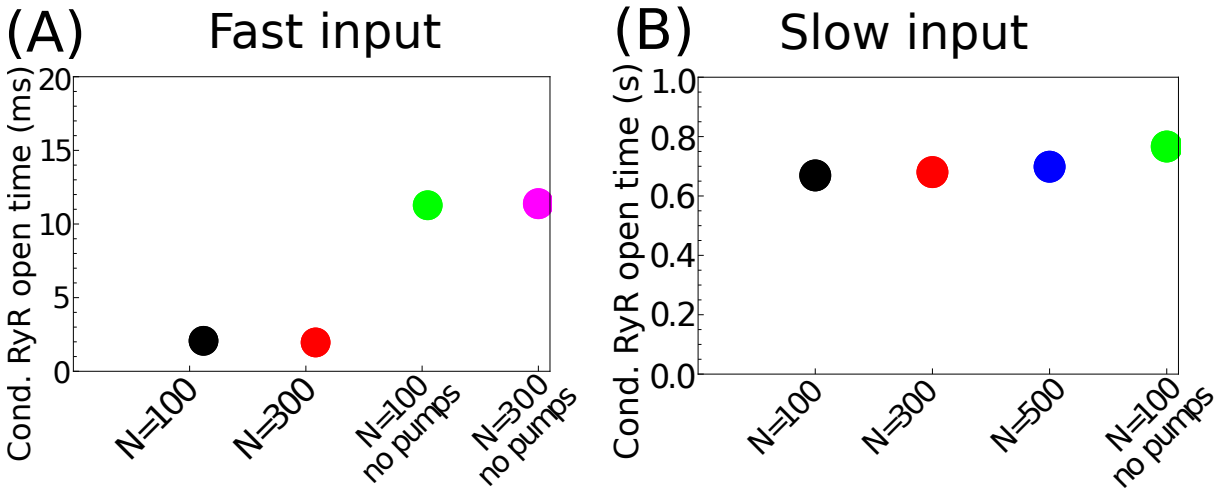

Figure 7.7: Conditional RyR opening times for fast (A) and slow (B) inputs computed from formula 7.29 using the parameter values corresponding to the conditions described in Fig. 7.5.

7.4.5 Derivation of the mean-field calcium-SA interaction from the Master equations

In this section, we present the Master equations [95] [72] [190] that we used to derive the mean field equation. We start with the change between time t and $t + \Delta t$ of the probability for not having 2 ions bound to a single RyR. It is given by

$$Pr\{n_2(t + \Delta t) = 0\} = \sum_{k,q} Pr\{n_2(t) = 0|q, k\} Pr\{n_1(t) = q, m_{ca}(t) = k\}(1 - \lambda qk\Delta t) \quad (7.30)$$

Thus if we use the joint probability $p_{q,k}(t) = Pr\{n_1(t) = q, m_{ca}(t) = k\}$ for having q RyR bound to one ions and the total of free calcium ions is k we get the different equation:

$$\dot{p}_2 = -\lambda \sum_{k,q} Pr\{n_2(t) = 0|q, k\} qkp_{q,k}(t) \quad (7.31)$$

and the conditional probability satisfies:

$$Pr\{n_2(t+\Delta t)=0|q,k\} = Pr\{n_2(t)=0|q,k\}(1-\lambda qk\Delta t), \tag{7.32}$$

which leads with $a_{q,k}(t) = Pr\{n_2(t)=0|q,k\}$ to the different equations:

$$\begin{aligned} \dot{a}_{q,k} &= -\lambda qk a_{q,k} \\ a_{q,k} &= A_{k,q}\exp\{-\lambda qkt\}, \end{aligned} \tag{7.33}$$

where $A_{k,q}$ are constants. Finally, we obtain the Markov chain (not considering the boundary equation)

$$\begin{aligned} p_{q,k}(t+\Delta t) &= p_{q,k}(t)(1-(\nu k+\mu q+\lambda k(n_R-q))\Delta \\ &+ \nu(k+1)\Delta p_{q,k+1}(t)+\mu(q+1)\Delta t p_{q+1,k}(t)+\lambda k(n_R-q+1)\Delta t p_{q-1,k}(t). \end{aligned} \tag{7.34}$$

Thus, using the boundary equations, we obtain the full system:

$$\begin{aligned} \dot{p}_{q,k}(t) &= -(\nu k+\mu q+\lambda k(n_R-q))p_{q,k}(t)+\nu(k+1)p_{q,k+1}(t) \\ &+ \mu(q+1)p_{q+1,k}(t)+\lambda k(n_R-q+1)p_{q-1,k}(t) \\ \dot{p}_{q,0}(t)) &= -(\mu q)p_{q,0}(t)+\nu p_{q,1}(t)+\mu(q+1)p_{q+1,k}(t) \\ \dot{p}_{n_R,k}(t) &= -(\nu k+\mu n_R)p_{n_R,k}(t)+\nu(n_R+1)p_{n_R,k+1}(t)+\mu(n_R+1)p_{n_R+1,k}(t)+\lambda k p_{n_R-1,k}(t) \\ \dot{p}_{0,k}(t) &= -(\nu k+\lambda k n_R)p_{0,k}(t)+\nu(k+1)p_{0,k+1}(t)+\mu p_{1,k}(t) \end{aligned}$$

with the initial condition

$$p_{q,k}(0) = \delta(q=0)\delta(k=N_0). \tag{7.35}$$

The process starts with the condition that no ions are inside a RyR, thus $n_1(0)=0$.

7.5 Impact of the distance between spine and SA membranes on CICR probabilities and initiation times

In Fig. 2Ci-Ciii, we studied the scenarios where calcium ions are not released from the SA. We now consider the cases where calcium ions could trigger an opening of at least one RyR, by the arrival of two calcium ions on the same receptor. One RyR activation leads to a transient depletion of SA calcium stores caused by the local calcium diffusion that can trigger the opening of in the neighbouring RyRs. We confirm here that SERCA-ORAI1 distance d_{SA} (Fig. 2A) influences the probability P_2 and initiation time of such events during fast (Fig. 7.8A) and slow (Fig. 7.8B) calcium influx conditions.
We simulated the instantaneous injection of N=100 calcium ions to the spine head (as in Fig. 2Bi), and find that the probability P_2 is less than 0.1 when the distance varies from zero to 250nm (Fig. 7.8A Top, black curve). In addition, the conditional opening time τ_2 computed over realizations where a RyR opening did occur is in the range of 15-35ms. When N=300 ion were injected, the probability P_2 increases and remains stable around 0.4-0.6 (Fig. 7.8A Top, red curve), while the conditional RyR activation times is slightly less than 20ms. When we repeated the same simulations after removing all calcium extrusion pumps, the probability P_2 increases higher than 0.75 in both N=100 (green curve) and N=300 (purple) injections as expected because more ions remain in the cytoplasm.
We confirm a non-intuitive result for RyR activation times (Fig. 7.8A bottom): for a low amount of calcium (N=100), the conditional time τ_2 increases to a value larger than 25ms, while in the presence of more calcium (N=300), the times decreases to less than 10ms. Indeed, with 300 ions, the RyR opening event is not very rare ($P_2 \approx 0.5$) and with the presence of pumps, the fastest ions that would have otherwise activated RyRs faster can disappear. Therefore, conditional RyR activation becomes faster when extrusion pumps are removed (Fig. 7.8A Bottom: red to magenta). In contrast, for N=100, the probability of RyR activation is extremely low thus triggering RyR is a rare event that must occur very fast before calcium ions are captured by pumps. When pumps are removed in this scenario, the number of realisations triggering RyR activation increases drastically leading to a high probability P_2 >0.75 (Fig. 7.8A Top, black to green) and an increase in the average conditional times (Fig. 7.8A Bottom, black to green).

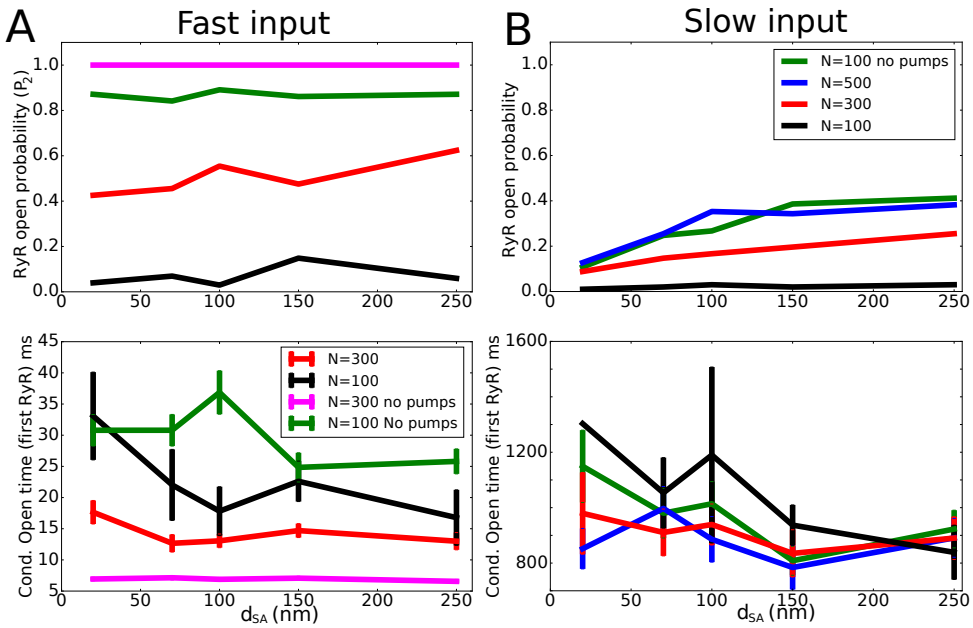

Figure 7.8: **Opening probabilities and conditional opening times of RyRs during slow and fast calcium entry. (A).** Following an instantaneous calcium entry we estimated the open probabilities (Top) for the first RyR and their conditional opening times (Bottom). Color-coded legend is common to both top and bottom panels. The simulation framework corresponds to Fig. 4F. In the black and red curves, N=100 and 300 ions were initially injected. For purple and green curves, identical conditions were used, except that the 50 extrusion pumps that were present in the spine head were removed. Probabilities, mean times and standard errors are computed with 100 trials. **(B)**. Probability and opening times computed as in A, but during a slow calcium entry shown (same as Fig. 4G), with the numbers of ions N as indicated, and without calcium pumps with N=100.

In the simulations with slow inputs (Fig. 7.8B), the probability P_2 increases gradually with the distance d_{SA} (from 0 to 250nm) and the number of ions injected (N=100, 300, 500). Interestingly, the probability with N=100 ions without pumps is equivalent to the case of N=500 injected ions with pumps. Therefore, we conclude that CICR is controlled by the distance d_{SA}, and also partially by the extrusion pumps.

7.6 Spine calcium dynamics during LTP stimulations

We present here the calcium dynamics in spines during the LTP protocol simulation starting from N=300 ions shown in Fig. 5Di and 5Dii.

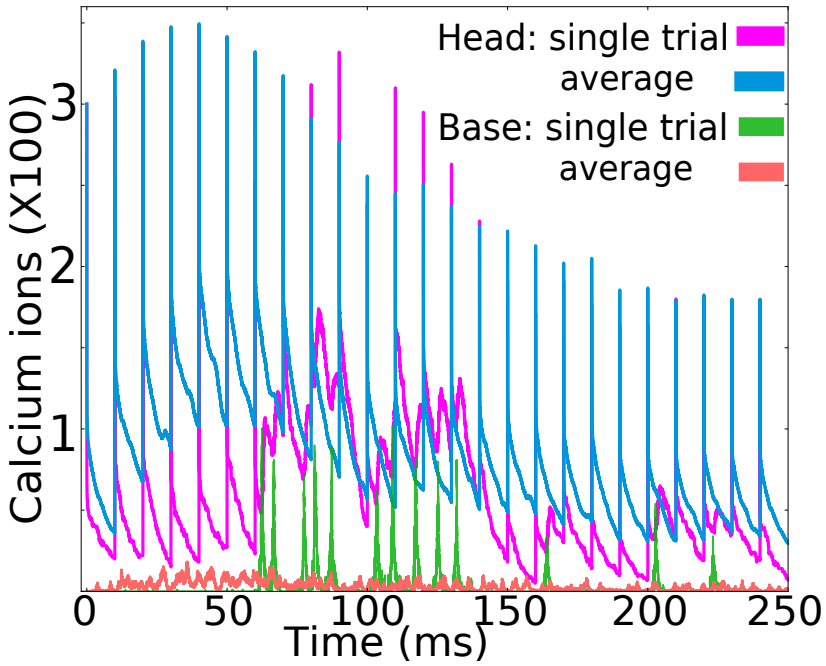

Figure 7.9: **Number of calcium ions during the first 250ms of the LTP simulations.** Each 100Hz high-frequency pulse impulse results in a strong calcium influx into the spine head. Calcium level in the head peaks with a delay of about 50ms and decays gradually with the stimulation strength (blue, averaged over 20 realizations). For each realization, calcium in the base increases due to successive arrivals and sporadic CICR events (peaks in green), while the average (orange) remains low compared to the concentration in the head.

7.7 Calcium refilling with ectopic release events

We describe here our algorithm to simulate stochastic ectopic vesicular release, a well-known phenomenon due to releasing vesicles not directly in the active zone, but on the sides [191]. Following such release events, post-synaptic currents as well as the calcium influx are much smaller compared to an evoked stimulation [192]. We study the consequences of these events by adding it to the SA replenishment simulation (Fig. 5Diii). We recall that the refilling occurs with a slow calcium influx mediated by SOCE (Fig. 2Ciii), and repeated every 2s. In addition, we introduce here ectopic release events modeled as small calcium spikes occurring every 1s with amplitudes randomly-alternating between N=25 and 50 ions. We simulated the overall calcium entry by adding these two components for a prolonged duration of one minute and observed the SA calcium refilling (Fig. 7.10 blue curve). We found that at the elapse of 30s, calcium uptake is not significantly different compared to simulation without ectopic release events (red curve).

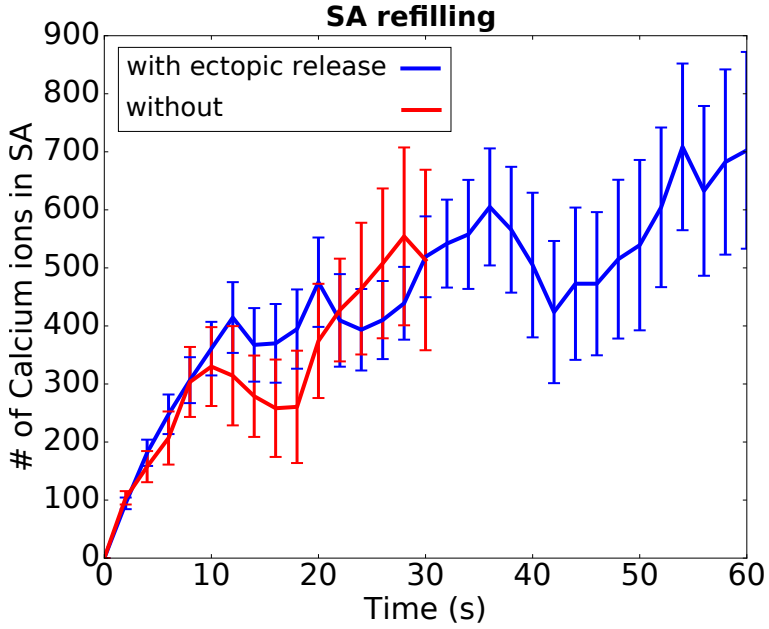

Figure 7.10: **Comparison of SA refilling with (blue) and without (red) ectopic refilling events.** In both cases slow calcium entry (similar to Fig. 2Ci with N=300 injected ions) is present. Ectopic release events (only in the blue curve) are modeled as 1Hz spikes with an amplitude that randomly switches between N=25 and 50 ions. The average and SEM values are calculated over 10 and 20 trials for the red and blue curves.

During the 30s period, 4500 ions enter the spine through the slow input. The ectopic injection contributes to about 1125 ions. However, such 25% difference in the refilling numbers is not reflected significantly in the final amount of calcium, because the ectopic release can also trigger more calcium release events from RyRs (decay phases in Fig. 7.10), interfering against the refilling process.

7.8 Spine calcium dynamics during LTD stimulations

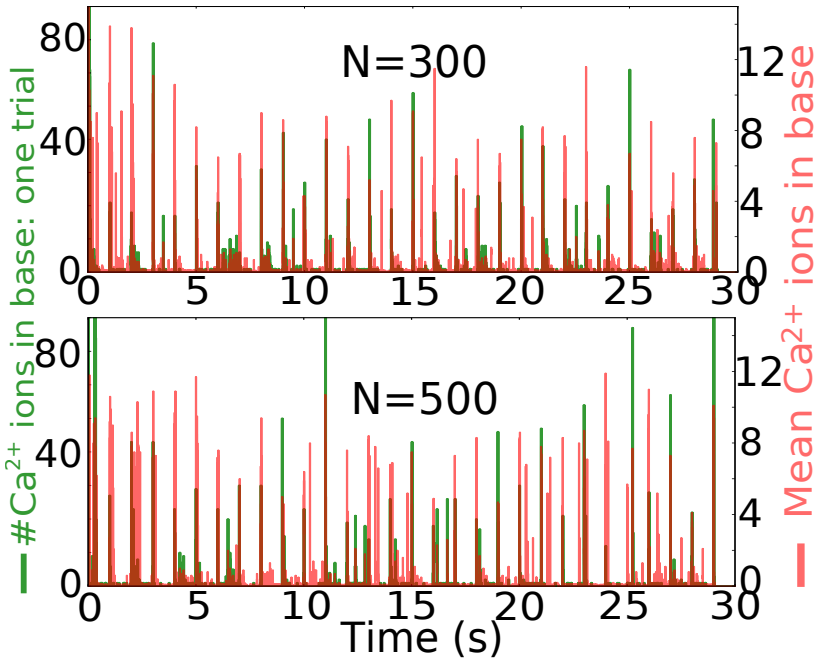

Figure 7.11: **Calcium ions at the base of a spine during the simulated LTD protocol.** For the two values of the number of injected calcium ions N=300 (top panel) and N=500 (bottom panel), we show single trials (green: left axis) and averages over 10 realizations (red: right axis).

Table S2: Parameters of the stochastic simulations

Parameter	Symbol	Value
Time step	Δt	10^{-7} s
Diffusion coefficient	D	600 $\mu m^2 s^{-1}$ [37]
Spine head radius	R	1 μm
Spine neck radius	a	0.15 μm
Spine neck length	L	1.5 μm
SA head radius	R_{SA}	0.25 μm
SA neck length	L_{SA}	1.5 μm
SA neck radius	a_{SA}	0.05 μm
Radius (RyR and SERCA)		10 nm
# SERCA pumps in the SA head	N_{SERCA}	36
# RyR in the SA base	N_{R}	36
# ions absorbed by one SERCA		2
# ions to activate one RyR		2
First Ca waiting time SER		100 ms
First Ca waiting time RyR		10 ms
Refractory period SER		10 ms
Refractory period RyR		3 ms

Chapter 8

Discussion and perspectives

Starting from fast calcium dynamics in dendritic spines measured in the timescale of a few milliseconds, I developed a framework based on extreme statistics with modeling and simulations that could explain these dynamics with the first calcium ions arriving to open a RyR. This led to the predictions regarding the nanoscale organisation of RyRs, SERCA pumps and ORAI channels in spines. I revisit here some remaining questions connected to spine's calcium-related nanophysiology as well as possible extensions of the same physical framework towards studying the timescales of other biophysical phenomena.

8.1 Future work on calcium activity

8.1.1 Downstream effects of spine calcium transients

The calcium dynamics I studied here occur mostly as the first line of activity in the durations immediately following a calcium input to spines. If the input is strong (eg. NMDA/AMPA current with a few hundreds ions entering within a few milliseconds), RyRs could get activated and trigger a CICR response. On the other hand, weak SOCE influxes through ORAI channels lead to a refilling of SA stores through SERCA pumps in a timescale of a few seconds. I also showed with simulations how the interplay between these uptake and release pathways could determine the spine's calcium dynamics for prolonged durations, particularly including the conditions following the stimulation protocols of LTP and LTD induction.

A question that remains to be answered is "what are the subsequent effects of these calcium transients, particularly in the base of the spine?". In other words, the pathways that are activated by the fast calcium increases at the base and how they determine the long term behaviour of synaptic strengths are unknown. One possible hypothesis is that calcium avalanches in the base could trigger the spine's energy supply as a release of ATP from mitochondria. It has been reported that "local" mitochondria units are present in spines [193] but their exact calcium dependency for energy supply is not understood quantitatively. The released ATP molecules could regulate plasticity mechanisms either by activating other pathways locally at the base or by diffusing into the spine head.

8.1.2 Spontaneous calcium activity in neuronal dendrites

We observed experimentally large calcium fluctuations in spine heads under an ample supply of calcium (in a calcium bath), during the blockage of synaptic inputs. We identified this as SOCE and quantified its contributions to refilling of SA stores. However, we also obtained data showing strong spontaneous calcium events in the dendrites below spines under no particular increases of the extra-cellular calcium level. These patterns occur with a rhythmic repetition in the timescales of a few seconds (Fig.8.1).
Preliminary data analysis also shows that the occurrence of such activity is more prominent in young cultures. Hence a possible physiological hypothesis is that spontaneous activity is a way of exploration to "tune" calcium dynamics towards adulthood neural activity. Therefore, a quantitative study would be interesting also from a developmental perspective of the nervous system.

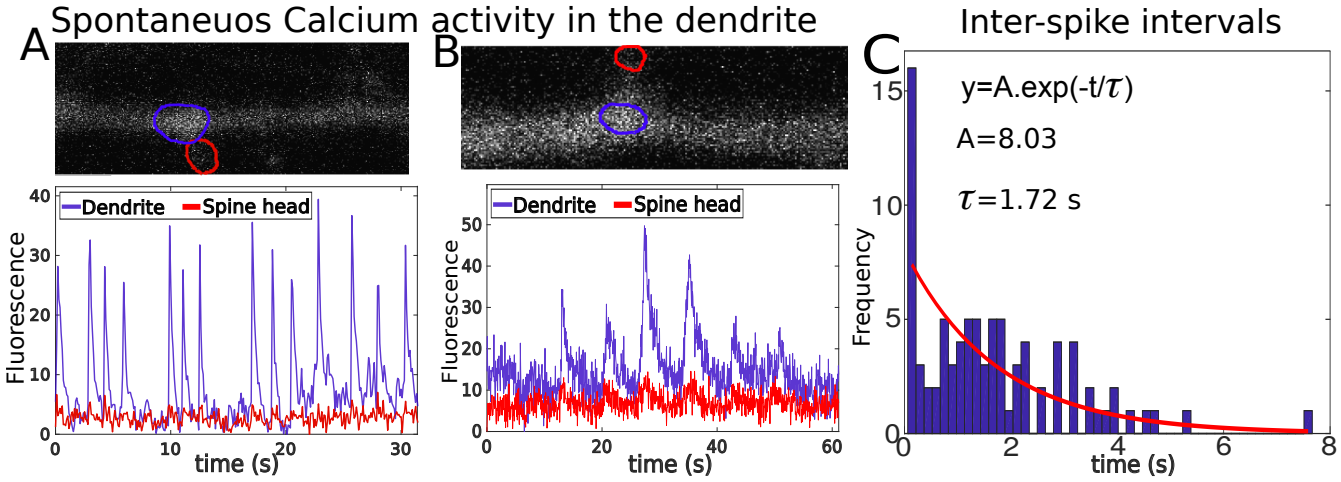

Figure 8.1: **Spontaneous calcium activity in the dendrite sections below spines. (A) & (B).** The calcium spikes measured from fluorescence imaging are strictly localised to the dendritic area near the spine base (area shown in blue, plotted also in blue), and does not propagate to the head (red). **(C).** Inter-spike intervals of two preliminary recordings, totalling 83 calcium spike events. The fit with the decaying exponential reveals a timescale of a few seconds.

A possible explanation for these activity patterns based on the nanoscale diffusion dynamics I delineated would be that these spikes arise from RyRs-induced CICR events that could occur due to random activation events by the baseline-level calcium concentration permanently present in the dendrite. Due to the scarcity of calcium ions under no input, such activation timescales could be very long compared to the milliseconds timescales of synaptic activity, and would need to be quantified in future. Computational models of dendritic activity should account not only for the distributions of RyRs, but also for the other calcium regulators along the dendrite such as local buffers, SERCA pumps and slow timescale calcium release channels such as IP3 that are not reported inside spines.

8.1.3 Expediting spontaneous activity simulations with extreme statistics

The computational framework I implemented in the thesis towards the findings about spines is a full-scale ion-by-ion simulation of many Brownian trajectories of calcium ions. This has served exceptionally well for studying the fast calcium dynamics occurring within tens of milliseconds. However, the same simulation setup would be computationally too expensive to run at the timescales of spontaneous activity, which could scale up to a few seconds. The theoretical findings of the thesis could be exploited to overcome this limitation, by accelerating the simulations that could enable expansions towards longer timescales appropriate for spontaneous activity.
By utilizing the theory of extreme statistics, it would be possible to develop a simulation algorithm that takes into account only the timing of the first few ions that trigger a calcium response in a cluster of receptors. Once the parameters such as the first activation time are determined, such implementation based on extreme statistics would eliminate the need to simulate the whole system of ions with their individual Brownian dynamics. Thereby the computational cost could be reduced drastically. Such framework would not only enable to delineate the mechanisms of calcium dynamics in microdomains containing a few spines, but would also assure the possibility to simulate long dendrites and even the spontaneous activity in whole neurons or astrocytes.

8.2 Theoretical generalizations to other biophysical systems

8.2.1 Redundancies with obstacles in three dimensions

During the theoretical and computational work of my thesis, I generalised the framework of extreme statistics, particularly concerning the dependency of fastest arrivals on the initial number of particles up to three dimensions. However, owing to the computational economy, convenience of visualisation and analytical tractability, I carried out the modeling and simulations of the trajectory lengths and path optimisations only in 2D confined domains. Indeed, the biological questions regarding the spine calcium dynamics is a 3D diffusion problem. Following up with the excellent computational agreement with the analytical results regarding the time for the first RyR to open, however, I did not conduct an extensive trajectory analysis was in three dimensions.
Such analysis about the path optimality of diffusing ions in a spine, particularly during the existence of the SA as a physical barrier, would be important in future to substantiate the extreme statistics theory in similar microdomains. In general, such analysis could address new questions such as the dependency of extreme statistics times on geometrical properties such as three-dimensional cusps and cones that are indiscernible with one- and two-dimensional analyses. Since these geometrical barriers manifest frequently biologi-

cal structures, 3D trajectory analysis would be important also for understanding other biological timescales with the redundancy principle.

8.2.2 Extreme statistics with killing

Killing processes are ubiquitous in biology at different timescales and different spatial dimensions such as neurodegeneration, cancer cell biology and population genetics [194]. In my study, the main biophysical players accounting for killing dynamics of calcium ions are SERCA and spatial pumps, both located in spine heads. I initially calculated the effect of pumps when calibrating the spine model using with the experimentally-measured decay times in the spine head.

In the extreme statistics framework, components with fast killing dynamics effectively reduces the initial number of diffusing particles initially present at the source position. In both simulations and in the mean-field model for SA refilling dynamics, I showed that injecting 500 ions to the head in the presence of 50 calcium pumps was roughly equivalent to about only 100 ions without the pumps.

Therefore, computing the effects of killing processes in diffusing domains is vital for the quantitative analysis of molecular concentrations as well as timescales. Particularly, future work should also focus on the interplay between the extreme statistics and multiple killing processes working in different timescales similar to surface pumps (few ms), SERCA pumps (in few tens-hundreds of ms), and calcium buffers (few hundred milliseconds). Analysis in generalised domains with multiple timescales would be critical for multiscale biophysical modeling and stochastic simulations.

Bibliography

1. F. A. Azevedo, L. R. Carvalho, L. T. Grinberg, J. M. Farfel, R. E. Ferretti, R. E. Leite, W. J. Filho, R. Lent, and S. Herculano-Houzel, "Equal numbers of neuronal and nonneuronal cells make the human brain an isometrically scaled-up primate brain," *Journal of Comparative Neurology*, vol. 513, no. 5, pp. 532–541, 2009.

2. D. A. Drachman, "Do we have brain to spare?," 2005.

3. I. Bars, J. Terning, and F. Nekoogar, *Extra dimensions in space and time*. Springer, 2010.

4. D. Marr, "Vision: A computational approach," 1982.

5. W. B. Scoville and B. Milner, "Loss of recent memory after bilateral hippocampal lesions," *Journal of neurology, neurosurgery, and psychiatry*, vol. 20, no. 1, p. 11, 1957.

6. E. G. Gray, "Axo-somatic and axo-dendritic synapses of the cerebral cortex: an electron microscope study," *Journal of anatomy*, vol. 93, no. Pt 4, p. 420, 1959.

7. G. L. Fain, *Molecular and cellular physiology of neurons*. Harvard University Press, 1999.

8. G.-q. Bi and M.-m. Poo, "Synaptic modifications in cultured hippocampal neurons: dependence on spike timing, synaptic strength, and postsynaptic cell type," *Journal of neuroscience*, vol. 18, no. 24, pp. 10464–10472, 1998.

9. T. Mizuno, I. Kanazawa, and M. Sakurai, "Differential induction of ltp and ltd is not determined solely by instantaneous calcium concentration: an essential involvement of a temporal factor," *European Journal of Neuroscience*, vol. 14, no. 4, pp. 701–708, 2001.

10. T. Nevian and B. Sakmann, "Spine ca2+ signaling in spike-timing-dependent plasticity," *Journal of Neuroscience*, vol. 26, no. 43, pp. 11001–11013, 2006.

11. T. V. Bliss and G. L. Collingridge, "A synaptic model of memory: long-term potentiation in the hippocampus," *Nature*, vol. 361, no. 6407, pp. 31–39, 1993.

12. A. Majewska, A. Tashiro, and R. Yuste, "Regulation of spine calcium dynamics by rapid spine motility," *Journal of Neuroscience*, vol. 20, no. 22, pp. 8262–8268, 2000.

13. M. J. Higley and B. L. Sabatini, "Calcium signaling in dendritic spines," *Cold Spring Harbor perspectives in biology*, vol. 4, no. 4, p. a005686, 2012.

14. N. Holbro, A. Grunditz, and T. G. Oertner, "Differential distribution of endoplasmic reticulum controls metabotropic signaling and plasticity at hippocampal synapses," *Proceedings of the National Academy of Sciences*, vol. 106, no. 35, pp. 15055–15060, 2009.

15. E. G. Gray, "Electron microscopy of synaptic contacts on dendrite spines of the cerebral cortex," *Nature*, vol. 183, no. 4675, pp. 1592–1593, 1959.

16. J. Spacek and K. M. Harris, "Three-dimensional organization of smooth endoplasmic reticulum in hippocampal ca1 dendrites and dendritic spines of the immature and mature rat," *Journal of Neuroscience*, vol. 17, no. 1, pp. 190–203, 1997.

17. T. Deller, T. Merten, S. U. Roth, P. Mundel, and M. Frotscher, "Actin-associated protein synaptopodin in the rat hippocampal formation: localization in the spine neck and close association with the spine apparatus of principal neurons," *Journal of Comparative Neurology*, vol. 418, no. 2, pp. 164–181, 2000.

18. T. Deller, M. Korte, S. Chabanis, A. Drakew, H. Schwegler, G. G. Stefani, A. Zuniga, K. Schwarz, T. Bonhoeffer, R. Zeller, *et al.*, "Synaptopodin-deficient mice lack a spine apparatus and show deficits in synaptic plasticity," *Proceedings of the National Academy of Sciences*, vol. 100, no. 18, pp. 10494–10499, 2003.

19. A. Vlachos, E. Korkotian, E. Schonfeld, E. Copanaki, T. Deller, and M. Segal, "Synaptopodin regulates plasticity of dendritic spines in hippocampal neurons," *Journal of Neuroscience*, vol. 29, no. 4, pp. 1017–1033, 2009.

20. A. H. Sharp, P. S. McPherson, T. M. Dawson, C. Aoki, K. P. Campbell, and S. H. Snyder, "Differential immunohistochemical localization of inositol 1, 4, 5-trisphosphate-and ryanodine-sensitive ca2+ release channels in rat brain," *Journal of Neuroscience*, vol. 13, no. 7, pp. 3051–3063, 1993.

21. N. Abu-Omar, J. Das, V. Szeto, and Z.-P. Feng, "Neuronal ryanodine receptors in development and aging," *Molecular neurobiology*, vol. 55, no. 2, pp. 1183–1192, 2018.

22. T. Nakamura, J.-G. Barbara, K. Nakamura, and W. N. Ross, "Synergistic release of ca2+ from ip3-sensitive stores evoked by synaptic activation of mglurs paired with backpropagating action potentials," *Neuron*, vol. 24, no. 3, pp. 727–737, 1999.

23. P. Jedlicka, A. Vlachos, S. W. Schwarzacher, and T. Deller, "A role for the spine apparatus in ltp and spatial learning," *Behavioural brain research*, vol. 192, no. 1, pp. 12–19, 2008.

24. E. Korkotian and M. Segal, "Fast confocal imaging of calcium released from stores in dendritic spines," *European Journal of Neuroscience*, vol. 10, no. 6, pp. 2076–2084, 1998.

25. I. Jayasinghe, A. H. Clowsley, R. Lin, T. Lutz, C. Harrison, E. Green, D. Baddeley, L. Di Michele, and C. Soeller, "True molecular scale visualization of variable clustering properties of ryanodine receptors," *Cell Reports*, vol. 22, no. 2, pp. 557–567, 2018.

26. J. S. Sham, L.-S. Song, Y. Chen, L.-H. Deng, M. D. Stern, E. G. Lakatta, and H. Cheng, "Termination of ca2+ release by a local inactivation of ryanodine receptors in cardiac myocytes," *Proceedings of the National Academy of Sciences*, vol. 95, no. 25, pp. 15096–15101, 1998.

27. O. Brandman, J. Liou, W. S. Park, and T. Meyer, "Stim2 is a feedback regulator that stabilizes basal cytosolic and endoplasmic reticulum ca2+ levels," *Cell*, vol. 131, no. 7, pp. 1327–1339, 2007.

28. F. Moccia, E. Zuccolo, T. Soda, F. Tanzi, G. Guerra, L. Mapelli, F. Lodola, and E. D'Angelo, "Stim and orai proteins in neuronal ca2+ signaling and excitability," *Frontiers in cellular neuroscience*, vol. 9, p. 153, 2015.

29. M. Hoth and B. A. Niemeyer, "The neglected crac proteins: Orai2, orai3, and stim2," *Current topics in membranes*, vol. 71, pp. 237–271, 2013.

30. H. Zhang, L. Wu, E. Pchitskaya, O. Zakharova, T. Saito, T. Saido, and I. Bezprozvanny, "Neuronal store-operated calcium entry and mushroom spine loss in amyloid precursor protein knock-in mouse model of alzheimer's disease," *Journal of Neuroscience*, vol. 35, no. 39, pp. 13275–13286, 2015.

31. E. Korkotian, E. Oni-Biton, and M. Segal, "The role of the store-operated calcium entry channel orai1 in cultured rat hippocampal synapse formation and plasticity," *The Journal of physiology*, vol. 595, no. 1, pp. 125–140, 2017.

32. P. G. Hogan, "The stim1–orai1 microdomain," *Cell calcium*, vol. 58, no. 4, pp. 357–367, 2015.

33. A. Einstein, *Investigations on the Theory of the Brownian Movement*. Courier Corporation, 1956.

34. P. Langevin, "Sur la théorie du mouvement brownien," *Compt. Rendus*, vol. 146, pp. 530–533, 1908.

35. M. Smoluchowski, "Studien über molekularstatistik von emulsionen und deren zusammenhang mit der brown'schen bewegung," *Pisma Mariana Smoluchowskiego*, vol. 1, no. 2, pp. 399–421, 1927.

36. V. Balakrishnan, *Elements of nonequilibrium statistical mechanics*, vol. 3. Ane Books, 2008.

37. D. Holcman and Z. Schuss, "The narrow escape problem," *SIAM Review*, vol. 56, no. 2, pp. 213–257, 2014.

38. A. Bensdorp, B. J. Cohlen, M. J. Heineman, and P. Vandekerckhove, "Intrauterine insemination for male subfertility," *Cochrane Database Syst Rev*, vol. 4, no. 4, 2007.

39. J. Yang, I. Kupka, Z. Schuss, and D. Holcman, "Search for a small egg by spermatozoa in restricted geometries," *Journal of mathematical biology*, vol. 73, no. 2, pp. 423–446, 2016.

40. D. Holcman, N. Hoze, and Z. Schuss, "Narrow escape through a funnel and effective diffusion on a crowded membrane.," *Phys Rev E*, vol. 84, p. 021906, 2011.

41. D. Holcman and Z. Schuss, "Stochastic narrow escape in molecular and cellular biology," *Analysis and Applications. Springer, New York*, 2015.

42. K. Basnayake, D. Mazaud, A. Bemelmans, N. Rouach, E. Korkotian, and D. Holcman, "Fast calcium transients in dendritic spines driven by extreme statistics," *PLoS biology*, vol. 17, no. 6, 2019.

43. R. L. Huganir and R. A. Nicoll, "Ampars and synaptic plasticity: the last 25 years," *Neuron*, vol. 80, no. 3, pp. 704–717, 2013.

44. E. Korkotian, M. Frotscher, and M. Segal, "Synaptopodin regulates spine plasticity: mediation by calcium stores," *Journal of Neuroscience*, vol. 34, no. 35, pp. 11641–11651, 2014.

45. M. V. Tsodyks and H. Markram, "The neural code between neocortical pyramidal neurons depends on neurotransmitter release probability," *Proceedings of the national academy of sciences*, vol. 94, no. 2, pp. 719–723, 1997.

46. N. Volfovsky, H. Parnas, M. Segal, and E. Korkotian, "Geometry of dendritic spines affects calcium dynamics in hippocampal neurons: theory and experiments," *Journal of neurophysiology*, vol. 82, no. 1, pp. 450–462, 1999.

47. D. Holcman, Z. Schuss, and E. Korkotian, "Calcium dynamics in dendritic spines and spine motility," *Biophysical journal*, vol. 87, no. 1, pp. 81–91, 2004.

48. C. Guerrier, E. Korkotian, and D. Holcman, "Calcium dynamics in neuronal microdomains: Modeling, stochastic simulations, and data analysis," *Encyclopedia of Computational Neuroscience*, pp. 486–516, 2015.

49. B. Katz, O. Voolstra, H. Tzadok, B. Yasin, E. Rhodes-Modrov, J.-P. Bartels, L. Strauch, A. Huber, and B. Minke, "The latency of the light response is modulated by the phosphorylation state of drosophila trp at a specific site," *Channels*, vol. 37, pp. 1–8, 2017.

50. O. P. Gross, E. N. Pugh, and M. E. Burns, "Calcium feedback to cgmp synthesis strongly attenuates single-photon responses driven by long rhodopsin lifetimes," *Neuron*, vol. 76, no. 2, pp. 370–382, 2012.

51. J. Reingruber, J. Pahlberg, M. L. Woodruff, A. P. Sampath, G. L. Fain, and D. Holcman, "Detection of single photons by toad and mouse rods," *Proceedings of the National Academy of Sciences*, vol. 110, no. 48, pp. 19378–19383, 2013.

52. A. Taflia and D. Holcman, "Estimating the synaptic current in a multiconductance ampa receptor model," *Biophysical journal*, vol. 101, no. 4, pp. 781–792, 2011.

53. D. Freche, U. Pannasch, N. Rouach, and D. Holcman, "Synapse geometry and receptor dynamics modulate synaptic strength," *PloS one*, vol. 6, no. 10, p. e25122, 2011.

54. B. Hille *et al.*, *Ion channels of excitable membranes*, vol. 507. Sinauer Sunderland, MA, 2001.

55. I. M. Sokolov, R. Metzler, K. Pant, and M. C. Williams, "First passage time of n excluded-volume particles on a line," *Physical Review E*, vol. 72, no. 4, p. 041102, 2005.

56. A. Zilman and G. Bel, "Crowding effects in non-equilibrium transport through nano-channels," *Journal of Physics: Condensed Matter*, vol. 22, no. 45, p. 454130, 2010.

57. S. B. Yuste and K. Lindenberg, "Order statistics for first passage times in one-dimensional diffusion processes," *Journal of statistical physics*, vol. 85, no. 3, pp. 501–512, 1996.

58. S. B. Yuste, L. Acedo, and K. Lindenberg, "Order statistics for d-dimensional diffusion processes," *Physical Review E*, vol. 64, no. 5, p. 052102, 2001.

59. S. N. Majumdar and A. Pal, "Extreme value statistics of correlated random variables," *arXiv preprint arXiv:1406.6768*, 2014.

60. T. Chou and M. D'orsogna, "First passage problems in biology," *First-Passage Phenomena and Their Applications*, vol. 35, p. 306, 2014.

61. G. Schehr, "Extremes of n vicious walkers for large n: application to the directed polymer and kpz interfaces," *Journal of Statistical Physics*, vol. 149, no. 3, pp. 385–410, 2012.

62. S. Redner and B. Meerson, "First invader dynamics in diffusion-controlled absorption," *Journal of Statistical Mechanics: Theory and Experiment*, vol. 2014, no. 6, p. P06019, 2014.

63. D. Holcman and Z. Schuss, "Escape through a small opening: receptor trafficking in a synaptic membrane," *Journal of Statistical Physics*, vol. 117, no. 5, pp. 975–1014, 2004.

64. A. Singer, Z. Schuss, and D. Holcman, "Narrow escape, part iii: Non-smooth domains and riemann surfaces," *Journal of statistical physics*, vol. 122, no. 3, pp. 491–509, 2006.

65. Z. Schuss, A. Singer, and D. Holcman, "The narrow escape problem for diffusion in cellular microdomains," *Proceedings of the National Academy of Sciences*, vol. 104, no. 41, pp. 16098–16103, 2007.

66. Y. Colin de Verdière, "Spectre du laplacien et longueurs des géodésiques périodiques i," *Compos. Math*, vol. 27, no. 1, pp. 83–106, 1973.

67. Z. Schuss and A. Spivak, "On recovering the shape of a domain from the trace of the heat kernel," *SIAM Journal on Applied Mathematics*, vol. 66, no. 1, pp. 339–360, 2005.

68. P. Krapivsky, S. N. Majumdar, and A. Rosso, "Maximum of n independent brownian walkers till the first exit from the half-space," *Journal of Physics A: Mathematical and Theoretical*, vol. 43, no. 31, p. 315001, 2010.

69. D. Holcman and Z. Schuss, "Diffusion escape through a cluster of small absorbing windows," *Journal of Physics A: Mathematical and Theoretical*, vol. 41, no. 15, p. 155001, 2008.

70. M. Abramowitz and I. A. Stegun, *Handbook of mathematical functions: with formulas, graphs, and mathematical tables*, vol. 55. Courier Corporation, 1964.

71. W. Chen and M. J. Ward, "The stability and dynamics of localized spot patterns in the two-dimensional gray–scott model," *SIAM Journal on Applied Dynamical Systems*, vol. 10, no. 2, pp. 582–666, 2011.

72. Z. Schuss, *Theory and applications of stochastic processes: an analytical approach*, vol. 170. Springer Science & Business Media, 2009.

73. D. Holcman, A. Marchewka, and Z. Schuss, "Survival probability of diffusion with trapping in cellular neurobiology," *Physical Review E*, vol. 72, no. 3, p. 031910, 2005.

74. Z. Schuss, *Brownian dynamics at boundaries and interfaces*. Springer, 2015.

75. A. J. Bray, S. N. Majumdar, and G. Schehr, "Persistence and first-passage properties in nonequilibrium systems," *Advances in Physics*, vol. 62, no. 3, pp. 225–361, 2013.

76. C. Mejía-Monasterio, G. Oshanin, and G. Schehr, "First passages for a search by a swarm of independent random searchers," *Journal of Statistical Mechanics: Theory and Experiment*, vol. 2011, no. 06, p. P06022, 2011.

77. B. Meerson and S. Redner, "Mortality, redundancy, and diversity in stochastic search," *Physical review letters*, vol. 114, no. 19, p. 198101, 2015.

78. S. N. Majumdar, "Brownian functionals in physics and computer science," in *The Legacy Of Albert Einstein: A Collection of Essays in Celebration of the Year of Physics*, pp. 93–129, World Scientific, 2007.

79. G. Schehr and S. N. Majumdar, "Exact record and order statistics of random walks via first-passage ideas," in *First-Passage Phenomena and Their Applications*, pp. 226–251, World Scientific, 2014.

80. K. Basnayake, Z. Schuss, and D. Holcman, "Asymptotic formulas for extreme statistics of escape times in 1, 2 and 3-dimensions," *Journal of Nonlinear Science*, vol. 29, no. 2, pp. 461–499, 2019.

81. T. Aubin, *Some nonlinear problems in Riemannian geometry*. Springer Science & Business Media, 2013.

82. M. Dykman, "Mi dykman, phys. rev. a 42, 2020 (1990).," *Phys. Rev. A*, vol. 42, p. 2020, 1990.

83. R. Graham and T. Tél, "On the weak-noise limit of fokker-planck models," *Journal of statistical physics*, vol. 35, no. 5-6, pp. 729–748, 1984.

84. M. Dykman, V. Smelyanskiy, D. Luchinsky, R. Mannella, P. V. McClintock, and N. Stein, "Large fluctuations in a periodically driven dynamical system," *International Journal of Bifurcation and Chaos*, vol. 8, no. 04, pp. 747–754, 1998.

85. R. S. Maier and D. L. Stein, "Escape problem for irreversible systems," *Physical Review E*, vol. 48, no. 2, p. 931, 1993.

86. M. I. Freidlin and A. D. Wentzell, "Random perturbations," in *Random Perturbations of Dynamical Systems*, pp. 15–43, Springer, 1998.

87. R. S. Maier and D. L. Stein, "A scaling theory of bifurcations in the symmetric weak-noise escape problem," *Journal of statistical physics*, vol. 83, no. 3-4, pp. 291–357, 1996.

88. M. I. Dykman, M. M. Millonas, and V. N. Smelyanskiy, "Observable and hidden singular features of large fluctuations in nonequilibrium systems," *arXiv preprint cond-mat/9410056*, 1994.

89. M. Dykman, D. Luchinsky, P. V. McClintock, and V. Smelyanskiy, "Corrals and critical behavior of the distribution of fluctuational paths," *Physical review letters*, vol. 77, no. 26, p. 5229, 1996.

90. A. Marchewka and Z. Schuss, "Path-integral approach to the schrödinger current," *Physical Review A*, vol. 61, no. 5, p. 052107, 2000.

91. Z. Schuss, *Nonlinear filtering and optimal phase tracking*, vol. 180. Springer Science & Business Media, 2011.

92. D. Holcman and Z. Schuss, "100 years after smoluchowski: stochastic processes in cell biology," *Journal of Physics A: Mathematical and Theoretical*, vol. 50, no. 9, p. 093002, 2017.

93. G. Malherbe and D. Holcman, "Search for a dna target site in the nucleus," *Phys. Lett. A.*, vol. 374, pp. 466–471, 2010.

94. K. Basnayake and D. Holcman, "Extreme escape from a cusp: When does geometry matter for the fastest brownian particles moving in crowded cellular environments?," *The Journal of chemical physics*, vol. 152, no. 13, p. 134104, 2020.

95. Z. Schuss, K. Basnayake, and D. Holcman, "Redundancy principle and the role of extreme statistics in molecular and cellular biology," *Physics of life reviews*, 2019.

96. S. Pillay, M. J. Ward, A. Peirce, and T. Kolokolnikov, "An asymptotic analysis of the mean first passage time for narrow escape problems: Part i: Two-dimensional domains," *Multiscale Modeling & Simulation*, vol. 8, no. 3, pp. 803–835, 2010.

97. A. F. Cheviakov, M. J. Ward, and R. Straube, "An asymptotic analysis of the mean first passage time for narrow escape problems: Part ii: The sphere," *Multiscale Modeling & Simulation*, vol. 8, no. 3, pp. 836–870, 2010.

98. D. Holcman and Z. Schuss, "Control of flux by narrow passages and hidden targets in cellular biology," *Reports on Progress in Physics*, vol. 76, no. 7, p. 074601, 2013.

99. T. G. Mattos, C. Mejía-Monasterio, R. Metzler, G. Oshanin, and G. Schehr, "Trajectory-to-trajectory fluctuations in first-passage phenomena in bounded domains," in *First-passage phenomena and their applications*, pp. 203–225, World Scientific, 2014.

100. K. Basnayake, A. Hubl, Z. Schuss, and D. Holcman, "Extreme narrow escape: Shortest paths for the first particles among n to reach a target window," *Physics Letters A*, vol. 382, no. 48, pp. 3449–3454, 2018.

101. G. H. Weiss, K. E. Shuler, and K. Lindenberg, "Order statistics for first passage times in diffusion processes," *Journal of Statistical Physics*, vol. 31, no. 2, pp. 255–278, 1983.

102. D. Holcman and Z. Schuss, "Brownian needle in dire straits: stochastic motion of a rod in very confined narrow domains," *Physical Review E*, vol. 85, no. 1, p. 010103, 2012.

103. D. Holcman and Z. Schuss, *Asymptotics of Elliptic and Parabolic PDEs: and their Applications in Statistical Physics, Computational Neuroscience, and Biophysics*, vol. 199. Springer, 2018.

104. M. Segal, "Dendritic spines and long-term plasticity," *Nature Reviews Neuroscience*, vol. 6, no. 4, pp. 277–284, 2005.

105. R. Yuste, *Dendritic spines*. MIT press, 2010.

106. H. Makino and R. Malinow, "Ampa receptor incorporation into synapses during ltp: the role of lateral movement and exocytosis," *Neuron*, vol. 64, no. 3, pp. 381–390, 2009.

107. E. J. Griffiths and G. A. Rutter, "Mitochondrial calcium as a key regulator of mitochondrial atp production in mammalian cells," *Biochimica et Biophysica Acta (BBA)-Bioenergetics*, vol. 1787, no. 11, pp. 1324–1333, 2009.

108. N. Demaurex, D. Poburko, and M. Frieden, "Regulation of plasma membrane calcium fluxes by mitochondria," *Biochimica et Biophysica Acta (BBA)-Bioenergetics*, vol. 1787, no. 11, pp. 1383–1394, 2009.

109. L. Contreras, I. Drago, E. Zampese, and T. Pozzan, "Mitochondria: the calcium connection," *Biochimica et Biophysica Acta (BBA)-Bioenergetics*, vol. 1797, no. 6-7, pp. 607–618, 2010.

110. J. N. Bourne and K. M. Harris, "Balancing structure and function at hippocampal dendritic spines," *Annu. Rev. Neurosci.*, vol. 31, pp. 47–67, 2008.

111. J. Noguchi, T. Hayama, S. Watanabe, H. Ucar, S. Yagishita, N. Takahashi, and H. Kasai, "State-dependent diffusion of actin-depolymerizing factor/cofilin underlies the enlargement and shrinkage of dendritic spines," *Scientific reports*, vol. 6, p. 32897, 2016.

112. J. Noguchi, M. Matsuzaki, G. C. Ellis-Davies, and H. Kasai, "Spine-neck geometry determines nmda receptor-dependent ca 2+ signaling in dendrites," *Neuron*, vol. 46, no. 4, pp. 609–622, 2005.

113. W. Rall, "Dendritic spines, synaptic potency and neuronal plasticity," in *Cellular mechanisms subserving changes in neuronal activity*, vol. 3, pp. 13–21, Brain Information Service, Los Angeles, 1974.

114. A. Zador, C. Koch, and T. H. Brown, "Biophysical model of a hebbian synapse," *Proceedings of the National Academy of Sciences*, vol. 87, no. 17, pp. 6718–6722, 1990.

115. K. Svoboda, D. W. Tank, and W. Denk, "Direct measurement of coupling between dendritic spines and shafts," *Science*, vol. 272, no. 5262, p. 716, 1996.

116. E. Korkotian, D. Holcman, and M. Segal, "Dynamic regulation of spine–dendrite coupling in cultured hippocampal neurons," *European Journal of Neuroscience*, vol. 20, no. 10, pp. 2649–2663, 2004.

117. J. Nishiyama and R. Yasuda, "Biochemical computation for spine structural plasticity," *Neuron*, vol. 87, no. 1, pp. 63–75, 2015.

118. D. Holcman and R. Yuste, "The new nanophysiology: regulation of ionic flow in neuronal subcompartments," *Nature Reviews Neuroscience*, vol. 16, no. 11, pp. 685–692, 2015.

119. R. Araya, T. P. Vogels, and R. Yuste, "Activity-dependent dendritic spine neck changes are correlated with synaptic strength," *Proceedings of the National Academy of Sciences*, vol. 111, no. 28, pp. E2895–E2904, 2014.

120. J. Cartailler, T. Know, R. Yuste, and D. Holcman, "Deconvolution of voltage sensor time series and electro-diffusion modeling reveal the role of spine geometry in controlling synaptic strength," *Neuron*, 2018.

121. J. I. Arellano, R. Benavides-Piccione, J. DeFelipe, and R. Yuste, "Ultrastructure of dendritic spines: correlation between synaptic and spine morphologies," *Frontiers in neuroscience*, vol. 1, p. 10, 2007.

122. M. Segal and E. Korkotian, "Roles of calcium stores and store-operated channels in plasticity of dendritic spines," *The Neuroscientist*, vol. 22, no. 5, pp. 477–485, 2016.

123. N. Holbro, A. Grunditz, J. S. Wiegert, and T. G. Oertner, "Ampa receptors gate spine ca2+ transients and spike-timing-dependent potentiation," *Proceedings of the National Academy of Sciences*, vol. 107, no. 36, pp. 15975–15980, 2010.

124. M. J. Berridge, "The endoplasmic reticulum: a multifunctional signaling organelle," *Cell calcium*, vol. 32, no. 5, pp. 235–249, 2002.

125. E. Korkotian and M. Segal, "Synaptopodin regulates release of calcium from stores in dendritic spines of cultured hippocampal neurons," *The Journal of physiology*, vol. 589, no. 24, pp. 5987–5995, 2011.

126. R. Yuste, A. Majewska, and K. Holthoff, "From form to function: calcium compartmentalization in dendritic spines," *Nature neuroscience*, vol. 3, no. 7, pp. 653–659, 2000.

127. J.-Y. Chang, P. Parra-Bueno, T. Laviv, E. M. Szatmari, S.-J. R. Lee, and R. Yasuda, "Camkii autophosphorylation is necessary for optimal integration of ca 2+ signals during ltp induction, but not maintenance," *Neuron*, vol. 94, no. 4, pp. 800–808, 2017.

128. B. L. Bloodgood and B. L. Sabatini, "Neuronal activity regulates diffusion across the neck of dendritic spines," *Science*, vol. 310, no. 5749, pp. 866–869, 2005.

129. F. W. Johenning, A.-K. Theis, U. Pannasch, M. Rückl, S. Rüdiger, and D. Schmitz, "Ryanodine receptor activation induces long-term plasticity of spine calcium dynamics," *PLoS biology*, vol. 13, no. 6, p. e1002181, 2015.

130. N. Hernjak, B. M. Slepchenko, K. Fernald, C. C. Fink, D. Fortin, I. I. Moraru, J. Watras, and L. M. Loew, "Modeling and analysis of calcium signaling events leading to long-term depression in cerebellar purkinje cells," *Biophysical journal*, vol. 89, no. 6, pp. 3790–3806, 2005.

131. D. X. Keller, K. M. Franks, T. M. Bartol Jr, and T. J. Sejnowski, "Calmodulin activation by calcium transients in the postsynaptic density of dendritic spines," *PLoS One*, vol. 3, no. 4, p. e2045, 2008.

132. D. A. Rusakov, "The role of perisynaptic glial sheaths in glutamate spillover and extracellular ca 2+ depletion," *Biophysical Journal*, vol. 81, no. 4, pp. 1947–1959, 2001.

133. M. J. Byrne, M. N. Waxham, and Y. Kubota, "The impacts of geometry and binding on camkii diffusion and retention in dendritic spines," *Journal of computational neuroscience*, vol. 31, no. 1, pp. 1–12, 2011.

134. A. Biess, E. Korkotian, and D. Holcman, "Diffusion in a dendritic spine: the role of geometry," *Physical Review E*, vol. 76, no. 2, p. 021922, 2007.

135. E. Korkotian, D. Oron, Y. Silberberg, and M. Segal, "Confocal microscopic imaging of fast uv-laser photolysis of caged compounds," *Journal of neuroscience methods*, vol. 133, no. 1-2, pp. 153–159, 2004.

136. L. P. Savtchenko and D. A. Rusakov, "The optimal height of the synaptic cleft," *Proceedings of the National Academy of Sciences*, vol. 104, no. 6, pp. 1823–1828, 2007.

137. L. P. Savtchenko, M. M. Poo, and D. A. Rusakov, "Electrodiffusion phenomena in neuroscience: a neglected companion.," *Nature reviews. Neuroscience*, vol. 18, no. 10, p. 598, 2017.

138. K. Mikoshiba, "Role of ip 3 receptor signaling in cell functions and diseases," *Advances in biological regulation*, vol. 57, pp. 217–227, 2015.

139. R. Iosub, D. Avitabile, L. Grant, K. Tsaneva-Atanasova, and H. J. Kennedy, "Calcium-induced calcium release during action potential firing in developing inner hair cells," *Biophysical journal*, vol. 108, no. 5, pp. 1003–1012, 2015.

140. A.-K. Theis, B. Rózsa, G. Katona, D. Schmitz, and F. W. Johenning, "Voltage gated calcium channel activation by backpropagating action potentials downregulates nmdar function," *Frontiers in cellular neuroscience*, vol. 12, 2018.

141. K. Zheng, L. Bard, J. P. Reynolds, C. King, T. P. Jensen, A. V. Gourine, and D. A. Rusakov, "Time-resolved imaging reveals heterogeneous landscapes of nanomolar ca2+ in neurons and astroglia," *Neuron*, vol. 88, no. 2, pp. 277–288, 2015.

142. A. Biess, E. Korkotian, and D. Holcman, "Barriers to diffusion in dendrites and estimation of calcium spread following synaptic inputs," *PLoS computational biology*, vol. 7, no. 10, p. e1002182, 2011.

143. N. Solovyova, N. Veselovsky, E. Toescu, and A. Verkhratsky, "Ca 2+ dynamics in the lumen of the endoplasmic reticulum in sensory neurons: direct visualization of ca 2+-induced ca 2+ release triggered by physiological ca 2+ entry," *The EMBO journal*, vol. 21, no. 4, pp. 622–630, 2002.

144. R. D. Burgoyne and T. R. Cheek, "Locating intracellular calcium stores," *Trends in biochemical sciences*, vol. 16, pp. 319–320, 1991.

145. Y. Hirabayashi, S.-K. Kwon, H. Paek, W. M. Pernice, M. A. Paul, J. Lee, P. Erfani, A. Raczkowski, D. S. Petrey, L. A. Pon, and F. Polleux, "Er-mitochondria tethering by pdzd8 regulates ca2+ dynamics in mammalian neurons," *Science*, vol. 358, no. 6363, pp. 623–630, 2017.

146. J. P. Keener and J. Sneyd, *Mathematical physiology*, vol. 1. Springer, 1998.

147. M. R. Sharma, L. H. Jeyakumar, S. Fleischer, and T. Wagenknecht, "Three-dimensional structure of ryanodine receptor isoform three in two conformational states as visualized by cryo-electron microscopy," *Journal of Biological Chemistry*, vol. 275, no. 13, pp. 9485–9491, 2000.

148. F. Van Petegem, "Ryanodine receptors: structure and function," *Journal of Biological Chemistry*, vol. 287, no. 38, pp. 31624–31632, 2012.

149. M. D. Stern, G. Pizarro, and E. Ríos, "Local control model of excitation–contraction coupling in skeletal muscle," *The Journal of General Physiology*, vol. 110, no. 4, pp. 415–440, 1997.

150. D. Friel, "Interplay between er ca2+ uptake and release fluxes in neurons and its impact on [ca2+] dynamics," *Biological research*, vol. 37, no. 4, pp. 665–674, 2004.

151. S. L. Hamilton and I. I. Serysheva, "Ryanodine receptor structure: progress and challenges," *Journal of Biological Chemistry*, vol. 284, no. 7, pp. 4047–4051, 2009.

152. G. Dupont, M. Falcke, V. Kirk, and J. Sneyd, "Models of calcium signalling," 2016.

153. L. M. Espinoza-Fonseca and D. D. Thomas, "Atomic-level characterization of the activation mechanism of serca by calcium," *PLoS One*, vol. 6, no. 10, p. e26936, 2011.

154. J. T. Koivumäki, J. Takalo, T. Korhonen, P. Tavi, and M. Weckström, "Modelling sarcoplasmic reticulum calcium atpase and its regulation in cardiac myocytes," *Philosophical Transactions of the Royal Society of London A: Mathematical, Physical and Engineering Sciences*, vol. 367, no. 1896, pp. 2181–2202, 2009.

155. J. A. Cummings, R. M. Mulkey, R. A. Nicoll, and R. C. Malenka, "Ca2+ signaling requirements for long-term depression in the hippocampus," *Neuron*, vol. 16, no. 4, pp. 825–833, 1996.

156. H. Murakoshi and R. Yasuda, "Postsynaptic signaling during plasticity of dendritic spines," *Trends in neurosciences*, vol. 35, no. 2, pp. 135–143, 2012.

157. R. Yuste and T. Bonhoeffer, "Morphological changes in dendritic spines associated with long-term synaptic plasticity," *Annual review of neuroscience*, vol. 24, no. 1, pp. 1071–1089, 2001.

158. P. Penzes, M. E. Cahill, K. A. Jones, J.-E. VanLeeuwen, and K. M. Woolfrey, "Dendritic spine pathology in neuropsychiatric disorders," *Nature neuroscience*, vol. 14, no. 3, pp. 285–293, 2011.

159. J. Lisman, H. Schulman, and H. Cline, "The molecular basis of camkii function in synaptic and behavioural memory," *Nature Reviews Neuroscience*, vol. 3, no. 3, pp. 175–190, 2002.

160. R. Yuste and W. Denk, "Dendritic spines as basic functional units of neuronal integration," *Nature*, vol. 375, no. 6533, pp. 682–684, 1995.

161. R. Y. Tshuva, E. Korkotian, and M. Segal, "Orai1-dependent synaptic plasticity in rat hippocampal neurons," *Neurobiology of learning and memory*, vol. 140, pp. 1–10, 2017.

162. Y. Liang, L.-L. Yuan, D. Johnston, and R. Gray, "Calcium signaling at single mossy fiber presynaptic terminals in the rat hippocampus," *Journal of neurophysiology*, vol. 87, no. 2, pp. 1132–1137, 2002.

163. G. Mahajan and S. Nadkarni, "Intracellular calcium stores mediate metaplasticity at hippocampal dendritic spines," *The Journal of physiology*, vol. 597, no. 13, pp. 3473–3502, 2019.

164. J. Lisman, R. Yasuda, and S. Raghavachari, "Mechanisms of camkii action in long-term potentiation," *Nature reviews neuroscience*, vol. 13, no. 3, pp. 169–182, 2012.

165. W. R. Holmes, "Is the function of dendritic spines to concentrate calcium?," *Brain research*, vol. 519, no. 1, pp. 338–342, 1990.

166. D. Holcman and Z. Schuss, "Modeling calcium dynamics in dendritic spines," *SIAM Journal on Applied Mathematics*, vol. 65, no. 3, pp. 1006–1026, 2005.

167. M. Bell, T. Bartol, T. Sejnowski, and P. Rangamani, "Dendritic spine geometry and spine apparatus organization govern the spatiotemporal dynamics of calcium," *Journal of General Physiology*, vol. 151, no. 8, pp. 1017–1034, 2019.

168. O. Rackham, K. Tsaneva-Atanasova, A. Ganesh, and J. Mellor, "A ca2+-based computational model for nmda receptor-dependent synaptic plasticity at individual post-synaptic spines in the hippocampus," *Frontiers in synaptic neuroscience*, vol. 2, p. 31, 2010.

169. G. A. Kerchner and R. A. Nicoll, "Silent synapses and the emergence of a postsynaptic mechanism for ltp," *Nature Reviews Neuroscience*, vol. 9, no. 11, pp. 813–825, 2008.

170. M. Marchena and B. Echebarria, "Computational model of calcium signaling in cardiac atrial cells at the submicron scale," *Frontiers in physiology*, vol. 9, p. 1760, 2018.

171. E. McIvor, S. Coombes, and R. Thul, "Three-dimensional spatio-temporal modelling of store operated ca2+ entry: Insights into er refilling and the spatial signature of ca2+ signals," *Cell calcium*, vol. 73, pp. 11–24, 2018.

172. M. Matsuzaki, N. Honkura, G. C. Ellis-Davies, and H. Kasai, "Structural basis of long-term potentiation in single dendritic spines," *Nature*, vol. 429, no. 6993, pp. 761–766, 2004.

173. M. Borczyk, M. A. Śliwińska, A. Caly, T. Bernas, and K. Radwanska, "Neuronal plasticity affects correlation between the size of dendritic spine and its postsynaptic density," *Scientific reports*, vol. 9, no. 1, pp. 1–12, 2019.

174. Y. J. Yoon, B. Wu, A. R. Buxbaum, S. Das, A. Tsai, B. P. English, J. B. Grimm, L. D. Lavis, and R. H. Singer, "Glutamate-induced rna localization and translation in neurons," *Proceedings of the National Academy of Sciences*, vol. 113, no. 44, pp. E6877–E6886, 2016.

175. V. Rangaraju, S. tom Dieck, and E. M. Schuman, "Local translation in neuronal compartments: how local is local?," *EMBO reports*, vol. 18, no. 5, pp. 693–711, 2017.

176. Q. Zhou, K. J. Homma, and M.-m. Poo, "Shrinkage of dendritic spines associated with long-term depression of hippocampal synapses," *Neuron*, vol. 44, no. 5, pp. 749–757, 2004.

177. M. D. Ehlers, "Dendritic trafficking for neuronal growth and plasticity," 2013.

178. L. Groc and D. Choquet, "Linking glutamate receptor movements and synapse function," *Science*, vol. 368, no. 6496, 2020.

179. J. M. Henley and K. A. Wilkinson, "Ampa receptor trafficking and the mechanisms underlying synaptic plasticity and cognitive aging," *Dialogues in clinical neuroscience*, vol. 15, no. 1, p. 11, 2013.

180. N. Hoze and D. Holcman, "Residence times of receptors in dendritic spines analyzed by stochastic simulations in empirical domains," *Biophysical journal*, vol. 107, no. 12, pp. 3008–3017, 2014.

181. M. Heine and D. Holcman, "Asymmetry between pre-and postsynaptic transient nanodomains shapes neuronal communication," *Trends in Neurosciences*, vol. 43, no. 3, pp. 182–196, 2020.

182. X. Chen, X. Wu, H. Wu, and M. Zhang, "Phase separation at the synapse," *Nature Neuroscience*, pp. 1–10, 2020.

183. A. Lee, Y. Hirabayashi, S.-K. Kwon, T. L. Lewis Jr, and F. Polleux, "Emerging roles of mitochondria in synaptic transmission and neurodegeneration," *Current opinion in physiology*, vol. 3, pp. 82–93, 2018.

184. V. Todorova and A. Blokland, "Mitochondria and synaptic plasticity in the mature and aging nervous system," *Current neuropharmacology*, vol. 15, no. 1, pp. 166–173, 2017.

185. E. Korkotian and M. Segal, "Structure-function relations in dendritic spines: Is size important?," *Hippocampus*, vol. 10, no. 5, pp. 587–595, 2000.

186. T. Lagache, K. Jayant, and R. Yuste, "Electrodiffusion models of synaptic potentials in dendritic spines," *Journal of computational neuroscience*, vol. 47, no. 1, pp. 77–89, 2019.

187. J. Sibille, K. D. Duc, D. Holcman, and N. Rouach, "The neuroglial potassium cycle during neurotransmission: role of kir4. 1 channels," *PLoS Comput Biol*, vol. 11, no. 3, p. e1004137, 2015.

188. D. Holcman and Z. Schuss, "Diffusion laws in dendritic spines," *The Journal of Mathematical Neuroscience*, vol. 1, no. 1, p. 10, 2011.

189. J. R. Groff and G. D. Smith, "Ryanodine receptor allosteric coupling and the dynamics of calcium sparks," *Biophysical journal*, vol. 95, no. 1, pp. 135–154, 2008.

190. S. Karlin and H. E. Taylor, *A second course in stochastic processes*. Elsevier, 1981.

191. A. Ratnayaka, V. Marra, T. Branco, and K. Staras, "Extrasynaptic vesicle recycling in mature hippocampal neurons," *Nature communications*, vol. 2, no. 1, pp. 1–11, 2011.

192. C. Guerrier and D. Holcman, "The first 100 nm inside the pre-synaptic terminal where calcium diffusion triggers vesicular release," *Frontiers in synaptic neuroscience*, vol. 10, p. 23, 2018.

193. Z. Li, K.-I. Okamoto, Y. Hayashi, and M. Sheng, "The importance of dendritic mitochondria in the morphogenesis and plasticity of spines and synapses," *Cell*, vol. 119, no. 6, pp. 873–887, 2004.

194. S. Karlin and S. Tavaré, "A diffusion process with killing: the time to formation of recurrent deleterious mutant genes," *Stochastic Processes and their Applications*, vol. 13, no. 3, pp. 249–261, 1982.

RÉSUMÉ

La plupart des terminaux post-synaptiques neuronaux sont formés par des épines dendritiques dont l'activité biochimique est régulée par le calcium. Les transmissions rapides de calcium dans les épines se produisent en quelques millisecondes et ne peuvent pas être expliquées par la théorie de la diffusion et restent donc mal comprises. J'ai développé des modèles mathématiques et des simulations basées sur les statistiques extrêmes pour calculer le temps mis par les ions les plus rapides pour arriver à une cible. Ce nouveau cadre explique les activités transitoires rapides du calcium dans les épines et il prédit également avec précision l'emplacement des canaux contrôlant l'apport, le stockage et la libération du calcium. Ces idées, issues de l'organisation moléculaire à l'ordre nanométrique et des statistiques extrêmes pourraient également être appliquées pour déterminer les différentes échelles temporelles de nombreux processus biophysiques, activés par les particules les plus rapides.

MOTS CLÉS

biophysique du neurone, plasticité synaptique, modélisation mathématique, épine dendritique, théorie de la diffusion

ABSTRACT

Dendritic spines that form the receiving terminals of neuronal signals are regulated biochemically by calcium. Fast calcium transmissions in spines remain poorly understood as they occur in a few milliseconds and cannot be explained by classical diffusion theory. I developed mathematical models and stochastic simulations based on extreme statistics to compute the time taken by the fastest ions to arrive at a target via an optimal path. This novel framework not only explained fast calcium transients in spines, but also predicted accurately the spatial distributions of three calcium channels in spines controlling intake, storage and release. I also modeled their interplay during calcium regulation that could lead to synaptic changes underlying learning and memory. These new paradigms of nanoscale molecular organization and extreme statistics could also characterize the timescales of many other biophysical processes driven by random arrivals of the fastest particles to a small target.

KEYWORDS

neuronal biophysics, synaptic plasticity, mathematical modeling, extreme statistics dendritic spines, diffusion theory